

# **ABSTRACT**

## **THE DEVELOPMENT AND CHARACTERIZATION OF A TWO-STAGE HYBRID HALL/ION THRUSTER**

**By**

**Peter Young Peterson**

Chair: Alec D. Gallimore

This dissertation represents a design and experimental effort of developing a two-stage hybrid Hall/ion thruster that can operate efficiently at increased acceleration potentials. The dissertation also examines the efficiency loss mechanisms, which limit current state-of-the-art Hall thrusters, through the external measurements of the ion current density distributions and the ion species fractions of the plasma plume. Understanding single- and two-stage Hall thruster operation at extended acceleration potentials aids in the future designs of high-voltage and high-power Hall thrusters.

The histories and physics of Hall and ion thrusters are presented in this dissertation as the baseline for the design of a combined two-stage hybrid Hall/ion thruster, referred to as the NASA-173GT. The design of the electron-bombardment ionization stage is based on previous NASA ion thruster ionization stages. The Hall

acceleration stage channel shares the same diameter and width parameters as the University of Michigan / United States Air Forces P5 5 kW single-stage Hall thruster. The NASA-173GT design utilizes the benefits of a plasma lens field topology in the Hall acceleration stage and a flexible ionization stage magnetic circuit that allows fine-tuning of the magnetic field topology in the ionization stage.

The work presented here describes the characterization of the NASA-173GT Hall acceleration and electron-bombardment ionization stages at various operating conditions. The ionization stage characterization is accomplished using an ion collector grid. The Hall acceleration stage magnetic field is determined by a Hall probe. The performance characterization of the NASA-173GT, for both single- and two-stage operations, was presented and discussed. The plume is characterized with two plasma diagnostic techniques: an **ExB** probe for determining the ion species fractions and a gridded Faraday probe for ion current density and plume divergence.

The performance and plume characterizations of the NASA-173GT provides the means of calculating the charge, current, propellant, and voltage utilization efficiencies of the thruster in both single- and two-stage configurations. It is determined that the NASA-173GT experiences large electron current leakage across the Hall acceleration stage and large voltage losses. These inefficiencies are thought to result from the design of the Hall acceleration stage.

# **THE DEVELOPMENT AND CHARACTERIZATION OF A TWO-STAGE HYBRID HALL/ION THRUSTER**

by

**Peter Young Peterson**

A dissertation submitted in partial fulfillment  
of the requirements for the degree of  
Doctor of Philosophy  
(Aerospace Engineering)  
in The University of Michigan  
2004

Doctoral Committee:

Professor Alec D. Gallimore, Chair  
Professor Iain Boyd  
Professor Ronald M. Gilgenbach  
John Foster, NASA Glenn Research Center

© Peter Young Peterson 2004  
All Rights Reserved

## **DEDICATION**

To Kelli Jo-Biederman Peterson,  
Who has been very patient, understanding, and loving.

## ACKNOWLEDGMENTS

The processes involved for a person attempting to earn a Ph.D. are lengthy, difficult, and sometimes require luck. I have been told many times in my life that I'm a lucky person; however I never realized the truth of those statements until Professor Alec Gallimore gave me a chance to prove myself. Alec had, in less than six years, put together one of the world's foremost electric propulsion research laboratories from the remains of one of the Apollo programs. I would like to believe that Alec again saw the same potential for a good scientist and engineer in me, as he did with an old vacuum facility. I would like to thank Alec for giving me a chance to prove to myself and to allow me to accomplish the goals, of working in space propulsion, which I set for myself when I was child.

I would also like to thank the other members of my dissertation committee, Professor Iain Boyd, Professor Ronald M. Gilgenbach, and Dr. John Foster for their time and guidance. I would like to extend an special thanks to Dr. John Foster for our discussions on ion thruster physics and technologies. The administration and technical staff at the University of Michigan department of Aerospace Engineering deserve recognition for their hard work, with special thanks to Margaret Fillion and Terry Larrow.

To my PEPL peers: Brian Beal, Matt Domonkos, Frank Gulczinski, James Haas, Dan Herman, Rich Hofer, Colleen Marrese, Josh Rovey, Tim Smith, John Van Noord, Mitchell Walker, and George Williams, I would like to thank you for teaching me and listening to my sometimes crazy ideas. James, I'm not sure how you put up with us new guys but thank you for all the help with the B-Dot probe and isn't it cool that another group of researches has confirmed our results. Rich, wow look how far we have both come and thank you for being part of an research team that has pushed Hall thruster technology to new hights. Mitchell, yes the thruster is finished.

The research presented in this dissertation was made possible by the NASA Graduate Student Resreach Program (GSRP), research grants, and the personnel from NASA GRC On-Board Propulsion Branch. The GSRP and the NASA research grants were the tools that allowed me to learn electric propulsion (EP) and eventually contribute to the EP community. I would like to thank Rob Jankovsky, David Jacobson, David Manzella, Luis Pinero, and Vince Rawlin for providing guidance and sometimes a fresh perspective on the development of the NASA-173GT. The design of the NASA-173GT would not have been as elegant, and at the same time practical, with out the aid of Chris Griffiths. The fabrication, frequent repairs, and upgrades of the NASA-173GT were only possible because of the help of Kevin Blake. Kevin Blake, Howard Eakin, Eli Green, Hardy Hartman, George Jacynycz, Terry Jansen, and the rest of the technical staff at NASA GRC went beyond the call of duty to support my research and made it possible to gather as much data as I did in the limited time frame that was available for testing the NASA-173GT.

My family and friends helped me more than they know to get to this point in my life. My parents, Don and Rosie Peterson, have always believed in me and went out of their way to make sure I had all possible opportunities available to me. Mom and Dad thank you and I hope I have surpassed all your expectations. My grandma Sis, wherever she is now is probably telling everyone what her grandson has done, thank you for being the person that you were. I would like to thank my bother, Don Peterson Jr., for giving an awesome graduation gift and more importantly for becoming a person I'm proud to call my brother. My wife's parents, Earl and Sandy Biederman, have shown a great deal of interest in the work I've done and have provided encouragement along the way. I would also like to acknowledge the patience of my good friends Art Hamm, Matt Koneda, and Sandy Walke for my extended absence from gaming and paintball. Now that I'm done guys I think things may change, well maybe and/or eventually.

My lovely wife Kelli Jo-Biederman Peterson, I would like to thank and try to repay but not sure if I could ever repay the debt I owe you for the many years of graduate school and research I put you through. However, I'm sure you will think of couple of honey-do jobs. Kelli thank you for the support, this dissertation is as much yours as it is mine.

Finally, for my daughter Sydney Anna Peterson, thank you for the beautiful smiles when I came home to Ann Arbor and eventually Brunswick. You and your mother made it possible for me to finish this dissertation.

## TABLE OF CONTENTS

<b>DEDICATION .....</b>	<b>ii</b>
<b>ACKNOWLEDGMENTS.....</b>	<b>iii</b>
<b>LIST OF FIGURES .....</b>	<b>ix</b>
<b>LIST OF TABLES.....</b>	<b>xix</b>
<b>LIST OF APPENDICES .....</b>	<b>xx</b>
<b>NOMENCLATURE.....</b>	<b>xxi</b>
<b>Chapter 1 INTRODUCTION .....</b>	<b>1</b>
<b>1.1 Electric Propulsion Overview .....</b>	<b>3</b>
<b>1.2 High-Specific Impulse Electrostatic Devices .....</b>	<b>6</b>
1.2.1 Ion Thruster Technology.....	7
1.2.1.1 Recent Ion Thrusters.....	16
1.2.2 Hall Thruster Technology.....	21
1.2.2.1 Two-Stage Hall Thrusters.....	29
1.2.2.2 Recent Single-Stage High-Specific Impulse Hall Thrusters.....	42
<b>1.3 Motivation for developing a hybrid Hall/ion thruster.....</b>	<b>51</b>
<b>Chapter 2 THRUSTER DEVELOPMENT .....</b>	<b>56</b>
<b>2.1 Acceleration Hall stage scaling and design.....</b>	<b>57</b>
2.1.1 Acceleration Hall stage parameters .....	60
2.1.2 Acceleration Hall stage magnetic circuit design.....	61
2.1.3 Acceleration Hall stage materials .....	69
2.1.4 Acceleration Hall stage cathode.....	72
<b>2.2 Ionization stage scaling and design .....</b>	<b>73</b>
2.2.1 Characteristics of the ionization stage .....	77
2.2.2 Magnetic circuit design for the ionization stage.....	80

2.2.3	Cathode sizing and positioning.....	85
<b>2.3</b>	<b>Acceleration and ionization stages coupling issues.....</b>	<b>88</b>
2.3.1	Flux Shunts.....	88
2.3.2	Isolation.....	89
2.3.3	Magnetic circuit integration.....	91
<b>Chapter 3</b>	<b>FACILITIES AND DIAGNOSTIC EQUIPMENT.....</b>	<b>94</b>
<b>3.1</b>	<b>Electric Propulsion Test Facility.....</b>	<b>94</b>
3.1.1	Vacuum Facility.....	95
3.1.2	Power Consoles.....	97
3.1.3	Propellant flow system.....	99
3.1.4	Data Acquisition system.....	100
<b>3.2</b>	<b>Electric Propulsion Diagnostic Equipment.....</b>	<b>101</b>
3.2.1	Thrust Stand.....	102
3.2.2	ExB probe.....	103
3.2.2.1	ExB probe theory.....	104
3.2.2.2	ExB probe characteristics and experimental setup.....	107
3.2.2.3	ExB probe data analysis and associated uncertainty.....	110
3.2.3	Faraday probe.....	113
3.2.3.1	Faraday probe theory.....	115
3.2.3.2	Faraday probe characteristics and experimental setup.....	116
3.2.3.3	Faraday probe data analysis and associated uncertainty.....	118
3.2.4	Ionization stage ion collection grid probe.....	121
3.2.5	Hall probe.....	123
3.2.6	Thermal measurements.....	125
<b>Chapter 4</b>	<b>RESULTS.....</b>	<b>128</b>
<b>4.1</b>	<b>Magnetic field characterization.....</b>	<b>128</b>
<b>4.2</b>	<b>Ionization stage characterization.....</b>	<b>132</b>
<b>4.3</b>	<b>Performance characterization.....</b>	<b>133</b>
4.3.1	Single-stage.....	133
4.3.2	Two-stage.....	138
<b>4.4</b>	<b>Thermal characterization.....</b>	<b>143</b>

<b>4.5</b>	<b>ExB investigation .....</b>	<b>143</b>
4.5.1	Single-stage.....	144
4.5.2	Two-stage.....	146
<b>4.6</b>	<b>Gridded Faraday probe investigation.....</b>	<b>153</b>
4.6.1	Single-stage.....	154
4.6.2	Two-stage.....	155
4.6.3	Ion collector bias study.....	164
<b>Chapter 5</b>	<b>ANALYSIS AND DISCUSSION.....</b>	<b>166</b>
<b>5.1</b>	<b>Applied magnetic field.....</b>	<b>166</b>
<b>5.2</b>	<b>Ionization stage.....</b>	<b>170</b>
<b>5.3</b>	<b>Thruster performance .....</b>	<b>173</b>
5.3.1	Single-stage.....	174
5.3.2	Two-stage.....	181
5.3.3	Utilization efficiencies.....	186
5.3.4	Single- vs. Two-stage.....	191
5.3.5	Thruster performance limitations.....	194
<b>5.4</b>	<b>Plume characterizartion.....</b>	<b>196</b>
5.4.1	Ion species fractions.....	197
5.4.2	Ion density profiles .....	204
<b>Chapter 6</b>	<b>SUMMARY AND FUTURE WORK.....</b>	<b>212</b>
<b>6.1</b>	<b>Performance .....</b>	<b>212</b>
<b>6.2</b>	<b>Plasma diagnostics and performance.....</b>	<b>213</b>
<b>6.3</b>	<b>Thruster design improvements.....</b>	<b>214</b>
<b>APPENDICES</b> .....		<b>217</b>
<b>BIBLIOGRAPHY</b> .....		<b>251</b>

## LIST OF FIGURES

Figure 1-1: An electron bombardment ion thruster schematic. ....	8
Figure 1-2: Axial applied potential profile for a two-grid acceleration stage of an ion thruster. ....	12
Figure 1-3: Ionization stage performance characterization [34]. ....	15
Figure 1-4: Photographs of the NSTAR functionality checkout on DS1 spacecraft propulsion system and a studio photograph of the thruster. ....	17
Figure 1-5: NASA 40 cm NEXT ion thruster. ....	18
Figure 1-6: A photograph of JPL's 20 kW NEXIS ion thruster [9]. ....	20
Figure 1-7: A Photograph of the HiPEP ion thruster. ....	21
Figure 1-8: SPT diagrams. ....	23
Figure 1-9: Sample potential distribution of a Hall thruster [59-61]. ....	23
Figure 1-10: Two-Stage SPT diagram. ....	32
Figure 1-11: The performance results of the Shizuoka University low-power two-stage Hall thruster in single-, and two-stage mode with and without intermediate electrode heating on argon [55]. ....	33
Figure 1-12: The P5-2 5 kW two-stage Hall thruster. ....	35
Figure 1-13: Comparison of the anode efficiencies of the single- and two-stage (without heating) operation of the P5-2 Hall thruster (From Ref. [71]). ....	35
Figure 1-14: PPPL segmented Hall thruster single- and two-stage performance results for 2 mg/s xenon flow [69]. ....	36
Figure 1-15: A photograph of TsNIIMASH single- and two-stage D-80 [29]. ....	38
Figure 1-16: The NTS-1 D-80 two-stage TAL anode efficiency as a function of the first-stage discharge voltage is increased while maintaining a constant total applied potential [29]. ....	39

Figure 1-17: D-80 two-stage performance results for an increasing first-stage discharge voltage while maintaining a fixed total applied voltage [75].	40
Figure 1-18: A photograph of the BHT-HD-1000 (reprinted courtesy of Busek Co. Inc.).	41
Figure 1-19: The performance results of the BHT-HD-1000 in both single- and two-stage operation at a xenon flow rate of 2.5 mg/s [73].	41
Figure 1-20: The performance results of the D-80 in single-stage TAL [29].	43
Figure 1-21: The performance results of the SPT-1 Hall thruster [94].	45
Figure 1-22: NASA-173Mv2 Hall thruster performance [28].	47
Figure 1-23: A photograph of the NASA-457M 50 kW class Hall thruster.	49
Figure 1-24: The performance results of the NASA-457M Hall thruster operating on krypton [31].	50
Figure 1-25: Performance data of the phase one high-specific impulse D-80, SPT-1, and the BHT-HD-1000 Hall thrusters [29, 73, 94].	53
Figure 1-26: Diagram of the NASA-173GT thruster.	54
Figure 2-1: A photograph of the NASA-173GT without Hall-stage cathode.	57
Figure 2-2: SPT Hall thruster outer wall diameters squared as a function of propellant mass flow rate [32, 64, 71, 84, 87, 96, 107, 109].	59
Figure 2-3: Diagram of a Hall thruster magnetic circuit.	61
Figure 2-4: Plasma lens topology for the P5-2 [71].	62
Figure 2-5: The inner wall, outer wall, and centerline normalized radial magnetic field profiles for the P5-2 [71].	63
Figure 2-6: The inner wall, outer wall, and centerline normalized axial magnetic field profiles for the P5-2 [71].	63
Figure 2-7: Predicted ion density in the Hall stage of the NASA-173GT based off computation model [115].	65
Figure 2-8: The NASA-173GT magnetic field topology.	67
Figure 2-9: The inner wall, outer wall, and centerline normalized radial magnetic field profiles for the NASA-173GT.	67

Figure 2-10: The inner wall, outer wall, and centerline normalized axial magnetic field profiles for the NASA-173GT. ....	68
Figure 2-11: A photograph of the NASA-173GT Hall acceleration stage magnetic circuit. ....	69
Figure 2-12: BH characteristics of several ferromagnetic materials considered for the NASA-173GT. ....	71
Figure 2-13: A photograph of the Hall stage cathode with respect to the thruster (cathode is covered with a plastic bag with a nitrogen purge to protect it from atmosphere). 73	
Figure 2-14: A diagram of the ionization stage for the NASA-173GT. ....	78
Figure 2-15: A photograph of the NASA-173GT anode shell illustrating the reverse-feed propellant distribution system. ....	80
Figure 2-16: Magnetic field density map for the NASA GRC 8-cm ion thruster ionization stage [119]. ....	81
Figure 2-17: A single set-point magnetic field density map for the NASA-173GT ionization stage. ....	83
Figure 2-18: A photograph of the NASA-173GT ionization stage magnetic circuit (includes the ionization stages anode shell). ....	84
Figure 2-19: A sketch of the centerline magnetic field intensity and the favorable location of the ionization cathode exit. ....	85
Figure 2-20: The relationship of ionization cathode emission current as a function of the beam current for various ion thrusters. ....	86
Figure 2-21: The NASA-173GT 60 A ionization stage cathode. ....	87
Figure 2-22: A photograph of the NASA-173GT anode shell isolation. ....	90
Figure 2-23: A photograph of the NASA-173GT BN isolation plate between the ionization and acceleration stages. ....	90
Figure 2-24: A photograph of the NASA-173GT BN flux shields. ....	91
Figure 2-25: The NASA-173GT magnetic field topologies for the ionization and acceleration stages. ....	92
Figure 3-1: A diagram of NASA GRC VF-12. ....	95
Figure 3-2: A photograph of NASA GRC VF-12. ....	96
Figure 3-3: The electrical schematic of the NASA-173GT thruster. ....	98

Figure 3-4: A photograph of VF-12 null-type thrust stand (photographed from the rear of the thrust stand).....	103
Figure 3-5: A diagram of an <b>ExB</b> ion velocity filter. ....	105
Figure 3-6: A sketch of the <b>ExB</b> probe trace for a multiple charged species ion beam at a constant acceleration voltage and ion mass. ....	107
Figure 3-7: Diagram of an <b>ExB</b> probe. ....	108
Figure 3-8: Electrical schematic of the <b>ExB</b> probe.....	110
Figure 3-9: Photographs of NASA GRC gridded and nude Faraday probes.....	116
Figure 3-10: A diagram of the NASA GRC gridded Faraday probe physical and electrical characteristics.....	117
Figure 3-11: A photograph of the NASA-173GT ionization stage characterization with an ion collector grid. ....	122
Figure 3-12: The electrical diagram of the ionization stage characterization.....	122
Figure 3-13: A photograph of mapping the magnetic field of the NASA-173GT acceleration stage. ....	124
Figure 3-14: A photograph of the thermocouple placement on the NASA-173GT. ....	125
Figure 4-1: Normalized measured maximum centerline radial magnetic field in the Hall acceleration stage of the NASA-173GT. ....	129
Figure 4-2: The NASA-173GT radial magnetic field profiles, normalized to the maximum centerline field intensity, operating at 50% coil current.....	130
Figure 4-3: The NASA-173GT radial magnetic field profiles, normalized to the maximum centerline field intensity, operating at 100% coil current.....	130
Figure 4-4: The NASA-173GT axial magnetic field profiles, normalized to the maximum centerline field intensity, operating at 50% coil current. ....	131
Figure 4-5: The NASA-173GT axial magnetic field profiles, normalized to the maximum centerline field intensity, operating at 100% coil current. ....	131
Figure 4-6: The ion production cost of the NASA-173GT as a function of input power, propellant flow rate distribution (5 mg/s), and applied magnetic field.....	132
Figure 4-7: The acceleration efficiency as a function of applied acceleration voltage for the NASA-173GT operating in single-stage at 5 mg/s. ....	134

Figure 4-8: The acceleration specific impulse as a function of applied acceleration voltage for the NASA-173GT operating in single-stage at 5 mg/s.....	135
Figure 4-9: The acceleration efficiency as a function of specific impulse for the NASA-173GT operating in single-stage at 5 mg/s. ....	135
Figure 4-10: Acceleration current oscillation for the NASA-173GT operating in single-stage at 5 mg/s.....	136
Figure 4-11: The acceleration efficiency as a function of applied acceleration voltage for the NASA-173GT operating in single-stage at 10 mg/s. ....	136
Figure 4-12: The acceleration specific impulse as a function of applied acceleration voltage for the NASA-173GT operating in single-stage at 10 mg/s.....	137
Figure 4-13: The acceleration efficiency as a function of specific impulse for the NASA-173GT operating in single-stage at 10 mg/s. ....	137
Figure 4-14: Acceleration current oscillation for the NASA-173GT operating in single-stage at 10 mg/s.....	138
Figure 4-15: The acceleration efficiency as a function of applied acceleration voltage for the NASA-173GT operating in two-stage at 5 mg/s.....	139
Figure 4-16: The acceleration specific impulse as a function of applied acceleration voltage for the NASA-173GT operating in two-stage at 5 mg/s. ....	139
Figure 4-17: The acceleration efficiency as a function of specific impulse for the NASA-173GT operating in two-stage at 5 mg/s.....	140
Figure 4-18: Acceleration current oscillation for the NASA-173GT operating in two-stage at 5 mg/s.....	140
Figure 4-19: The acceleration efficiency as a function of applied acceleration voltage for the NASA-173GT operating in two-stage at 10 mg/s.....	141
Figure 4-20: The acceleration specific impulse as a function of applied acceleration voltage for the NASA-173GT operating in two-stage at 10 mg/s. ....	141
Figure 4-21: The acceleration efficiency as a function of specific impulse for the NASA-173GT operating in two-stage at 10 mg/s.....	142
Figure 4-22: Acceleration current oscillation for the NASA-173GT operating in two-stage at 10 mg/s.....	142
Figure 4-23: Thermal characteristics of the NASA-173GT operating in a two-stage at a total power input of 3.7 kW. ....	143

Figure 4-24: <b>ExB</b> trace of the NASA-173GT in single-stage at 200 V acceleration potential and a propellant flow rate of 10 mg/s. ....	145
Figure 4-25: <b>ExB</b> trace of the NASA-173GT in single-stage at 300 V acceleration potential and a propellant flow rate of 10 mg/s. ....	145
Figure 4-26: <b>ExB</b> trace of the NASA-173GT in single-stage at 400 V acceleration potential and a propellant flow rate of 10 mg/s. ....	146
Figure 4-27: <b>ExB</b> trace of the NASA-173GT in two-stage at 100 V acceleration potential, ionization current of 15 A, and a propellant flow rate of 5 mg/s.....	147
Figure 4-28: <b>ExB</b> trace of the NASA-173GT in two-stage at 200 V acceleration potential, ionization current of 15 A, and a propellant flow rate of 5 mg/s.....	147
Figure 4-29: <b>ExB</b> trace of the NASA-173GT in two-stage at 300 V acceleration potential, ionization current of 15 A, and a propellant flow rate of 5 mg/s.....	148
Figure 4-30: <b>ExB</b> trace of the NASA-173GT in two-stage at 400 V acceleration potential, ionization current of 15 A, and a propellant flow rate of 5 mg/s.....	148
Figure 4-31: <b>ExB</b> trace of the NASA-173GT in two-stage at 500 V acceleration potential, ionization current of 15 A, and a propellant flow rate of 5 mg/s.....	149
Figure 4-32: <b>ExB</b> trace of the NASA-173GT in two-stage at 100 V acceleration potential, ionization current of 15 A, and a propellant flow rate of 10 mg/s.....	149
Figure 4-33: <b>ExB</b> trace of the NASA-173GT in two-stage at 200 V acceleration potential, ionization current of 15 A, and a propellant flow rate of 10 mg/s.....	150
Figure 4-34: <b>ExB</b> trace of the NASA-173GT in two-stage at 300 V acceleration potential, ionization current of 15 A, and a propellant flow rate of 10 mg/s.....	150
Figure 4-35: <b>ExB</b> trace of the NASA-173GT in two-stage at 400 V acceleration potential, ionization current of 15 A, and a propellant flow rate of 10 mg/s.....	151
Figure 4-36: <b>ExB</b> trace of the NASA-173GT in two-stage at 200 V acceleration potential, ionization current of 25 A, and a propellant flow rate of 10 mg/s.....	151
Figure 4-37: <b>ExB</b> trace of the NASA-173GT in two-stage at 300 V acceleration potential, ionization current of 25 A, and a propellant flow rate of 10 mg/s.....	152
Figure 4-38: <b>ExB</b> trace of the NASA-173GT in two-stage at 400 V acceleration potential, ionization current of 25 A, and a propellant flow rate of 10 mg/s.....	152
Figure 4-39: Ion current trace of the NASA-173GT operating in single-stage at 400 V acceleration potential and propellant flow rate of 10 mg/s.....	154

Figure 4-40: Two-stage ion current trace of the NASA-173GT at 200 V, propellant flow rate of 5 mg/s, and Id of 15 A. ....	155
Figure 4-41: Two-stage ion current trace of the NASA-173GT at 300 V, propellant flow rate of 5 mg/s, and Id of 15 A. ....	156
Figure 4-42: Two-stage ion current trace of the NASA-173GT at 400 V, propellant flow rate of 5 mg/s, and Id of 15 A. ....	156
Figure 4-43: Two-stage ion current trace of the NASA-173GT at 500 V, propellant flow rate of 5 mg/s, and Id of 15 A. ....	157
Figure 4-44: Two-stage ion current trace of the NASA-173GT at 100 V, propellant flow rate of 5 mg/s, and Id of 25 A. ....	157
Figure 4-45: Two-stage ion current trace of the NASA-173GT at 200 V, propellant flow rate of 5 mg/s, and Id of 25 A. ....	158
Figure 4-46: Two-stage ion current trace of the NASA-173GT at 300 V, propellant flow rate of 5 mg/s, and Id of 25 A. ....	158
Figure 4-47: Two-stage ion current trace of the NASA-173GT at 400 V, propellant flow rate of 5 mg/s, and Id of 25 A. ....	159
Figure 4-48: Two-stage ion current trace of the NASA-173GT at 500 V, propellant flow rate of 5 mg/s, and Id of 25 A. ....	159
Figure 4-49: Two-stage ion current trace of the NASA-173GT at 100 V, propellant flow rate of 10 mg/s, and Id of 15 A. ....	160
Figure 4-50: Two-stage ion current trace of the NASA-173GT at 200 V, propellant flow rate of 10 mg/s, and Id of 15 A. ....	160
Figure 4-51: Two-stage ion current trace of the NASA-173GT at 300 V, propellant flow rate of 10 mg/s, and Id of 15 A. ....	161
Figure 4-52: Two-stage ion current trace of the NASA-173GT at 400 V, propellant flow rate of 10 mg/s, and Id of 15 A. ....	161
Figure 4-53: Two-stage ion current trace of the NASA-173GT at 100 V, propellant flow rate of 10 mg/s, and Id of 25 A. ....	162
Figure 4-54: Two-stage ion current trace of the NASA-173GT at 200 V, propellant flow rate of 10 mg/s, and Id of 25 A. ....	162
Figure 4-55: Two-stage ion current trace of the NASA-173GT at 300 V, propellant flow rate of 10 mg/s, and Id of 25 A. ....	163

Figure 4-56: Two-stage ion current trace of the NASA-173GT at 400 V, propellant flow rate of 10 mg/s, and $I_d$ of 25 A. ....	163
Figure 4-57: Gridded Faraday probe bias study for an ion collector plate ranging from 0 to +50 V at the 0.45 m radial sweep location. ....	164
Figure 4-58: Gridded Faraday probe bias study for an ion collector plate ranging from 0 to +50 V at the 0.95 m radial sweep location. ....	165
Figure 5-1: A comparison of the measured acceleration stage normalized centerline radial magnetic field, at the axial location of the maximum field, with the modeled results for non-heat-treated and heat-treated iron and coil currents ranging from 0 to 100% of the design maximum. ....	167
Figure 5-2: The operation of the ionization stage of the NASA-173GT with ion collection grid viewed from downstream. ....	171
Figure 5-3: Ion current and ion current fraction as a function of ionization stage current. ....	172
Figure 5-4: The ion beam extraction of the NASA-173GT operating in two-stage configuration. ....	173
Figure 5-5: Single-stage anode efficiency as a function of acceleration potential for anode flow rates of 5 and 10 mg/s. ....	175
Figure 5-6: The ratio of the acceleration current to the total anode propellant equivalent current as a function of acceleration voltage at propellant flow rates of 5 mg/s and 10 mg/s in single-stage operation mode compared to the NASA-173Mv2 [64]. ....	176
Figure 5-7: The single-stage specific-impulse results for 5 and 10 mg/s propellant flow rates compared to a theoretical and corrected specific-impulse calculation for the 400 V and 10 mg/s measured utilization efficiencies. ....	178
Figure 5-8: A photograph of the NASA-173GT operating in single-stage configuration that illustrates the interaction of the Hall current with the BN flux shunt shields. .	179
Figure 5-9: Two-stage anode efficiency as a function of acceleration potential for an anode flow rates of 5 and 10 mg/s and an ionization power level between 100 and 600 W. ....	182
Figure 5-10: The ratio of the acceleration current to the total anode propellant flow rate as a function of acceleration voltage at propellant flow rates of 5 mg/s and 10 mg/s for the NASA-173GT operating in two-stage as compared to the NASA-173Mv2. ....	183
Figure 5-11: The two-stage specific-impulse results for 5 and 10 mg/s propellant flow rates compared to a theoretical and corrected specific-impulse calculation for each case. ....	185

Figure 5-12: The acceleration and utilization efficiencies of two-stage operation at a flow rate of 5 mg/s and an ionization stage current of 15 A. ....	188
Figure 5-13: The acceleration and utilization efficiencies of two-stage operation at a flow rate of 10 mg/s and an ionization stage current of 15 A. ....	189
Figure 5-14: The acceleration and utilization efficiencies of two-stage operation at a flow rate of 10 mg/s and an ionization stage current of 25 A. ....	189
Figure 5-15: Comparison of the single- and two-stage acceleration efficiencies as a function of acceleration potential at 5 mg/s propellant flow rate. ....	192
Figure 5-16: Comparison of the single- and two-stage acceleration efficiencies as a function of acceleration potential at 10 mg/s propellant flow rate. ....	192
Figure 5-17: The single- and two-stage thrust-to-acceleration power ratios as a function of acceleration voltage for 5 mg/s propellant flow rate. ....	193
Figure 5-18: The single- and two-stage thrust-to-acceleration power ratios as a function of acceleration voltage for 10 mg/s propellant flow rate. ....	194
Figure 5-19: The <b>ExB</b> responsiveness for single-stage 200, 300, and 400 V acceleration potential data as a function of plate potential. ....	197
Figure 5-20: The <b>ExB</b> responsiveness for two-stage 200, 300, and 400 V acceleration potential data at 10 mg/s propellant flow rate and 15 A ionization stage current as a function of plate potential. ....	198
Figure 5-21: The ion species fractions as a function of acceleration voltage for the NASA-173GT operating in a two-stage configuration. ....	201
Figure 5-22: <b>ExB</b> trace of the NASA-173GT in single-stage mode at 400 V acceleration potential and a propellant flow rate of 10 mg/s with an illustration of the secondary peak. ....	202
Figure 5-23: The divergence as a function of acceleration potential for 5 mg/s propellant flow rate and ionization stage currents of 15 and 25 A. ....	206
Figure 5-24: The divergence as a function of acceleration potential for 10 mg/s propellant flow rate and ionization stage currents of 15 and 25 A. ....	206
Figure 5-25: Comparison of the single- and two-stage NASA-173GT ion current density traces from the 0.45 m gridded Faraday probe location at similar operating conditions. ....	209
Figure 5-26: Comparison of the uncertainty of the ion current traces between both radial probe locations. ....	211

Figure 6-1: Alternative NASA-173GT design..... 215

## LIST OF TABLES

Table 3-1: List of the input power supplies employed during the NASA-173GT performance and plume characterization. ....	99
Table 3-2: Basic parameters for the <b>ExB</b> probe used in the investigation as compared to the <b>ExB</b> probes used in Refs [64, 134]. ....	108
Table 3-3: The characteristics of the gridded Faraday probes. ....	117
Table 3-4: The CEX cross-section for singly ionized xenon ( $\text{Xe}^+ + \text{Xe} \rightarrow \text{Xe} + \text{Xe}^+$ ) at ion beam energies [146]. ....	120
Table 5-1: Comparison of the single- and two-stage utilization efficiencies. ....	187
Table 5-2: The ion species fractions and charge utilization efficiency results for the NASA-173GT in both single- and two-stage configurations. ....	200
Table 5-3: Tabulated results of the gridded Faraday probe investigation of the NASA-173GT. ....	205
Table A-1: The single-stage performance characterization of the NASA-173GT. ....	217
Table A-2: The two-stage performance characterization results of the NASA-173GT. ....	218

## LIST OF APPENDICES

Appendix A: .....	217
Appendix B: .....	219

## NOMENCLATURE

$A$	Conductor cross-sectional area	[m <sup>2</sup> ]
$\alpha$	Acceptance angle	[°]
$\alpha$	Temperature Coefficient	[1/C]
$a_1$	Collimator entrance orifice diameter	[mm]
$a_2$	Collimator entrance orifice diameter	[mm]
$a_3$	Drift tube entrance orifice diameter	[mm]
$a_4$	ExB collector diameter	[mm]
$A_{\text{anode}}$	Anode surface area	[m <sup>2</sup> ]
$\phi_{\text{accel}}$	Potential between anode and acceleration grid	[V]
$A_{\text{channel}}$	Open area fraction of the channel	[-]
$A_{\text{Collector}}$	Ion collection area	[m <sup>2</sup> ]
$A_d$	Collection area, directed ion flux	[m <sup>2</sup> ]
$A_{\text{grid}}$	Open area fraction of the grid	[-]
$A_p$	Probe surface area	[m <sup>2</sup> ]
$B$	Scalar magnetic field	[G]

<b>B</b>	Magnetic field vector	[G]
$B_0$	Radial magnetic field for 300 V operation	[G]
$\beta_{0.45m}$	Divergence angle from 0.45 m gridded Faraday probe	[°]
$\beta_{0.95m}$	Divergence angle from 0.95 m gridded Faraday probe	[°]
$B_{r \max}$	Centerline maximum radial magnetic field	[G]
$D_c$	Hall thruster/discharge channel diameter	[mm]
$d_{\text{grid}}$	Axial grid gap	[m]
$d_{\text{plates}}$	Electrode spacing	[m]
<b>E</b>	Electric field vector	[V/m]
$E$	Scalar electric field	[V/m]
$\epsilon_{\text{ion}}$	Ion production cost	[eV/ion = W/A]
$\epsilon_{\text{ion-cath}}$	Ionization stage cathode cost	[eV/ion = W/A]
<b>F</b>	Force	[N]
$f$	Particle flux	[1/m <sup>2</sup> ·s]
$\phi_{\text{Xe}^+}$	Measured Xe <sup>+</sup> potential	[V]
$g$	Gravitational constant	[m/s <sup>2</sup> ]
$I_{\text{accel}}$	Total acceleration stage current	[A]
$I_B$	Ion beam current	[A]
$I_C$	Gridded Faraday probe pressure corrected total current	[A]

$I_{\text{Discharge}}$	Discharge current	[A]
$I_e$	Electron leakage current	[A]
$I_{\text{GP}}$	Gridded Faraday probe total current	[A]
$I_{\text{ion}}$	Ion current from ionization stage	[A]
$I_m$	Grid current	[A]
$I_{\text{probe},i}$	Ion current fraction	[A]
$I_{\text{sat}}$	Ion saturation current	[A]
$I_{\text{sp}}$	Specific Impulse	[s]
$j$	Scalar current density at the face of the gridded Faraday probe collector	[A/m <sup>2</sup> ]
$j_{\text{max}}$	Space-charge beam current density	[A/m <sup>2</sup> ]
$j_{\text{open}}$	Scalar current density at the face of the gridded Faraday probe	[A/m <sup>2</sup> ]
$j_z$	Scalar current density at the thruster exit	[A/m <sup>2</sup> ]
$L$	Conductor length	[m]
$l_c$	Hall thruster/discharge channel length	[mm]
$m_e$	Mass of electron	[kg]
$M_{\text{final}}$	Final propellant mass	[kg]
$M_{\text{initial}}$	Initial propellant mass	[kg]
$M_{\text{propellant}}$	Mass of propellant ion	[kg]
$n$	number density	[1/m <sup>3</sup> ]

$n_0$	Neutral Loss Rate	[A]
$n_b$	Neutral background pressure	[1/m <sup>3</sup> ]
$n_e$	Electron number density	[1/m <sup>3</sup> ]
$n_i$	Ion number density	[1/m <sup>3</sup> ]
$n_n$	Neutral number density	[1/m <sup>3</sup> ]
P	Plasma Pressure	[Pa]
P/A	Power density	[W/m <sup>2</sup> ]
$P_{\text{accel}}$	Acceleration stage power	[W]
$p_{\text{base}}$	Base pressure of the facility	[Torr]
$p_c$	Corrected operating pressure	[Torr]
$p_{\text{indicated}}$	Indicated pressure with propellant flow	[Torr]
$P_{\text{input}}$	Input power	[W]
$P_{\text{ion}}$	Ionization stage power	[W]
$p_o$	Discharge channel pressure	[Pa]
q	Electron charge	[C]
$\theta$	Radial position	[°]
R	Resistance	[ $\Omega$ ]
$r_e$	Electron gyro radius in Hall thruster channel	[m]
$R_f$	Final resistance	[ $\Omega$ ]
$r_i$	Ion gyro radius in Hall thruster channel	[m]

$R_o$	Initial resistance	$[\Omega]$
$\sigma_{CEX}$	Charge Exchange Cross-Section	$[m^2]$
$T$	Thrust	$[N]$
$T_0$	Initial electromagnetic coil temperature	$[C]$
$T_{coil}$	Electromagnetic coil temperature	$[C]$
$U_e$	Propellant exit velocity	$[m/s]$
$V_{accel}$	Acceleration Potential	$[V]$
$V_{discharge}$	Discharge Potential	$[V]$
$v_e$	Electron velocity	$[m/s]$
$V_{ExB}$	Electron drift velocity	$[m/s]$
$v_i$	Ion velocity	$[m/s]$
$v_{pass}$	<b>ExB</b> ion pass potential	$[V]$
$V_{plates}$	Electrode potential	$[V]$
$w_c$	Hall thruster/discharge channel width	$[mm]$
$\Omega_i$	Ion current fraction	$[-]$
$Z$	Degree of ionization	$[-]$
$Z_{Collimator}$	Collimator length	$[mm]$
$Z_{Drift}$	Drift tube length	$[mm]$
$Z_{ExB}$	<b>ExB</b> section length	$[mm]$
$\Delta V_{accel-\phi}$	Potential difference	$[V]$

$\eta_{\text{current}}$	Current utilization efficiency	[%]
$\eta_d$	Utilization efficiency of beam divergence and multiple charged ion	[%]
$\eta_e$	Utilization efficiency of the electrical power	[%]
$\eta_q$	Charge utilization efficiency	[%]
$\eta_T$	Thruster efficiency	[%]
$\eta_u$	Propellant utilization efficiency	[%]
$\eta_{ud}$	Ionization stage propellant utilization efficiency	[%]
$\eta_v$	Voltage utilization efficiency	[%]
$\Lambda$	Plasma parameter	[-]
$\rho$	Resistivity	[ $\Omega \cdot \text{m}$ ]
$\dot{m}_a$	Anode propellant mass flow rate	[sccm]
$\dot{m}_{\text{Total}}$	Total propellant mass flow rate	[sccm]
$\bar{v}$	Electron thermal speed	[m/s]
$\phi$	Potential	[V]
$\sigma_0$	Scalar conductivity	[ $1/\Omega \cdot \text{m}$ ]
$\zeta_i$	Ion species fraction	[-]

## Chapter 1 INTRODUCTION

The concept of applying electrical power as a means of producing thrust for spacecraft has been envisioned, researched, and then applied over the past century. Rocket propulsion pioneers Robert Goddard and Herman Oberth first proposed the idea of using accelerated ionized particles as a means of advanced propulsion to overcome the limitations of chemical propulsion for in-space applications [1, 2]. Serious research in the field of Electric Propulsion (EP) was not begun until the initiation of the “Space Race” between the United States and the former Soviet Union and the development of power plants that could meet the power requirements of EP devices [2]. The development and improvement of EP propulsion devices is still in strong stride all over the world for applications ranging from north-south-station-keeping (NSSK) to interplanetary exploration [3-10].

The advantage of EP for space applications (i.e. low gravity fields) can be understood by examination of the rocket equation:

$$\frac{M_{initial}}{M_{final}} = e^{\frac{\Delta V}{U_e}} \quad \text{Eqn. 1-1}$$

where  $\Delta V$  is the required change in spacecraft velocity to complete the mission,  $M_{initial}$  is the initial mass of the spacecraft including propellant,  $M_{final}$  is the mass of the spacecraft

after thrusting to the determined  $\Delta V$ , and  $U_e^1$  is the exit velocity of the exhausted propellant. The specific impulse of a propulsion system is described as the ratio between the thrust (T) and the product of the propellant mass flow rate ( $\dot{m}$ ) and gravitational acceleration (g):

$$I_{sp} \equiv \frac{T}{\dot{m}g} = \frac{\dot{m}U_e}{\dot{m}g} = \frac{U_e}{g}. \quad \text{Eqn. 1-2}$$

Typical chemical propulsion systems eject the propellant at exit velocities up to 4.4 km/s, or a specific impulse of 450 seconds. EP devices have demonstrated exit velocities from 3 km/s (~300 seconds) to 70 km/s (~7000 seconds) [11-13]. The thruster efficiency of an EP device is defined as the ratio of jet power to the applied power:

$$\eta_T = \frac{P_{jet}}{P_{input}} = \frac{1}{2} \frac{TU_e}{P_{input}}, \quad \text{Eqn. 1-3}$$

where  $P_{input}$  is the total applied power required to operate the EP device. The anode specific impulse and efficiency are defined strictly by the parameters of accelerating the propellant and do not include subsystem inefficiency costs<sup>2</sup>.

---

<sup>1</sup> The  $U_e$  represents an effective velocity of the accelerated ionized propellant exiting the thruster. The effective velocity of a Hall thruster is dependent on radial components of the ion velocity, location of the ionization in the discharge channel, elastic collisions, and charge exchange collisions that the ionized propellant suffer during the acceleration.

<sup>2</sup> Considering a thruster anode specific impulse and efficiency, instead of the propulsion system total specific impulse and efficiency, is a common practice for researchers when developing and testing a laboratory thruster.

Exchanging chemical propulsion devices with EP devices for NSSK allows either an increase in operational time by as much as 300% for a fixed propellant mass fraction, or a substantial decrease in the amount of station-keeping propellant required for the lifetime of the spacecraft. EP devices provide the mission planner a possibility of using a smaller launch vehicle, due to reduced propellant requirements, thereby reducing the cost of placing the spacecraft in orbit [14]. Hall thrusters (one form of EP) are capable of meeting the total in-space propulsion requirements of spacecrafts, ranging from orbit transfer, NSSK, and eventual de-orbiting [15-19].

The continued research and development of EP devices for commercial and exploration missions are ongoing efforts of private industry, academia, and governmental agencies in the United States and abroad [4-10, 20-23]. The work presented in this thesis covers the development and investigation of a hybrid two-stage Hall/ion thruster, referred to as the NASA-173GT, for high specific impulse applications.

## **1.1 Electric Propulsion Overview**

The definition of electric propulsion was put forth by Professor Robert G. Jahn in the 1968 book “*Physics of Electric Propulsion*,” [2, 24]

*The acceleration of gases for propulsion by electrical heating and/or by electric and magnetic body forces.*

The definition of EP can be further subdivided into three categories that are dependent on the physical process of accelerating ionized propellant. The three categories are discussed as follows.

- *Electrothermal Propulsion* devices electrically heat a propellant gas and allow the heated gas to expand through a suitable nozzle to produce an optimal thrust. Two major EP devices use this method for producing thrust: resistojets and arcjets. Resistojets, as the name implies, function by resistively heating an element that imparts its energy to the propellant through convection and electromagnetic radiation. Arcjets heat the propellant by establishing an electrically driven plasma arc between two electrodes. The energy an arcjet imparts to the propellant gas is primarily from the propellant passing through the core region of the arc, as well as convection from the chamber walls that are heated by electromagnetic radiation from the arc. The heated propellant from both systems is then allowed to expand in a nozzle, thus producing thrust [12, 24]. The typical specific impulse and thruster efficiencies for resistojets are 300 seconds and 80%, respectively for power levels up to 500 W. Arcjets have specific impulses and thruster efficiencies ranging between 500 to 1000 seconds and 27% to 40% for power levels from 300 W to 100 kW [12].
- *Electrostatic Propulsion* devices accelerate ionized propellant with an applied static electric field. To avoid spacecraft charging, the ion beam is neutralized by an external source of electrons. There are two major EP devices that fall into this

category, ion thrusters<sup>3</sup> and Hall Effect thrusters<sup>4</sup>. Ion and Hall thrusters have been highly researched and developed for both Earth orbit and interplanetary missions. The physical mechanisms of both the ion thruster and Hall thruster will be discussed in further detail in Sections 1.2.1 and 1.2.2, respectively. Ion thrusters have demonstrated specific impulses ranging from 2500 seconds to over 8000 seconds and thruster efficiencies up to 78% at power levels ranging from 300 W to 200 kW [8, 12, 13, 20, 25]. Hall thrusters have demonstrated<sup>5</sup> specific impulses ranging from 800 seconds to above 4500 seconds and thruster efficiencies up to 70% at power levels ranging from 100 W to 98 kW [20, 26-32].

- *Electromagnetic Propulsion* devices accelerate ionized propellant through the interaction of an applied electric field and an induced or applied magnetic field resulting in a  $\mathbf{j} \times \mathbf{B}$  accelerating force on the plasma. The induced magnetic field is created by driving a large, pulsed, or steady-state current through a plasma. Two major EP devices fit into the electromagnetic description. The first is a low-power device (1 to 200 W) known as a pulsed plasma thruster (PPT) [4]. PPTs operate by producing a plasma armature near a solid propellant bar, typically Teflon™.

The plasma armature ablates a portion of the bar and provides additional material

---

<sup>3</sup> Ion thrusters are also referred to as gridded ion thrusters.

<sup>4</sup> The classification of modern EP devices occasionally falls into more than one of Jahn's categories. For example, the Hall thruster is considered by some to be an electromagnetic device due to the required applied magnetic field for acceleration. However, some disagree with this assessment stating that the applied magnetic field helps to establish the ionization processes and the "virtual" cathode used to accelerate the ions. If one examines the methodology of increasing the exit velocity of a Hall thruster compared to electromagnetic devices, increasing the applied electrostatic potential field is required to have a major influence on the exit velocity of the propellant ions for a Hall thruster. Whereas for a magnetostatic device one needs to increase the plasma current density either through increased propellant flow rate and/or discharge current due the  $\mathbf{j} \times \mathbf{B}$  acceleration.

<sup>5</sup> For noble propellants such as xenon and krypton.

for ionization. The ionized propellant is then accelerated between two electrodes by a  $\mathbf{j} \times \mathbf{B}$  accelerating force. PPTs have been developed and used for small orbit correction maneuvers for spacecrafts, with specific impulse of 1000 seconds and thruster efficiencies up to 7% [12].

The second propulsion device that is classified as electromagnetic propulsion is known as the magnetoplasmadynamic (MPD) thruster. MPD thrusters operate in a similar manner as PPTs except at much greater power densities (kilowatts to megawatts) and typically incorporate gas or liquid metal as propellants [4, 12, 24]. The MPD thrusters are still under laboratory development due to its short operational lifetimes. However, MPD thrusters show great promise for high-thrust space applications such as piloted missions to Mars.

The research presented in this thesis focuses on combining the benefits of the two primary electrostatic devices discussed above into a hybrid Hall/ion thruster for high specific applications.

## **1.2 High-Specific Impulse Electrostatic Devices**

Ion and Hall thrusters are the primary electrostatic EP devices that have progressed from laboratory to successfully demonstrated spacecraft application. Both thrusters fulfill separate but substantial rolls for spacecraft propulsion requirements. The ion thruster can achieve high specific impulse in the range of 5000-15000 seconds for

missions that require large  $\Delta V$ . Ion thrusters are not desirable in high gravitational environments such as orbit changing or breaking maneuvers. These maneuvers optimize with specific impulses up to 5000 seconds, which are ideal for Hall thrusters. The Hall thruster is enabling for missions where trip time and launch vehicle size are the limiting factors. Sections 1.2.1 through 1.2.2 discuss the physics of operation, merits, and brief histories of ion and Hall thrusters in the United States and abroad.

### **1.2.1 Ion Thruster Technology**

The ion thruster electrostatic propulsion system has undergone research directed towards development and refinement for space propulsion applications since the early 1960's [1, 2, 33-37]. The ion thruster technology was originated in the United States in the early 1960's at what is now known as the NASA Glenn Research Center (GRC) [33]. The early ion thruster results, 5500 seconds specific impulse at efficiencies as high as 70%, showed great promise for space applications that required much larger propellant exit velocities than was possible with chemical systems. The first space applications of ion thrusters came in 1964 with the launch of Space Electric Propulsion Test I (SERT I), which was followed by SERT II and Advanced Technology Satellite (ATS 6) in 1970 and 1974, respectively. The two mercury ion thrusters on SERT II were successfully operated for 22 years with over 5700 accumulated hours of full power operation on the two thrusters [38]. The ATS 6 operated both of its two cesium ion thrusters briefly before the propellant caused electrical shorts to develop across the propellant isolators. The successful completion of the NASA Deep Space 1 (DS1) mission in 2001, with the

NASA Solar electric Propulsion Technology Application Readiness (NSTAR) ion thruster, closed the 24-year gap of ion thruster use as a propulsion system. This long absence of the use of ion thrusters was due to the complexity of the systems and the unavailability of sufficient spacecraft power. The primary focus of research in ion thrusters, until present, has been to develop a highly efficient device while reducing the complexity of power supply, propellant management, and support systems [34].

The ion thruster is an electrostatic acceleration device that is composed of ionization and acceleration stages. A simple sketch of an ion thruster is presented in Figure 1-1.

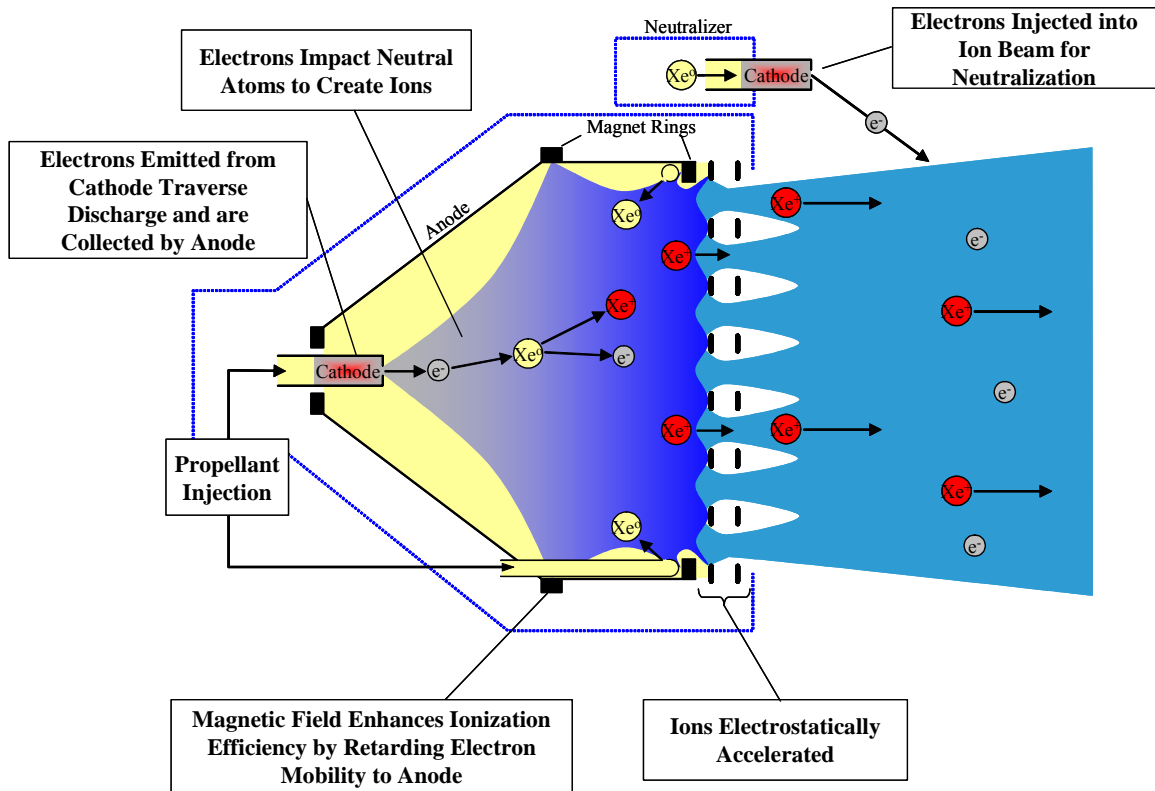


Figure 1-1: An electron bombardment ion thruster schematic.

The first stage of an ion thruster is composed of an ionization source and the propellant distribution system. The ionization of the propellant is typically achieved by one of three methods: an electron bombardment; a radio frequency (RF); or microwave ( $\mu\text{W}$ ) processes. Electron bombardment is the primary method used in the United States [34]. RF ion thrusters have been developed and successfully used on European Space Agency (ESA) ARTEMIS telecommunication spacecrafts. The ESA ARTEMIS spacecraft incorporated two Radio-frequency Ion Thruster Assembly (RITA) thrusters and two Electron bombardment Ion Thruster Assembly (EITA) thrusters [39]. A failure of the ARTEMIS spacecraft chemical upper launch stage placed the spacecraft in a low orbit. The ion thrusters, which were meant only for NSSK, were used to salvage the mission by transferring the spacecraft to the proper mission orbit.

The incorporation of the  $\mu\text{W}$  technique as the ionization mechanism for ion thrusters has been developed and successfully used in the Japanese scientific spacecraft MUSES-C that is currently underway to a near Earth asteroid [7]. The MUSES-C spacecraft has four  $\mu\text{W}$  Electron Cyclotron Resonance (ECR) discharge ion thrusters. One advantage of the RF and  $\mu\text{W}$  ionization techniques for ion thrusters is that the ionization stage does not require an electron source. Hollow cathode electron sources have been shown to be one of the major life-limiting components of electron bombardment ionization sources. Two disadvantages of the RF and  $\mu\text{W}$  ionization techniques are their poor scalability to large chambers [33] and limited throttling range [34].

The electron bombardment ionization source incorporates a hollow cathode that acts as a source of electrons for the ionization chamber. A hollow cathode usually operates by thermionically emitting electrons from a low work function material; such as lanthanum hexaboride ( $\text{LaB}_6$ ) or porous tungsten impregnated with a 4:1:1 molar mixture of barium oxide ( $\text{BaO}$ ), calcium oxide ( $\text{CaO}$ ), and aluminum oxide ( $\text{Al}_2\text{O}_3$ ). The heated low work function material emits electrons into a hollow tube in the presence of a neutral propellant at a sufficient density to allow ionization. The ionized propellant is attracted to the negative electrode of the system while the emitted electrons and the electrons from the ionization are accelerated out of the hollow cathode [40]. The electrons produced by the cathode in the ionization stage with sufficient energy to ionize a propellant particle if encountered are referred to as primary electrons. These mobile primary electrons have a finite probability of undergoing an ionization collision with the neutral propellant as they travel towards the anode. The neutral propellant is injected into the ionization chamber near the screen grid, towards the ionization cathode, and a portion of the neutral propellant is injected into the ionization chamber through the cathode without undergoing ionization. To enhance the electron bombardment ionization technique, applied magnetic fields have been incorporated in the ionization chamber to reduce the primary electron mobility. This decreased electron mobility increases the residence time of the primary electrons and thereby the probability of ionization.

There have been several magnetic field topologies that have been used in ion thruster ionization sources. These topologies have included axial, divergent, and multipole fields [35, 41]. The various forms of applied magnetic fields have been generated by either electromagnetic coils or permanent magnets. Modern day ion

thrusters have incorporated permanent magnets in a ring-cusp configuration to reduce the complexity of the power supply requirements and to increase the ionization stage effectiveness [33, 34, 41-44]. The ring-cusp configuration limits the primary electrons from reaching the anode through a magnetic mirror effect [45], as illustrated in the following expression:

$$\frac{v_{\parallel}^2 + \frac{2e\phi}{m_e}}{v_{\perp}^2} < \frac{|\vec{B}|_{anode}}{|\vec{B}|_{cathode}} - 1, \quad \text{Eqn. 1-4}$$

where  $|\mathbf{B}|_{anode}$  and  $|\mathbf{B}|_{cathode}$  are the magnetic field strengths at the anode and cathode of the ionization stage,  $\phi$  is the potential increase that the primary electrons experience from the ionization chambers cathode to anode, and  $v_{\parallel}$  and  $v_{\perp}$  are the parallel and perpendicular velocity components of the primary electrons, respectively. Primary electrons experience the mirroring effect as long as Equation 1-4 is satisfied, thereby increasing the residence time and the probability of ionization.

The second stage of an ion thruster is composed of multiple grids with various applied potentials to accelerate the ionized propellant. The grid that faces the ionization chamber is known as the screen grid and is biased at the cathode potential to attract the low-energy ions. The next downstream grid is known as the acceleration grid, which is biased with respect to the ionization stage anode, and completes the circuit of the acceleration mechanism. The acceleration grid potential is set below thruster ground and the plasma potential of the plume downstream of the thruster. The acceleration grid

potential is set with respect to the neutralizer common. Then the ions are then decelerated back up to space plasma potential, as well to reduce the back streaming of the electrons generated by the neutralizing cathode. The applied potential profile of an ion thruster is illustrated in Figure 1-2. Back streaming electrons from the thruster plume can be a source of failure of the discharge cathode assembly [46, 47].

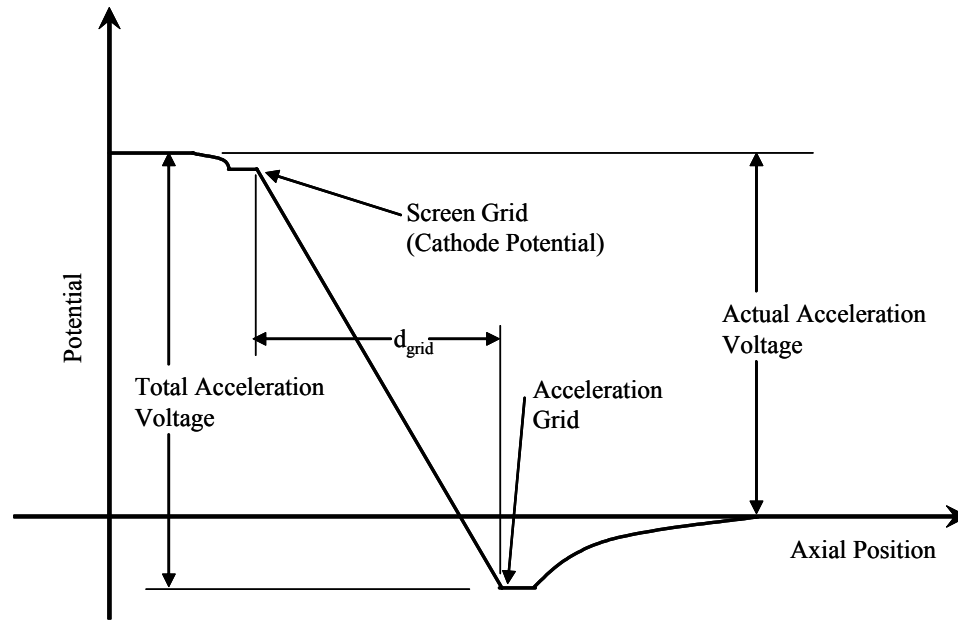


Figure 1-2: Axial applied potential profile for a two-grid acceleration stage of an ion thruster.

The grids are composed of apertures of various diameters, depending on the function of the grid. The screen grid apertures are larger than the acceleration grid apertures. The open area fraction of the acceleration grid is selected to be a small fraction of the thruster beam area to reduce the loss of neutral propellant out of the ionization stage. The ion transparency of the screen grid is on the order of 60% to 80% during extraction [33]. The screen grid transparency is much larger for the ions than the

neutral propellant because of the formation of a sheath at each of the apertures [34, 35]. A limitation of an ion thruster acceleration stage is that as the current density of the thruster increases, the number of ions entering the gap between the screen and acceleration grids increase. As the ion current density in the gap increases, the ions begin to experience less of a potential drop until the ions are no longer accelerated between the grids. This phenomenon is referred to as a space-charge limited beam current [2, 34], expressed as:

$$j_{\max} = \frac{4\epsilon_0}{9} \left( \frac{2q}{M_{\text{propellant}}} \right)^{1/2} \frac{\phi_{\text{accel}}^{3/2}}{d_{\text{grid}}^2}, \quad \text{Eqn. 1-5}$$

where  $\phi_{\text{accel}}$  is the applied potential between the ionization stage anode and the acceleration grid,  $d_{\text{grid}}$  is the gap distance between the screen and acceleration grids, and  $M_{\text{propellant}}$  is the mass of the propellant molecule. The ion beam current densities of ion thrusters are limited by Equation 1-5 for a given diameter. To achieve higher current density operation an ion thruster beam area must be scaled accordingly to meet the desired power requirements [34]. Other possibilities of increasing beam current are to increase the acceleration voltage and decrease the gap distance between the grids.

The neutralizer hollow cathode located downstream of the acceleration stage is the same as the hollow cathode used in the ionization stage. The neutralizer ejects electrons into the ion beam to prevent spacecraft charging that would reduce the ability of the ion thruster to accelerate ionized propellant.

The overall operating efficiency of an ion thruster can be expanded from Equation 1-3 to reflect the unique characteristics of these devices [34]. Equation 1-3 can be rewritten in the following form:

$$\eta_T = \frac{P_{jet}}{P_{input}} = \frac{T^2}{2\dot{m}_{total} P_{input}} \approx \eta_e \eta_u \eta_d^2, \quad \text{Eqn. 1-6}$$

where  $\eta_e$  is the utilization efficiency of the electrical power,  $\eta_u$  is the ionization stage propellant utilization efficiency, and  $\eta_d$  captures the effects of beam divergence and multiple charged ion generation. The effects of plume divergence and multiple charged ions in state-of-the-art (SOA) ion thrusters are slightly less than unity. The propellant and electrical power utilization efficiencies range between 70% and 90% for SOA ion thrusters. The propellant utilization efficiency is defined as the ratio of ion beam current to the equivalent total propellant flow rate current. The propellant utilization efficiency can be improved by increasing the applied power of the ionization stage. The electrical power utilization is defined as the ratio of the acceleration energy imparted on an ion to the energy required to ionize and accelerate the propellant. The propellant utilization and electrical power utilization are driven by the design of the ion thruster and are closely coupled. Equation 1-6 can be further refined to capture the details of ion thruster operation [34]:

$$\eta_T \approx \frac{\eta_u \eta_d^2}{1 + \left( \frac{\mathcal{E}_{ion}}{\phi_{accel}} \right)}, \quad \text{Eqn. 1-7}$$

where  $\epsilon_{ion}$  is defined as the energy required to produce a beam. This term is also referred to as the ion production cost. A relationship between the ion production cost and the propellant utilization efficiency is shown in Equation 1-7. The ionization stage applied power can be reduced to minimize the  $\epsilon_{ion}$ . A consequence of reducing the available power for the ionization stage, however, is a decrease in the propellant utilization efficiency. This results in an increased amount of neutral propellant that escapes the ionization stage, thereby decreasing the overall thruster efficiency. The ionization stage power, and thus the  $\epsilon_{ion}$ , can be increased to enhance the ionization fraction to the point that the  $\eta_u$  approaches unity. Once again there is a consequence placed on the ion thruster overall efficiency. By increasing  $\epsilon_{ion}$   $\eta_u$  approaches unity, however, Equation 1-7 decreases. The relationship between the  $\epsilon_{ion}$  and  $\eta_u$  is illustrated in Figure 1-3 from Ref. [34].

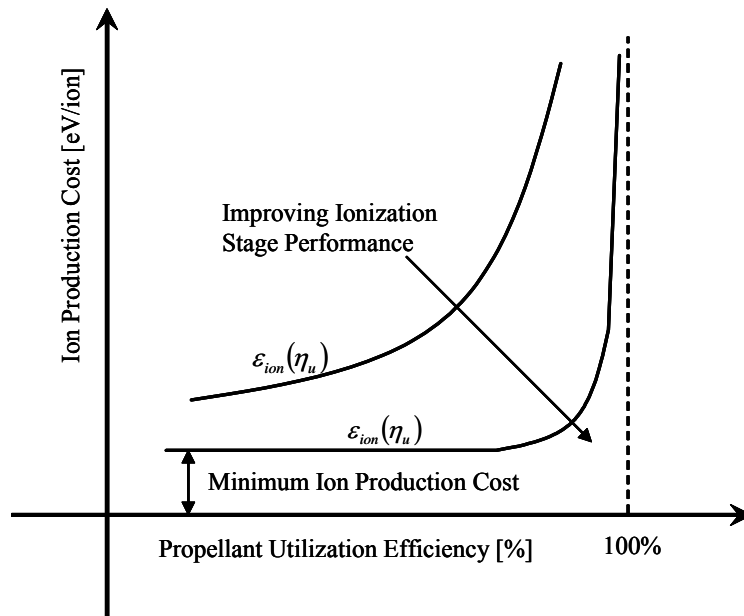


Figure 1-3: Ionization stage performance characterization [34].

To achieve efficient ion thruster operation, the ionization stage should be designed to operate near the knee of the performance curve, as illustrated in Figure 1-3, thereby maintaining a low ion production cost with sufficient propellant utilization efficiency.

#### **1.2.1.1 Recent Ion Thrusters**

A number of foreign agencies have utilized ion thruster technology recently for in-space applications with great success. ESA has successfully demonstrated electron-bombardment and radio-frequency ion thrusters as a primary propulsion system for the ARTEMIS (Advanced Relay and Technology Mission Satellite) telecommunications spacecraft [39]. The Japan Aerospace and Exploration Agency (JAXA) and the Institute of Space and Astronautical Science (ISAS) have developed and launched the Microwave Discharge Ion Thrusters on Mu Space Engineering Spacecraft-C (MUSES-C) to conduct a near Earth asteroid rendezvous and sample return mission [7]. The MUSES-C spacecraft contains four microwave electron cyclotron resonance (ECR) discharge ion thrusters that have demonstrated over 18,000 hours of life during ground tests [7, 48].

The United States has also been successful in using ion propulsion in space in recent years as well as developing new engines for future missions. NASA's 2.3 kW electron-bombardment NSTAR ion thruster successfully demonstrated the application of an EP device as the primary spacecraft propulsion system on the DS1 mission [33, 49, 50]. The DS1 ion propulsion system was not only able to perform its primary mission objectives, but had sufficient propellant left to execute both a July 1999 flyby of the

asteroid Braille and a September 2001 flyby of the comet Borrelly. The two extended mission flybys provided scientists with never before obtained information on the two bodies. The DS1 spacecraft was retired in December of 2001 after processing more than 65 kg of xenon propellant for a total operational time in excess of 15,000 hours [33]. Photographs of the NSTAR ion thruster during the DS1 spacecraft functional testing and a studio shot are shown in Figure 1-4.

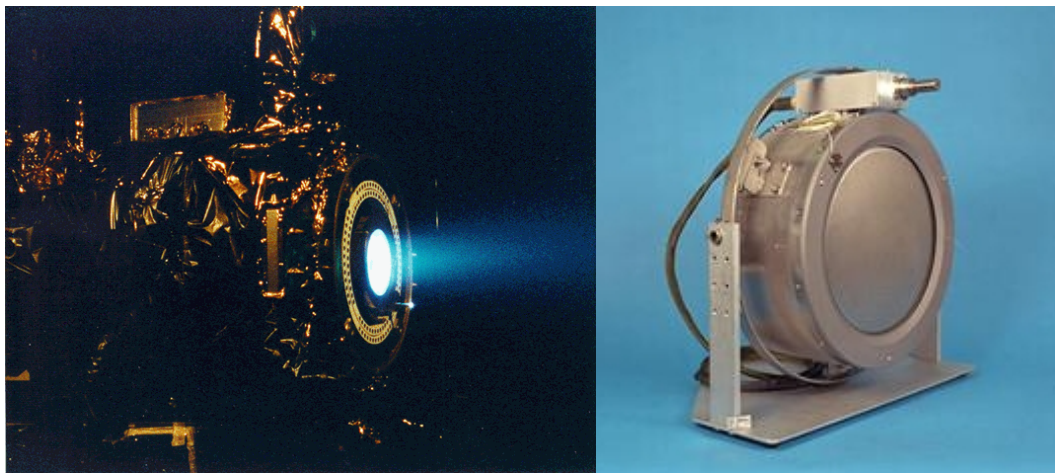


Figure 1-4: Photographs of the NSTAR functionality checkout on DS1 spacecraft propulsion system and a studio photograph of the thruster.

A spare NSTAR ion thruster was tested in parallel to the DS1 mission at NASA Jet Propulsion Laboratory (JPL) to examine life-limiting mechanisms of the thruster. The spare NSTAR thruster accumulated over 30,000 hours of operation, processing 235 kg of xenon, before the testing was voluntarily stopped [51].

NASA GRC is selected to develop NASA evolutionary xenon thruster system (NEXT) after the success of the NSTAR ion thruster on DS1 [44]. The goal of the NEXT ion thruster program is to develop a thruster system capable of meeting scientific

requirements identified by NASA Space Science Enterprise, for Discovery Class interplanetary missions. The NEXT ion thruster system design goal is to achieve greater than 4000 seconds specific impulse at thruster efficiency up to 68% with a power throttling range of 8:1, twice that of NSTAR, and a maximum power up to 8 kW. The NASA GRC ion thruster program decided to increase the grid area to 40 cm for NEXT, from 30 cm for NSTAR, thereby doubling the effective cross-sectional area. This increase in grid area allows for a larger beam current to be processed while avoiding space-charge limiting effects, as discussed in Section 1.2.1, and sustaining grid lifetime. The NEXT ion thruster maintained approximately the same specific mass of 3.6 kg/kW as NSTAR due to the increased thruster operating power level and mass. At an input power level of 6 kW, the engineer model (EM) NEXT thruster demonstrated a specific impulse of 4060 seconds at a thruster efficiency of 68.4% [43]. A photograph of the NASA GRC 40 cm NEXT ion thruster is shown in Figure 1-5.



Figure 1-5: NASA 40 cm NEXT ion thruster.

The NASA GRC project office was assigned the management responsibilities over all EP systems development efforts funded through NASA's nuclear power/propulsion project, Prometheus. Prior to the formation of project Prometheus, NASA's office of Space Science, Solar System Exploration Division, had awarded two contracts to develop a high-power EP system that could be coupled with a space-based nuclear power system. The goals of the NASA Research Announcements (NRA) were to demonstrate an EP system with the following performance objectives:

Power per Thruster = 20-50 kW  
Total EP System Power = 100 kW  
Specific Impulse = 6000-9000 seconds  
Total Thruster Efficiency  $\geq$  65%  
Propellant Throughput  $\geq$  50 kg/kW  
Total EP System Specific Mass  $<$  35 kg/kW

Two ion thruster proposals were selected and later rolled into project Prometheus. The first was the Nuclear Electric Xenon Ion System (NEXIS) by JPL [9]. The NEXIS ion thruster was based on a scaled-up version of the NSTAR ion thruster with several key improvements to meet the more stringent performance requirements. JPL's NEXIS development team ruled out the use of radio frequency or microwave plasma generation techniques in favor of a DC electron bombardment ionization source. The JPL team has developed a new technique of hollow cathode operation to overcome the inherent life-limiting concerns of SOA hollow cathode sources. JPL new hollow cathode design, known as a reservoir hollow cathode, contains a low work function emitting material that operates at a lower temperature, thereby increasing cathode lifetime. The NEXIS ion thruster was designed to have a nominal operating power level of 20 kW at a predicted

specific impulse of 7500 seconds and thruster efficiency of 78%. To achieve the increased operating power level at the acceleration potential needed for 7500 seconds specific impulse, a grid diameter of 65 cm was selected for NEXIS. A photograph of the NEXIS thruster ionization stage is presented in Figure 1-6.



Figure 1-6: A photograph of JPL's 20 kW NEXIS ion thruster [9].

The second thruster concept selected by NASA was the NASA GRC High Power Electric Propulsion (HiPEP) ion thruster. The HiPEP thruster is scaled to operate up to 50 kW at a maximum specific impulse of 9000 seconds. To meet the NRA goals, the HiPEP is derated for a nominal power level of 25 kW. The HiPEP deviated from SOA NASA ion thruster designs by incorporating a rectangular configuration instead of a circular design. The HiPEP ionization stage was to be composed of a microwave ECR [8] for increased lifetime, similar to the MUSES-C ion thruster. A second configuration of the HiPEP ion thruster, being developed under the Prometheus task, is an electron bombardment type of ionization. The rectangular configuration is selected to simplify future ion thruster scaling based on the HiPEP thruster. The HiPEP ion beam extraction plane measured 91 cm by 41 cm. Both HiPEP thruster configurations incorporate a

microwave ECR neutralizer cathode, to overcome the lifetime issues of the current SOA cathodes<sup>6</sup>, or SOA hollow cathode. A photograph of the HiPEP ion thruster is presented in Figure 1-7.

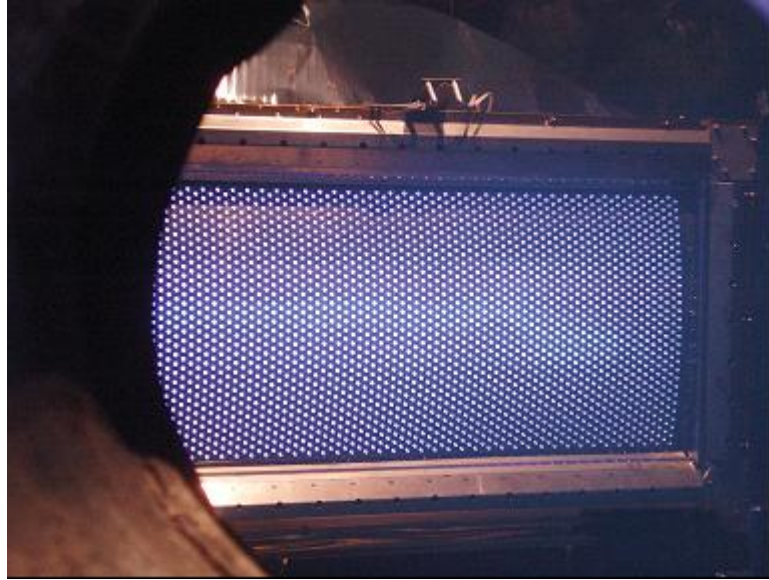


Figure 1-7: A Photograph of the HiPEP ion thruster.

### 1.2.2 Hall Thruster Technology

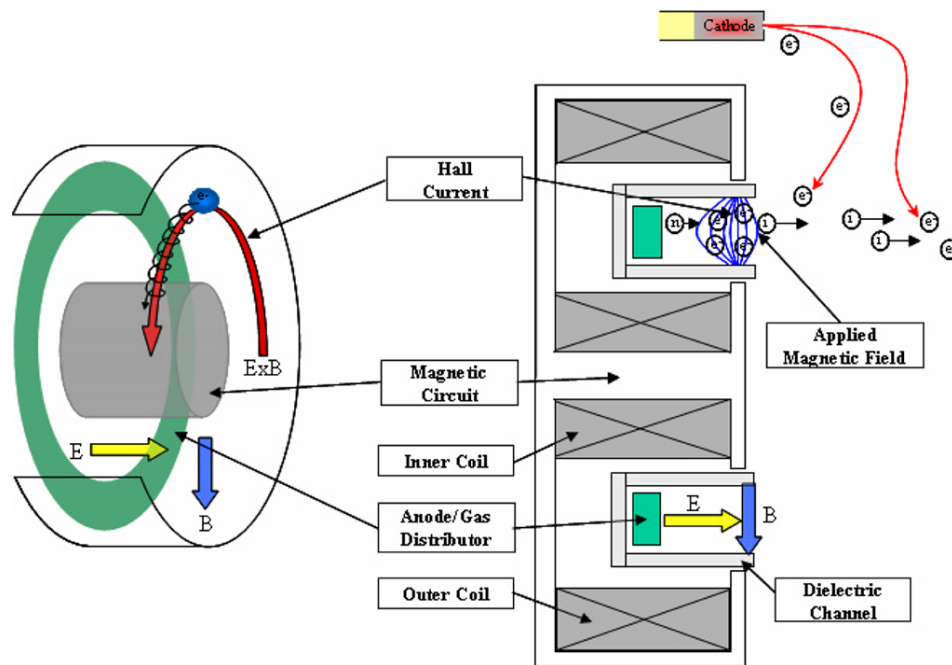
A Hall thruster is typically composed of a coaxial plasma source, although there has been work conducted on linear [52, 53] and racetrack configurations [54], that ionizes and accelerates propellant through an **ExB** process. A Hall thruster can be in either a single-stage or two-stage configuration [24, 29, 55-60]. A single-stage Hall thruster is the most developed and flight demonstrated configuration and will be the topic of the

---

<sup>6</sup> The current SOA NASA hollow cathode has a lifetime demonstrated up to 30,000 hours [51] A. Sengupta, J. R. Brophy, and K. D. Goodfellow, "Status of the Extended Life Test of the Deep Space 1 Flight Spare Ion Engine after 30,352 Hours of Operation," presented at Joint Propulsion Conference, AIAA-03-4558, Huntsville, Alabama, 2003.

following discussion. The characteristics of two-stage Hall thrusters will be discussed in Section 1.2.2.1.

There are two variants of single- and two-stage Hall thruster devices that have been developed, researched, and used as propulsion systems on spacecraft<sup>7</sup>. The two variants are known as stationary plasma thruster<sup>8</sup> (SPT) and the anode layer thruster (ALT). The single-stage SPT will be discussed first to develop a basic understanding of the governing physics and operation of a Hall thruster. A single-stage SPT is comprised of an anode inside of a dielectric discharge channel, a downstream cathode to provide electrons, and an applied mostly “radial” steady-state magnetic field topology in the discharge channel, as can be seen in Figure 1-8.



<sup>7</sup> There have been over one hundred Hall thrusters used on Russian spacecrafts since the first demonstration flight in 1972 on the Meteor spacecraft with an SPT-60 Hall thruster. Two-stage devices have only been tested on the ground.

<sup>8</sup> SPT-type Hall thrusters are also referred to as magnetic layer thruster.

Figure 1-8: SPT diagrams.

The magnetic field topology is established by a magnetic circuit composed of either electromagnetic coils or permanent magnets, and a ferromagnetic iron structure that behaves as flux channels for the magnetic fields generated by the field sources<sup>9</sup>. An axial electric field is developed between the anode, which also functions as the neutral propellant distribution system in the discharge channel, and the thermionic emitting hollow cathode (Figure 1-9).

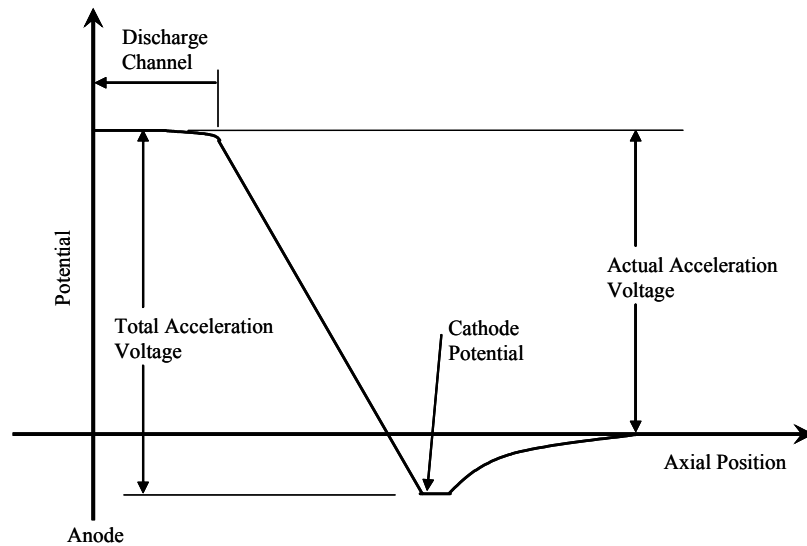


Figure 1-9: Sample potential distribution of a Hall thruster [59-61].

Electrons emitted from the cathode are attracted towards the anode due to the potential gradient applied between the cathode and anode. The electrons that are accelerated towards the anode enter the discharge channel where they begin to experience an

---

<sup>9</sup> The electromagnetic system of the majority of conventional Hall thrusters is comprised of a single center coil and a number of opposing individual outer coils (typically four) arranged symmetrically around the center coil at a diameter greater than the discharge channel diameter. This arrangement in conjunction with the magnetic circuit produces a radial magnetic field across the discharge channel. Recent Hall thruster designs incorporate only two azimuthal electromagnetic coils.

azimuthal  $\mathbf{E} \times \mathbf{B}$  drift, creating what is referred to as the Hall current. The azimuthal  $\mathbf{E} \times \mathbf{B}$  drift effectively impedes the majority of the axial electron motion towards the anode. The radial mobility of the trapped electrons is much larger than their axial mobility, allowing increased collisions with the walls of the discharge channel [59, 60]. A non-conducting wall material with a high secondary electron emission coefficient (SEE) is incorporated in the SPT. The high SEE coefficient walls moderate the electron temperature in the discharge channel, thereby increasing the containment of electrons. The Hall current region forms what is described as a “virtual cathode.” The trapped electrons gyrate azimuthally around the discharge channel until they are either lost to the walls or anode, recombined, or are involved in an ionization collision with a neutral propellant particle. The ionization process of a Hall thruster contributes to the thermalization of the trapped electrons by removing the energy from the impacting electron and releasing a secondary electron at the thermal energy of the neutral propellant. The plasma in the ionization and acceleration regions of the Hall thruster supports a large axial potential close to the applied voltage, as a result of the suppressed axial mobility. The established potential field profiles in the discharge channel follow the applied magnetic field topology to a first order. This approximation tends to hold true along the center of the discharge channel but breaks down near the anode where the applied magnetic field is small and near the channel walls where the electron pressure gradient becomes significant [59].

The radial magnetic field strength is selected in the range of several hundred gauss such that the Larmor radius of the electrons is less than the width and length of the Hall thruster discharge channel ( $w_c$  and  $l_c$ ), while the ionized propellant gyroradius is

larger. The following expressions describe the conditions that the applied magnetic field must satisfy for effective thruster operation [27, 59]:

$$r_e = \frac{m_e v_e}{eB} < l_c \quad \& \quad w_c < r_i = \frac{m_i v_i}{eB} \quad , \quad \text{Eqn. 1-8}$$

where  $m_e$  and  $m_i$  are the masses of an electron and propellant ion, respectively,  $B$  is the applied magnetic field strength, and  $v_e$  and  $v_i$  are the electron and propellant ion velocities. The propellant ions have greater mass than the electrons; therefore, the radial magnetic field has little to no effect on the acceleration trajectory of the propellant ions. The ionized propellant is then accelerated through the electrostatic potential held by the electrodes. Since the plasma in the discharge channel of a Hall thruster is populated by both ions and electrons, the plasma remains in a quasi-neutral steady-state. The plasma discharge of a Hall thruster therefore does not suffer from space-charge issues associated with ion thrusters. Hall thrusters can process larger power and current densities than ion thrusters<sup>10</sup>.

The second single-stage variant of the Hall thruster family is known as the anode layer thruster (TAL). A TAL is composed of metallic walls at the anode potential with cathode potential guard rings slightly downstream of the anode at the exit plane. The axial length of a TAL from the anode to the exit plane is much less than in a SPT. TALs behave similar to SPTs but possess greater electron temperature in the Hall current region

---

<sup>10</sup> NASA JPL's NEXIS high power ion thruster has a screen diameter of 750 mm for power level of 20 kW. Whereas the NASA-457M Hall thruster, which has a diameter of 457 mm, was designed for a nominal operating power of 50 kW and has demonstrated 98 kW. Scaling both thrusters to 500 kW power levels would require a Hall thruster of approximately 2 m in diameter (1000 V and 500 A discharge) and an ion thruster of approximately 3.75 m in diameter (6000 V and 83 A beam).

and shorter ionization and acceleration regions. Further information on the specific differences between SPTs and TALs are discussed in reference [62].

The factors that tend to limit the overall efficiency of a Hall thruster are listed below and are referred to as utilization efficiencies. While not exhaustive, the list below contains several of the most significant utilization efficiencies from a thruster engineering point of view.

- Current utilization efficiency ( $\eta_{\text{current}}$ ): The current utilization efficiency and the discharge current are defined as:

$$\eta_{\text{current}} = \frac{I_B}{I_{\text{Discharge}}}, \quad \text{Eqn. 1-9}$$

where,

$$I_{\text{Discharge}} = I_B + I_e, \quad \text{Eqn. 1-10}$$

where the  $I_B$  is the accelerated ion current,  $I_e$  is the electron leakage current, and  $I_{\text{Discharge}}$  is the measured discharge current of a Hall thruster. The electrons that are lost to the anode from the external cathode result in the largest Hall thruster inefficiency. This electron leakage current reduces the amount of electrons that are available for ionization and reduces the available ion beam current for a fixed discharge current, as shown in Equation 1-10. An optimized Hall thruster electron leakage current ranges from 20-30% of the total discharge current [63].

The electron leakage current can be reduced by improving the applied magnetic field topology [64], decreasing the electron temperature, increasing the electron path length, and reducing the near wall conductivity in the discharge channel.

- Voltage loss utilization efficiency ( $\eta_v$ ): The voltage loss utilization efficiency is described as follows in Ref. [64]:

$$\eta_v = \frac{V_{accelerated}}{V_{discharge}} . \quad \text{Eqn. 1-11}$$

This efficiency loss is due to the amount of the applied potential that is not available for acceleration, either due to the radial acceleration of the ions and/or the location in the discharge channel where an ion is created. The voltage loss utilization efficiency can be reduced by improved applied magnetic field topology.

- Charge utilization efficiency ( $\eta_q$ ): The charge utilization efficiency is defined in Ref. [64] as follows:

$$\eta_q = \frac{\left( \sum \frac{\Omega_i}{\sqrt{Z_i}} \right)^2}{\sum \frac{\Omega_i}{Z_i}} , \quad \text{Eqn. 1-12}$$

where  $\Omega_i$  is the ion current species fraction of the, and  $Z_i$  is the charge state for the  $i^{\text{th}}$  species. Generation of multiple-charge ions represents an efficiency loss

mechanism because it costs additional energy to ionize an ion to higher charge states. Hall thruster ion species fractions are approximately 90% Xe<sup>+</sup>, 9% Xe<sup>++</sup>, and <1% Xe<sup>+++</sup> [65, 66].

- Propellant utilization efficiency ( $\eta_u$ ): This utilization efficiency is defined as the ratio of the ion beam current to an equivalent neutral propellant mass flow rate current, based on anode temperature. The propellant utilization efficiency, for a singly ionized plasma, is shown in the following equation:

$$\eta_u = \frac{\dot{m}_i}{\dot{m}_a} \approx \frac{I_B}{I_a} \propto \frac{n_i}{n_a} \frac{v_i(300V)}{v_a(1000K)} \approx 85\% \rightarrow 99\%, \quad \text{Eqn. 1-13}$$

where  $I_a$  is the equivalent neutral propellant mass flow rate current,  $n_i$  is the density of ions,  $n_a$  is the density of neutral propellant in the thruster,  $v_i$  is the velocity of the accelerated ions, and  $v_a$  is the thermal velocity of the neutral propellant. The singly-charge propellant utilization efficiency describes how well the number of ions, which are created in the thruster, carries the beam current. A Hall thruster can have an ionization fraction ( $n_i/n_a$ ) as low as 15% [64] and still have a propellant utilization efficiency above 80%. This is possible due to the definition of the propellant utilization efficiency, which is an indication of how well the ionized propellant carries the beam current. The propellant utilization efficiency can increase above unity if increased populations of multiple charged ions are created. Equation 1-13 above does not take into account of multiply-charged ions and results in an inflated propellant utilization. The propellant

utilization efficiency was redefined in Ref. [64] to account for the ion species current fraction as illustrated in the following equation:

$$\eta_u = \eta_{current} \frac{M_{Propellant} I_{discharge}}{\dot{m}_{anode} e} \sum_i \frac{\Omega_i}{Z_i}, \quad \text{Eqn. 1-14}$$

where  $M_{Propellant}$  is the mass of a xenon atom,  $\dot{m}_{anode}$  is the anode propellant mass flow rate,  $\Omega_i$  is the ion current species fraction for the  $i^{\text{th}}$  species, and  $Z_i$  is the charge state for the  $i^{\text{th}}$  species.

- Ion Production Cost: Ref. [60] indicates that the ion production cost in a Hall thruster is approximately three times the ionization potential of xenon (36 eV/ion) and five to six times the ionization potential when one accounts for wall losses (60-70 eV/ion) for an efficiently operating Hall thruster. Whereas, a SOA ion thrusters have ion production cost as low as 100 eV/ion.

### 1.2.2.1 Two-Stage Hall Thrusters

The incorporation of decoupled ionization and acceleration mechanisms, known as two-stage operation, in a Hall thruster has been researched since the early 1960's in the former Soviet Union. In the 1990's, the United States, Russia, and other countries continued two-stage Hall thruster research [29, 53, 67-75]. The early research on two-stage Hall thrusters was primarily conducted on TALs at TsNIIMASH [76]. It was determined, by the Soviet Union mission planners, that an efficient propulsion system

would be required for interplanetary exploration missions with specific impulse values ranging from 2000-8000 seconds at thruster power levels approaching hundreds of kilowatts. To reach this specific impulse range, several propellants were studied including condensable materials such as bismuth and cesium, and noble gases such as xenon and krypton [58]. A two-stage TAL was developed and tested in the 1960's at power levels up to 100 kW, which resulted in specific impulse up to 8000 seconds at efficiencies approaching 80% [56]. Two-stage high-power TALs never went beyond laboratory devices, due to the limitations of spacecraft power supplies. The focus of Hall thruster research in the 1970's and 80's went towards lower power kilowatt-class single-stage thrusters operating on xenon propellant, given the mission requirements and available spacecraft power supplies of the time [76]. In the 1990's, multi-kilowatt powered spacecraft became achievable and therefore high specific impulse EP devices (such as two-stage TALs) were sought after for applications such as NSSK and interplanetary exploration. These missions required devices that could deliver high specific impulse operation at high thruster efficiency. The D-80 [29, 75], D-100 [77], and TM-50 [78] two-stage TALs operating on xenon were developed and demonstrated by TsNIIMASH in Russia and tested in US laboratories. The goals of these devices were to overcome the thruster efficiency limitation above 600 to 800 V that are experienced by other SOA Hall thrusters. The efficiency peak was believed to result from the increased generation of multiply charged propellant ions, and the increase of electron leakage current to the anode [64].

In the last decade, the development of several two-stage SPTs was conducted. These thrusters included the Shizuoka University low-power Hall thruster with an

intermediate emissive electrode [55], Princeton University 1 kW SPT with an emissive and non-emissive intermediate electrode [67-70, 79-83], Busek BHT-HD-1000 [73], the University of Michigan P5-2<sup>11</sup> and LGIT [53, 71], and the Institute of Space and Astronautical Science (ISAS) ECR discharge Hall thruster [72]. The primary objective of the two-stage SPT, as with the two-stage TAL, was to improve thruster efficiency at higher discharge voltages by reducing the influence of multiple charged propellant ions and by mitigating the electron leakage current to the anode. It has been shown in analytical Hall thruster modeling that the amount of electron leakage is the major limiting factor of maximizing thruster efficiency [64, 84-86].

The basic concept of a two-stage Hall thruster, either SPT or TAL configuration, is to decouple and/or enhance the ionization and acceleration processes. The SPT and TAL type two-stage Hall thruster concepts have approached this objective with the addition of an intermediate electrode downstream of the anode and upstream of the exit plane of the discharge channel, as can be seen in Figure 1-10. The intermediate emissive electrode for two-stage SPTs is fabricated from either lanthanum hexaboride ( $\text{LaB}_6$ ) or impregnated porous tungsten (4:1:1 molar ratio of  $\text{BaO}$ ,  $\text{CaO}$ , and  $\text{Al}_2\text{O}_3$ ). The intermediate electrode serves as the cathode for the ionization stage and the anode for the acceleration stage. The use of the intermediate electrode allows the ionization stage to operate in a high-current, low-voltage mode, which allows for optimum propellant utilization. The emissive intermediate electrode generates low-temperature electrons for ionization in the first stage. These first stage electrons experience a much smaller

---

<sup>11</sup> The P5-2 two-stage Hall thruster name was later changed to the NASA-173M which was only utilized as a single-stage Hall thruster in ref. [63]

potential, usually less than 150 V, in the ionization stage of the thruster. The production of multiple charged propellant ions is controlled in the first stage by limiting the electron temperature.

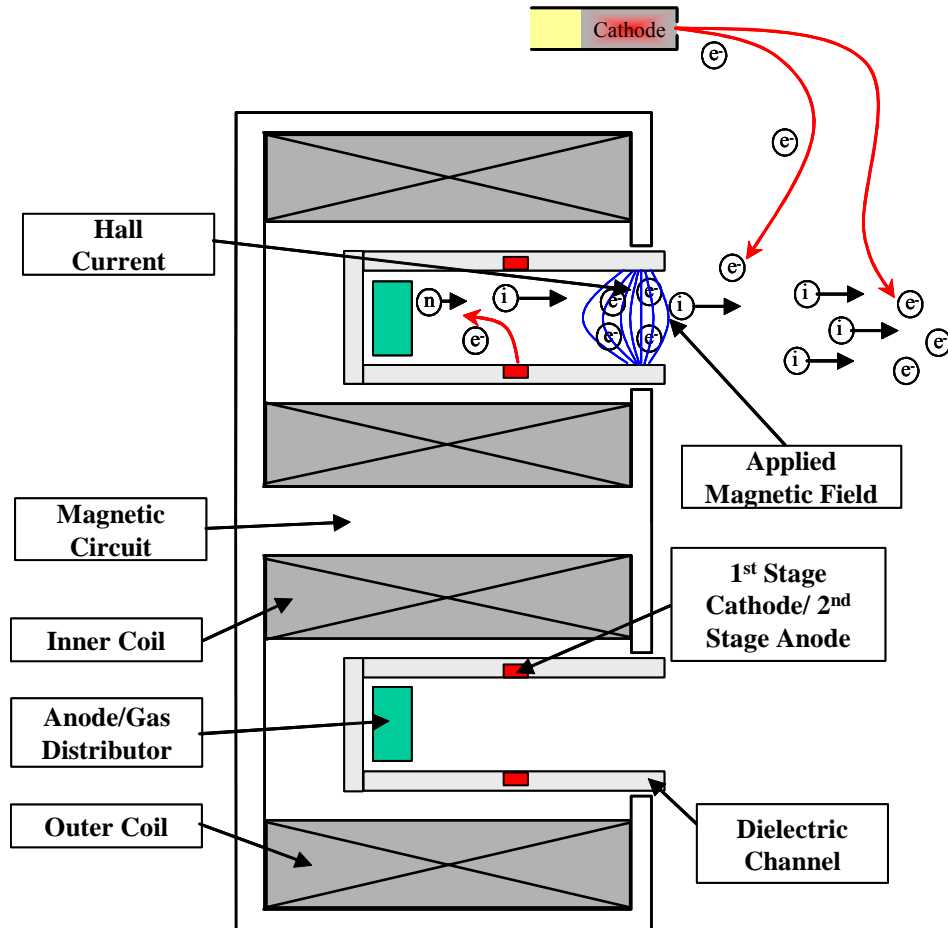


Figure 1-10: Two-Stage SPT diagram.

The Shizuoka University low-power two-stage Hall thruster has an emissive intermediate electrode that acts as the first-stage cathode and the second-stage anode. The operators are able to control the heating of the intermediate electrode to evaluate the thruster performance. The thruster is operated over a range of acceleration voltages (up to 175 V) in three different configurations; single-stage, two-stage without additional

intermediate electrode heating besides the plasma self-heating, and two-stage with external heating of the intermediate electrode. The experimental results clearly indicate an improvement of the two-stage operation over the single-stage operation. The external heating of the emissive electrode indicate improved thruster efficiency as compared to self-heating operation in the two-stage configuration, as shown in Figure 1-11 [55].

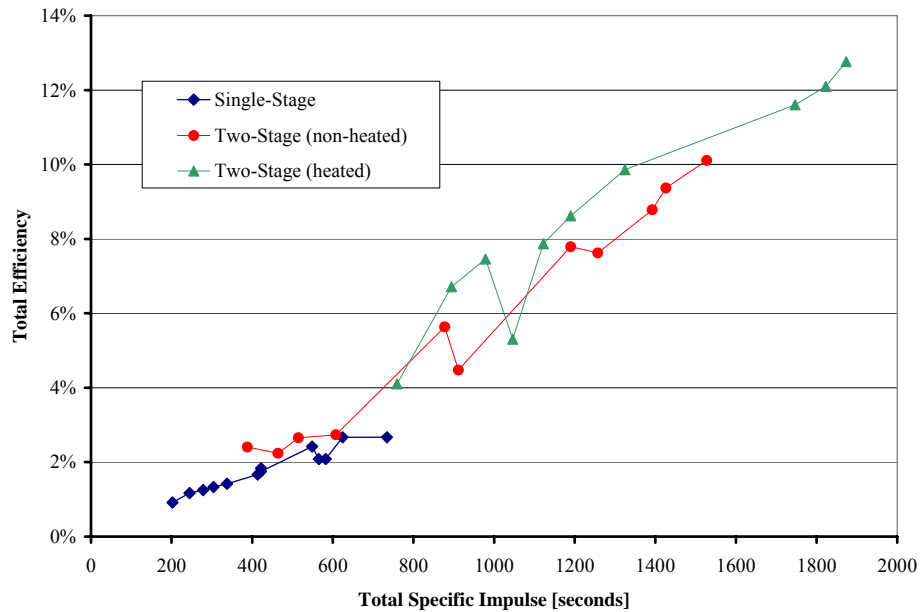


Figure 1-11: The performance results of the Shizuoka University low-power two-stage Hall thruster in single-, and two-stage mode with and without intermediate electrode heating on argon [55].

Shizuoka University low-power two-stage Hall thruster efficiency was below previously measured SOA efficiencies. This is a result of operating the thruster at an acceleration potential of 175 V, which is lower than SOA thruster design voltages (300 V). It has been shown that as the discharge voltage in a single-stage Hall thruster is lowered below the design voltage, the propellant utilization efficiency decreases [30]. Moreover, the

Shizuoka University thruster was operated with argon as the propellant. Argon has an atomic mass of 39.948 and thus will have a shorter residence time in the thruster as compared to xenon with an atomic mass of 131.3. The shorter residence time of the argon particles in the thruster reduces the probability of ionization as compared to xenon. The channel wall losses were significant due to the excessive channel length [55].

The University of Michigan Plasmadynamics and Electric Propulsion Laboratory (PEPL) in cooperation with NASA GRC developed and demonstrated a two-stage SPT known as the P5-2 [71]. The P5-2 shared a scaling heritage with the 5 kW single-stage P5Hall thruster developed earlier at the University of Michigan in cooperation with United States Air Force [87]. The P5-2 supported an improved magnetic circuit design that produced an applied magnetic field topology known as a plasma lens. The plasma lens topology has been shown to improve Hall thruster performance [64, 71, 88-90]. The P5-2 also included the ability to configure the thruster as a two-stage device with an emissive intermediate electrode that could be independently heated. A photograph of the P5-2 is shown in Figure 1-12. The P5-2 was successfully tested in both single- and two-stage configurations, with only a self-heated emissive intermediate electrode. The initial evaluation of the P5-2 two-stage operation showed that the thruster operated at a reduced efficiency for the various propellant flow rates as compared to the single-stage configuration (Figure 1-13). Further improvements on the P5-2 two-stage Hall thruster were proposed in Ref. [71], but never realized due to a shift in focus. The proposed improvements in Ref. [71] included heating the emissive intermediate electrode, modifying the axial location of the intermediate electrode, and making *in-situ* modifications to the applied magnetic field with a trim coil located behind the anode.

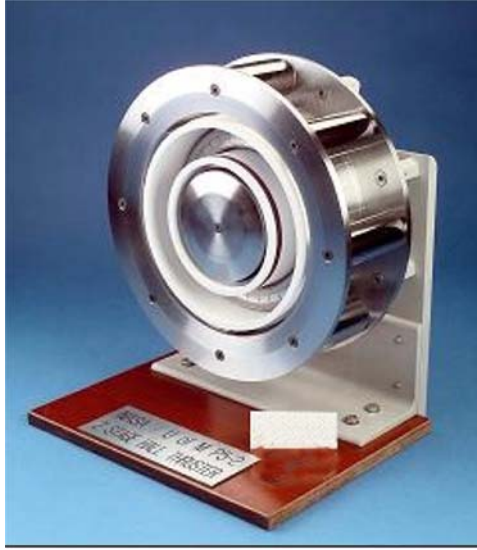


Figure 1-12: The P5-2 5 kW two-stage Hall thruster.

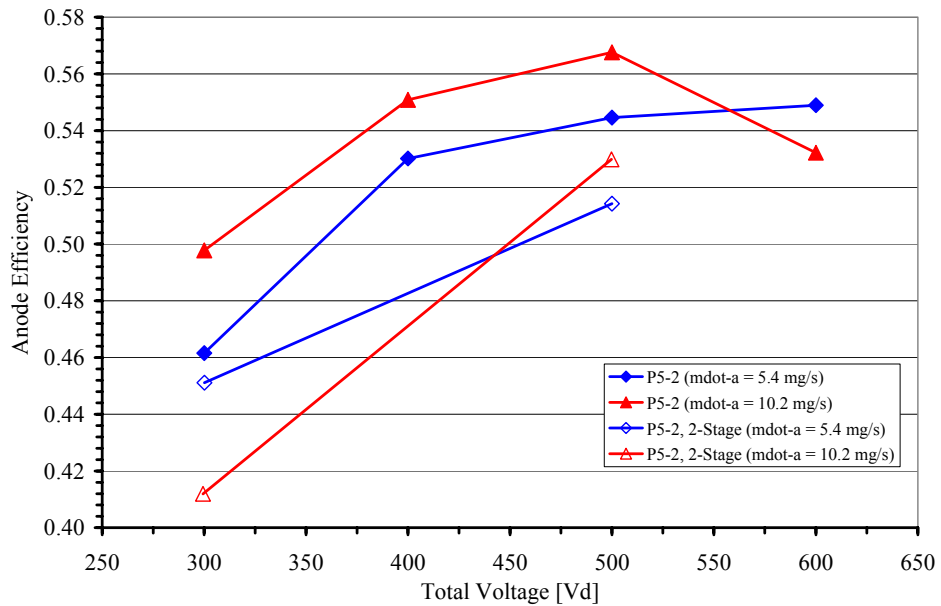


Figure 1-13: Comparison of the anode efficiencies<sup>12</sup> of the single- and two-stage (without heating) operation of the P5-2 Hall thruster (From Ref. [71]).

<sup>12</sup> Anode efficiency is a convenient expression to illustrate the functionality of the Hall thruster independent of the design and operation of the electromagnetic coils and the hollow cathode.

Princeton Plasma Physics Laboratory (PPPL) at Princeton University developed and demonstrated a segmented electrode<sup>13</sup> SPT in single- and two-stage configurations. PPPL's segmented Hall thruster was designed such that the placement and material of the intermediate electrode could be interchanged for either single- or two-stage operation. PPPL's segmented Hall thruster was not necessarily developed to investigate high-specific impulse operation, but to examine the basic operation of Hall thruster devices. PPPL's segmented Hall thruster demonstrated an increase in thruster efficiency when operated in a two-stage configuration over single-stage, as seen in Figure 1-14.

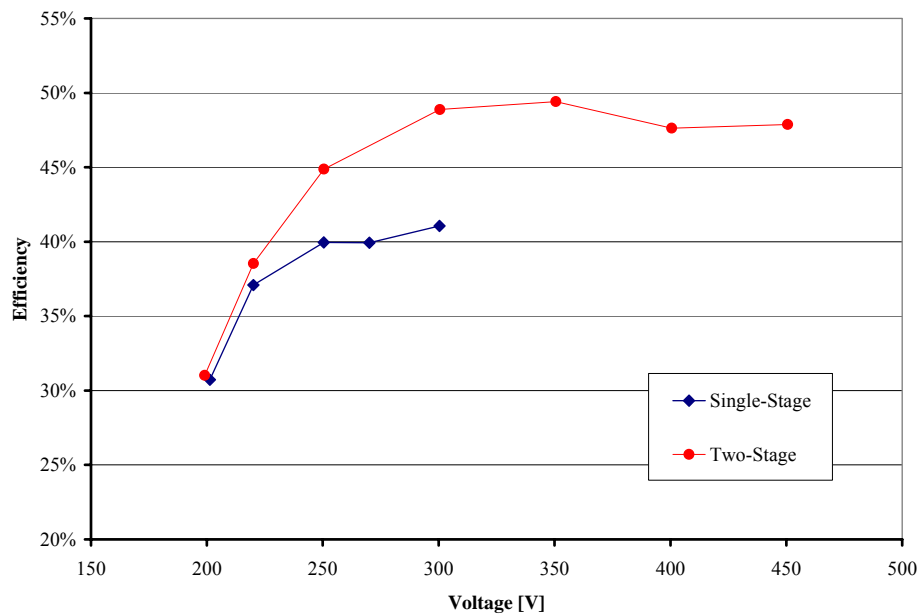


Figure 1-14: PPPL segmented Hall thruster single- and two-stage performance results for 2 mg/s xenon flow [69].

Recent computational model research conducted at ETSI Aeronauticos Madrid, in Ref. [91, 92], examined the concept of an intermediate electrode in a two-stage SPT .

<sup>13</sup> A segmented Hall thruster concept is the same as the intermediate electrode referred to earlier in the description of two-stage Hall thrusters.

The results indicated that the location and applied bias voltage of the intermediate electrode is an important factor for successful operation of a two-stage device. The optimal placement of the second-stage emissive electrode was shown to be near the exit plane of the discharge channel within the acceleration region, and beyond the boundary of the ionization and acceleration region, as was suggested by Kaufman [93]. The model predicted an efficiency gain from 52% to 62% between single- and two-stage operation, at a first-stage voltage of approximately 137 V and a total applied voltage of 296 V. The authors attribute this performance increase to a reduction of the electron leakage current. As mentioned earlier, the electron leakage is considered one of the biggest efficiency loss mechanisms in a Hall thruster and has been studied in single- and two-stage Hall thruster research as a means of improving thruster operation [64] and performance [73].

The D-80 two-stage TAL, developed by TsNIIMASH under contract with Boeing Rocketdyne, was capable of operating in a single- or two-stage configuration. Two versions of the D-80 (NTS-1 and NTS-2) were provided to NASA GRC by Boeing through a subcontract with TsNIIMASH. The two versions of the D-80 were characterized at TsNIIMASH before being delivered to NASA GRC. NTS-1 was tested at NASA GRC in both single- and two-stage modes. The D-80 was one of two thrusters developed and tested as a result of a NASA contract to demonstrate a high-specific impulse Hall thruster operation. The intermediate electrode in the D-80 two-stage Hall thruster was composed of a non-emitting material. The additional electrode in this type of two-stage configuration was thought to improve the potential distribution in the ionization and acceleration stages. This type of two-stage device, as with a single-stage

Hall thruster, requires some electron leakage to sustain the ionization. A photograph of the D-80 thruster is presented in Figure 1-15.



Figure 1-15: A photograph of TsNIIMASH single- and two-stage D-80 [29].

The two-stage performance of the D-80 indicated no performance gain over single-stage operation at propellant flow rates above 4 mg/s, as can be seen in Figure 1-16 from Ref. [29]. The single-stage results are illustrated by the initial performance data points (discharge-stage voltage of zero) in Figure 1-16. The thruster performance at the two lowest propellant flow rates increased as the first-stage discharge voltage increased up to a point (e.g. 120 V for 4.1 mg/s). However, thruster performance for the higher flow rates (above 4.1 mg/s) tended to decrease as more of the total voltage was supplied to the discharge stage. The experimental performance data of the second version of the D-80 (NTS-2) in a two-stage configuration showed improved high-voltage operation by increasing the thruster efficiency from 51% to 59%, at 700 V acceleration potential, during performance testing in Russia [75]. Figure 1-17 illustrates additional two-stage

performance improvements over single-stage operation. Figure 1-17 shows that the maximum thruster efficiency occurred at a first stage discharge voltage of approximately 150 for the NTS-2 D-80.

The D-80 NTS-2 preliminary results from TsNIIMASH did indicate that two-stage operation could provide performance benefits. The performance improvements of the NTS-2 over the NTS-1 were the result of configuration changes between the two stages. Unfortunately, the NTS-2 improvements have not been confirmed at NASA GRC.

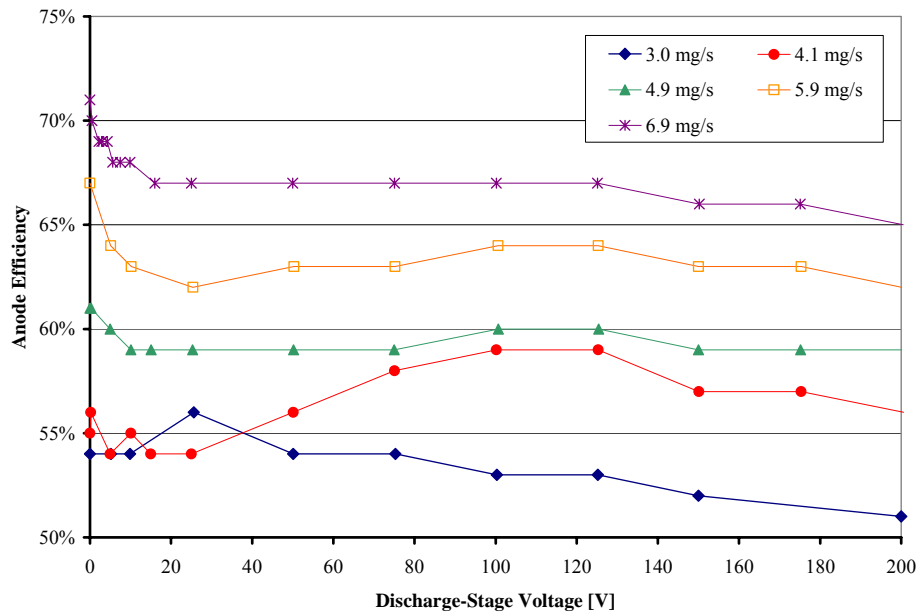


Figure 1-16: The NTS-1 D-80 two-stage TAL anode efficiency as a function of the first-stage discharge voltage is increased while maintaining a constant total applied potential [29].

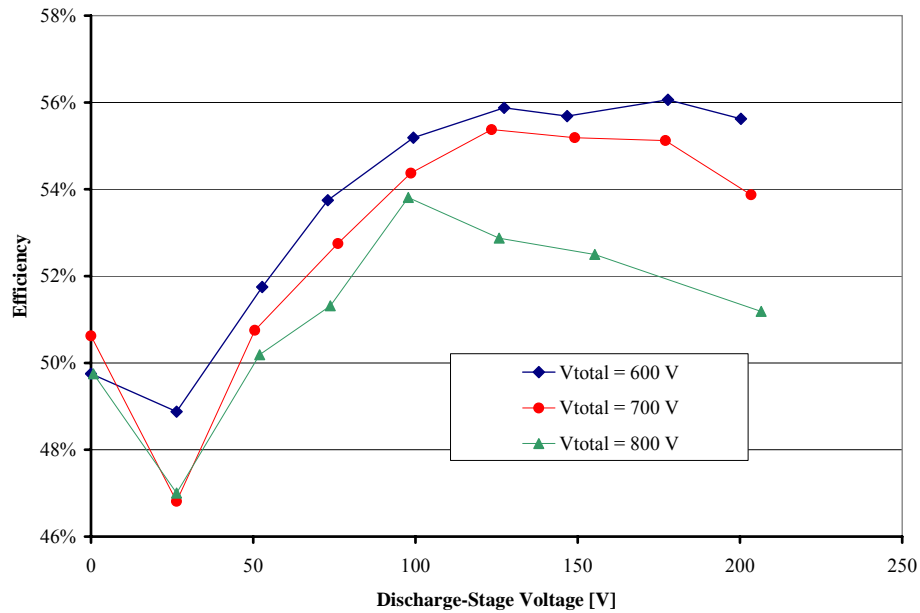


Figure 1-17: D-80 two-stage performance results for an increasing first-stage discharge voltage while maintaining a fixed total applied voltage [75].

The Busek Corporation Inc. developed and evaluated a 1 kW SPT (BHT-HD-1000) which can operate in a single- or two-stage configuration to achieve high-specific impulse. The work was sponsored by NASA GRC under a small businesses innovation research (SBIR) to develop and demonstrate a 3000 second specific impulse Hall thruster at 2.3 kW, while generating 100 mN of thrust [73]. A photograph of the Busek’s BHT-HD-1000 is shown in Figure 1-18. The performance evaluation of the BHT-HD-1000 in single- and two-stage operation indicated little or no advantage of two-stage operation (Figure 1-19).

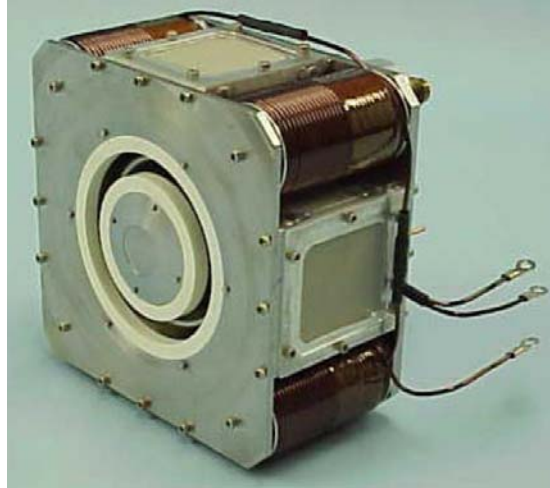


Figure 1-18: A photograph of the BHT-HD-1000 (reprinted courtesy of Busek Co. Inc.).

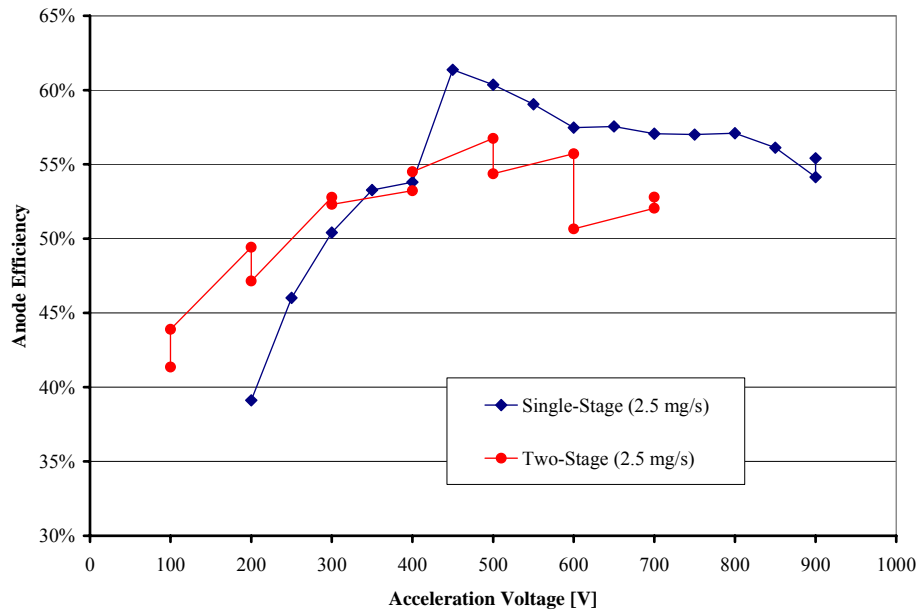


Figure 1-19: The performance results of the BHT-HD-1000 in both single- and two-stage operation at a xenon flow rate of 2.5 mg/s [73].

The researchers in Ref. [73] attributed the decrease of performance of the BHT-HD-1000 to increased electron leakage current from approximately 21% of the discharge current to

at least 35%. Thermal limitations of the BHT-HD-1000 design also limited the maximum input voltage to 1000 V over the range of propellant mass flow rates investigated.

In conclusion, the development and study of two-stage Hall thrusters have provided vast amounts of information on high-specific impulse operation. The benefits of two-stage Hall thrusters have never been definitively demonstrated on noble gas propellants other than low-power, low-voltage laboratory devices. However, not all the possible two-stage Hall thruster configurations have been investigated. This dissertation will explore one of the more innovative two-stage Hall thruster configurations, a combination of the ionization stage of an ion thruster with the acceleration stage of a Hall thruster.

#### **1.2.2.2 Recent Single-Stage High-Specific Impulse Hall Thrusters**

The single-stage Hall thruster was not completely dropped from consideration for the development of efficient high-voltage operation. Several single-stage Hall thrusters were designed to operate at elevated discharge voltages<sup>14</sup>. These thrusters incorporated an improved applied magnetic field distribution, thermal design, scaling, and propellant distribution system [29, 31, 64, 71, 89, 94].

---

<sup>14</sup> In a single-stage Hall thruster, the applied discharge voltage is used for both the ionization and acceleration of the propellant ions. Whereas in a two-stage Hall thruster, the discharge voltage refers to the voltage applied only to the ionization stage.

The D-80 TAL, developed by TsNIIMASH, was capable of operating in a single- or two-stage configuration. The D-80, in a single-stage configuration, was operated at NASA GRC to a discharge voltage of 1700 V, which resulted in a specific impulse of 4140 seconds at an anode efficiency of 56% [29]. However, the thruster efficiency peaked between 500 to 800 V for the various propellant flow rates investigated, as seen in Figure 1-20.

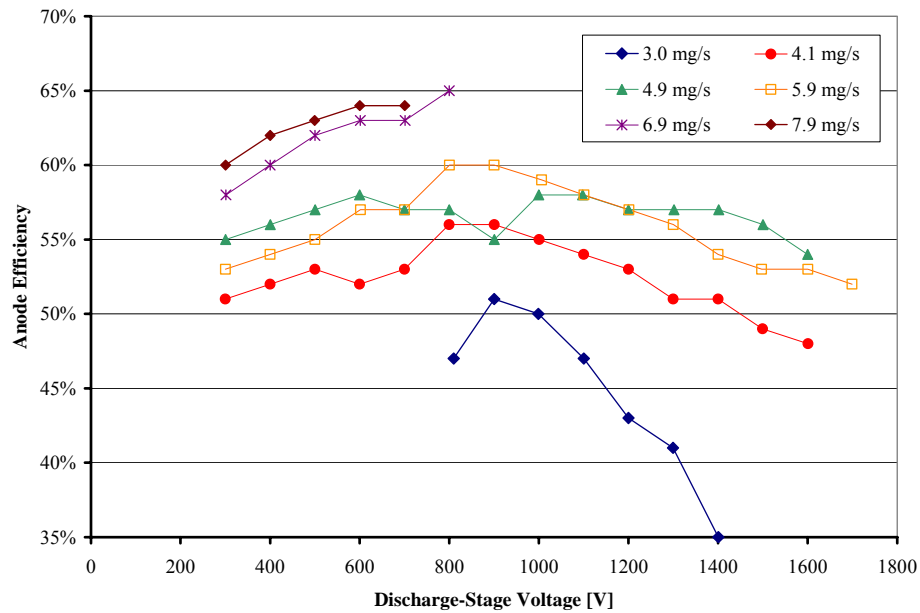


Figure 1-20: The performance results of the D-80 in single-stage TAL [29].

The decrease of the thruster performance, as the discharge potential was increased beyond the SOA levels (300-500 V) was thought to be a result of either a combination of increased electron leakage current and increased multiple ionization of the propellant. Subsequent testing of the D-80, to investigate the erosion characteristics of the high-voltage operation, indicated that components of the magnetic circuit were exposed to the

plasma between the 600 and 900 hours of operation [95], which essentially represents the end of thruster life. While several theories were examined in Ref. [95] to determine the cause of the accelerated erosion rate over the designed 8000 hours, none provided a clear answer to the increased erosion. Later research conducted at NASA GRC on the erosion mechanisms of SPTs linked the amount of eroded wall material to the applied radial magnetic field near the wall of the discharge chamber [96]. Similar results were observed during an accelerated guard ring erosion test on a single-stage TAL by Marrese, *et. al.* in Ref. [97]. It was discovered that due to the particular design of the magnetic circuit of the D-55 thruster, there were regions of lower radial magnetic fields that occurred between the electromagnetic coils. These zones of decreased magnetic field corresponded with the regions of greater erosion. The results of Ref. [96, 97] suggest that the applied magnetic field of the D-80 thruster may be insufficient for operation at elevated voltages. Concurrent research conducted by NASA GRC and the University of Michigan on high-specific impulse SPTs [28, 64, 71, 89] determined that improvements made to the applied magnetic field topology increased thruster performance at elevated discharge voltages. It is possible that if the magnetic circuit of the D-80 were redesigned, then the thruster could operate efficiently at higher specific impulses and with an increased lifetime.

The SPT-1 magnetic layer Hall thruster, developed by the Fakel Design Bureau under contract with Atlantic Research Corporation, was provided to NASA GRC as one of two thrusters developed and tested as a result of a NASA contract to demonstrate a high-specific impulse Hall thruster operation [23, 73, 94, 98]. The SPT-1 incorporated boron nitride insulator rings only in the exit region of the discharge channel, where the

magnetic field maximizes. A metal anode cup comprised the rest of the discharge channel. The outer diameter of the SPT-1 was 100 mm, similar to the diameter of the widely used and documented SPT-100, with an anode capable of independently injecting the propellant from the rear of the anode towards the exit of the channel or injecting the propellant near the exit of the discharge channel backwards toward the anode [94]. The investigation of the SPT-1 at NASA GRC focused only on propellant injection from the rear of the discharge channel as is characteristic of Hall thruster devices. The SPT-1 demonstrated an anode specific impulse of 3500 seconds, at a discharge voltage of 1200 V, and an anode efficiency of 50% [94]. The performance results of the SPT-1 from Ref. [94] is illustrated in Figure 1-21.

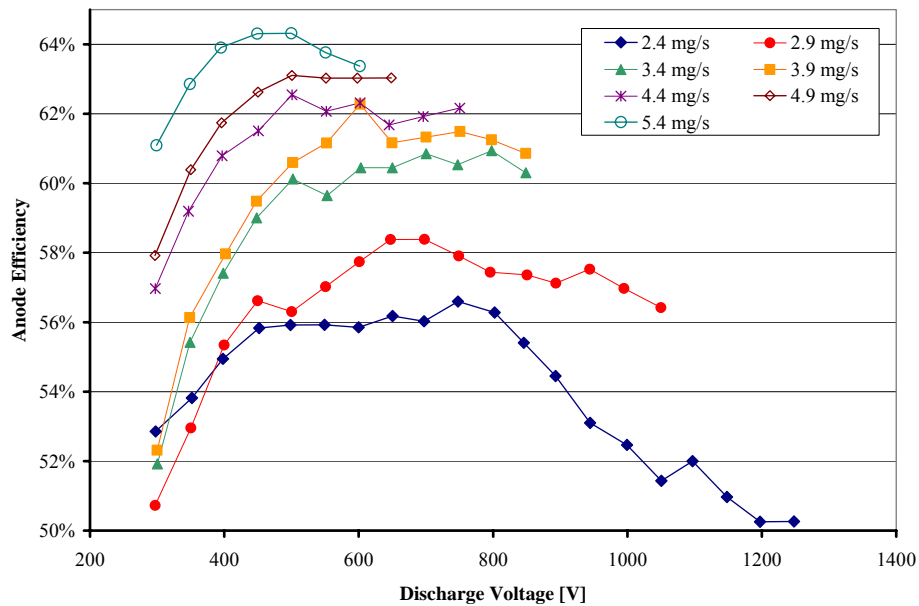


Figure 1-21: The performance results of the SPT-1 Hall thruster [94].

As was observed with most of the earlier high-voltage single- or two-stage thruster investigations prior to NASA in-house Hall thruster development efforts, the performance of the SPT-1 peaked around 500 to 700 V for the various propellant flow rates investigated. It was suggested by Manzella in Ref. [94] that an increased electron leakage current was causing the discharge current to increase with voltage.

The NASA-173M series of SPTs was developed to examine high-specific impulse operation of single-stage devices as part of a joint thruster development effort between the University of Michigan and NASA GRC. Both the NASA-173Mv1 and NASA-173Mv2 incorporated improved magnetic circuit designs that produce a “plasma lens” field topology [59, 60, 64, 71, 88, 89, 99] in the discharge channel. Since the applied magnetic field approximates the equipotentials of the electric field [59, 64] a focusing magnetic field should create electric fields that drive the ions towards the center of the channel. Additional coils, known as trim coils, were included in the design of both thrusters to allow for *in-situ* magnetic field modifications. At anode propellant flow rates of 10 and 15 mg/s, the NASA-173Mv2 demonstrated thruster efficiencies that remained constant or even increased with discharge voltage (Figure 1-22). The NASA-173Mv2 demonstrated a maximum anode specific impulse above 3700 seconds with an anode efficiency of 68.5% for a discharge voltage of 1000 V and a discharge power of 9.8 kW [28].

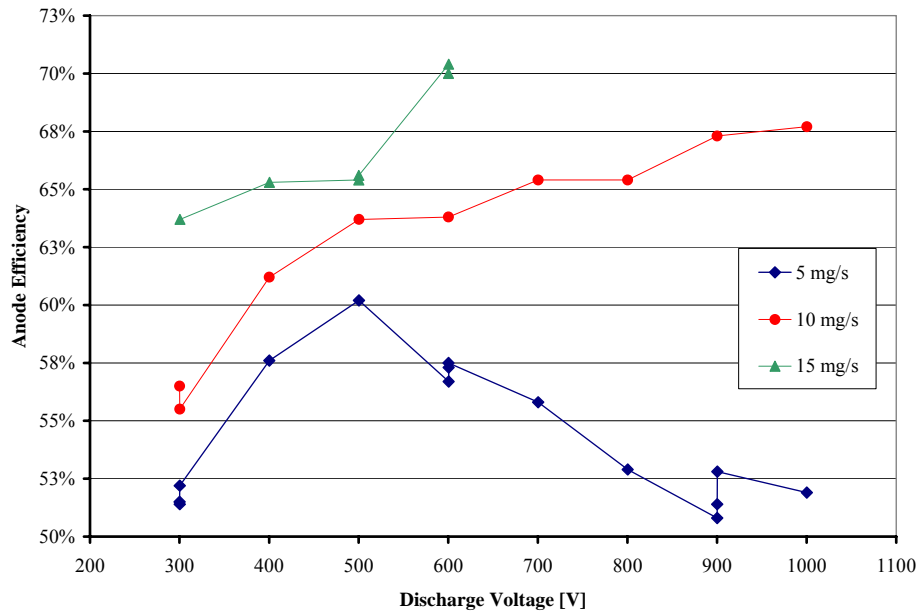


Figure 1-22: NASA-173Mv2 Hall thruster performance [28].

The use of alternative propellants, such as krypton and xenon/krypton mixtures, with Hall thruster devices have been investigated at NASA GRC and other electric propulsion organizations in recent years [31, 100-102]. The appeal of using krypton over xenon for high-specific impulse operation is that while the mass of krypton is less than xenon, krypton is still massive enough to provide sufficient thrust at high efficiency. Recall that the specific impulse is related to the ratio of the exit velocity of the propellant to the gravitational acceleration on Earth (Equation 1-2).

An electrostatic device accelerates propellant to an exit velocity that is proportional to the applied potential and the mass of the propellant. Ignoring the location of the ionization event of the propellant and any perpendicular velocity components, the ionized propellant velocity is described as follows:

$$U_e = \sqrt{\frac{2qZ\phi}{M_{propellant}}}, \quad \text{Eqn. 1-15}$$

where  $q$  is the charge of an electron,  $Z$  is the degree of ionization of the propellant,  $\phi$  is the applied acceleration potential, and  $M_{propellant}$  is the mass of the propellant. As it can be seen in Equation 1-15, if the applied potential remains constant, either increasing the charge state of the ion and/or reducing the mass of the propellant will increase the exit velocity of the ionized propellant. Since additional ionization of the propellant represents a power loss and would reduce the overall efficiency of the thruster, as discussed in Section 1.2.2, reducing the propellant mass is the better option for high-specific impulse operation. However, it is not as simple as choosing a light propellant for high-specific impulse, low-thrust operation and a heavier propellant for low-specific impulse, high-thrust operation. Several factors must be considered when choosing a suitable propellant for EP devices; such as ionization potential, mass, storability, and chemical stability in either stored or plasma form. At a given discharge voltage krypton can theoretically produce a 22% increase in specific impulse over xenon. A majority of past research with Hall thrusters operating on krypton has involved lower power thrusters. The performance results of these thrusters suffered up to a 25% in thruster efficiency with krypton propellant relative to xenon. These low efficiency numbers negated the specific impulse advantages of krypton [100, 101]. The efficiency loss with krypton was attributed to a reduced propellant utilization. Kim found it was necessary to increase the krypton propellant mass flow rate to an equivalent xenon mass flow rate to recover the a

efficiency decrease measured when matching the volumetric flow rates<sup>15</sup> [103]. These krypton operating conditions resulted in an increase neutral propellant densities in the discharge channel.

Recent experimental investigation at NASA GRC with the NASA-457M 50 kW-class Hall thruster [32] has achieved efficient operation on krypton without the need to increase the krypton volumetric flow rate above an equivalent xenon volumetric flow rate [31]. A photograph of the NASA-457M is shown in Figure 1-23.



Figure 1-23: A photograph of the NASA-457M 50 kW class Hall thruster.

The NASA-457M was operated on krypton from 7.8 kW to 72 kW with anode efficiencies ranging from 48% to 64%, anode specific impulse ranging from 2000 to 4500

---

<sup>15</sup> Matching the volumetric flow rates of krypton and xenon for a given operating condition results in the same particle density in the discharge channel. Matching the mass flow rates of the krypton and xenon for a given operating condition results in the particle number density of the krypton atoms being greater than the xenon atoms.

seconds, and thrust from 0.39 to 2.5 N. The maximum anode specific impulse of 4500 seconds occurred at a discharge voltage of 1000 V and an anode efficiency of 63%. The anode efficiency as a function of discharge voltage is shown in Figure 1-24.

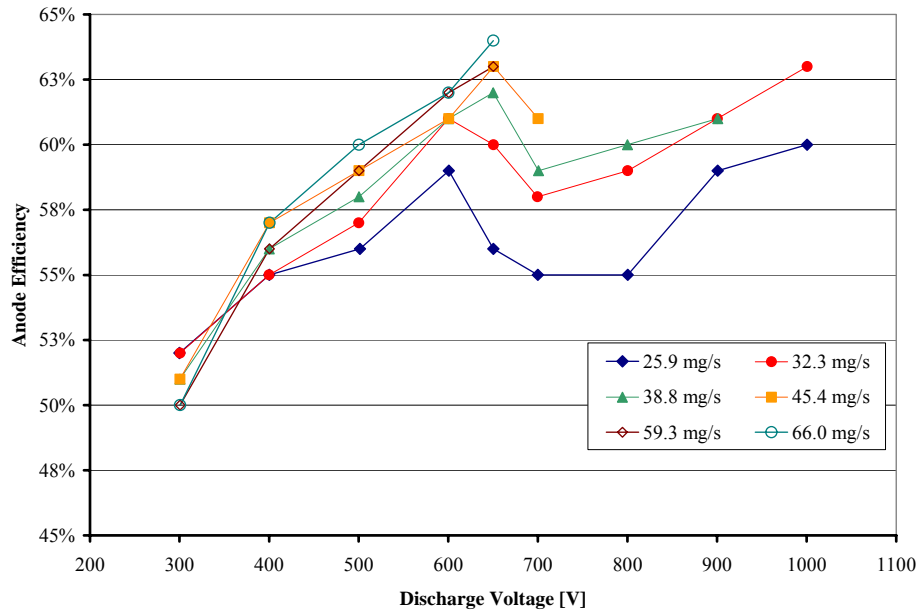


Figure 1-24: The performance results of the NASA-457M Hall thruster operating on krypton [31].

According to Figure 1-24, the NASA-457M began to exhibit an efficiency peak, similar to the lower power high-specific impulse Hall thrusters, but recovers from the efficiency loss as the discharge voltage was increased. Jacobson, in Ref. [31], explains this efficiency depression as a result of maintaining a constant applied magnetic field

topology<sup>16</sup> throughout the performance mapping. Optimizing the magnetic field topology in this region could improve the efficiency.

In conclusion, recent studies of single-stage Hall thrusters have indicated that efficient high-specific impulse operation can be accomplished if the thruster applied magnetic field is tailored properly. The investigation into a novel two-stage Hall thruster design was part of the effort that resulted in the NASA-173M series and NASA-457M Hall thrusters.

### **1.3 Motivation for developing a hybrid Hall/ion thruster**

In an attempt to extend the operational envelope of SOA Hall thrusters, NASA GRC awarded two contracts, an SBIR, and a university grant to develop high-specific impulse Hall thrusters that could match the operational parameters of the SOA ion thruster [23, 29, 64, 71, 73, 94, 98], provided below:

Power = 2.3 kW  
Thrust = 100 mN  
Specific Impulse = 3200 seconds  
Lifetime = 8000 hours

---

<sup>16</sup> The performance characterization of a Hall thruster usually involves the adjustment of the electromagnetic coils at the various operating parameters to minimize the discharge current, thereby optimizing the thruster operation. The minimization of the discharge current by optimizing the electromagnetic coils is thought to reduce the electron leakage current, therefore increasing the thruster efficiency. The NASA GRC high-power series of Hall thrusters seem to require little or no adjustment of the electromagnetic coils to achieve efficient operation.

Three high-specific impulse Hall thrusters were developed through the two contracts and a SBIR. The two contract thrusters were the D-80 and the SPT-1, which were both delivered to NASA GRC and evaluated in NASA facilities. The third Hall thruster was the BHT-HD-1000 developed by and evaluated at Busek Corporation Inc. The results of the D-80, SPT-1, and the BHT-HD-1000 are discussed in Sections 1.2.2.1 and 1.2.2.2, respectively. The NASA grant to the University of Michigan resulted in three Hall thruster designs. The first Hall thruster developed was the P5-2, which is discussed in Section 1.2.2.1. The concept of the P5-2 was an attempt to utilize the theorized benefits of a two-stage intermediate electrode Hall thruster [93]. The P5-2 later evolved into the NASA-173 series of single-stage Hall thrusters, which utilized an improved magnetic field topology to achieve efficient high-specific impulse operation [64]. The third thruster concept developed jointly by PEPL and NASA GRC was the hybrid-Hall/ion thruster, which is the subject of this dissertation. The hybrid-Hall/ion thruster was labeled as the NASA-173GT, where the 173 represents the outer diameter in millimeters and the GT acronym stands for “griddless<sup>17</sup> thruster”. The NASA-173 series of Hall thrusters and the NASA-173GT hybrid-Hall/ion thruster were developed concurrently. However, testing of the NASA-173 series occurred before the NASA-173GT. The magnetic field topology improvement that was responsible for the success of the NASA-173 series was also implemented in the NASA-173GT<sup>18</sup>. The focus of this research is to examine several methods of reducing the efficiency-limiting effects that conventional Hall thrusters experience at high discharge voltages (Figure 1-25).

---

<sup>17</sup> The terms “gridded” and “griddless” have been used in the past as a means to identify the difference between ion and Hall electrostatic thrusters. For this dissertation, the acronym GT will stand for an ion thruster with a Hall acceleration mechanism.

<sup>18</sup> The author of this dissertation was a member of the team that designed the magnetic circuit of the University of Michigan’s P5-2, which later evolved into the NASA-173 series of Hall thrusters.

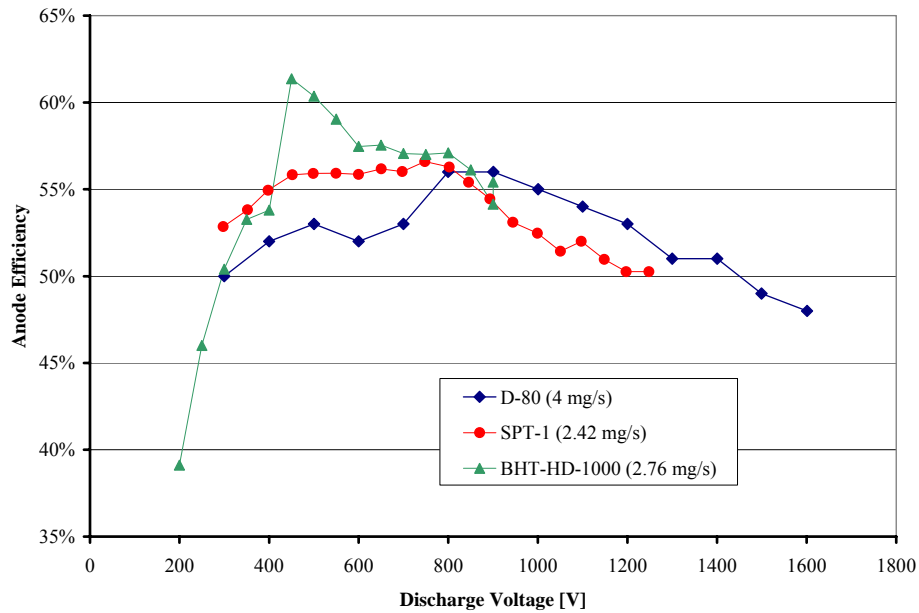


Figure 1-25: Performance data of the phase one high-specific impulse D-80, SPT-1, and the BHT-HD-1000 Hall thrusters [29, 73, 94].

The three primary factors that are believed to be the cause of the Hall thruster efficiency losses above SOA include: electron leakage across the applied magnetic fields; poor propellant utilization; and poor discharge voltage utilization for ion acceleration. The research presented in this thesis focuses on these three factors.

The idea of the NASA-173GT two-stage thruster is to decouple and/or enhance the ionization and acceleration processes of a single-stage Hall thruster. In single-stage Hall thrusters, as described in Section 1.2.2, the ionization and acceleration are closely coupled mechanisms<sup>19</sup>. The idea of separating the ionization and acceleration processes of the thruster allows for greater flexibility in isolating the utilization efficiencies described earlier. A single-stage Hall thruster design can show performance deficiencies

<sup>19</sup> High-specific impulse Hall thruster studies have shown that as the discharge voltage is increased the ionization region length increases towards the anode.

at either low or high voltages. At low voltages, the ion production cost becomes too significant of a fraction of the overall applied power for a given beam current. A high voltage multiply-charged ion production reduces efficiency since at fixed beam current fewer propellant molecules contribute to thrust production. The two-stage thruster configuration investigated in this dissertation examines the possibility of augmenting the ionization processes of a Hall thruster by coupling an additional ionization source upstream of the acceleration zone of a single-stage Hall thruster. The addition of an ionization source allows externally generated propellant ions to drift into the acceleration region. These ions are combined with the ions generated in the Hall-stage ionization region and are accelerated out of the thruster. A diagram of the NASA-173GT is shown in Figure 1-26.

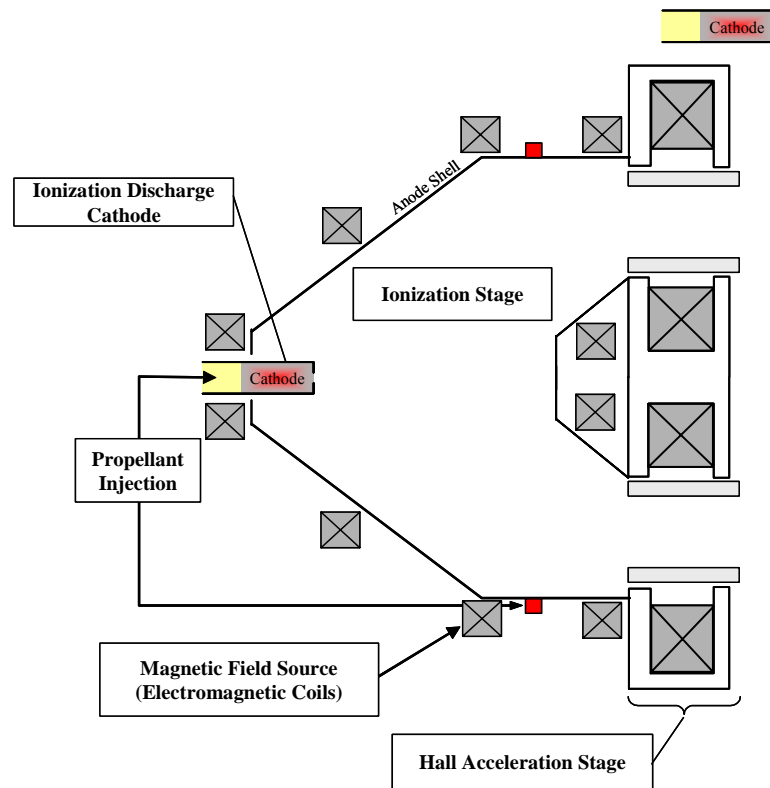
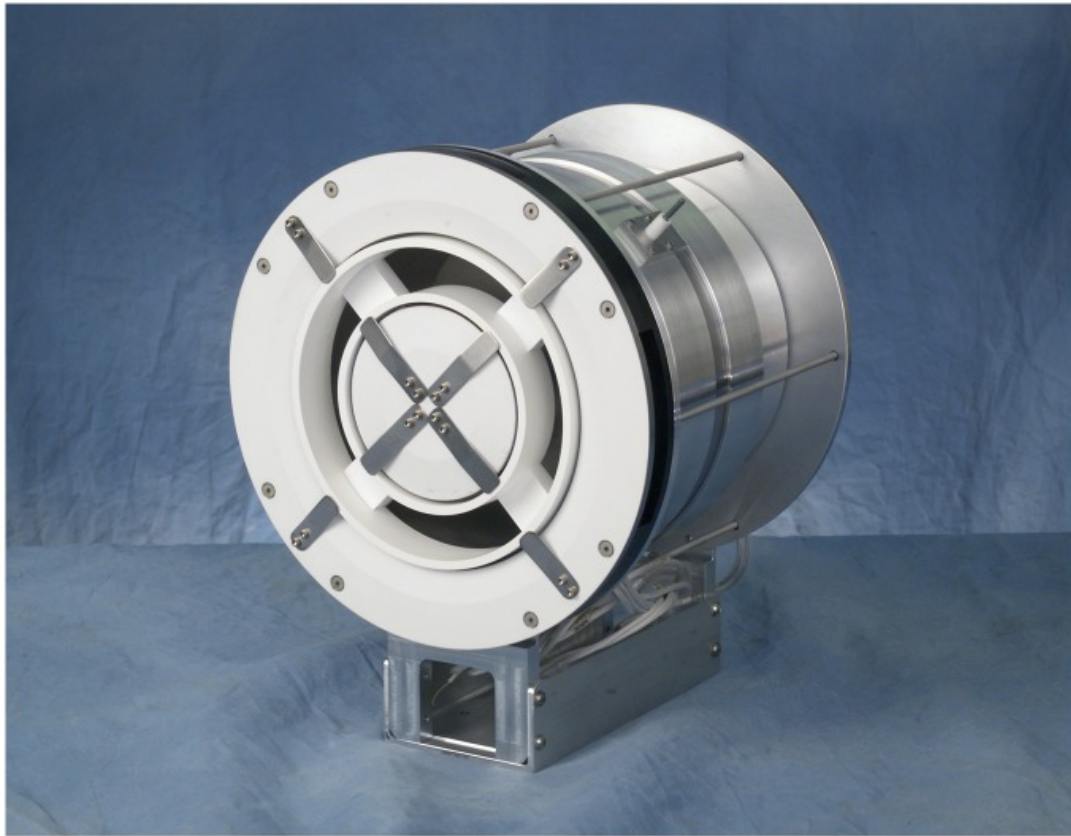


Figure 1-26: Diagram of the NASA-173GT thruster.

The work presented here will discuss scaling of the Hall acceleration and ionization stages of the NASA-173GT, the design of the magnetic circuits for the ionization and acceleration stages, and the material selection for each stage. Issues of coupling the acceleration and ionization mechanisms of a single-stage SPT with the ionization stage of an ion thruster will be discussed. To quantify the operation of the NASA-173GT thruster, several diagnostic systems are utilized. The NASA-173GT performance is determined by measuring the thrust, propellant flow rate, and input power. The plume generated by the thruster is measured with two standard plasma diagnostic techniques. The first is an **ExB** probe for determining the ion species fractions, and the second are two gridded Faraday probes for ion current density measurements. A discussion of the performance and the plume results are presented and future work is suggested.

## **Chapter 2 THRUSTER DEVELOPMENT**

In this chapter, the design and development processes of the University of Michigan's and NASA GRC's NASA-173GT laboratory hybrid Hall/ion thruster is described. The NASA-173GT is comprised of separate ionization and acceleration stages, as shown in Figure 1-26. The scaling of the Hall acceleration stage and the electron-bombardment ionization stage, the design of the magnetic circuits, and the material selections for both stages are discussed in Sections 2.1 and 2.2. Issues and solutions of integrating the two stages will be covered in Section 2.3. Due to possible International Traffic in Arms Regulations (ITAR) restrictions that are placed on EP technologies, a detailed discussion of the magnetic circuit for both stages will be forgone in favor of a generalized description of the NASA-173GT device. A photograph of the NASA-173GT is shown in Figure 2-1.



National Aeronautics and Space Administration  
John H. Glenn Research Center at Lewis Field

Figure 2-1: A photograph of the NASA-173GT without Hall-stage cathode.

## 2.1 Acceleration Hall stage scaling and design

The processes of selecting the primary dimensions for an efficient and stable Hall thruster are accomplished by scaling the new device from SOA Hall thrusters [27, 104]. The two factors that are commonly used for scaling a Hall thruster are the current and power densities<sup>20</sup>. A current density approximately 100 mA/cm<sup>2</sup> has been shown to

---

<sup>20</sup> The current and power densities of a Hall thruster are defined by the desired beam current and power divided by exit area of the discharge channel.

provide a stable and efficient operation. Deviating from this current density can influence the Hall current electron temperature in the discharge channel, thereby increasing the electron mobility towards the anode. Additionally, deviating from this current density can adversely affect the propellant utilization efficiency by reducing the ionization cross-section and the available energy for ionization [105-107]. The power density scaling of a Hall thruster is less constrained than the current density scaling to achieve thermally stable operation. The power density of a Hall thruster determines the maximum operational power level a thruster can handle without suffering from thermal issues, that may include thermal growth of various components and surpassing the Curie temperature of the magnetic circuit [71, 108].

The discharge channel diameter and width of an SPT determine the cross-sectional area of the thruster and are selected in conjunction with the desired thruster parameters to match the current and power density goals. The depth of the channel, from the face of the anode to the exit plane of the discharge channel, is another factor that is normally scaled. The depth of the discharge channel has been shown to depend on the desired operating voltage and even the type of propellant used<sup>21</sup>. The degrees of freedom of the diameter and width are bound by the ability to apply the appropriate magnetic field topology in the discharge channel. The diameter of the thruster is therefore scaled as a function of the propellant mass flow rate. A plot of outer ceramic wall diameter squared versus propellant mass flow rate for SOA thrusters at their nominal operational parameters are illustrated in Figure 2-2.

---

<sup>21</sup> Personal communications with Dave Manzella at NASA GRC.

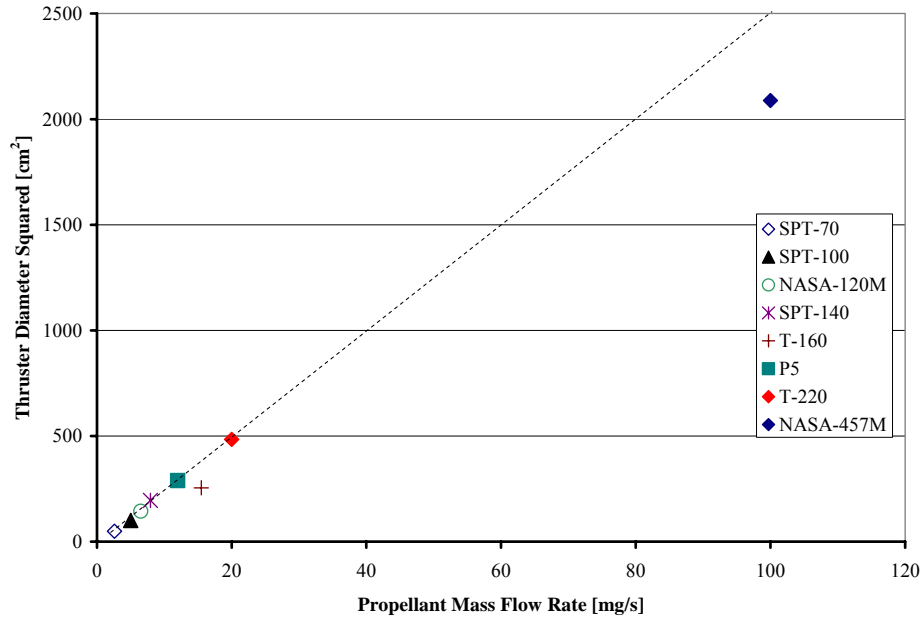


Figure 2-2: SPT Hall thruster outer wall diameters squared as a function of propellant mass flow rate [32, 64, 71, 84, 87, 96, 107, 109].

For the purpose of scaling a Hall thruster, a single ampere of discharge current is assumed to be equivalent to 1 mg/s of propellant. The width of the discharge channel is then determined from the discharge current density goal. It also has been shown that the diameter of a Hall thruster can deviate from the value predicted from Figure 2-2 and still have SOA performance [30-32] if the thruster maintains a proper magnetic field topology. The NASA-457M thruster diameter does not follow the scaling of the other thrusters illustrated in Figure 2-2. During the design phase of the NASA-457M thruster, the designers chose reduce the diameter of the thruster and increase the width to maintain a fixed channel area due to the availability BN material sizes.

### **2.1.1 Acceleration Hall stage parameters**

The physical parameters of the NASA-173GT Hall acceleration stage is derived from the University of Michigan PEPL and the United States Air Force Research Laboratory (AFRL) jointly developed P5 5 kW class laboratory Hall thruster [107, 110]. The P5 is scaled for 5 kW operation based on empirical design equations presented at a design seminar at MIT in 1991 [111]. The decision to retain the diameter and width of the P5 for the acceleration stage of the NASA-173GT is due to the success of various forms of plasma diagnostic techniques employed on the P5 and the performance envelope that the P5 and NASA-173M demonstrated. The depth of the acceleration stage on the NASA-173GT is reduced to limit the loss of the ionized propellant extracted from the ionization stage and created in the acceleration stage to the acceleration channel walls, while still allowing sufficient space for the magnetic circuit. The propellant utilization efficiency, of a Hall thruster, is strongly dependent on the length of the channel [112]. The propellant distribution occurs upstream of the Hall stage, as described in Section 2.2, therefore concerns over uniformity of the propellant flow is addressed in the NASA-173GT design [113]. The acceleration channel length of the NASA-173GT is 30 mm from the interface of the ionization and the acceleration stages to the exit plane of the acceleration stage. The incorporation of four magnetic field shunts across the acceleration channel, to provide the necessary magnetic field profile in the Hall stage, are required due to integration issues of coupling the ionization stage of an ion thruster with the acceleration mechanism of a Hall thruster.

### 2.1.2 Acceleration Hall stage magnetic circuit design

The magnetic circuit of a Hall thruster is composed of a magnetic flux source (electromagnetic solenoid coil or permanent ferromagnetic) coupled with a ferromagnetic material in a configuration that provides the desired magnetic field topology in the discharge channel. A diagram of a typical Hall thruster magnetic circuit is shown in Figure 2-3.

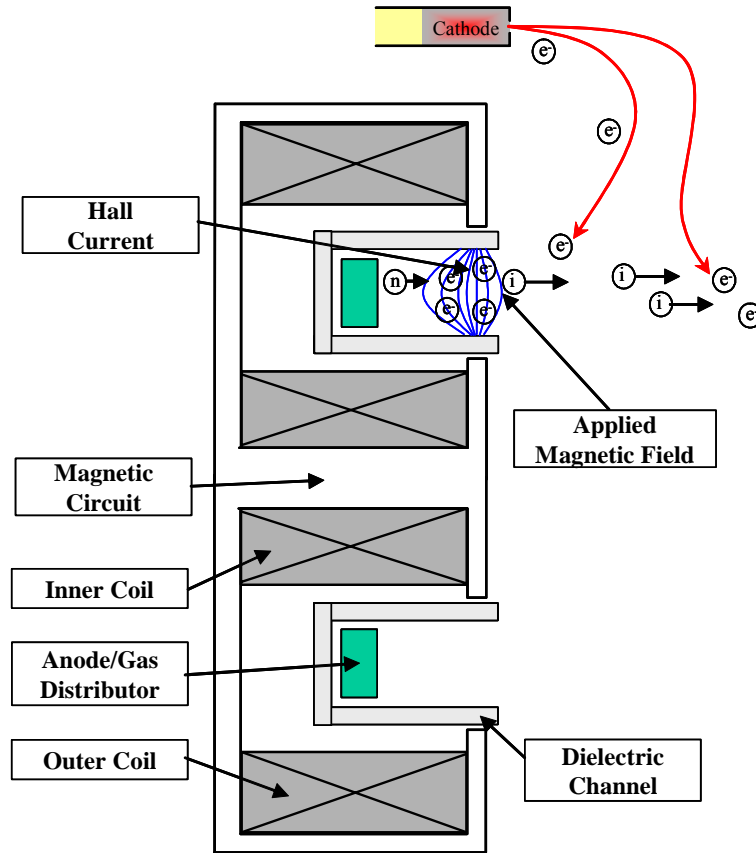


Figure 2-3: Diagram of a Hall thruster magnetic circuit.

The magnetic circuit of a Hall thruster is comprised of four major components. The inner and outer magnetic flux sources, in conjunction with ferromagnetic core material, provide

the magnetic field. A ferromagnetic pole located in the rear of the thruster couples the inner and outer magnetic field sources. The magnetic field is delivered to the discharge channel of the Hall thruster by inner and outer exit plane ferromagnetic pole pieces. The fourth component of the magnetic circuit modifies and shapes the applied magnetic field topology in the discharge channel and are commonly referred to as magnetic screens [28, 60, 71, 87, 89, 99, 108, 111, 114].

A plasma lens magnetic field topology has been shown to provide efficient operation, decreased ion beam divergence, and increase thruster life time [64, 71, 88-90]. A plot of the plasma lens magnetic field topology for the P5-2 is presented in Figure 2-4. The radial and axial magnetic field profiles are shown in Figure 2-5 and Figure 2-6, respectively.

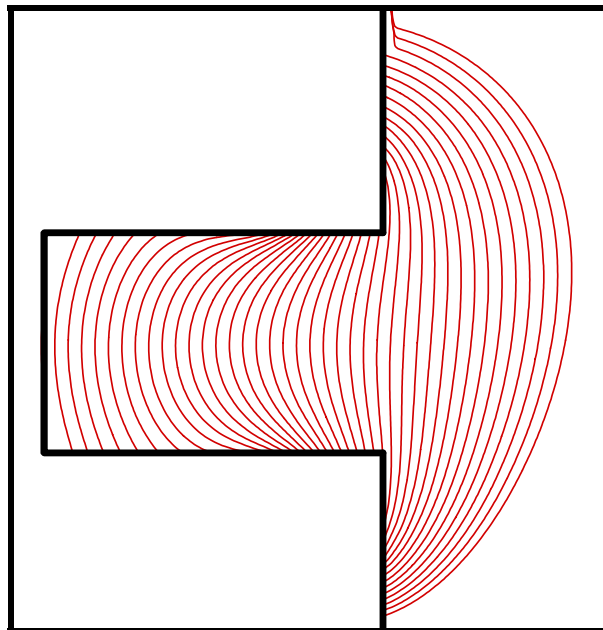


Figure 2-4: Plasma lens topology for the P5-2 [71].

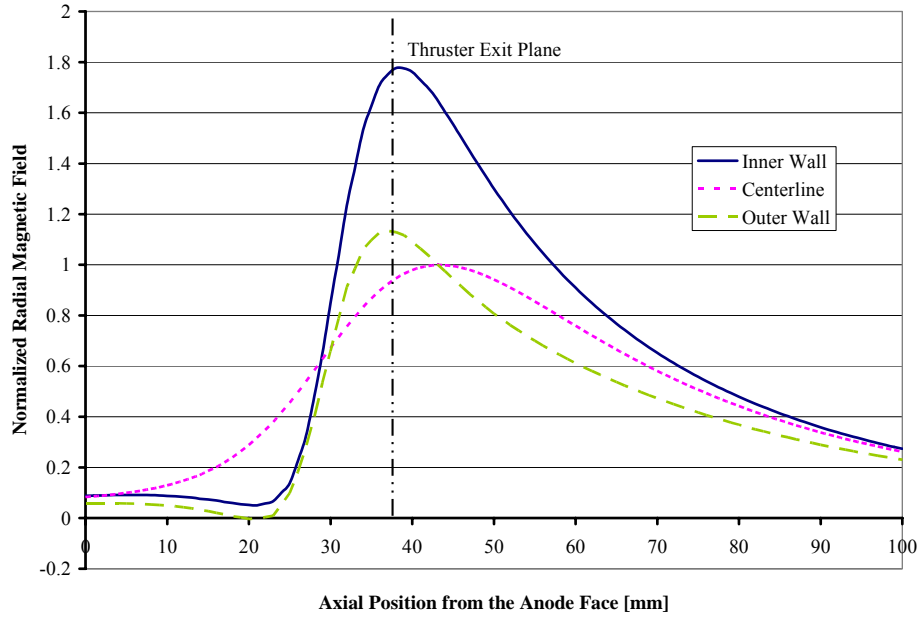


Figure 2-5: The inner wall, outer wall, and centerline normalized radial magnetic field profiles for the P5-2 [71].

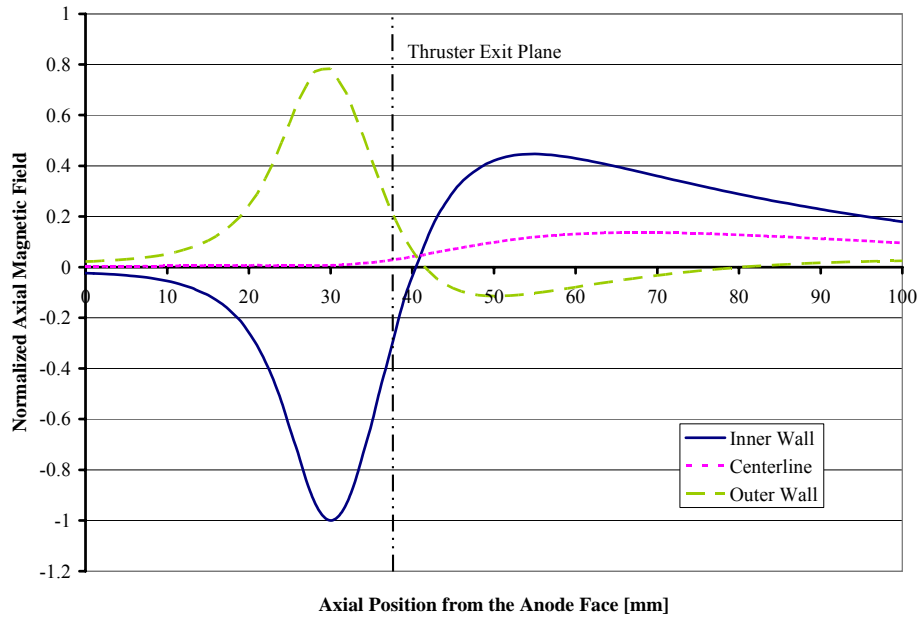


Figure 2-6: The inner wall, outer wall, and centerline normalized axial magnetic field profiles for the P5-2 [71].

A plasma lens improves operation by establishing an effective magnetic insulation along the walls of the discharge channel. This insulation is accomplished by creating curved of the field lines and radial field profiles that form a minimum along the center of the channel, as shown in Figure 2-5. Three factors come into play with the plasma lens topology. The first is the assumption that the equipotentials are approximates of the applied radial magnetic fields and that the established equipotentials direct the ionized propellant towards the centerline of the channel and away from the walls. This preferential acceleration of the ions away from the walls has been shown to increase the performance and lifetime of Hall thruster devices [64, 96]. The second factor is due to the increase in curvature of the radial magnetic field where the electrons that are trapped on a given field line experience a greater path length and thereby increased probability for an ionizing collision. The third factor is the radial magnetic field profiles along the channel walls obtain a greater radial magnetic intensity than the centerline field (Figure 2-5). The plasma in the discharge channel can be described by the radial component of a single-fluid MHD approximation [107] since the propellant is sufficiently ionized in the upstream location near 80% of the centerline radial magnetic field strength (80%  $B_{rmax}$ ) [99, 107] and because the centerline axial field approaches zero near this ionization region:

$$\frac{\partial}{\partial r} \left( P + \frac{B^2}{2\mu_0} \right) = 0 . \quad \text{Eqn. 2-1}$$

As it can be seen in Equation 2-1, the plasma pressure (P) balances the magnetic pressure  $\left( \frac{B^2}{2\mu_0} \right)$ . As a result of this balance, the plasma will tend to reside in the regions of lowest

magnetic field. Placing the plasma, ionization and acceleration regions, near the center of the discharge channel will limit the ionized propellant interactions with the walls.

During the initial design stages of the NASA-173GT acceleration stage, Koo incorporated a version of the plasma lens configuration into his two-dimensional Hall thruster code [115]. The code accounts for the plasma and magnetic pressure terms from the MHD equation. The ion density field in the Hall stage was calculated for 300 V acceleration potential and 5 mg/s propellant flow rate. As shown in Figure 2-7, the plasma of a Hall thruster should be located in the center region of the discharge channel because of the plasma lens magnetic field topology<sup>22</sup>.

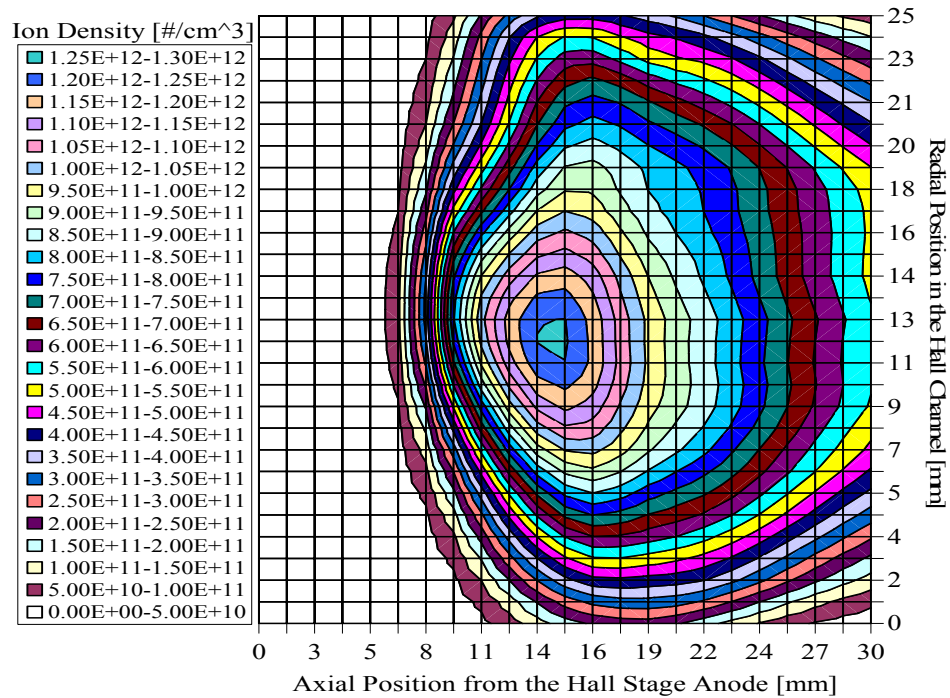


Figure 2-7: Predicted ion density in the Hall stage of the NASA-173GT based off computation model [115].

<sup>22</sup> The results from Koo's model, Figure 2-7, did not take into account the ions that will be produced in the ionization stage.

The design of the NASA-173GT Hall acceleration stage magnetic circuit was accomplished by means of a commercial three-dimensional, magnetostatic, finite-element code called Magnet 6, by Infolytica. The design of the Hall stage for the NASA-173GT had two primary requirements:

- 1) Establish a plasma lens field topology in the acceleration stage; and
- 2) Shorten the axial length of the Hall stage to improve mechanical integration of the two stages while providing sufficient ceramic length for efficient Hall stage operation.

The NASA-173GT magnetic circuit consisted of two coaxial electromagnetic coils in inner and outer magnetic circuits coupled by four flux shunts, and inner and outer exit plane poles. The elimination of the Hall thruster magnetic screens were accomplished through innovative circuit design. The final magnetic field topology for the Hall acceleration stage of the NASA-173GT is illustrated in Figure 2-8. The final radial and axial magnetic field profiles for the NASA-173GT are shown in Figure 2-9 and Figure 2-10, respectively.

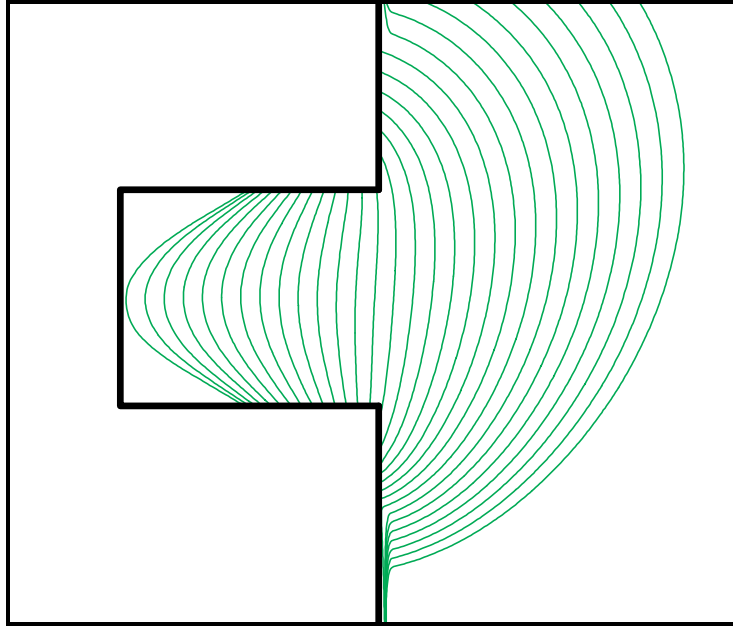


Figure 2-8: The NASA-173GT magnetic field topology.

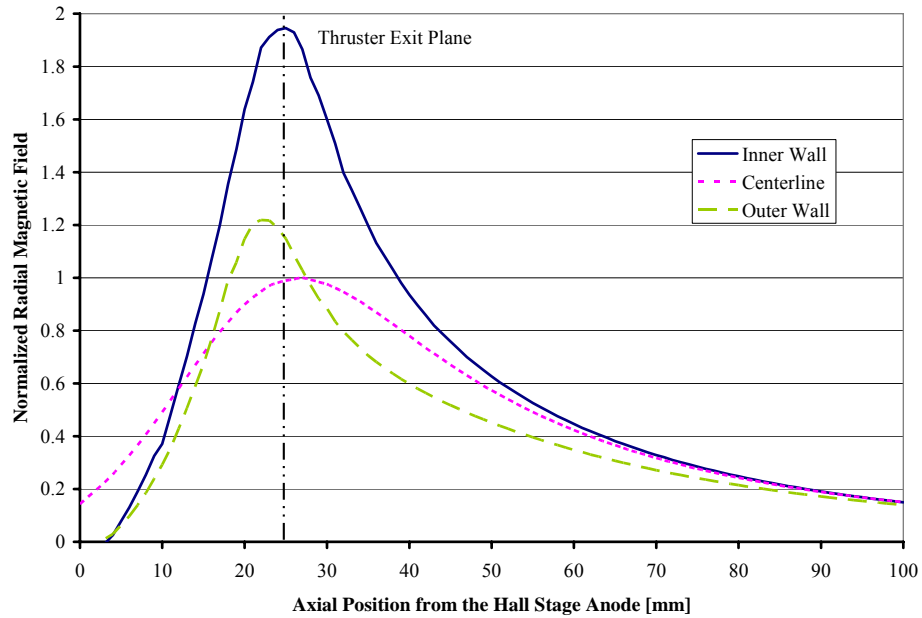


Figure 2-9: The inner wall, outer wall, and centerline normalized radial magnetic field profiles for the NASA-173GT.

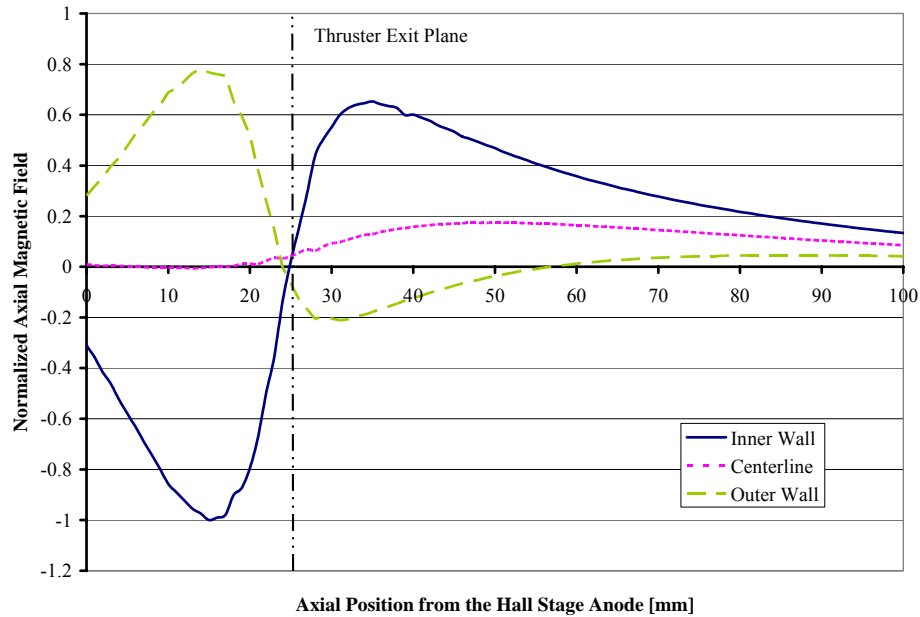


Figure 2-10: The inner wall, outer wall, and centerline normalized axial magnetic field profiles for the NASA-173GT.

The goals set forth for the magnetic circuit of the NASA-173GT acceleration Hall stage were accomplished. The axial length of the Hall stage was decreased to a length such that ions generated in the ionization stage would not experience substantial losses to the acceleration channel walls. The formation of a plasma lens magnetic field topology in the acceleration stage channel enhanced the acceleration and additional ionization processes in the Hall stage. A photograph of the NASA-173GT Hall acceleration stage is shown in Figure 2-11.



Figure 2-11: A photograph of the NASA-173GT Hall acceleration stage magnetic circuit.

### **2.1.3 Acceleration Hall stage materials**

The material selection for the three primary components, ferromagnetic circuit material, the ceramic discharge material, and the electromagnetic coil material of the acceleration stage are described. The P5 and P5-2 Hall thrusters ceramic discharge channels are fabricated from a boron nitride (BN) grade M26 supplied by Saint-Gobain. The use of BN as the primary material for Hall thrusters has been shown to have good

secondary electron emission characteristics [116, 117] and erosion resistance properties [96, 118]. Several other grades of BN have been studied for their erosion resistance and operational characteristics for Hall thruster applications [96]. One grade of BN referred to as HP (High Purity) has shown similar operational characteristics [89] and erosion resistance [96] to M26. The cost of the HP grade BN is less than the M26 grade BN. One unfavorable characteristic of the HP grade BN is that after exposure to the atmosphere, the next operation of the thruster requires a short “conditioning” interval before nominal operation can be achieved. It is thought that under the initial heat load of the discharge plasma, trapped moisture and gasses are released from the BN channel. Once the initial conditioning is completed, the thruster operates nominally during subsequent start-ups until the device is once again exposed to atmosphere.

The magnetic circuit of the Hall stage is comprised of two components, the ferromagnetic material, and the electromagnetic coils. The choice of wire for the electromagnetic coils is motivated by the melting temperature of the conductor material and insulation, the packing ratio of the wire, and the conductivity properties of the conductor. The wire selected for the electromagnetic coils for the NASA-173GT is the same as incorporated into the P5 and P5-2. The wire is composed of a solid copper conductor<sup>23</sup> wrapped with three layers of fiberglass insulation. The ratio of the overall wire diameter to the diameter of the bare conductor is 1.15 for an 18 gauge wire. The complexity of a Hall thruster magnetic circuit requires a material with high, uniform permeability. The selection of a “commercial pure iron”, also referred to as low-carbon

---

<sup>23</sup> Copper conductors, for magnetic wires, are used for electromagnetic coils due to their relatively low resistance and good thermal conductivity.

magnetic iron, is chosen for the NASA-173GT magnetic circuit. To guarantee the improvements sought from the magnetic iron, the material is heat-treated according to the procedure developed at NASA GRC. A plot of the BH characteristics of mild steel, raw magnetic iron, and heat-treated iron is illustrated in Figure 2-12.

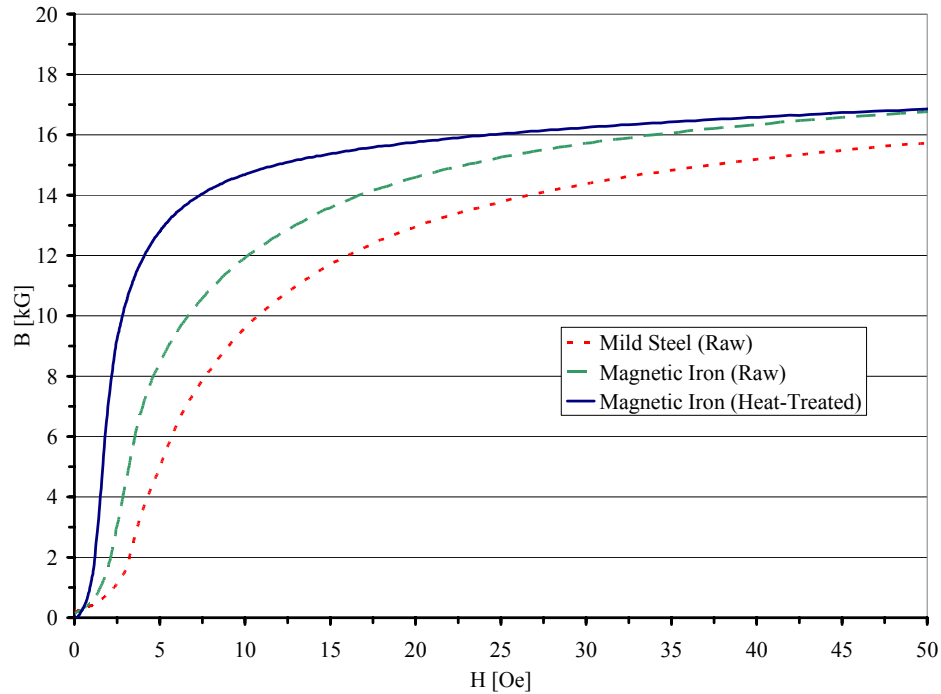


Figure 2-12: BH characteristics of several ferromagnetic materials considered for the NASA-173GT.

The P5-2, as an example, is capable of generating 30% larger radial magnetic fields in the discharge channel compared to the P5, without saturating the magnetic circuit by employing heat-treated iron instead of raw iron [71]. Another argument in favor of heat-treating a material is that the treatment guarantees a uniform permeability throughout the magnetic circuit<sup>24</sup>. Whereas with raw ferromagnetic material, regions of

<sup>24</sup> Based on communication with Jim Rossi of Scientific Alloys.

lower permeability may exist in the magnetic circuit causing localized reduction of the applied radial magnetic field. Abnormal erosion of the D-55 TAL is thought to be the cause of non-uniform applied magnetic fields [97]. Heat-treatment of the magnetic iron to impart a known BH curve allows for an accurate modeling of the magnetic circuit before fabrication. Heat-treating iron improves the magnetic properties of the material; however there is the potential of inducing unfavorable results if the heat-treatment is done incorrectly. This possibility will be discussed further in Section 4.1.

#### **2.1.4 Acceleration Hall stage cathode**

A Hall acceleration stage cathode is required to provide electrons for the Hall stage ionization and acceleration, as well as provide a source of electrons to neutralize the ion beam. A 20 A NASA GRC hollow cathode provides the electrons needed by the Hall stage. A photograph of the 20 A cathode installed on the NASA-173GT is presented in Figure 2-13. The cathode is positioned at a 45° with respect to the exit plane of the thruster. The cathode orifice is axially located one inch downstream of the exit plane and one inch radially from the outer diameter of the thruster body.

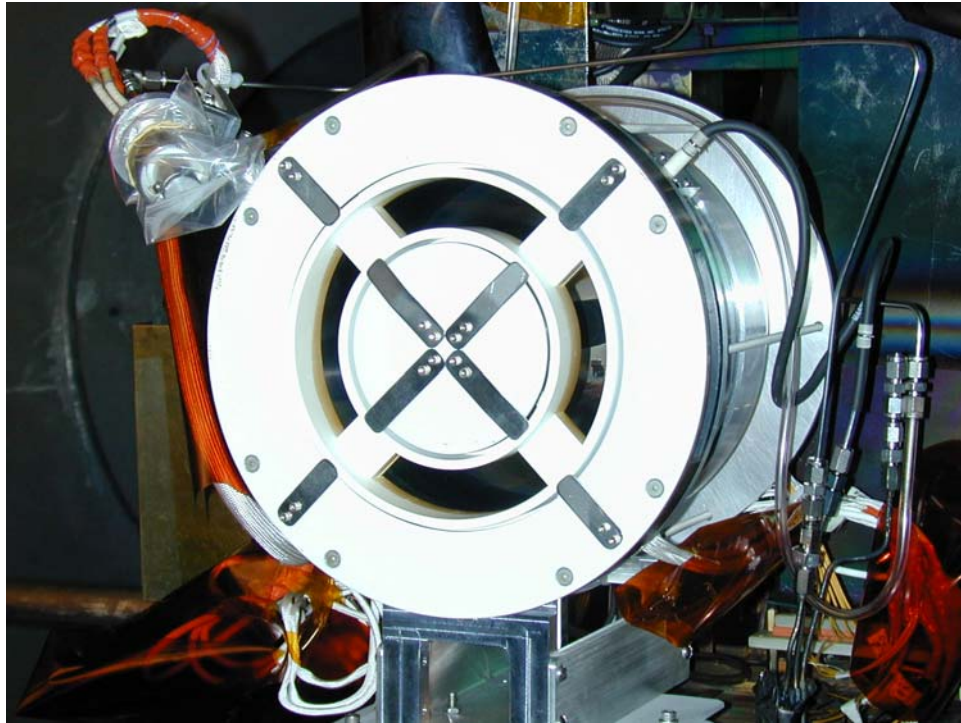


Figure 2-13: A photograph of the Hall stage cathode with respect to the thruster (cathode is covered with a plastic bag with a nitrogen purge to protect it from atmosphere).

## 2.2 Ionization stage scaling and design

There are three different types of ion generation techniques that are currently employed as ionization stages for various ion thrusters, as discussed in Section 1.2.1. Due to the complexity, scalability, and equipment cost of either RF or  $\mu$ W ionization techniques the electron bombardment method was chosen for the NASA-173GT. The electron bombardment ion source is composed of an applied magnetic field that serves as a magnetic insulation layer preventing the primary electrons from flowing directly to the anode. This mirroring effect, described in Section 1.2.1, in turn enhances the residence time that the primary electrons spend in the ionization stage, thereby decreasing the ion

production cost. The applied magnetic field is structured to include a large region in which the applied field is below 50 G, also referred to as the “field-free” region. The large field-free region is desired to allow for uniform distribution of the ionized propellant before the acceleration stage. The electron bombardment ion source has had two different applied magnetic field configurations; divergent and multipole. The multipole ionization stage configuration has been further defined as line-cusp and ring-cusp.

The ring-cusp electron bombardment configuration has been shown to provide the lowest ion-production cost of the different methods, resulting in the most efficient ion thruster [41, 119, 120]. The ring-cusp configuration has been shown to reduce the ion current to the walls over the line-cusp configuration by a factor of two [41]. The influence that the ring-cusp configuration has on the primary and secondary electrons is responsible for the reduced ion losses to the walls. Since the ion gyroradius<sup>25</sup> is greater than the dimensions of the ionization chamber, the ions are not influenced by the applied magnetic field. However, the electrons are influenced and thus the ions are indirectly affected by the magnetic field through ambipolar diffusion. A ring-cusp magnetic field configuration produces a preferential drift on the ions towards the exit of the ionization chamber [33].

The scaling and design of the ionization chamber for the NASA-173GT is similar to the processes employed for Hall thruster scaling. The ionization stage scaling is based

---

<sup>25</sup> The ion gyroradius is a function of the intensity of the magnetic field, the charge state, the mass, and the thermal velocity of the ions.

on previous successful ion thrusters<sup>26</sup>. The critical dimensions of the ionization chamber can be calculated by examining the probabilities of ionization from the residence times of the neutral particles and the mean time of ionization [53]. However, these prediction methods generate ionization chamber volumes that are smaller than what is actually found in SOA thrusters. The primary problem with this general method of scaling is that the majority of the actual electron dynamics are not taken into account. Processes, such as enhanced ionization in the cusp regions as well as electron and ion depletion, are not included in these approximations. The actual physical characteristics used in scaling the NASA-173GT ionization stage are not reported in this dissertation due to ITAR restrictions. However, a list of the design goals and requirements for the ionization stage are as follows:

- 1) Neutral propellant density is sufficiently high to assure an electron mean free path suitable for ionization of the propellant with minimal double-charged ion production [35].
- 2) The ionization chamber should have a small ratio of the wall surface area to volume to reduce ion recombination losses with the walls and the number of primary electrons lost to the walls [119]. Small thrusters have a large wall surface area to volume ratio, which leads to higher recombination losses, thus reducing the number of ions produced in the ionization stage.

---

<sup>26</sup> The scaling of the NASA-173GT ionization stage was based on the NSTAR, NEXT, NEXIS, and NASA GRC's 8 cm laboratory ion thruster.

- 3) The applied magnetic field should be high at the walls to enhance plasma confinement and a relatively “field-free” region of 50 G or less in the center of the ionization stage for efficient plasma distribution. The primary electrons will be reflected by the higher fields in the cusp regions to allow for greater electron residence time.
- 4) A ring-cusp design will be used, which has been shown to provide the lowest ion-production cost for electron bombardment type ionization sources [41, 119, 120].
- 5) The propellant distribution will be a split flow configuration, providing propellant for both the ionization and Hall acceleration stages. A portion of the propellant source will be delivered by the ionization stage cathode<sup>27</sup> and the rest of the propellant through a “reverse-feed” plenum. The reverse-feed plenum is oriented such that the propellant is injected towards the rear of the ionization stage where the discharge cathode is located. The method of propellant distribution has been shown to increase the propellant utilization of a ion thruster by as much as 5% [121-123].

The diameter of the NASA-173GT acceleration stage is established in Section 2.1.1 as 173 mm. Therefore, the diameter of the ionization stage is fixed to the diameter of the acceleration stage. Setting the ionization stage diameter to the acceleration stage

---

<sup>27</sup> The ionization stage cathode for ion thrusters is also referred to as the discharge cathode. For the remainder of this dissertation, “discharge cathode” refers to the ionization stage cathode.

diameter simplifies the mechanical coupling issues of the two stages. The propellant utilization efficiency of the ionization stage is related to the neutral loss rate and the neutral density. The length of the ionization chamber is increased to minimize the neutral loss rate, thereby increasing the ionization stage propellant utilization efficiency [121].

The neutral loss rate ( $n_0$ ) is expressed as:

$$n_0 = I_B \left( \frac{1}{\eta_{ud}} - 1 \right), \quad \text{Eqn. 2-2}$$

where  $I_B$  is the ion beam current and  $\eta_{ud}$  is the ionization stage propellant utilization. As well, increasing the neutral density of the ionization stage, to a certain extent, will increase the propellant utilization. The length of the NASA-173GT ionization stage was determined to be approximately 190 mm by employing the diameter-to-length and the surface area-to-volume ratios of several ion thrusters.

### 2.2.1 Characteristics of the ionization stage

The general shape of the ionization stage for the NASA-173GT is comprised of a cylindrical section upstream of the acceleration stage followed by a conical section tapering down to a discharge stage cathode, as shown in Figure 2-14.

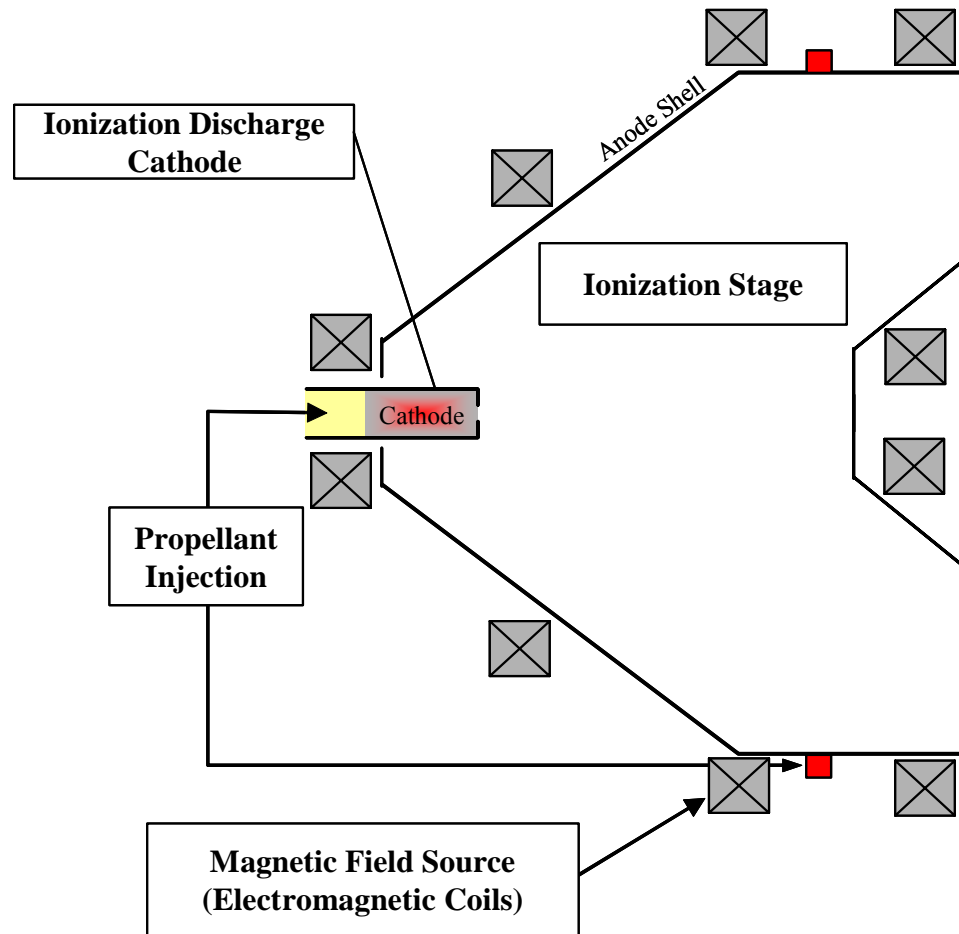


Figure 2-14: A diagram of the ionization stage for the NASA-173GT.

The anode shell of the NASA-173GT ionization stage is fabricated out of non-ferrous stainless steel with a wall thickness of 2.54 mm. The thickness of the anode shell is increased to handle larger ionization stage power levels and current densities. For example, NASA GRC NEXT ion thruster is designed to operate with a beam current of 3.52 A which requires a discharge current up to 40 A [124]. The surface area of the NEXT ionization chamber anode is approximately seven times as large as the NASA-173GT anode. Therefore, to handle the increased heat load and to reduce thermal expansion the anode shell thickness is increased.

The open area fraction for the neutral propellant escaping the interface region between the ionization and acceleration stages of the NASA-173GT is approximately 38%; due to the obstruction of the four flux shunts and the center portion of the acceleration stage. Compared to the SOA NSTAR ion thruster open area fraction for neutrals of 24% [33], the NASA-173GT is approximately 50% larger. This larger open area fraction for the NASA-173GT would normally result in a shorter residence time for the neutral propellant in the ionization stage and increase ion production cost. The concept of the NASA-173GT, hybrid Hall/ion system, allows for escaping neutral propellant to be ionized in the Hall acceleration stage<sup>28</sup> as well as in the ionization stage. Combining the ionization capabilities of the two thrusters, the larger open area fraction of the NASA-173GT is determined to be acceptable.

A split flow system is used on the NASA-173GT to distribute propellant in the ionization and acceleration stages. The propellant is fed through the ionization stage cathode and a reverse-feed plenum. The reverse-feed plenum is designed such that the propellant is directed towards the ionization-stage cathode. A photograph of the reverse-feed plenum of the NASA-173GT is illustrated in Figure 2-15.

---

<sup>28</sup> As discussed in section 1.2.2, a Hall thruster is an efficient ionizer with propellant utilization efficiencies in the 80%-90% range.

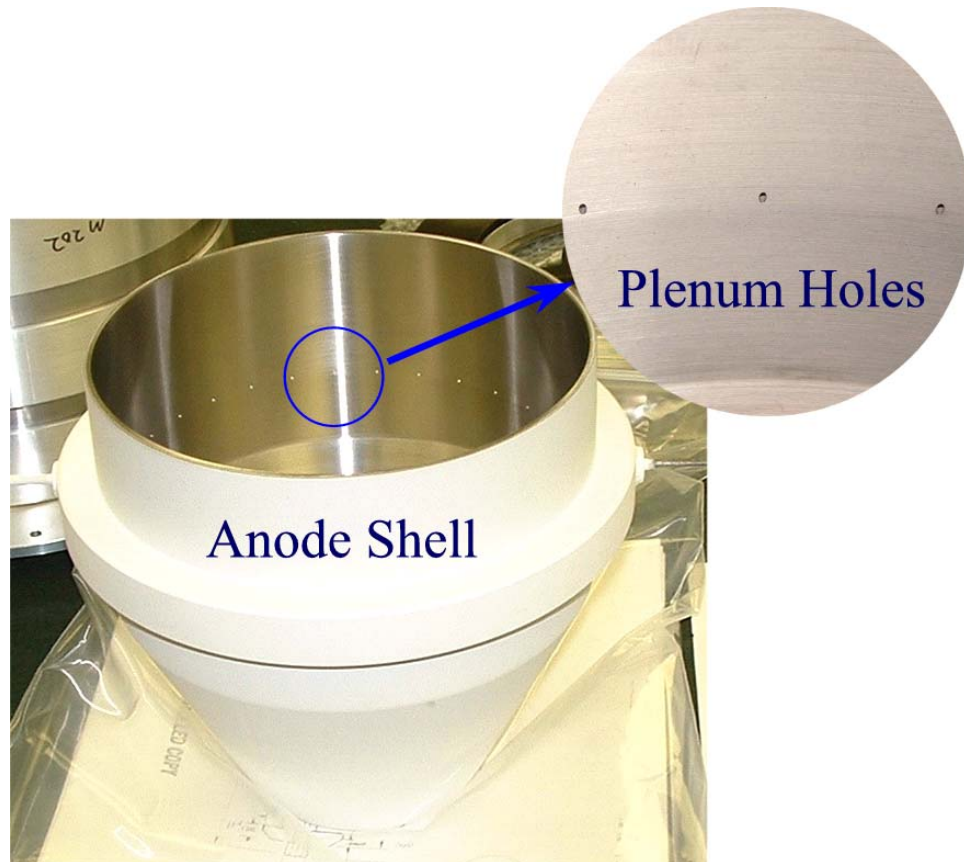


Figure 2-15: A photograph of the NASA-173GT anode shell illustrating the reverse-feed propellant distribution system.

### 2.2.2 Magnetic circuit design for the ionization stage

The design of the magnetic circuit for the ionization stage of the NASA-173GT is accomplished by means of a commercial three-dimensional, magnetostatic, finite-element code called Magnet 6, by Infolytica. The magnetic circuit design goals consisted of selecting the type of magnetic field sources, number of ring-cusps, topology of the field-free and near wall regions, and the profile and intensity of the magnetic field at the cathode location.

Ionization stage designs, for recent ion thrusters, are composed of a number of permanent magnet rings parallel to the exit plane of the ionization stage. The shape, location, and strength of the permanent magnets are usually based on previous SOA ion thrusters that are scaled to the new dimensions of the device being developed. The prototype ion thruster is then run through a series of experiments to evaluate the capabilities of the device so that improvements can be made to the circuit. This methodology has proven successful in the development of ion thrusters. However, due to the scope of the NASA-173GT thruster development, extensive design iterations are not possible. Given the capabilities of the Magnet 6 as a design tool, it is determined that the magnetic circuit of the ionization stage could be accomplished with electromagnetic coils instead of permanent magnets. The incorporation of electromagnetic coils as the magnetic field source of the ionization stage required several new design features that allows the electromagnetic circuit to produce field topologies similar to permanent magnets. The magnetic field of NASA GRC 8-cm ion thruster is illustrated in Figure 2-16.

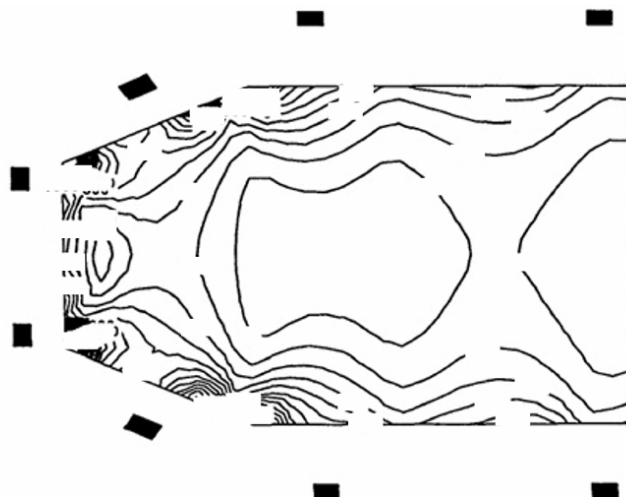


Figure 2-16: Magnetic field density map for the NASA GRC 8-cm ion thruster ionization stage [119].

The number of ring-cusps included in the ionization stage of an ion thruster is reduced to the least number necessary to maintain efficient thruster operation<sup>29</sup>. There are two primary reasons to reduce the number of coils. The first reason is that in the location of the magnetic cusp, the primary electrons have a greater mobility and the cusp areas act as collection regions. The second reason is the added mass of the additional ring-cusps magnets. However, the number of ring-cusps have been shown, experimentally and numerically, to improve the operation of some ion thrusters [119, 120, 123]. Due to the experimental nature of the NASA-173GT, it was determined that the number of ring-cusps would be based solely on the development of the magnetic circuit and the capabilities of providing the desired magnetic field topology. The final number of ring-cusps for the NASA-173GT optimized to five rings. Four of the NASA-173GT ring-cusps are located in similar locations found in ion thruster designs; e.g. Figure 2-16. The additional ring-cusp is located behind the inner portion of the Hall acceleration stage magnetic circuit, as shown in Figure 2-14. The placement of the fifth ring-cusp is chosen to aid in shielding the primary electrons from the closed region behind the Hall acceleration stage, and to influence the drift of the ionized propellant towards the entrance regions of the acceleration stage.

As illustrated in Figure 2-16, and discussed in Section 2.2, the magnetic field topology of the ionization stage required a large field-free region while maintaining sufficient wall fields for enhanced electron confinement and ionization. The selection of the electromagnetic coil (ring-cusp) locations and the magnetic circuit configuration that would direct the field generated by the coils into the ionization chamber involved a

---

<sup>29</sup> The NSTAR ion thruster contains only three ring-cusps for the ionization stage.

number of three-dimensional models. Figure 2-17 shows the ionization stage nominal magnetic field topology, was a result of magnetostatic models that examined the placement which direction of the current through the coils, and the shape of the magnetic circuit.

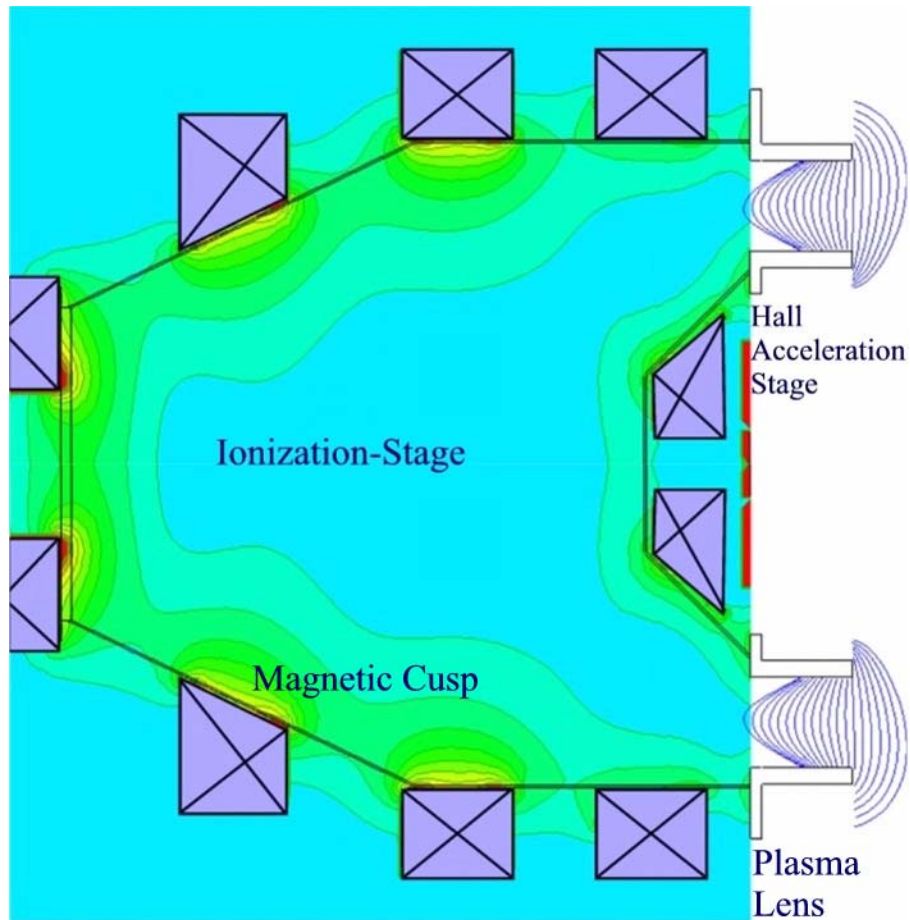


Figure 2-17: A single set-point magnetic field density map for the NASA-173GT ionization stage.

The magnetic field topology in the ionization stage was configured such that in the interface region, between the ionization and acceleration stages, the applied magnetic field was below 50 G. Sovey showed, in Ref. [41], that tailoring the applied magnetic

field in the ionization chamber, especially near the ion extraction region, could improve the discharge propellant utilization efficiency and reduce the ion production cost.

The goals set forth for the magnetic circuit of the NASA-173GT ionization stage were accomplished. An adjustable magnetic circuit design was developed that would allow changes to the field-free region topology and the wall magnetic field intensities, thus establishing efficient ionization and ion extraction from the ionization stage. A photograph of the NASA-173GT ionization stage is illustrated in Figure 2-18.



Figure 2-18: A photograph of the NASA-173GT ionization stage magnetic circuit (includes the ionization stages anode shell).

### 2.2.3 Cathode sizing and positioning

The position of the discharge cathode in the ionization chamber, with respect to the applied magnetic field, has been shown to influence the efficiency of the ionization stage of ion thrusters [119, 125]. The ionization cathode, for SOA ion thrusters, is located in the rear of the ionization stage and directed towards the acceleration stage. The exit orifice of the ionization stage cathode is positioned downstream of the first peak of the applied magnetic field from the upstream anode wall, as illustrated in Figure 2-19.

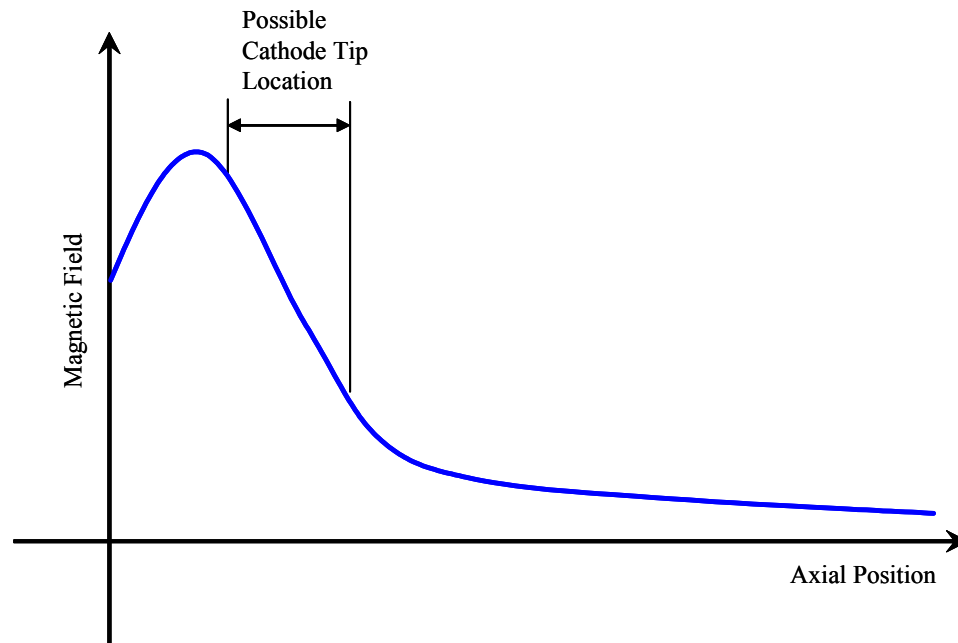


Figure 2-19: A sketch of the centerline magnetic field intensity and the favorable location of the ionization cathode exit.

Positioning the ionization cathode in this region has provided the maximum ion current to the extraction region at a given ionization power level [125]. The NASA-173GT ionization cathode is mounted on an adjustable fixture that could be moved axially into or out of the ionization stage as a means of optimizing the cathode location.

The emission current requirements for the NASA-173GT ionization cathode was estimated from SOA and advanced laboratory ion thruster operating conditions. The relationship between the discharge emission currents and the corresponding beam currents for several ion thrusters is shown in Figure 2-20.

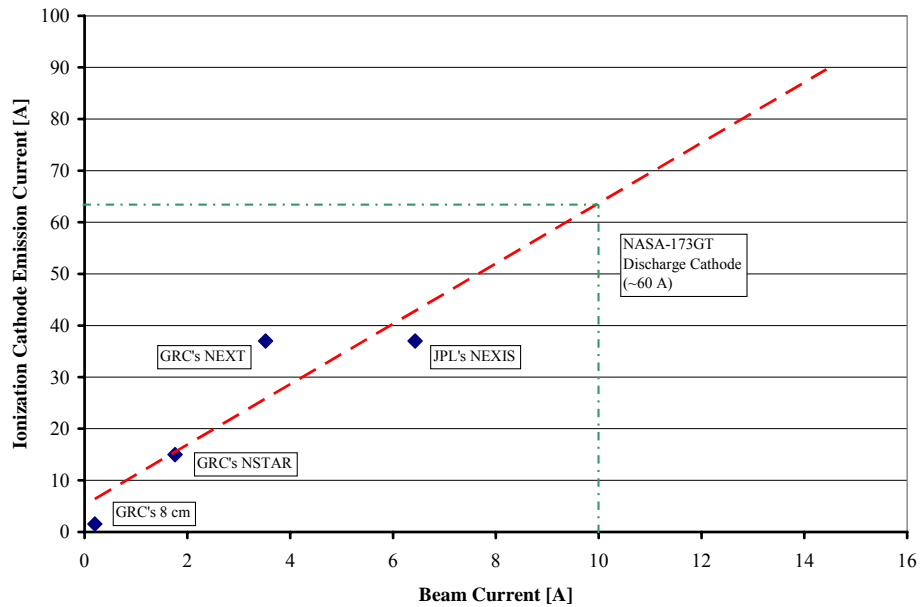


Figure 2-20: The relationship of ionization cathode emission current as a function of the beam current for various ion thrusters.

The NASA-173GT ionization cathode maximum emission current was determined from a linear fit of SOA ion thrusters operating properties. For a nominal beam current of 10 A, for the NASA-173GT, an electron emission current of approximately 60 A was required for the ionization stage cathode. However, one aspect of ionization chamber design that was not taken into account for determining the emission current requirements was the thermal limit of the ionization stage based on the power dissipation in the chamber. The ion thrusters illustrated in Figure 2-20 represented thruster power increases from sub-

kilowatt to tens of kilowatts input power levels. The internal surface areas of the ionization stages listed in Figure 2-20 increased along with the thruster power levels. The power dissipated per unit area of the illustrated ion thrusters remained small. The ionization stage of the NASA-173GT was operated at greater power densities to the anode surface as compared to the ion thrusters listed in Figure 2-20. As discussed in Section 2.2.1, the anode shell wall thickness was increased to handle the increased power densities to the walls. Ionization stages, of SOA ion thrusters, operating at decreased power levels will have lower propellant utilization and thruster efficiencies, as discussed in Section 1.2.1. Operation of the NASA-173GT ionization stage at lower than optimal power densities should not affect the overall operation of the hybrid Hall/ion device due to propellant ionization occurring in both stages.

The selection of a high-emission current cathode involved non-government industrial sources. Several hollow cathode vendors were considered, based on the capabilities, proven design, and the cost of the cathode and replacement parts, Busek Corporation Inc. was chosen to provide a 60 A cathode for this research. A photograph of the 60 A Busek cathode is shown in Figure 2-21.

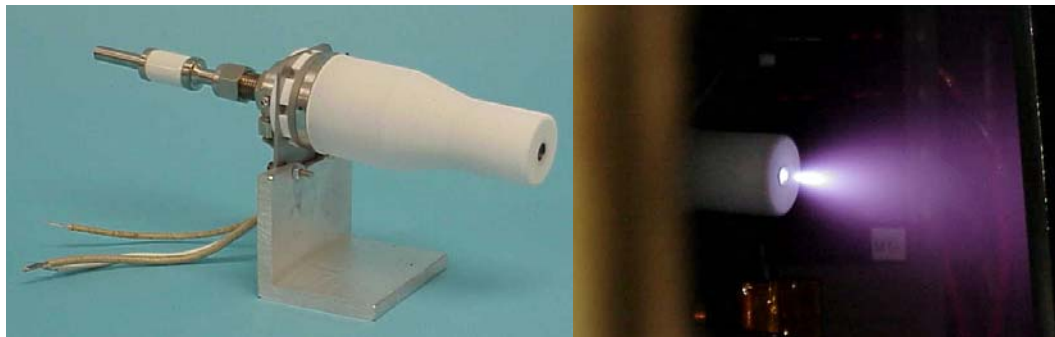


Figure 2-21: The NASA-173GT 60 A ionization stage cathode.

## **2.3 Acceleration and ionization stages coupling issues**

The integration of the ionization and acceleration stages involved developing methods of isolating the magnetic circuits from the anode potential, coupling the inner and outer magnetic circuit components of the acceleration stage, and determining integration issues of coupling the two magnetic circuits.

### **2.3.1 Flux Shunts**

The magnetic circuit of the acceleration stage is comprised of inner and outer circuits connected by four flux shunts, as discussed in Section 2.2.2 and illustrated in Figure 2-11. The shunts are required to provide proper plasma lens field topology in the Hall acceleration stage. Incorporating the four flux shunts was a compromise in the design of the NASA-173GT Hall acceleration stage. Coupling the ionization and acceleration stages required minimal restriction for extracting ionized propellant generated in the ionization stage. Several other configurations were investigated, however the design of the NASA-173GT with the four shunts represented the least complex design and presented the minimal fabrication issues for the thruster. Alternate design approaches for the NASA-173GT are further discussed in Section 6.3.

### 2.3.2 Isolation

The isolation of the ionization and acceleration stage magnetic circuits, which are at ground potential, from anode potential and the ionized propellant is required. The isolation involved the incorporation of plasma sprayed ceramic on the outer surface of the anode shell and BN ceramic shields between the two stages and around the four flux shunts. The choice of electromagnetic coils, to drive the magnetic field in the ionization stage, presented an issue of isolating the coils from the anode potential. As discussed in Section 2.2.2, recent SOA and advanced laboratory ion thruster magnetic circuits are driven by permanent magnets that float to the anode potential. The design of the NASA-173GT required adjustable electromagnetic coils for the ionization stage to insure optimal performance at non-standard operating conditions. To insure that the ionization stage magnetic circuit is isolated from the anode and that the anode is isolated from the structure of the thruster, a layer of plasma sprayed ceramic is applied to the outer surface of the anode and a layer of flexible mica is installed around the anode, as shown in Figure 2-22.

The isolation of the ionization and acceleration stages is accomplished with a BN plate shaped to allow the ionized propellant from the ionization stage to enter the Hall acceleration stage. This BN plate served as part of the isolation scheme for the four flux shunts, the electrical connections of the center portion of the acceleration stage magnetic circuit, and the inner anode component of the ionization stage as discussed in Section 2.2.2. A photograph of the BN isolation plate is shown in Figure 2-23.

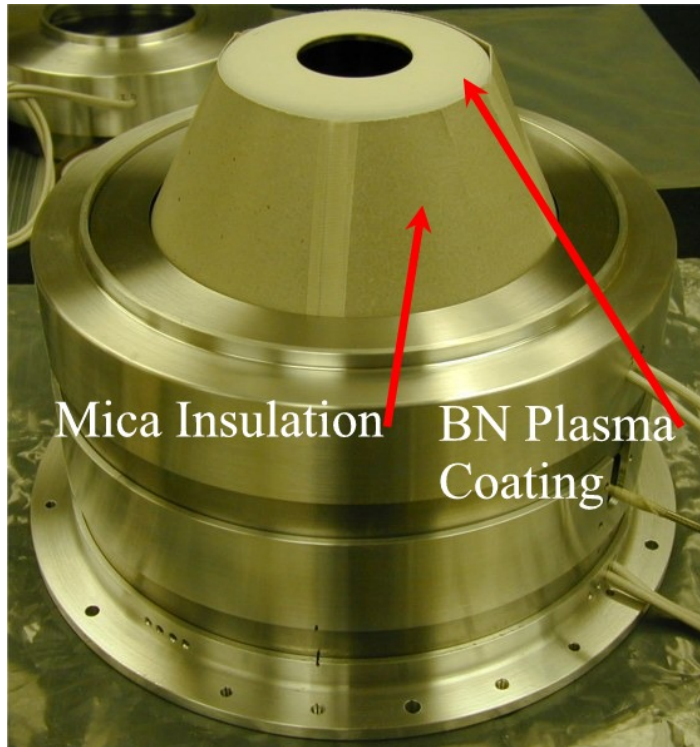


Figure 2-22: A photograph of the NASA-173GT anode shell isolation.

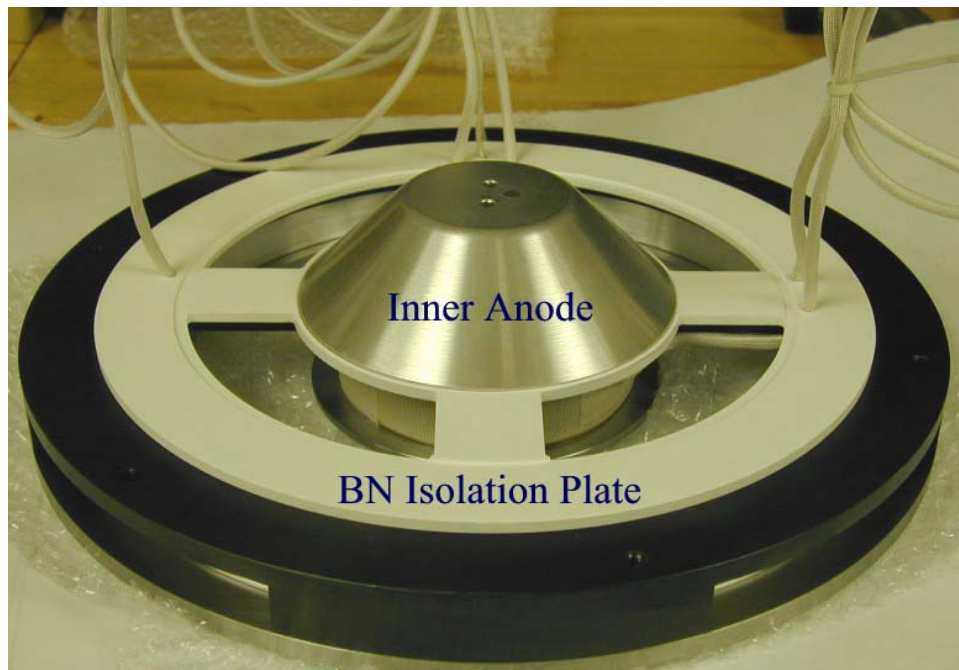


Figure 2-23: A photograph of the NASA-173GT BN isolation plate between the ionization and acceleration stages.

The other part of the isolation scheme involved the reverse side of the BN plate, as shown in Figure 2-23, and four flux shunt covers, as shown in Figure 2-24. These components served to shield the magnetic circuit flux shunts, and the electrical connections of the electromagnetic coils and inner anode from the plasma.

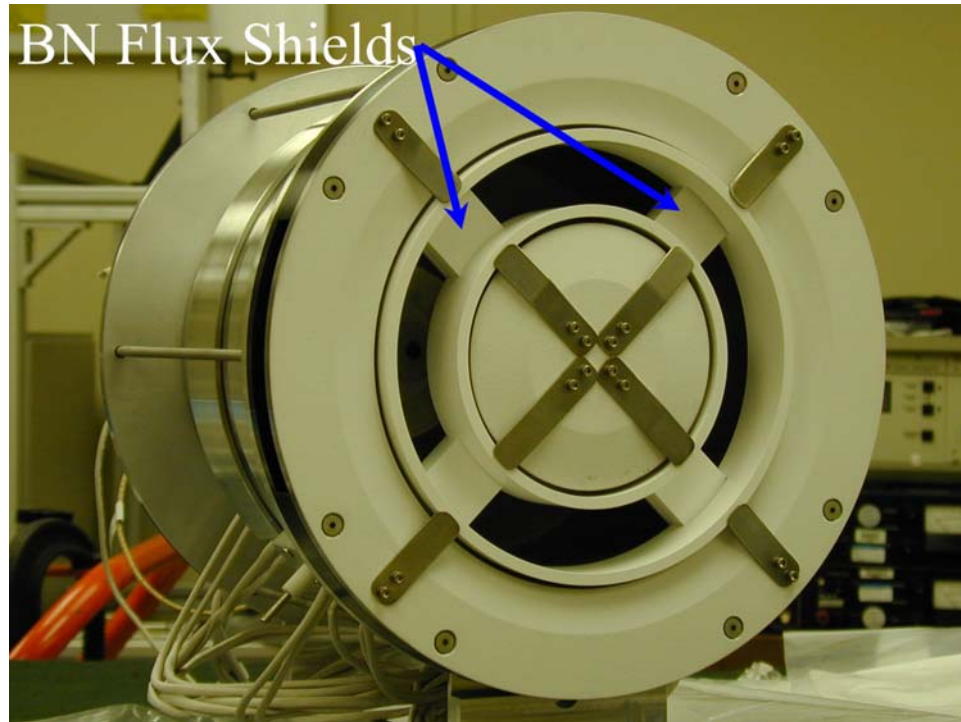


Figure 2-24: A photograph of the NASA-173GT BN flux shields.

### 2.3.3 Magnetic circuit integration

The integration of the ionization and acceleration stage magnetic circuits presented a difficult issue not normally experienced in designing Hall or ion thrusters. An ion thruster magnetic circuit requires a suitable magnetic field profile to enhance ionization and a relatively field-free region at the extraction plane of the acceleration

stage. A Hall thruster magnetic circuit provides a magnetic field, which is zero at the anode and increases towards the exit of the Hall channel while maintaining a plasma lens field topology. Combining the two types of magnetic circuits, and the required magnetic field topologies, was accomplished with several iterations of the magnetic model with Magnet 6. The requirement of a large field-free region at the interface of the two stages was limited due to the actual physical space of the acceleration stage as discussed earlier in Section 2.2.1. A field contour plot of the ionization stage and a streamline plot of the acceleration stage of the NASA-173GT are illustrated in Figure 2-25.

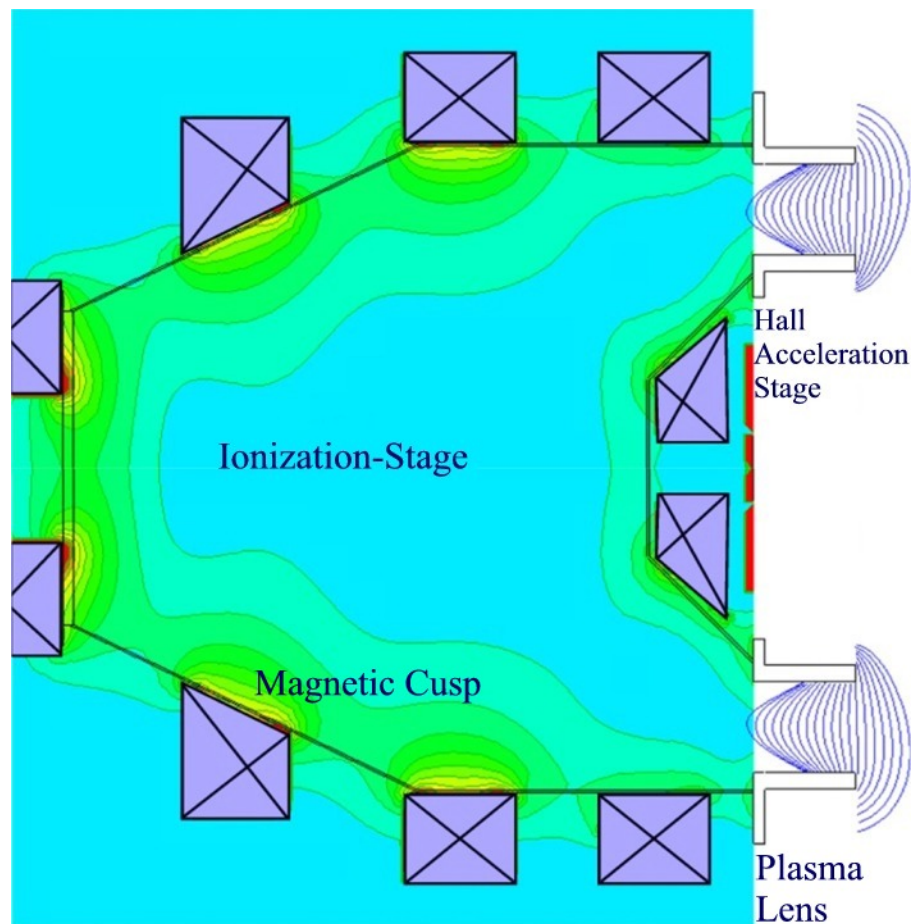


Figure 2-25: The NASA-173GT magnetic field topologies for the ionization and acceleration stages.

In Figure 2-25, the interface region between the two stages corresponds to a minimum of the magnetic field, for the ionization and acceleration stages. The thought was that ions generated in the ionization stage would drift towards the interface region. Once the ions entered the interface region, they would experience the potential drop maintained by the acceleration stage.

## **Chapter 3 FACILITIES AND DIAGNOSTIC EQUIPMENT**

The performance characterization and plasma property measurements of the NASA-173GT were conducted at NASA GRC Electric Propulsion Laboratories vacuum facility number twelve (VF-12). This chapter contains detailed descriptions of the vacuum facility, power console, and the propellant mass flow systems in Section 3.1. The diagnostic equipment employed to characterize the NASA-173GT and evaluate the thruster plasma properties are discussed in Section 3.2.

### **3.1 Electric Propulsion Test Facility**

VF-12 is the NASA GRC premier facility for high-voltage Hall thruster research and long duration wear testing of Hall thruster devices. The facility is equipped and capable of automated data acquisition, autonomous thruster operation, motion control system for plasma diagnostic devices, and integral high-voltage power console for high voltage Hall thruster testing. VF-12 was used in the successful 1000-hour wear investigation of the Pratt & Whitney 10 kW T-220 [109] and the 1200-hour Boeing/TsNIIMASH high voltage D-80 wear investigation [95]. VF-12 is the primary facility in NASA GRC in-house high-voltage Hall thruster (NASA-173M series) development program [64], which has demonstrated increased thruster performance at a discharge voltage up to 1000 V on both xenon and krypton.

### 3.1.1 Vacuum Facility

The vacuum chamber of the VF-12 facility is a 3 m in diameter by 9 m in length tank with a pumping speed in excess of 1,000,000 liters per second (air) provided by liquid helium cryopanel surfaces. The pumping of non-condensable gases is achieved by 1000 liters per second (air) turbo pump. A diagram of VF-12 is shown in Figure 3-1, and a photograph of the facility is illustrated in Figure 3-2.

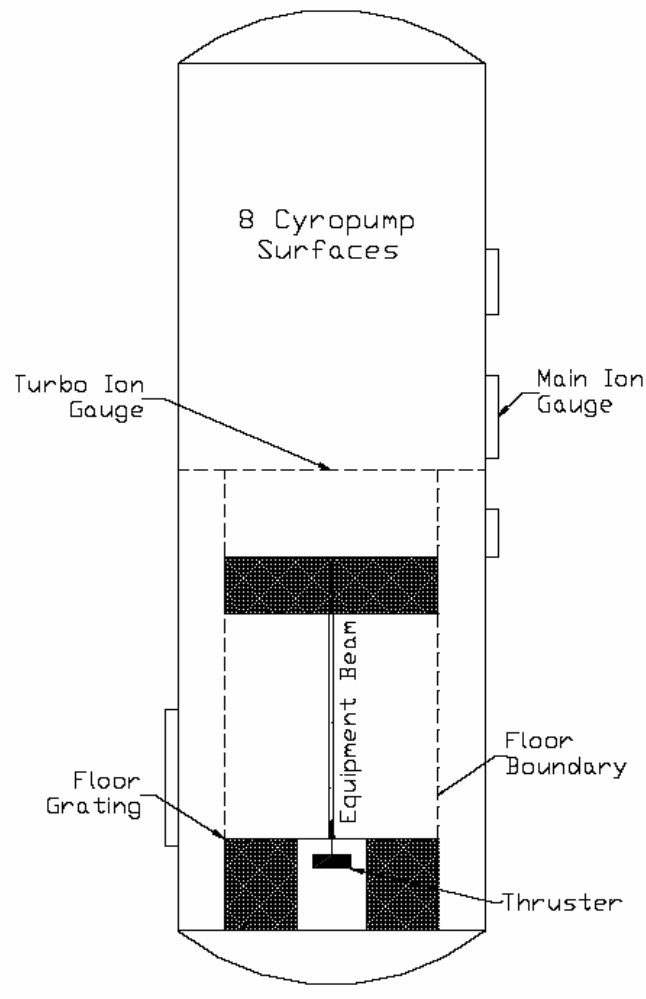


Figure 3-1: A diagram of NASA GRC VF-12.



Figure 3-2: A photograph of NASA GRC VF-12.

The VF-12 pressure, during the NASA-173GT testing, was monitored by two ionization gauges labeled as main chamber pressure and turbo pump pressure, as seen in Figure 3-1. The pressure reading from the main ionization gauge was accepted as the most accurate pressure indication for VF-12<sup>30</sup>. VF-12 was subjected to an internal cold and hot flow pressure mapping with an array of ionization gauges by Walker in Ref. [126] and to a lesser extent Hofer compared the VF-12 operation pressure at two locations in Ref. [64]. The two studies showed that the pressure increased from the locations of the cryopanel surfaces to the position of the thruster test stand. However, at the propellant flow rates investigated in this dissertation, 5-10 mg/s, the pumping speed

---

<sup>30</sup> The main ionization gauge is the most representative pressure indication for VF-12, due to its proximity to the main volume. The turbo pump ionization gauge is located next to the turbo pump behind a gate valve and functions as a facility diagnostic instrument.

of VF-12 under a xenon load has been shown to be sufficient to ensure that background pressure has a negligible influence on the performance measurements [64, 109, 127].

The ionization gauges on VF-12 were calibrated and the gauges indicated pressure measurement based on air. A pressure correction was applied to the readings to obtain an actual xenon pressure. The correction to the pressure readings was based on partial pressures of air and the operating gas [128] as shown in Equation 3-1:

$$P_c = \frac{P_{indicated} - P_{base}}{2.87} + P_{base} \quad \text{Eqn. 3-1}$$

The factor 2.87 is a correction for air to xenon [128],  $p_c$  is the corrected operating pressure,  $p_{base}$  is the base pressure of the facility, and  $p_{indicated}$  is the indicated pressure with propellant flow.

### 3.1.2 Power Consoles

The input power for the two stages of the NASA-173GT was provided by two separate power consoles comprised of commercially available power supplies. The primary power console was composed of two acceleration stage power supplies each capable of producing a constant voltage output ranging from 0-2000 V at current levels of 0-10 A or constant voltage output ranging from 0-1200 V at current levels of 0-16 A. The primary power console also contained supplies for six electromagnetic coils and the operation of the hollow cathode. The primary power console contained circuitry needed

for autonomous operation when coupled with the data acquisition system. The second power console provided power for the ionization stage of the NASA-173GT. Individual power supplies included heater and keeper power supplies for the ionization stage cathode and a separate supply for the ionization stage discharge. The ionization discharge power supply was selected to provide up to 60 A of current and 50 V. The ionization stage power supplies were isolated from ground by three isolation transformers that allowed the power supplies to float to the potential of the acceleration stage.

The electrical schematic for the NASA-173GT is shown in Figure 3-3 and a list of the power supplies incorporated in the power console is illustrated in Table 3-1.

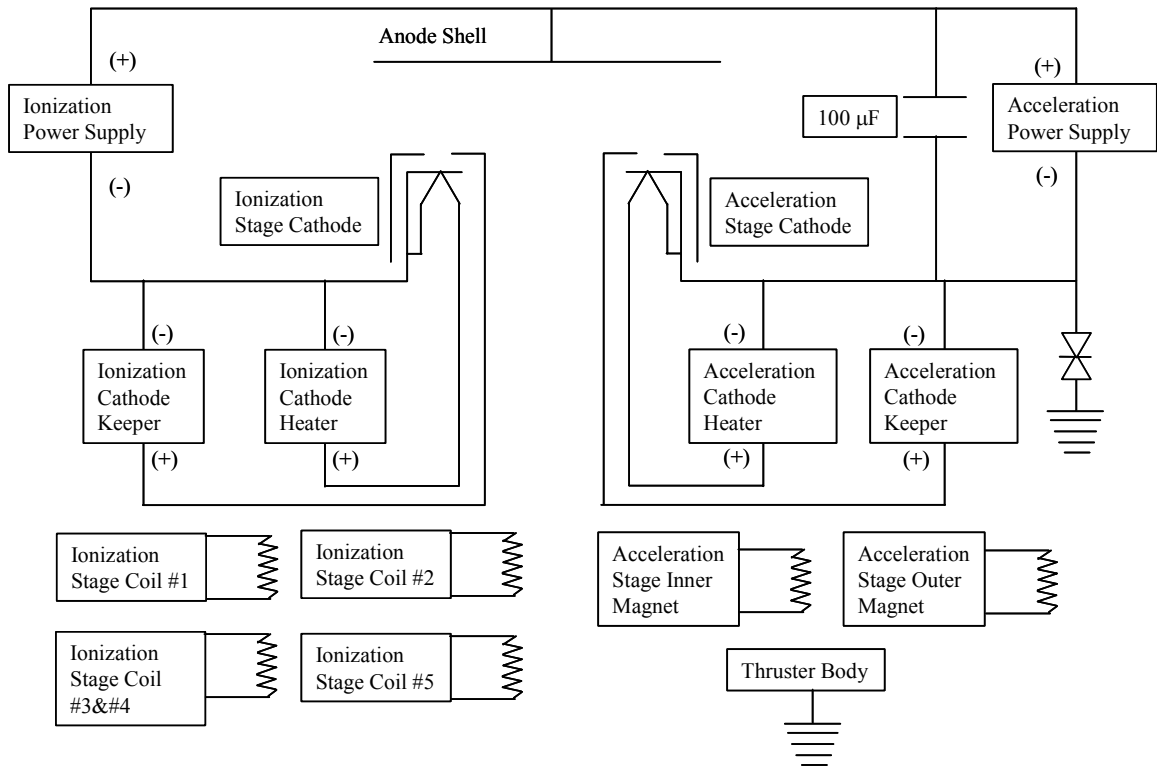


Figure 3-3: The electrical schematic of the NASA-173GT thruster.

Table 3-1: List of the input power supplies employed during the NASA-173GT performance and plume characterization.

<i>Supply</i>	<i>Power</i>	<i>Maximum Voltage</i>	<i>Maximum Current</i>	<i>Comments</i>
Ionization Stage	15 kW	60 V	250 A	Required 60 A for operation
Ionization Stage Cathode Heater	1 kW	60 V	18 A	
Ionization Stage Cathode Keeper	1 kW	150 V	7 A	
Acceleration Stage	19.2 kW	1200 V	16 A	Two 600 V 16 A power supplies in series
Acceleration Stage Cathode Heater	1 kW	60 V	18 A	
Acceleration Stage Cathode Keeper	1 kW	150 V	7 A	
Electromagnetic Coils	1 kW	60 V	18 A	Six independent power supplies for seven coils (Ionization Stage coils #3 and #4 were connected in series)

### 3.1.3 Propellant flow system

The NASA-173GT configuration utilized three independent propellant flow controllers. A combination of the anode plenum and ionization stage cathode flows provided the total propellant flow for the ionization and acceleration stages. A combination of the anode plenum and ionization stage cathode flows provided the total propellant flow for the ionization and acceleration stages. The propellant used for the evaluation of the NASA-173GT was 99.999% pure xenon. The xenon was controlled with a 200 SCCM mass flow controller for the anode in the ionization stage, a 100 SCCM flow controller for the ionization stage cathode, and a 20 SCCM flow controller for the acceleration stage cathode. The flow controllers were calibrated before and after

testing using a constant volume flow technique. The observed error between flow calibrations was no greater than 1% for the anode, 1.2% for the ionization stage cathode, and 1.7% for the acceleration stage cathode.

### **3.1.4 Data Acquisition system**

The data acquisition system used for the NASA-173GT characterization was a 22-bit multiplexer datalogger with computer interface. The datalogger monitored the voltages, currents, temperatures, propellant flow rates, chamber pressure, and thrust every second during testing. The computer interface had an additional benefit of allowing a number of channels to be monitored and alarmed with a five-volt transistor-transistor logic (TTL) output. The TTL output from the datalogger was routed to the power console and was incorporated into the emergency shutdown system. If an alarm condition was encountered, the datalogger drops the TTL output and the power console and propellant flow system shutdown. Another advantage of the computer interface for the datalogger was the ability to compute real time operating power levels, thrust to power levels, efficiency, specific impulse, and calculated coil temperatures.

The uncertainty of the datalogger measurements was limited to the calibration. The calibration uncertainty for the voltage and current was 0.05%. The accuracy of the calibrations was determined by the hand held digital multimeter voltage output readings. The datalogger voltage readings were conducted at the electrical feedthrough on the VF-12 bulkhead interface. The current readings for the acceleration stage and

electromagnetic coil power supplies were obtained by current shunts in the power console. The uncertainty of the current shunts was limited to the accuracy of the high-precision low resistance current shunt and the hand held digital multimeter voltage output readings used for calibration. The ionization stage current readings were obtained by three Hall probes located in the power console. The need to use the less accurate Hall probes over the current shunts was due to floating the ionization stage to the acceleration potential.

### 3.2 Electric Propulsion Diagnostic Equipment

NASA GRC VF-12 is equipped with plasma diagnostic equipment, motion control system for plasma diagnostic devices, *in-situ* laser profilometry system for erosion profile measurements [109], thrust stand for performance characterization [64, 109], and thermocouples for thermal characterization of EP devices. The plasma diagnostic equipment that has been utilized in VF-12 include **ExB** ion velocity probes [129], retarding potential analyzers (RPA) for ion energy measurements [61], electrostatic Langmuir probes for floating and plasma potential measurements [130], and nude and gridded Faraday probes for ion beam current distributions. For the purposes of this dissertation and due to the availability of the plasma diagnostic equipment and VF-12, the NASA-173GT was subjected to thrust stand, **ExB** probe, two gridded Faraday probes, ionization stage characterization, thermal characterization, and table-top magnetic field mapping.

### 3.2.1 Thrust Stand

The inverted pendulum null-type thrust stand, which has become the industry standard for low thrust measurements, was developed at NASA GRC and is currently employed to measure thrust with accuracies down to  $\pm 1\%$  of full scale. The operation and theory of the inverted pendulum null-type thrust stand was described in detail in Refs. [64, 131, 132]. The inverted pendulum null-type thrust stand was based on the null coil technology, which allows the thruster to remain stationary while operating. The inclination of the thrust stand was monitored to gauge the influence of thermal effects from an operating thruster. If the level of the thrust stand changes due to thermal effects, a stepper motor was activated to return the inclination to the position in which the thruster was calibrated. The thrust stand was surrounded by a copper shell that was water cooled by a closed loop chiller, which was maintained at  $20^{\circ}$  C for the performance characterization of the NASA-173GT. The thrust stand was calibrated in-situ during a test with calibrated masses on a pulley system connected to a stepper motor to simulate known thrust levels. The thrust stand was calibrated before and after each performance mapping period and no thermal drift was observed in the zero baseline thrust measurements after thruster operation. An overall uncertainty in the thrust measurement presented was approximately 1.5 % of full scale. A photograph of the VF-12 thrust stand is illustrated in Figure 3-4.

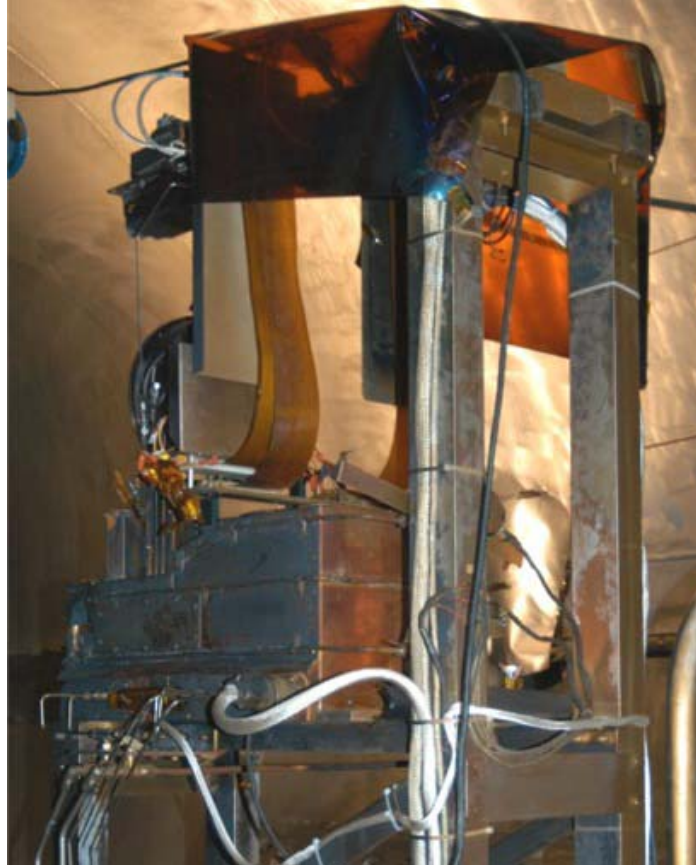


Figure 3-4: A photograph of VF-12 null-type thrust stand (photographed from the rear of the thrust stand)

### 3.2.2 **ExB** probe

An **ExB**<sup>31</sup> probe is an established plasma diagnostic tool that is used in velocity filtering measurements of accelerated plasmas when coupled with an ion collector downstream of the **ExB** region [133-135]. The ability to differentiate between the collected ion velocities, by adjusting either of the applied electric or magnetic fields, allows the **ExB** probe to be employed as a method distinguishing the ion species fractions from uniformly accelerated plasma. The observed velocity peaks, in the measured

---

<sup>31</sup> An **ExB** probe is also known as a Wien filter.

velocity spectrum, for ions that are accelerated in a fixed potential field, are representative by the velocity differences due to the charge states of the ions, as shown in Equation 1-15.

The ionized propellant species fractions of the NASA-173GT were characterized by a NASA Jet Propulsion Laboratory (JPL) **ExB** probe in VF-12. The JPL **ExB** probe was delivered to the ion thruster group at NASA GRC for characterization of the NEXT ion thruster. The JPL **ExB** probe was used for the characterization of the NASA-173GT due to the unavailability of NASA GRC Hall group in-house built **ExB** probe. The GRC and JPL **ExB** probes shared similar design features with slightly different individual improvements. The JPL **ExB** probe utilized an elongated ion collection cup versus a planar disc currently incorporated in NASA GRC **ExB** probe. The ion collection cup was designed to minimize and/or eliminate the influence of secondary electron emission from the collector surface during the collection of accelerated propellant ions. The escape of electrons from the ion collection surface increased the uncertainty in the species fraction measurements, as discussed in Ref. [64].

### 3.2.2.1 **ExB** probe theory

The basic premise of an **ExB** ion velocity filter is governed by the Lorentz force equation, as shown in Equation 3-2:

$$\vec{F} = qZ(\vec{E} + \vec{v} \times \vec{B}), \quad \text{Eqn. 3-2}$$

where  $\mathbf{F}$  is the force acting on the charged particle,  $q$  is the electron charge,  $Z$  is the degree of ionization,  $\mathbf{E}$  is the applied electric field,  $\mathbf{v}$  is the charged particle velocity vector, and  $\mathbf{B}$  is the applied magnetic field. The basic concept of an  $\mathbf{E} \times \mathbf{B}$  probe is to allow a charged particle, traveling at a fixed velocity, to pass through the  $\mathbf{E} \times \mathbf{B}$  drift region with the correct combination of orthogonally applied electric and magnetic fields, and to be collected by a Faraday probe. Charged particles with different velocity vectors will be turned by the interaction of the  $\mathbf{E} \times \mathbf{B}$  applied fields. The basic concept of the  $\mathbf{E} \times \mathbf{B}$  ion velocity filter is shown in Figure 3-5.

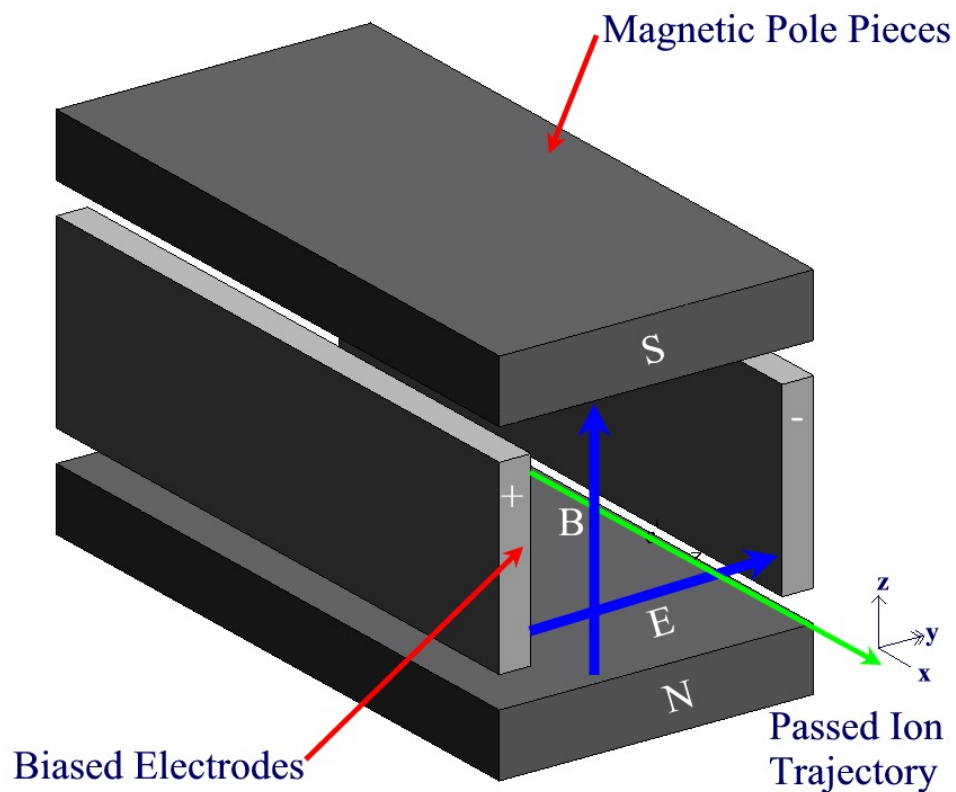


Figure 3-5: A diagram of an  $\mathbf{E} \times \mathbf{B}$  ion velocity filter.

Coupling the physical nature of the **ExB** influence on a moving charged particle with a properly scaled drift tube, orifices, and a charged-particle accounting system results in a plasma diagnostic tool able to accurately distinguish between charge-states of ions accelerated in an fixed potential field.

The **ExB** probes that are incorporated in plume diagnostics of EP devices have a fixed applied magnetic field. The magnetic field is generated by parallel permanent magnets with a set of electrodes, connected to a variable voltage source, perpendicular to the magnetic field. The electrodes are separated at a fixed gap distance. The **ExB** probe is oriented such that the applied fields are orthogonal to the ion beam, thus reducing Equation 3-2, with zero force acting on a charged particle to the following expression:

$$v_{pass} = -\frac{E}{B} = -\frac{\left(-\frac{V_{plates}}{d_{plates}}\right)}{B} = \frac{V_{plates}}{Bd_{plates}} \quad \text{Eqn. 3-3}$$

Equation 3-3 illustrates the velocity of a charged particle that is unaffected as it travels through the **ExB** region for an applied electrode potential  $V_{plates}$  across an electrode gap of  $d_{plates}$  for a fixed magnetic field  $B$ . The ability of adjusting the electrode applied potential leads to a plasma diagnostic tool capable of measuring ion velocities when coupled to an ion accounting system. Combining equations 1-15 and 3-3, and solving for the applied electrode voltages results in the following expression:

$$V_{plates} = Bd_{plates}v_{pass} = Bd_{plates}\sqrt{\frac{2eZ\phi}{M_{propellant}}} \quad \text{Eqn. 3-4}$$

Equation 3-4 indicates at which plate potentials the velocity peaks occur, in a velocity spectrum, given an accelerating voltage, ion mass, and degree of ionization. A sketch of a velocity spectrum of a Hall thruster is illustrated in Figure 3-6. The energy resolution of the ExB probe is defined as width of the ion velocity peak, as illustrated in Figure 3-6.

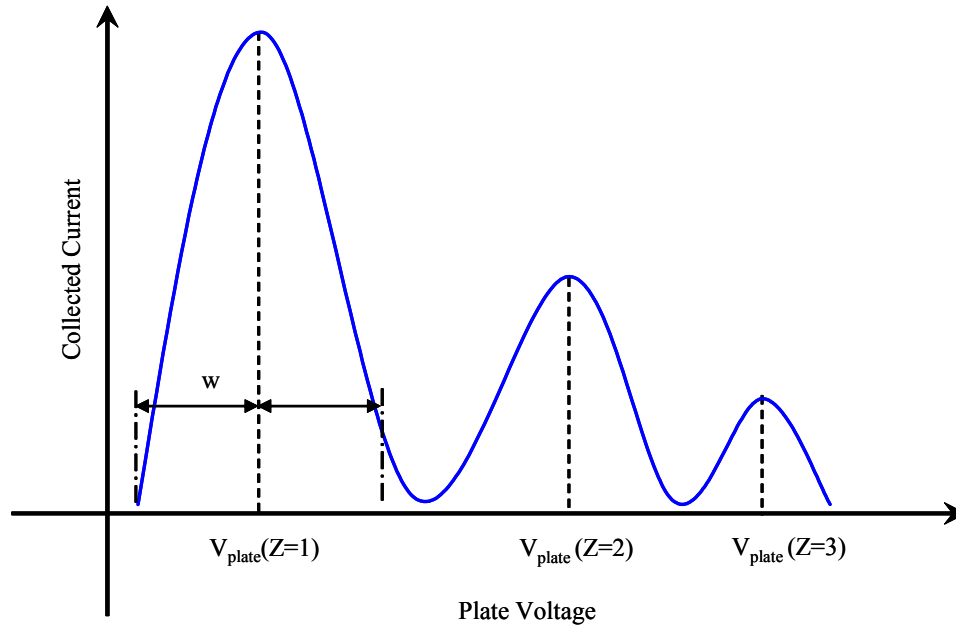


Figure 3-6: A sketch of the **ExB** probe trace for a multiple charged species ion beam at a constant acceleration voltage and ion mass.

### 3.2.2.2 **ExB** probe characteristics and experimental setup

The JPL **ExB** probe employed during the plasma characterization of the NASA-173GT is a similar design of the **ExB** probes used for the SPT-100 [134] and the NASA-173Mv2 [64] Hall thrusters. An **ExB** probe is composed of three main components. The primary components of an **ExB** probe are the collimator, the **ExB** region, and the

drift/collector region. A diagram of an **ExB** probe, illustrating the primary components and notable dimensions, is shown in the Figure 3-7.

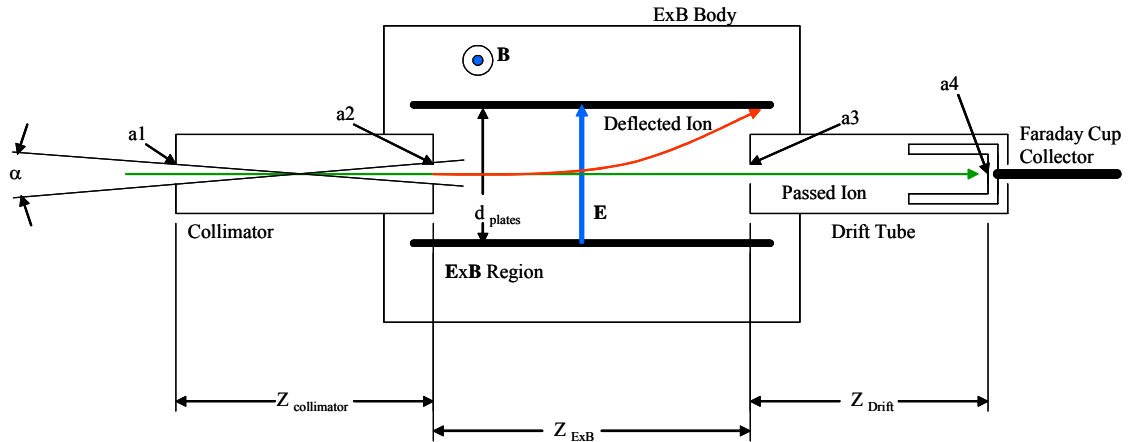


Figure 3-7: Diagram of an **ExB** probe.

The primary dimensions, acceptance angle, and the energy resolution of the **ExB** probe employed in this investigation and the **ExB** probes used in Refs. [64, 134] are listed in Table 3-2. The acceptance angle and the **ExB** probe resolution are determined based on the methodology established by Kim in Ref. [134].

Table 3-2: Basic parameters for the **ExB** probe used in the investigation as compared to the **ExB** probes used in Refs [64, 134].

<b>ExB</b> Probes	$a_1$ [mm]	$a_2$ [mm]	$a_3$ [mm]	$a_4$ [mm]	$Z_{Collimator}$ [mm]	$Z_{ExB}$ [mm]	$Z_{Drift}$ [mm]	$d_{plates}$ [mm]	$\alpha$	Resolution
JPL <sup>32</sup>	0.5	0.5	2	11.1	152.4	127	9.5	27.94	0.38°	30%
GRC [64]	0.5	1	3.2	23	127	127	127	42.5	2.4°	7%
PEPL [134]	1.27	1.27	3.2	8.7	152.4	254	152.4	23.9	0.96°	1%

<sup>32</sup> The JPL **ExB** probe's low resolution was primarily due to the short length of the drift region.

The **ExB** probe was installed in VF-12 on a pedestal located downstream of the NASA-173GT thruster. The height of the **ExB** probe centerline was adjusted to align it with the centerline of the thruster with an uncertainty of  $\pm 0.25$  cm. The entrance orifice of the **ExB** probe was positioned approximately 2.04 m downstream of the thruster exit plane with an axial uncertainty of  $\pm 0.5$  cm. The **ExB** probe was positioned radially such that the interrogation area was aligned along the center line of the acceleration stage channel with an uncertainty of  $\pm 0.25$  cm. The radial position was selected due to the size of the interrogation area of  $1.43 \text{ cm}^2$ , which corresponds to a diameter of 13.5 mm, from the acceptance angle of  $0.38^\circ$  at 2.04 m downstream of the thruster. The **ExB** probe interrogation area diameter was smaller than the width of the acceleration stage channel, hence the decision to align the radial position of the probe along the centerline of the acceleration channel.

The design of the **ExB** probe did not require alignment of the three components of the probe. A laser was used to confirm the initial alignment of the probe with the examination region on the exit plane of the thruster. The Faraday cup collector was removed from the probe and a low-power laser was attached to the end of the drift tube in place of the collector. The laser light then passed through the probe three orifices and the **ExB** region to illuminate the region of interrogation on the thruster face. The use of the laser confirmed the correct alignment of the three components of the **ExB** probe.

An electrical schematic of the **ExB** probe setup used in the characterization of the NASA-173GT thruster is illustrated in Figure 3-8. The **ExB** probe required a voltage source, for the **ExB** plates, that was capable of sweeping through a voltage range at set

voltage increments. The GPIB<sup>33</sup> controlled commercially available power supply used during this investigation had an associated uncertainty of  $\pm 0.1$  V. Two one mega-ohm resistors were attached to the positive and negative outputs of the power supply to ground, thereby allowing the two **ExB** plates to float to equivalent positive and negative potential around the ground potential. The collected ion current from the Faraday cup located inside of the **ExB** probe was attached to a picoammeter through a 50  $\Omega$  BNC shielded cable.

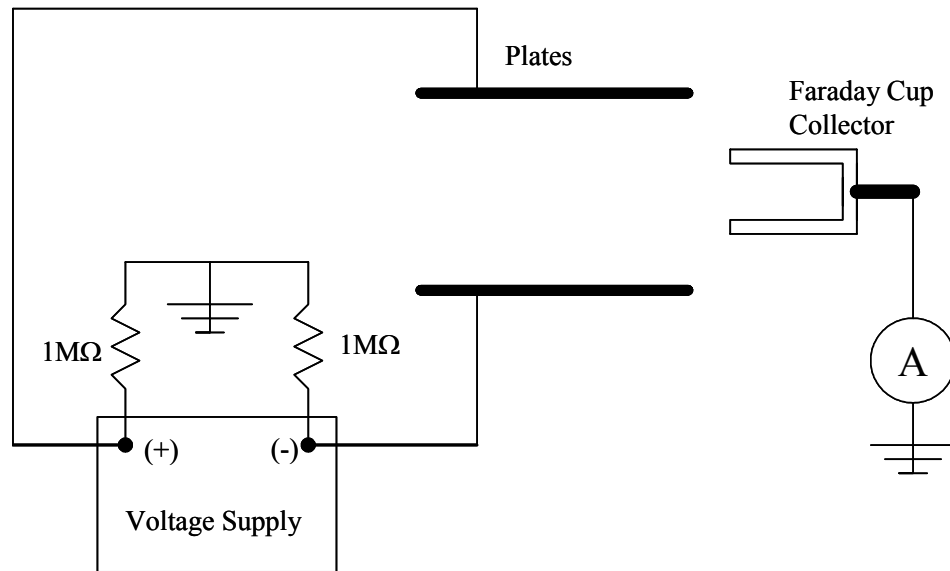


Figure 3-8: Electrical schematic of the **ExB** probe.

### 3.2.2.3 **ExB** probe data analysis and associated uncertainty

An expression for the ion currents for each species fraction is expressed as:

<sup>33</sup> GPIB stands for General Purpose Interface Bus (IEEE standard number IEEE488.1)

$$I_{probe,i} = eZ_i n_i \langle v_i \rangle A_{Collector} , \quad \text{Eqn. 3-5}$$

where  $A_{Collector}$  is the area of the ion collection,  $i$  is for the ion species,  $n_i$  is the number density of each ion species. The ion species current fraction ( $\Omega_i$ ), in terms of the species fractions ( $\zeta_i$ ) for the **ExB** probe from Ref. [64] at a constant acceleration potential, is expressed as:

$$\Omega_i = \frac{I_{probe,i}}{\sum I_{probe,i}} = \frac{Z_i^2 \zeta_i^{\frac{3}{2}}}{\sum Z_i^2 \zeta_i^{\frac{3}{2}}} \text{ for } i = 1, 2, 3, \quad \text{Eqn. 3-6}$$

where

$$\sum \Omega_i = 1. \quad \text{Eqn. 3-7}$$

The ion species fraction from [64] is expressed as:

$$\zeta_i = \frac{n_i}{\sum n_i} \text{ for } i = 1, 2, 3, \quad \text{Eqn. 3-8}$$

where

$$\sum \zeta_i = 1. \quad \text{Eqn. 3-9}$$

Examining equations 3-6 and 3-9, a system of equations is formed in which the ion species fraction can be determined.

The major sources of error for an **ExB** probe were categorized as uncertainty in the applied and measured probe voltages and currents, the resolution of the probe discussed in Section 3.2.2.2, the probability of secondary electron emission from the collector due to ion impacts, and the uncertainty of particle interaction inside of the probe. The uncertainty of particle interaction inside of the **ExB** probe was examined and determined to be insignificant compared to the other uncertainties of the probe and the actual operation of the Hall thruster [134]. The uncertainty of the applied plate biases and the measured ion current from the collector was estimated to be approximately 2%. The uncertainty in the **ExB** measurements, due to the secondary electron emission of the collector surface as experienced in Ref. [64], was addressed by the design of the **ExB** probe ion collector. The JPL **ExB** probe included a different type of collector design than the GRC probe, an elongated Faraday cup design as shown in Figure 3-7. The GRC **ExB** probe attempted to reduce the secondary electron emission by coating the collector with low emission tungsten. The Faraday cup concept incorporated into the JPL **ExB** probe design addressed the influence of secondary electron emission through the physical design of the collector. A properly designed Faraday cup, like the ion collector incorporated in the JPL **ExB** probe, insured that any secondary electrons generated are not allowed to escape and thus influence the measured ion current [136].

The energy resolution of the **ExB** probe was calculated and discussed in Section 3.2.2.2. The energy resolution of the **ExB** probe was determined to be approximately 30%, which was much greater than the 1.5% measured ion energy spread acquired by Manzella near the exit plane of the SPT-100 in Ref. [137]. According to Ref. [64], employing an ion energy distribution model to evaluate the **ExB** results required the **ExB**

probe energy resolution be less than the ion energy spread, otherwise the uncertainty in the ion species fractions would be large. The ion species fractions of the NASA-173GT were determined by identifying the peak location and their corresponding pass voltages.

### **3.2.3 Faraday probe**

The use of Faraday probes as a means of measuring ion current densities in a flowing plasma is a well established plasma diagnostic tool [136, 138]. Faraday probes that have been employed for ion current measurements in the plume of Hall and ion thrusters are composed of similar designs. The general design of a Faraday probe consists of an ion collector plate that is biased to a negative potential sufficient to repel electrons from the discharge and the neutralizer cathode. An equivalent biased guard ring is placed around the collector plate to reduce the edge effects of the sheath that is formed around the probe. As the described Faraday probe, referred to as a nude Faraday probe, is swept along a constant radial path through the plume centered on the exit plane of the thruster, an ion current density profile is obtained. This ion density profile can be used to determine total ion current and the ion beam plume divergence. The total ion current in the plume, calculated from the measured ion current traces, normally over predicts the ion current as compared to the measured discharge current by as much as 200% [107, 139]. This over prediction in the actual ion current has been primarily associated with charge-exchange (CEX) collisions in the discharge channel exit region, where the neutral and singly ionized propellant densities are relatively large, and to a lesser extent in the plume of the thruster. The material selection of the collector also plays a role in the over

prediction of the ion current due to the secondary electron emission coefficient of the collector material. However, the influence of the collector can be minimized by selecting materials with low secondary electron emission coefficients and/or the design of the Faraday probe. Another factor that increases the observed ion current is the CEX collisions of high order charge states of the ions in the beam. It has been shown that in Hall thrusters the population of the  $\text{Xe}^{++}$  and  $\text{Xe}^{+++}$  are sufficient to influence the attenuation of the acceleration ions from the thruster [107]. The addition of multiple ionization states of the propellant, the attenuation of the ion beam by CEX collisions, and secondary electron emissions from the collector surface complicated the analysis of the Faraday probe data. A simplified method of estimating the results is discussed in Section 3.2.3.3.

The Faraday probe employed during the plume characterization of the NASA-173GT contains an additional component to mitigate the effects of the low-energy CEX collisions. This additional component is an electron repelling grid added upstream of the collector's surface. The gridded Faraday probe design allows the negatively biased grid to handle the electron repelling responsibilities, while the collector plate can be biased positively to function as a low ion energy CEX filter. This probe configuration is not a new concept in plasma diagnostics [138] or even in EP plume diagnostics [35]. The goal of the gridded probe is not to develop a plume diagnostic that is facility insensitive [140, 141], but a probe capable of excluding low-energy thermal CEX ions. Excluding the low-energy ions generated in the plume that do not contribute to producing thrust will allow for more accurate calculations of the thruster current and propellant utilization efficiencies based on the observed ion current density traces.

### 3.2.3.1 Faraday probe theory

The basic concept of a gridded Faraday probe employed as a plasma plume diagnostic tool for the NASA-173GT is described below. The grid is biased to a fixed negative potential, less than the cathode to ground floating potential, to insure that the electrons are reflected by the grid. The ion collection plate is then biased to a positive potential to reflect thermal CEX ions, up to several electron volts. The gridded Faraday probe is rotated through the plume at a fixed radial distance and measures an ion current density at every rotation increment throughout the sweep. The total beam current ( $I_B$ ) is calculated from the ion current density traces by the following expression [107, 142, 143]:

$$I_B = 2\pi z^2 \int_0^{\pi/2} j_z(\theta) \sin(\theta) d\theta, \quad \text{Eqn. 3-10}$$

where  $z$  is the probe distance from the thruster and  $j_z(\theta)$  is the ion current density measured by the collector plate at the angular position,  $\theta$ . The total ion beam current calculated from Equation 3-10 is the actual measured ion beam current for ions that make it through the plume without undergoing CEX collisions, pass through the electron repel grid, and are not repelled by the positive biased collector.

The measured radial ion current density profile is used to compute the divergence angle of the plume, which is an indirect method of observing the thruster efficiency. The plume divergence  $\beta$  is defined as the half angle with respect to the thruster centerline in which 95% of the ion current density occurs for a beam profile from  $-90^\circ$  to  $+90^\circ$  [64].

### 3.2.3.2 Faraday probe characteristics and experimental setup

The two gridded Faraday probes used during the ion current density mapping of the NASA-173GT plume consisted of a NASA GRC nude Faraday probe coupled with an electron repelling grid. Photographs of nude and gridded NASA GRC Faraday probes are shown in Figure 3-9.

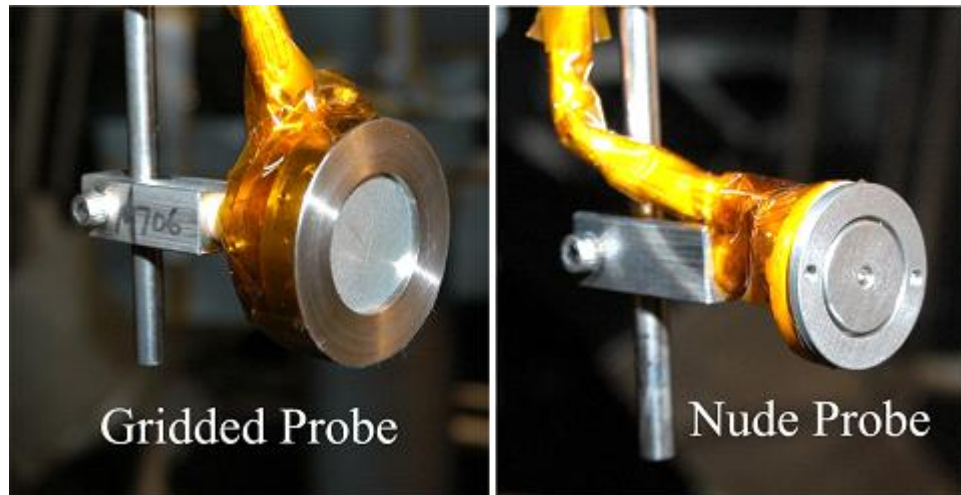


Figure 3-9: Photographs of NASA GRC gridded and nude Faraday probes.

The collector plate and the guard ring are both made from molybdenum mounted on an alumina disk, which was enclosed in quartz tube. The stainless steel electron repelling grid and the aluminum mounting ring were isolated from the collector plate and guard ring by the quartz tube. The quartz tube also served to shield the collector from low-energy CEX ions in the vicinity of the gridded Faraday probe which was described as a major source of the elevated measured ion current density in Ref. [107]. A physical and electrical diagram of the gridded Faraday probe is illustrated in Figure 3-10. A summary of the gridded Faraday probe characteristics is presented in Table 3-3.

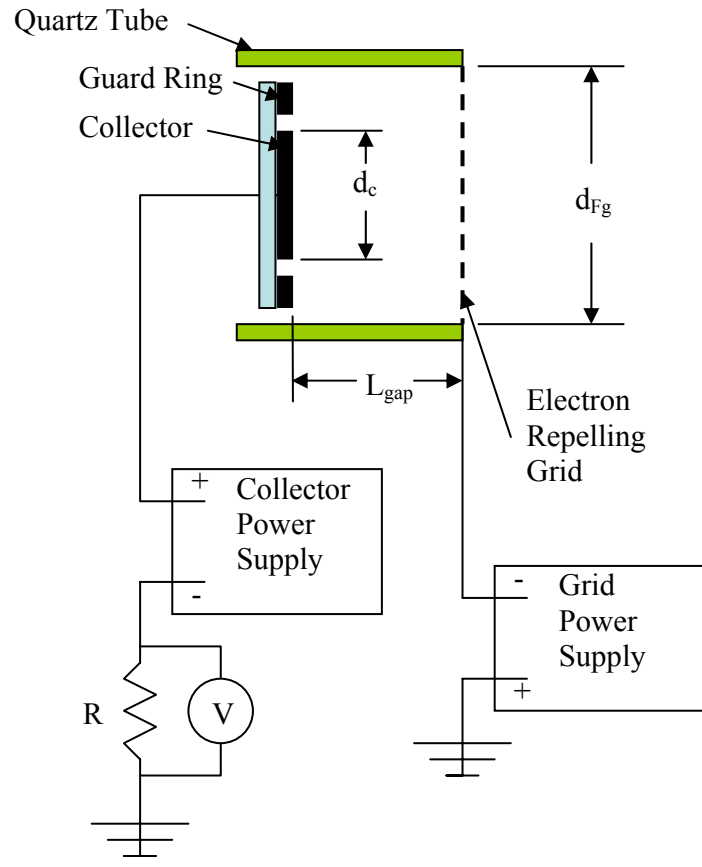


Figure 3-10: A diagram of the NASA GRC gridded Faraday probe physical and electrical characteristics.

Table 3-3: The characteristics of the gridded Faraday probes.

	<i>Gridded Faraday Probe</i>
Collector Diameter ( $d_c$ )	1.74 cm
Guard Ring Inner Diameter	1.85 cm
Guard Ring Outer Diameter	2.84 cm
Alumina Insulator Diameter	2.84 cm
$L_{gap}$	0.51 cm
Grid Diameter ( $d_{Fg}$ )	2.6 cm
Open Area Fraction	17%

The grid diameter ( $d_{Fg}$ ) and the length of the gap between the collector and the grid ( $L_{gap}$ ) was sized such that any attenuation of the ion current density was minimized according to methodology presented in Ref. [141]. The acceptance angles of the gridded Faraday probes were determined to be  $126^\circ$ . The two gridded Faraday probes were located 0.45 m for probe #1 and 0.95 m for probe #2 downstream of the exit plane of the thruster with an uncertainty of  $\pm 0.5$  cm. At the two axial positions of the gridded Faraday probes, an interrogation area of greater than two meters in diameter at the thruster face is observed. The acceptance angle of the probe is large enough to include the whole thruster throughout the radial sweeps. The two probes were radially separated by approximately  $21.5^\circ$  to eliminate ion beam shadowing of the 0.95 m probe from the 0.45 m probe as the probes are swept through the plume.

The open area fraction of the grid was provided by the vendor and was experimentally determined by passing a defuse laser beam through the grid and measuring the transferred intensity with both a light power meter and a laser diode connected to a digital multimeter. The open area fraction was measured several times for both grids and was determined to be 17%.

### **3.2.3.3 Faraday probe data analysis and associated uncertainty**

The raw attenuated ion current density profile of the gridded Faraday probes represents the ions that pass through the plume of the thruster without undergoing a low-energy CEX collision, colliding with the electron repelling grid, and are not repelled by

the positive biased collector. The open area fraction of the electron repelling grids on both gridded Faraday probes, as described in Section 3.2.3.2, is 17%. The open area correction factor for both gridded Faraday probes is expressed as:

$$\frac{j_z(\theta)}{j_{open}(\theta)} = 17\%, \quad \text{Eqn. 3-11}$$

where  $j_{open}(\theta)$  is the ion current density at the face of the gridded probe at the radial position  $\theta$ .

As the accelerated ions from the thruster travel axially in the plume, to the gridded Faraday probes, a percentage of the fast ions will be lost to form slow ions from CEX collisions. The ion beam attenuation, due to CEX collisions, can be obtained by considering the ion continuity equation in one dimension, a neutral propellant temperature, a singly charged ion ( $Xe^+$ ), and the CEX cross-section [144]. The ion beam attenuation can be expressed as the ratio of the ion current density, at the surface of the gridded Faraday probe, to the ion current density leaving the thruster by the following expression [145]:

$$\frac{j_{open}(\theta)}{j(\theta)} = \exp(-n_b \sigma_{ceX} z), \quad \text{Eqn. 3-12}$$

where  $z$  is the axial downstream position of the probe,  $n_b$  is the neutral background number density, and  $\sigma_{ceX}$  is the CEX collision cross-section estimated based on the  $Xe^+$  cross-section at a given ion energy [146]. Table 3-4 summarizes the CEX collision cross-

sections for the primary ion energies investigated in this dissertation. These values will provide an order of magnitude estimation of the beam attenuation.

Table 3-4: The CEX cross-section for singly ionized xenon ( $Xe^+ + Xe \rightarrow Xe + Xe^+$ ) at ion beam energies [146].

Average Ion Energy	100 eV	200 eV	300 eV	400 eV	500 eV	600 eV
CEX Cross Section [ $\text{\AA}^2$ ]	62	57	55	53	51	50

Combining equations 3-11 and 3-12 the total attenuation of the ion current density measurements for the gridded Faraday probes is expressed as follows:

$$\frac{j_z(\theta)}{j(\theta)} = \frac{j_z(\theta)}{j_{open}(\theta)} * \frac{j_{open}(\theta)}{j(\theta)} = (17\%)* \exp(-n_b \sigma_{cex} z). \quad \text{Eqn. 3-13}$$

The primary sources of uncertainty for the gridded Faraday probe study of the NASA-173GT are the axial and radial positioning of the probes, the voltage drop readings across the shunt resistor, the measurement of the open area fraction, the loss of secondary electrons from the collector plate to the guard ring, and CEX collisions between the probe and the thruster exit plane (see Section 5.4.2).

### 3.2.4 Ionization stage ion collection grid probe

The ion production cost of propellant ions in the ionization stage of an ion thruster is normally determined through a detailed characterization [120]. The typical method employed to measure the ion production cost is to replace the acceleration stage grids with a single grid that closely approximates the acceleration stage open area fraction to the neutral propellant particles. The collection grid is biased until the ion saturation of the grid occurs. The grid current is monitored to determine the ion saturation current. The ion current to the grid is then measured as a voltage drop across a calibrated current shunt. The ion production cost for the ionization stage is calculated from the following expression [36]:

$$\varepsilon = \frac{\left( \frac{P_{ion}}{A_{anode}} \right)}{\left( \frac{I_{ion}}{A_{collector}} \right)} + \varepsilon_{ion-cath}, \quad \text{Eqn. 3-14}$$

where  $P_{ion}$  is the ionization stage input power,  $A_{anode}$  is the surface area of the anode,  $I_{ion}$  is the ion current generated in the ionization stage and is available for extraction,  $A_{collector}$  is the ion grid collection area, and  $\varepsilon_{ion-cath}$  is the energy cost of operating the ionization stage cathode. A photograph of the ion collection grid employed on the NASA-173GT is shown in Figure 3-11. The diagram of the electrical circuit for the ionization stage characterization is shown in Figure 3-12.

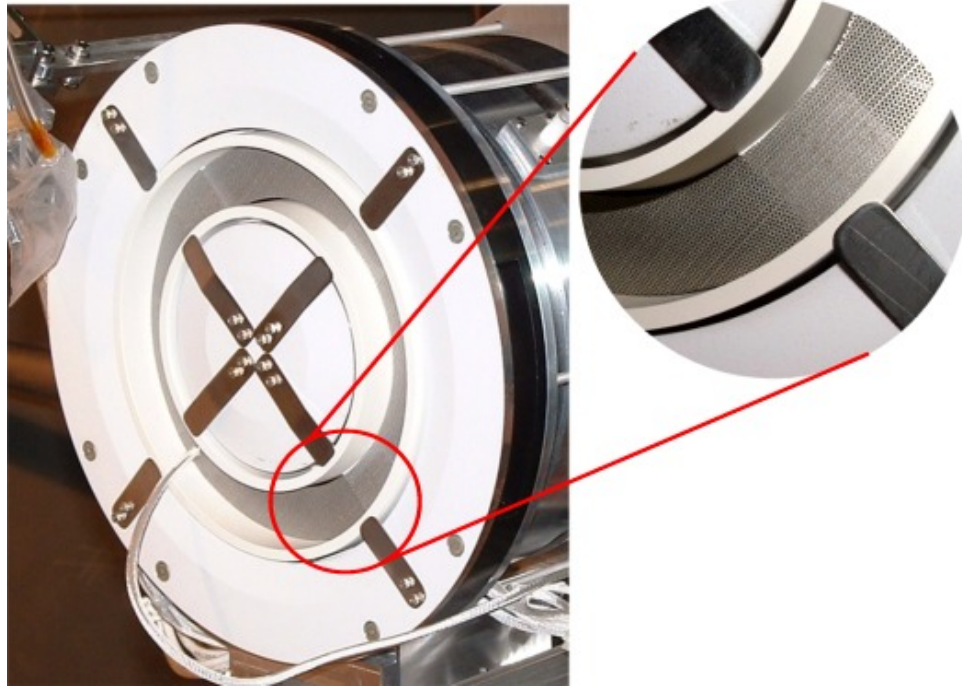


Figure 3-11: A photograph of the NASA-173GT ionization stage characterization with an ion collector grid.

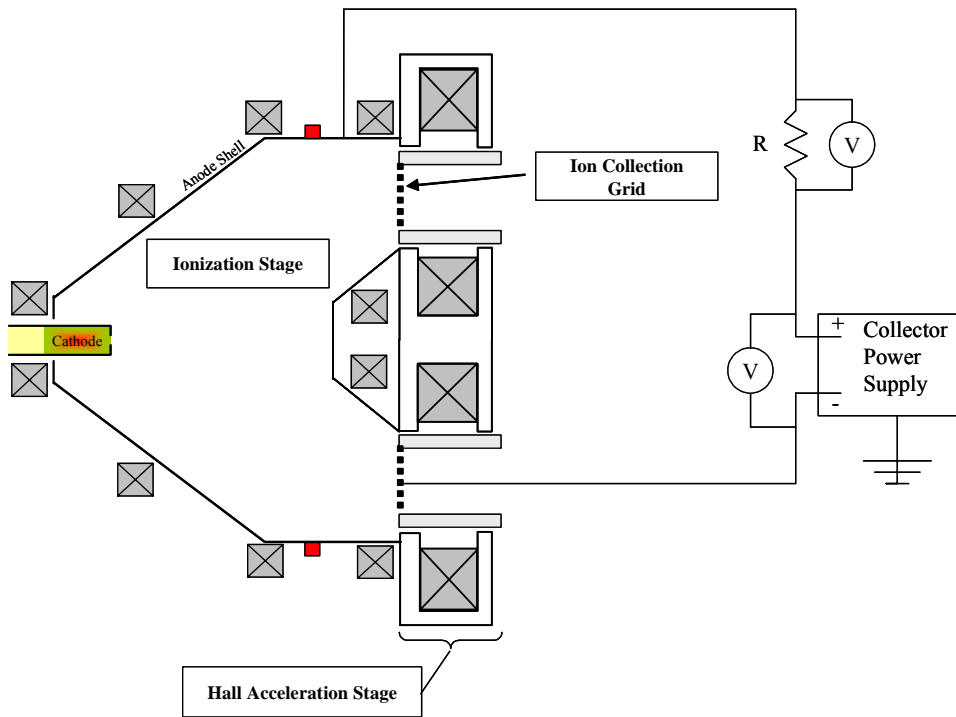


Figure 3-12: The electrical diagram of the ionization stage characterization.

The ion collection grid only collects the ions for the ionization stage that impact the area between the aperture patterns on the grid. A number of ions will make it through the ion collection grid. To compensate for the ions that pass through the grid the measured ion current ( $I_m$ ) is corrected by the grids open area fraction ( $A_{grid}$ ) and the open area fraction of the acceleration channel ( $A_{channel}$ ). The open area fraction of the channel represents a correction factor for the number of ions lost to recombination collisions with the non-anode surfaces. The following equation expresses the ion flux produced in the ionization stage:

$$I_{ion} = \frac{I_m}{(1 - A_{grid})(1 - A_{channel})} \quad \text{Eqn. 3-15}$$

The open area fraction for the collection grid was determined to be approximately 20%, employing the same method used to determine the open area fraction gridded Faraday probe. The open area fraction was calculated to be 38% for the acceleration channel, as discussed in Section 2.3.1.

### 3.2.5 Hall probe

As discussed in Section 1.2.2, the applied magnetic field in the discharge channel of a Hall thruster is a key factor in the successful operation. The magnetic circuit of the NASA-173GT was developed and refined with Magnet 6. To confirm the applied magnetic field of the thruster a three-axis commercially available Hall probe system was used to map the magnetic fields of the acceleration stage. The three-axis Hall probe was

mounted on a vertical arm connected to a scaled optics slide. This configuration has been employed many times to map the magnetic field of several Hall and ion thrusters at NASA GRC and the PEPL. A photograph of the Hall probe magnetic field mapping of the acceleration stage of the NASA-173GT is shown in Figure 3-13.



Figure 3-13: A photograph of mapping the magnetic field of the NASA-173GT acceleration stage.

The electromagnetic coils are energized by a number of commercially available power supplies and the output current is measured by calibrated digital multimeters. The Hall probe alignment is carefully adjusted such that a peak in the radial field and a minimum in the azimuthal field are observed at the exit plane of the thruster. The Hall probe arm is leveled prior to determining the Hall probe alignment. The greatest uncertainty in the magnetic field measurements is the error in the probe radial and axial locations. Due to the radial and axial slopes of the applied field in the channel and the uncertainty in the

position of the Hall probe, the uncertainty in the measured magnetic field is conservatively estimated at 10%.

### 3.2.6 Thermal measurements

The NASA-173GT was instrumented with three k-type thermocouples which were located on the external face of the outer front pole, near the outer electromagnetic coil on the back pole, and the outer surface of the discharge coil number two (DC2). The thermocouple output was logged by the data acquisition system. A photograph of the thermocouple locations on the NASA-173GT is presented in Figure 3-14. The thermocouples served to monitor the temperature of the thruster, to insure the Curie temperature of the magnetic circuit was not surpassed.

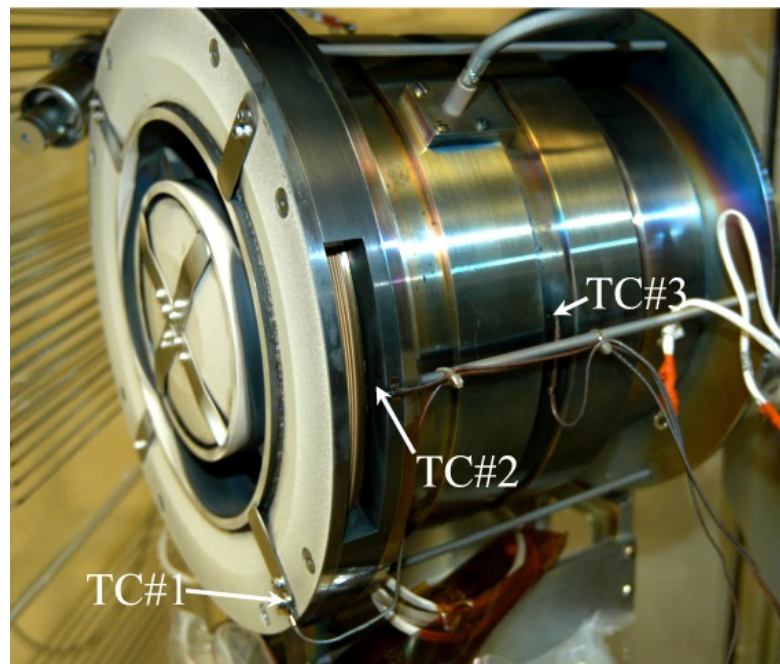


Figure 3-14: A photograph of the thermocouple placement on the NASA-173GT.

The operating temperatures of the seven electromagnetic coils were monitored by estimating each coil temperature from the measured coil voltages and currents. The temperature estimates of the coils were calculated based on the physical properties of the conductors. The resistance of a metallic conductor is dependent upon the material resistivity ( $\rho$ ), cross-sectional area ( $A$ ), conductor length ( $L$ ), and the material temperature ( $T$ ) and is expressed as follows:

$$R = \frac{\rho(T)L}{A}. \quad \text{Eqn. 3-16}$$

The following expression relates the change of a material resistance to a change in temperature:

$$R_f = R_0(1 + \alpha(T_{coil} - T_0)), \quad \text{Eqn. 3-17}$$

where  $R_f$  is the final resistance of the coil under a heat load,  $T_{coil}$  is the operating temperature of the coil,  $T_0$  is room or initial temperature of the coil,  $R_0$  is the resistance of the coil at the initial temperature, and  $\alpha$  is the temperature coefficient of the coil material. Combining Equation 3-17 with the definition of Ohm's law, the following equation relates the average coil temperature to the observed voltage and current characteristics:

$$T_{coil} = \frac{\left( \frac{V_{coil}}{I_{coil}} \right)}{\alpha R_0} - \frac{1}{\alpha} + T_0, \quad \text{Eqn. 3-18}$$

where  $V_{coil}$  and  $I_{coil}$  are the measured operating parameters for each of the coils. The accuracy of Equation 3-18 is primarily limited by the initial estimate of the resistance of each coil and the initial temperature. However, Equation 3-18 provides a relative indication of each coil temperature, either from Joule heating and/or heat conduction from the surrounding thruster components.

## **Chapter 4 RESULTS**

The experimental results of the NASA-173GT characterization are presented in this chapter. The magnetic field mapping results are presented in Section 4.1. The ionization stage characterization results are presented in Section 4.2. The NASA-173GT performances in single- and two-stage operation are presented in Section 4.3. The thermal characterization results of the thruster are presented in Section 4.4. The plasma plume results from the **ExB** and gridded Faraday probes are illustrated in Sections 4.5 and 4.6, respectively.

### **4.1 Magnetic field characterization**

The applied magnetic fields in the acceleration and ionization stages play a dominant role in the successful operation of each stage. To confirm the predicted magnetic field from the computational model, the acceleration stage was experimentally mapped with the Hall probe, as discussed in Section 3.2.5. The electromagnetic coils were energized to current set points to match conditions modeled.

The Hall acceleration stage centerline peak radial magnetic field is used as an indication of the performance capabilities of a Hall thruster magnetic circuit. The

normalized maximum centerline radial magnetic field for the NASA-173GT is shown in Figure 4-1.

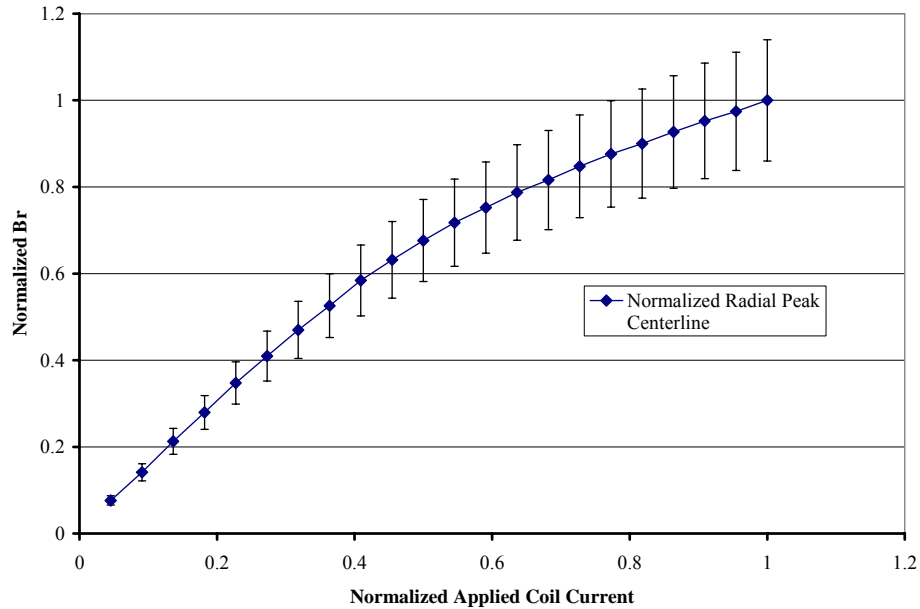


Figure 4-1: Normalized measured maximum centerline radial magnetic field in the Hall acceleration stage of the NASA-173GT.

The normalized measured radial magnetic field profiles along the inner wall, centerline, and outer wall of the NASA-173GT operating at 50% and 100% of the designed maximum applied currents are presented in Figure 4-2 and Figure 4-3, respectively. The normalized measured axial magnetic field profiles along the same radial positions and operating conditions are presented in Figure 4-4 and Figure 4-5, respectively. The magnetic field results are normalized to the maximum in the centerline radial magnetic field for each operating condition.

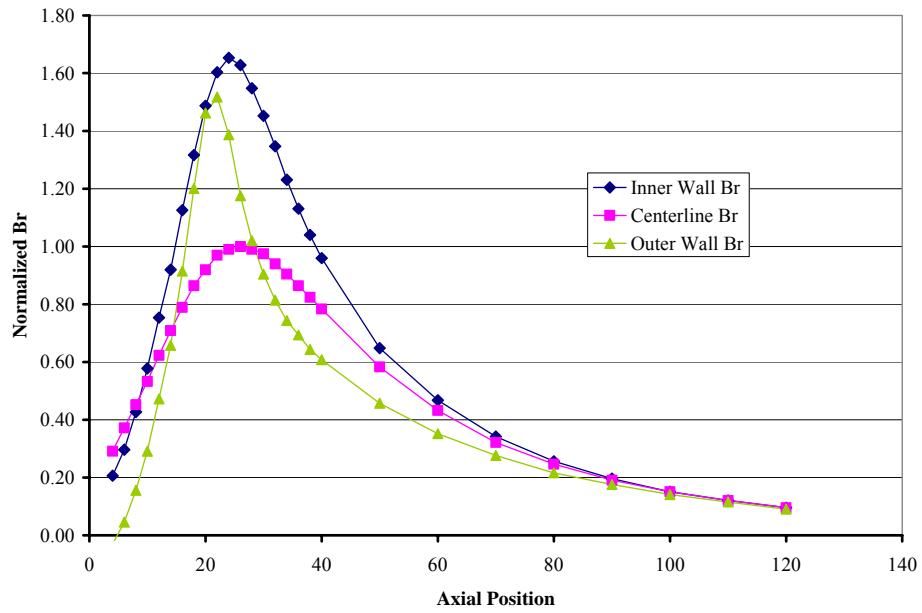


Figure 4-2: The NASA-173GT radial magnetic field profiles, normalized to the maximum centerline field intensity, operating at 50% coil current.

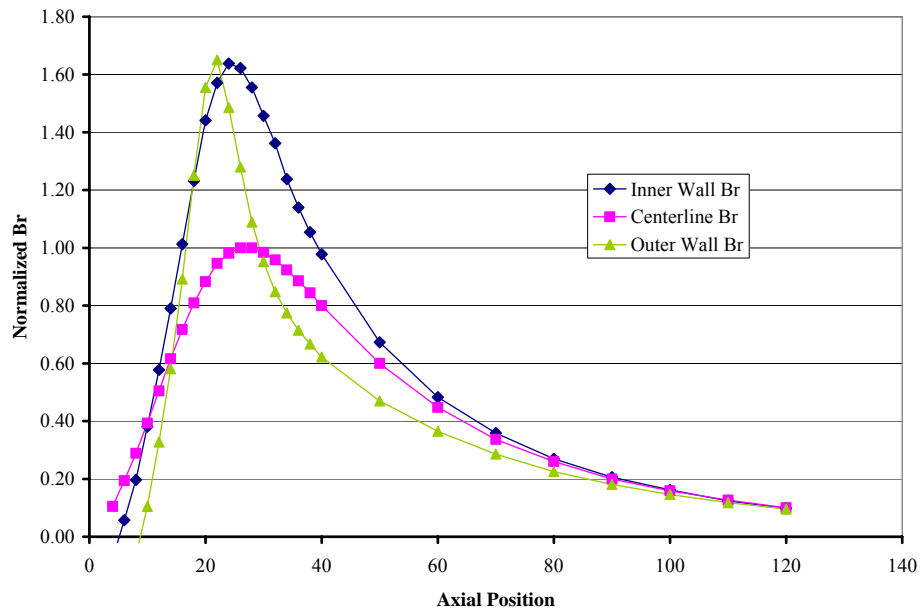


Figure 4-3: The NASA-173GT radial magnetic field profiles, normalized to the maximum centerline field intensity, operating at 100% coil current.

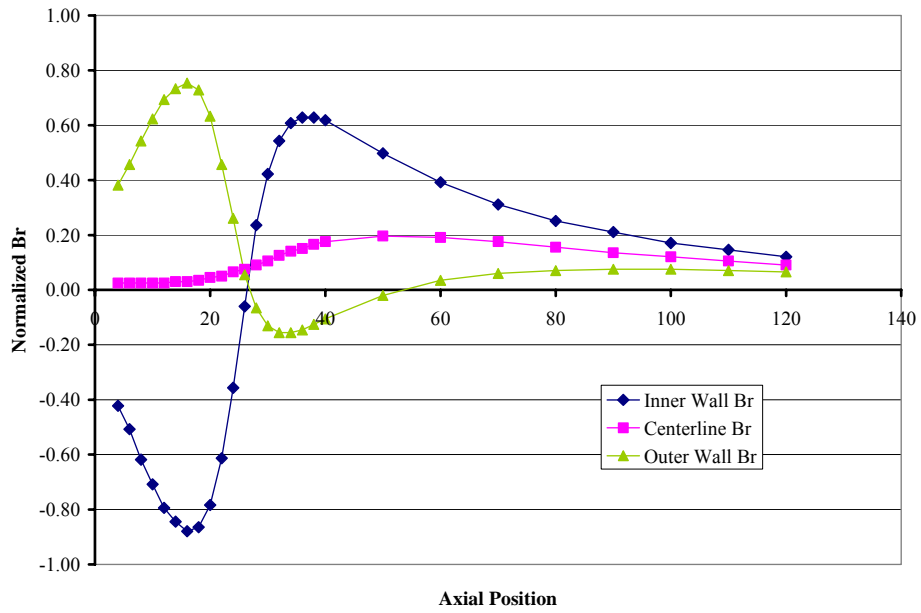


Figure 4-4: The NASA-173GT axial magnetic field profiles, normalized to the maximum centerline field intensity, operating at 50% coil current.

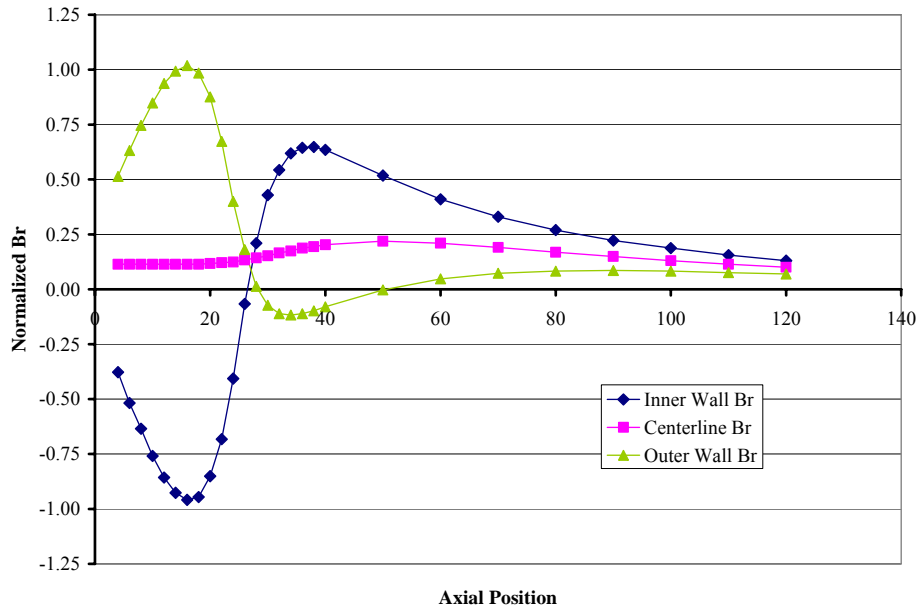


Figure 4-5: The NASA-173GT axial magnetic field profiles, normalized to the maximum centerline field intensity, operating at 100% coil current.

## 4.2 Ionization stage characterization

The ability of the ionization stage to ionize the propellant is determined by the correct combination of propellant flow rates, applied magnetic fields, ionization stage design, ionization cathode location, and the ionization stage input power. The design of the NASA-173GT ionization stage allowed for the optimization of the applied magnetic field, propellant flow rate, the ratio of the propellant flow through the cathode and anode plenum, and the input power of the ionization stage. The ion production cost was measured for a total propellant flow rate of 5 mg/s, ionization-stage input powers ranging from 250 to 580 W, and various combinations of electromagnetic coil currents. The results of the 5 mg/s ion production cost characterization are illustrated in Figure 4-6.

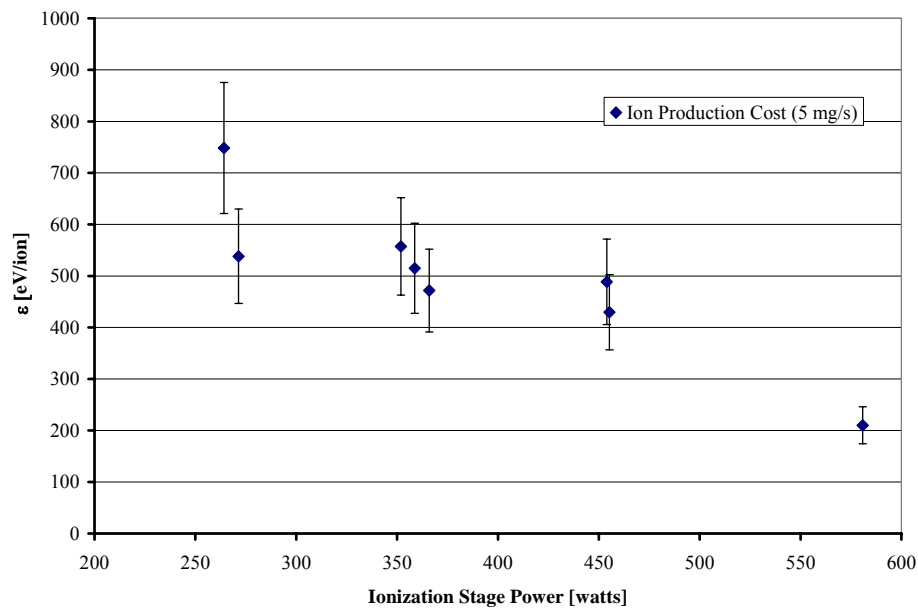


Figure 4-6: The ion production cost of the NASA-173GT as a function of input power, propellant flow rate distribution (5 mg/s), and applied magnetic field.

Several other flow rates above 5 mg/s were investigated but insufficient data was gathered to draw any conclusions from the results.

### **4.3 Performance characterization**

The performance of the NASA-173GT was acquired with a NASA EP thrust stand as discussed in Section 3.2.1 in VF-12 at NASA GRC. The thruster was operated in both a single- and two-stage configuration for propellant flow rates ranging from 5 to 10 mg/s xenon and acceleration voltages<sup>34</sup> ranging from 100 to 600 V. The single-stage results are presented in Section 4.3.1 and the two-stage results are presented in Section 4.3.2.

#### **4.3.1 Single-stage**

The single-stage performance characterization of the NASA-173GT was performed by disconnecting the ionization stage power supplies and allowing the ionization cathode to float. The distribution of the propellant in the ionization stage was maintained between the cathode and the anode shell plenum in similar ratios as investigated in the two-stage operation (ionization-stage cathode/plenum [(mg/s)/(mg/s)]: 4/1, 3/2, 9/1, and 8/2) . The ionization stage electromagnetic coils were designed not to influence the formation of the magnetic field topology in the acceleration channel;

---

<sup>34</sup> In the single-stage configuration the acceleration voltage also refers to the discharge voltage, which is the nomenclature used to identify applied voltage for Hall thruster operation.

therefore, the ionization stage coils were not energized during the single-stage experiments. The single-stage performance results for the two propellant flow rates are illustrated in Figure 4-7 through Figure 4-14 and the tabulated results are presented in Appendix-A Table A-1.

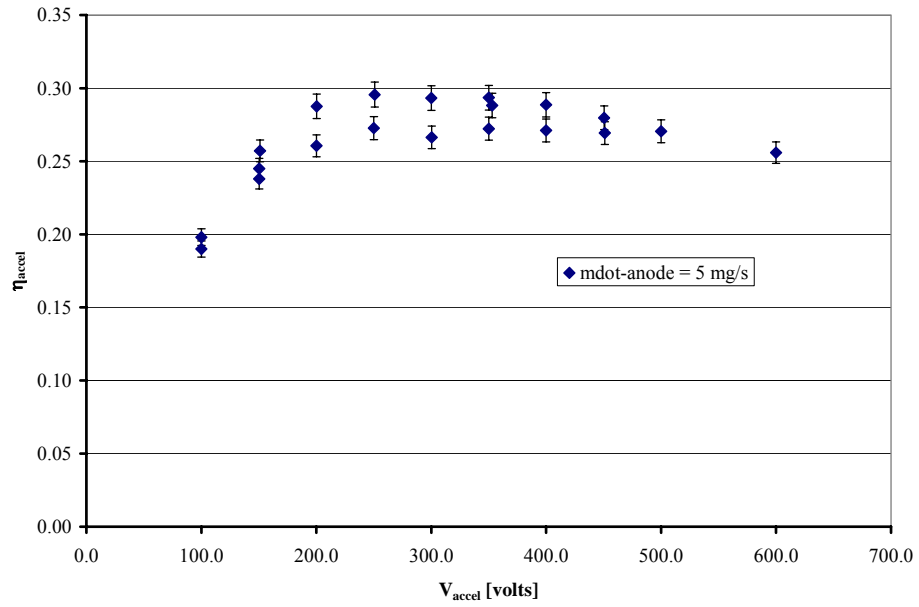


Figure 4-7: The acceleration efficiency as a function of applied acceleration voltage for the NASA-173GT operating in single-stage at 5 mg/s.

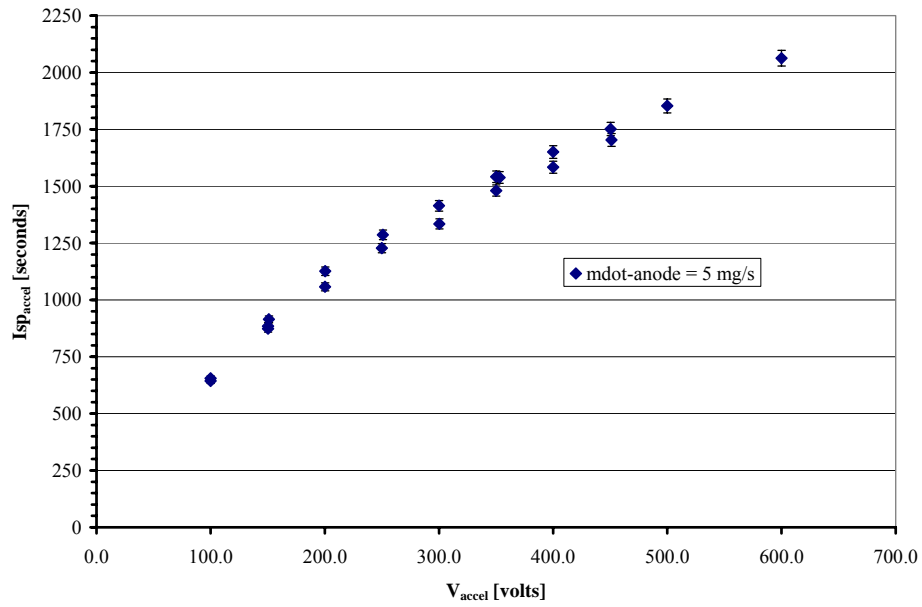


Figure 4-8: The acceleration specific impulse as a function of applied acceleration voltage for the NASA-173GT operating in single-stage at 5 mg/s.

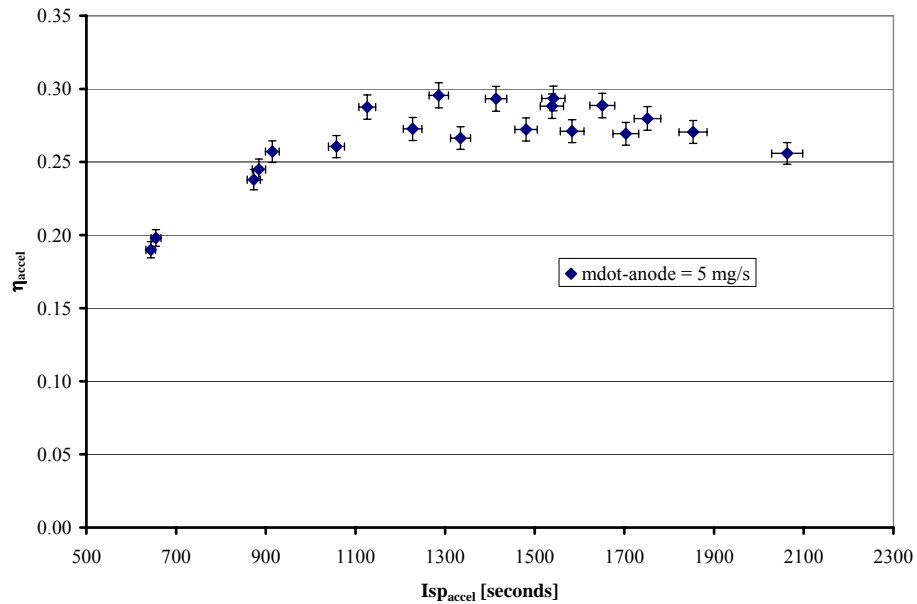


Figure 4-9: The acceleration efficiency as a function of specific impulse for the NASA-173GT operating in single-stage at 5 mg/s.

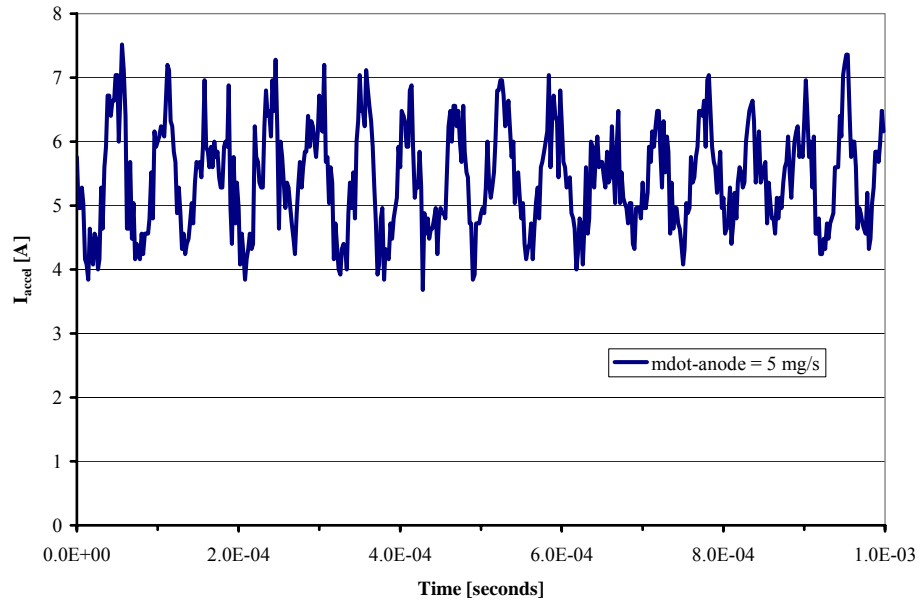


Figure 4-10: Acceleration current oscillation for the NASA-173GT operating in single-stage at 5 mg/s.

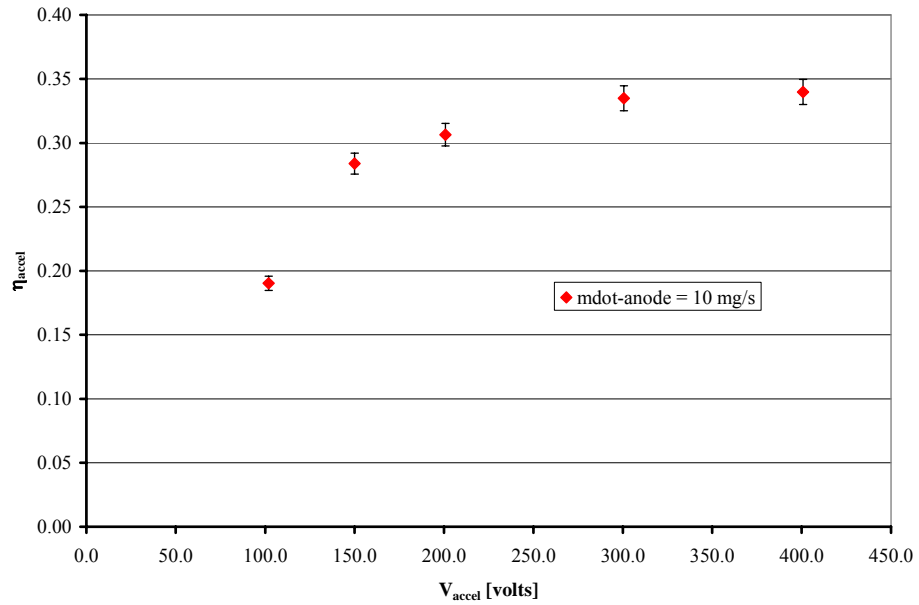


Figure 4-11: The acceleration efficiency as a function of applied acceleration voltage for the NASA-173GT operating in single-stage at 10 mg/s.

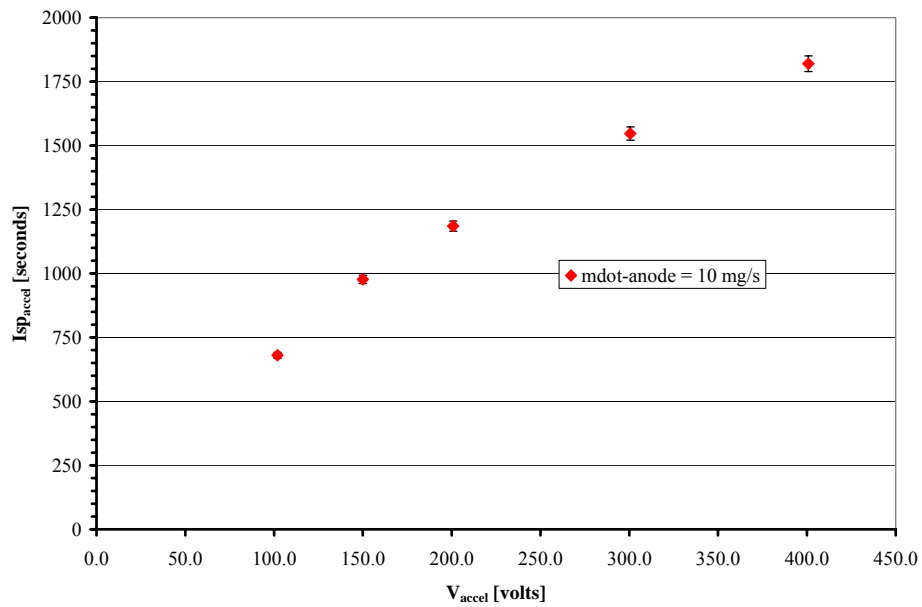


Figure 4-12: The acceleration specific impulse as a function of applied acceleration voltage for the NASA-173GT operating in single-stage at 10 mg/s.

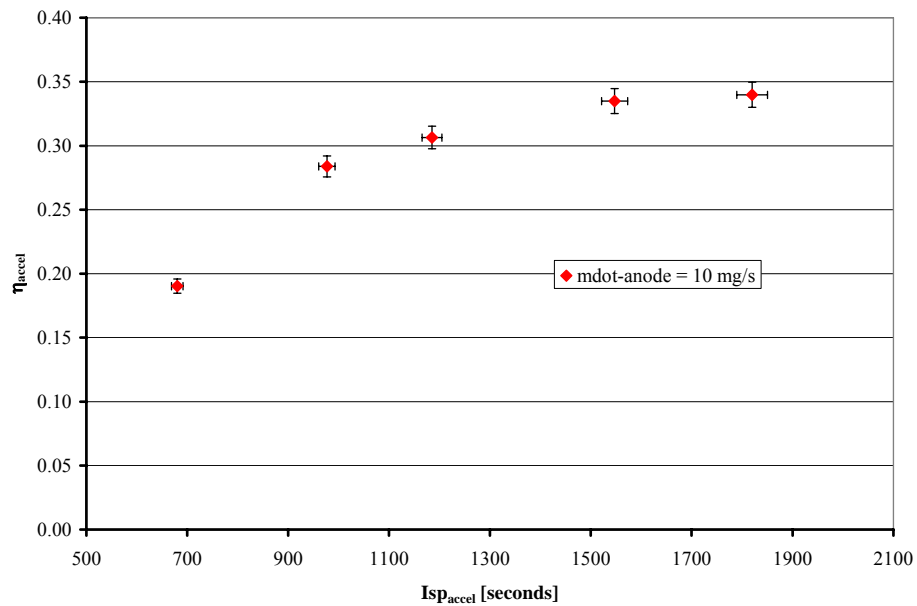


Figure 4-13: The acceleration efficiency as a function of specific impulse for the NASA-173GT operating in single-stage at 10 mg/s.

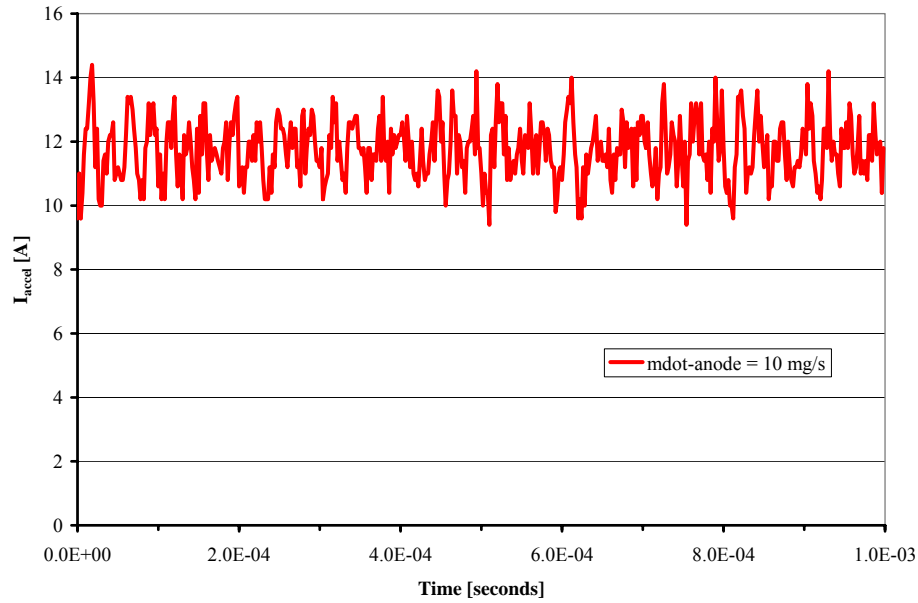


Figure 4-14: Acceleration current oscillation for the NASA-173GT operating in single-stage at 10 mg/s.

### 4.3.2 Two-stage

The two-stage performance characterization of the NASA-173GT was performed at 5 and 10 mg/s propellant flow rates, various applied magnetic field topologies, various combinations of propellant distributions between the anode plenum and the ionization cathode, and several ionization stage power levels. The two-stage performance results for the two propellant flow rates operated under the various combinations of parameters are illustrated in Figure 4-15 through Figure 4-22 and the tabulated results are presented in Appendix A Table A-2.

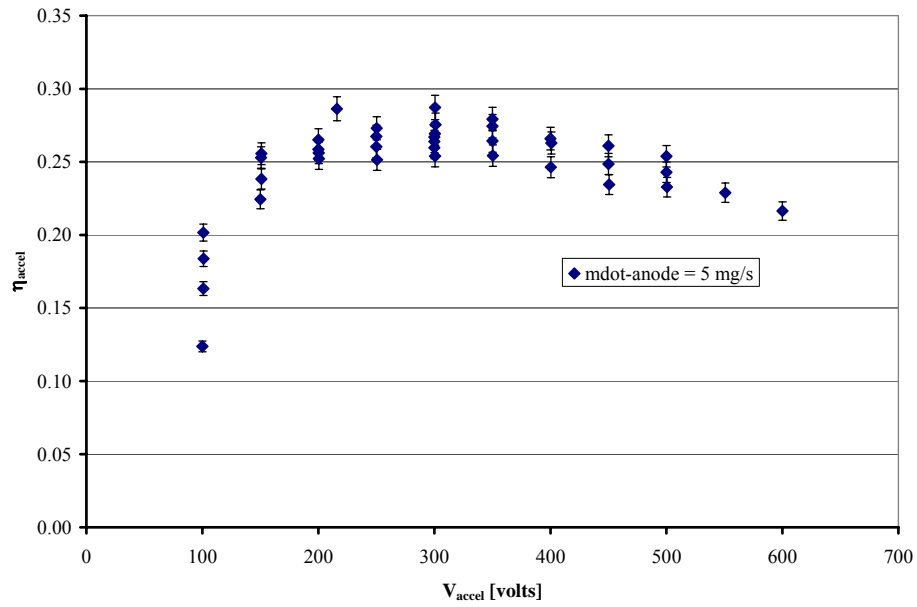


Figure 4-15: The acceleration efficiency as a function of applied acceleration voltage for the NASA-173GT operating in two-stage at 5 mg/s.

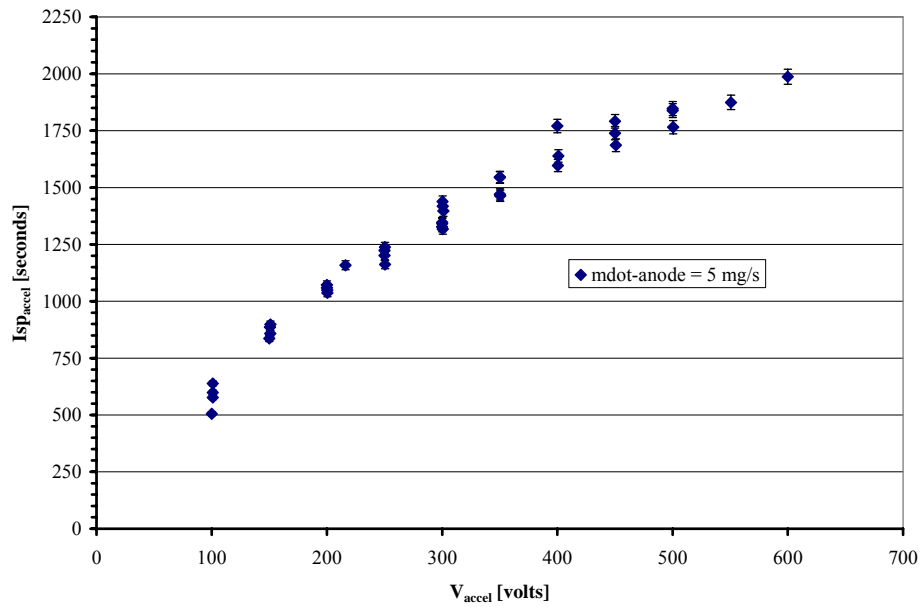


Figure 4-16: The acceleration specific impulse as a function of applied acceleration voltage for the NASA-173GT operating in two-stage at 5 mg/s.

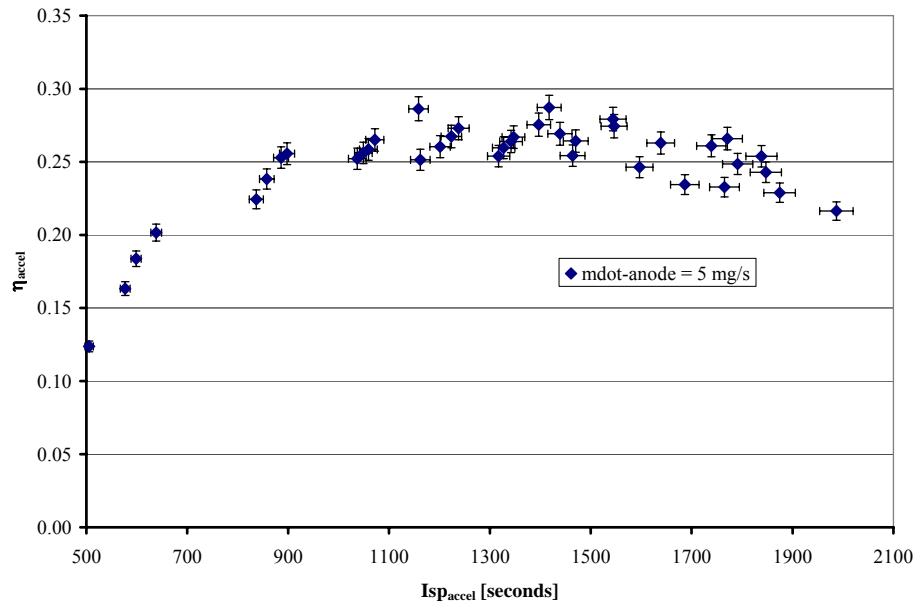


Figure 4-17: The acceleration efficiency as a function of specific impulse for the NASA-173GT operating in two-stage at 5 mg/s.

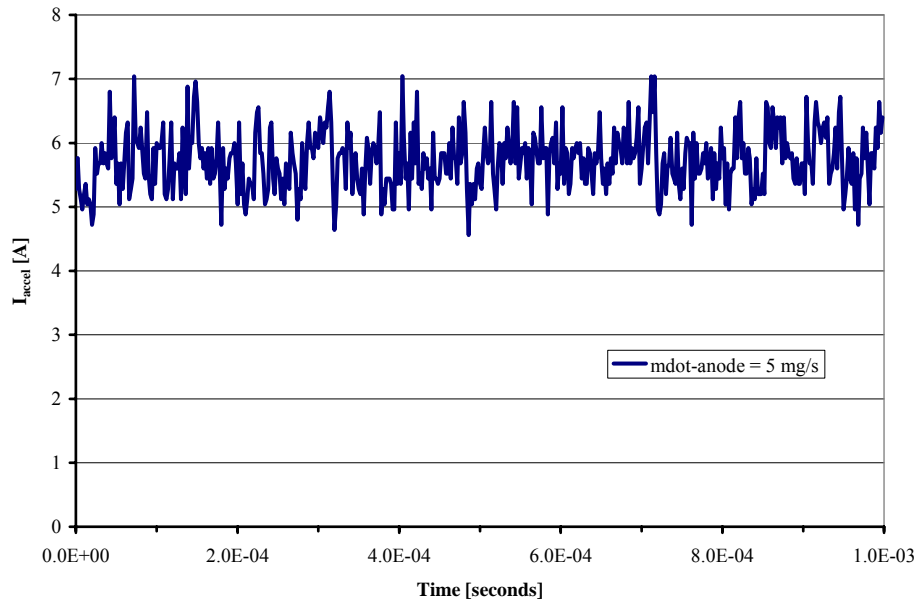


Figure 4-18: Acceleration current oscillation for the NASA-173GT operating in two-stage at 5 mg/s.

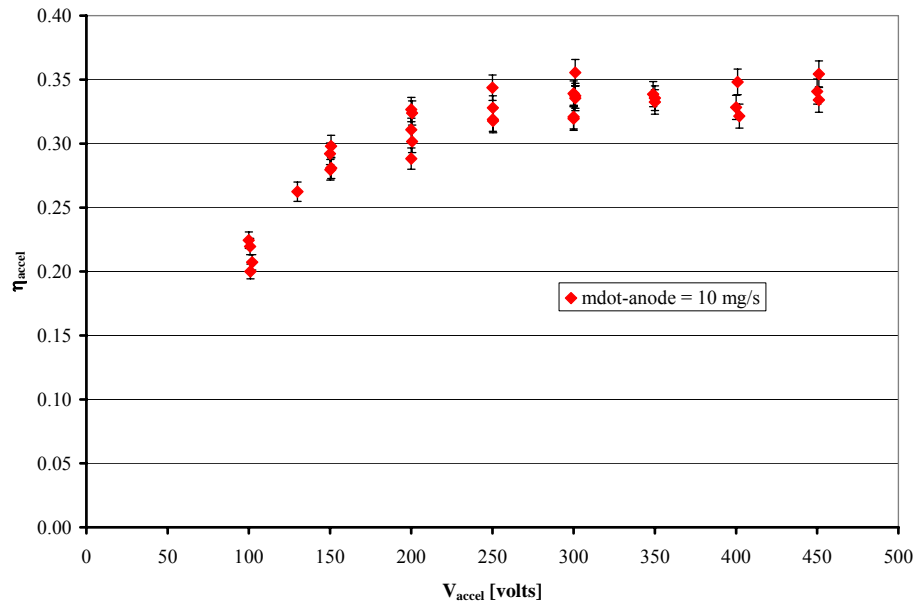


Figure 4-19: The acceleration efficiency as a function of applied acceleration voltage for the NASA-173GT operating in two-stage at 10 mg/s.

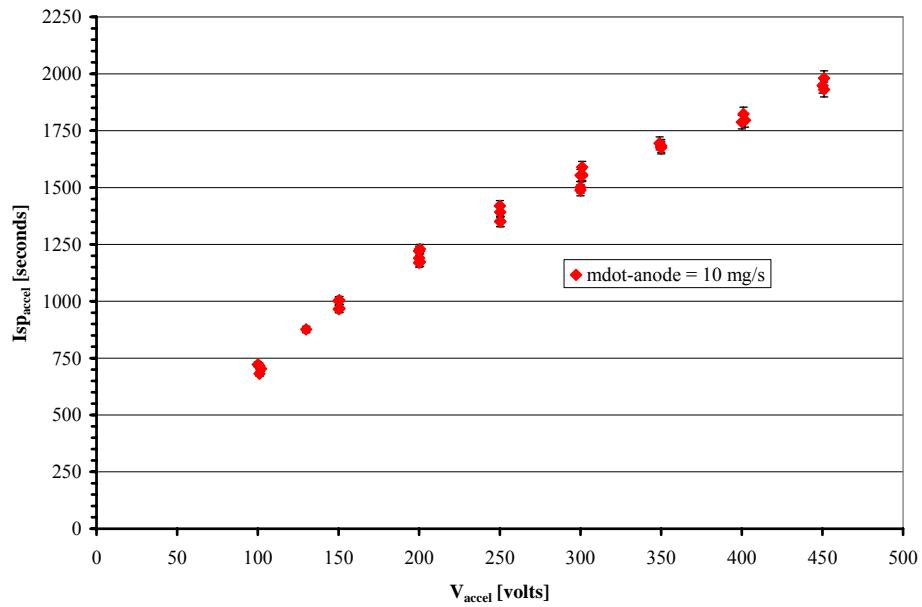


Figure 4-20: The acceleration specific impulse as a function of applied acceleration voltage for the NASA-173GT operating in two-stage at 10 mg/s.

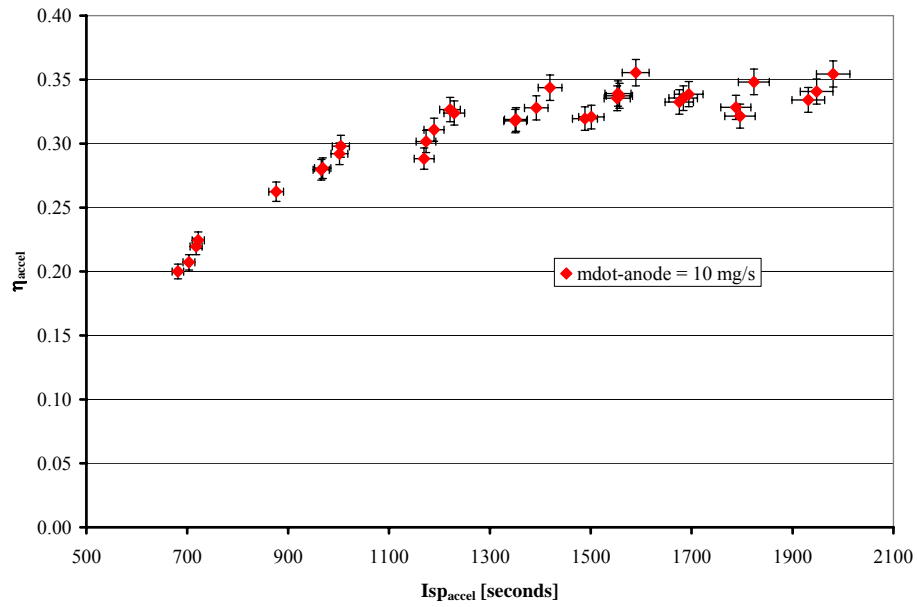


Figure 4-21: The acceleration efficiency as a function of specific impulse for the NASA-173GT operating in two-stage at 10 mg/s.

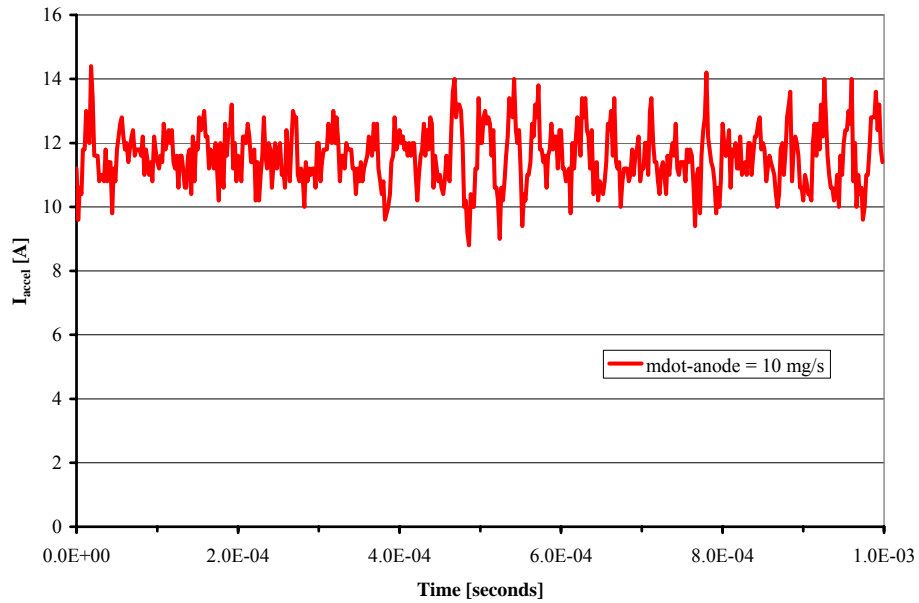


Figure 4-22: Acceleration current oscillation for the NASA-173GT operating in two-stage at 10 mg/s.

#### 4.4 Thermal characterization

As described in Section 3.2.6, the thermal characterization of the NASA-173GT was conducted in a limited fashion. The three physical thermocouples were attached onto the NASA-173GT primarily to monitor the magnetic circuit heat load. The calculated electromagnetic coil temperatures were first order estimates of the bulk coil temperatures. The NASA-173GT thruster was never operated for the purpose of determining the thermal steady-state of the device. Figure 4-23 represents long duration operation of the NASA-173GT at a fixed operating condition of 3.7 kW.

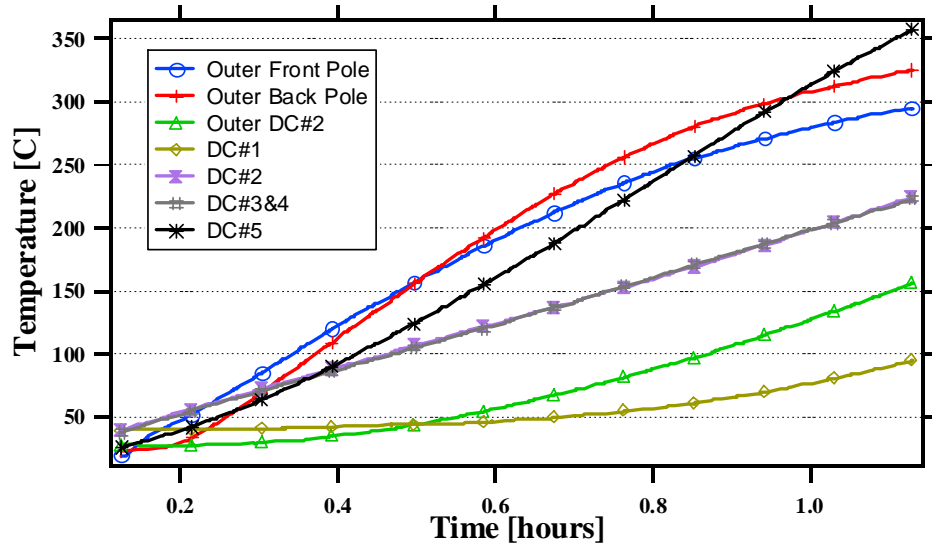


Figure 4-23: Thermal characteristics of the NASA-173GT operating in a two-stage at a total power input of 3.7 kW.

#### 4.5 ExB investigation

The NASA-173GT far field ion species fractions were measured with the JPL ExB probe, discussed in Section 3.2.2, in VF-12 at NASA GRC. The thruster was

operated in both single- and two-stage configurations for propellant flow rates of 5 and 10 mg/s xenon and acceleration voltages ranging from 100 to 600 V. The single-stage results are presented in Section 4.5.1 and the two-stage results are presented in Section 4.5.2. The **ExB** measurements were repeated several times at each operating case to reduce the uncertainty in the observed data.

#### 4.5.1 Single-stage

The single-stage ion species fractions measurements of the NASA-173GT were performed by disconnecting the ionization stage power supplies and allowing the ionization cathode to float. The distribution of the propellant in the ionization stage was maintained between the cathode and the anode shell plenum in similar ratios as investigated in the two-stage operation. The ionization stage electromagnetic coils were designed not to influence the formation of the magnetic field topology in the acceleration channel; therefore, the ionization stage coils were not energized during the single-stage experiments. The single-stage **ExB** probe traces of the NASA-173GT operating at a propellant flow rate of 10 mg/s, for acceleration voltages ranging from 200 to 400 V, are presented in Figure 4-24 to Figure 4-26.

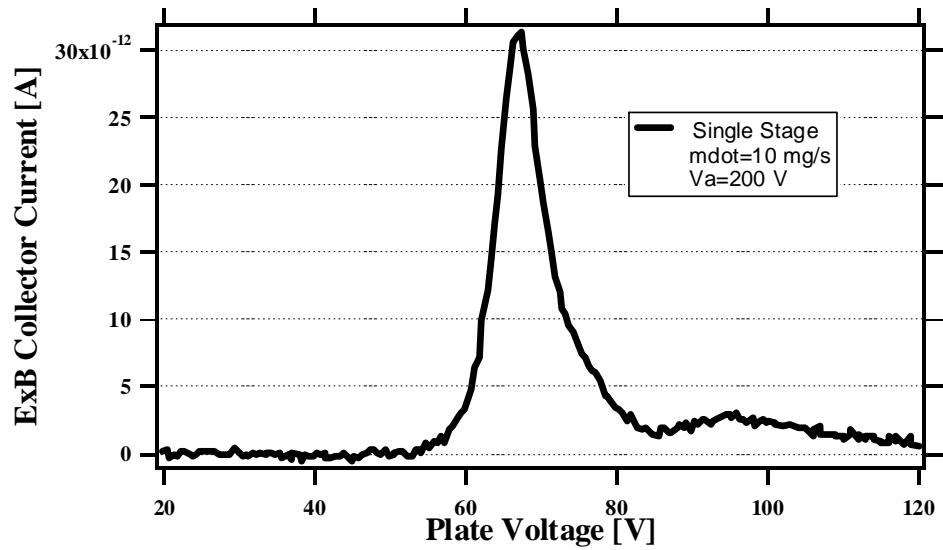


Figure 4-24: **ExB** trace of the NASA-173GT in single-stage at 200 V acceleration potential and a propellant flow rate of 10 mg/s.

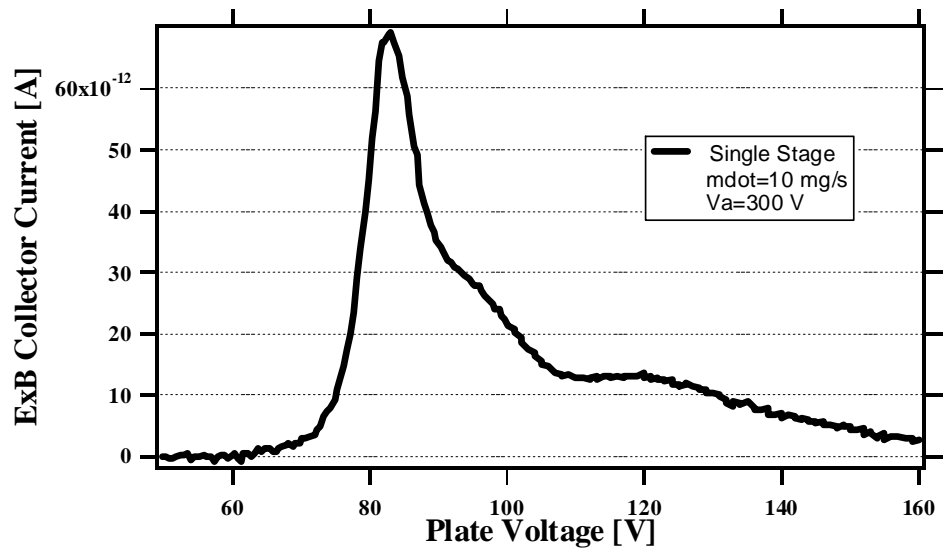


Figure 4-25: **ExB** trace of the NASA-173GT in single-stage at 300 V acceleration potential and a propellant flow rate of 10 mg/s.

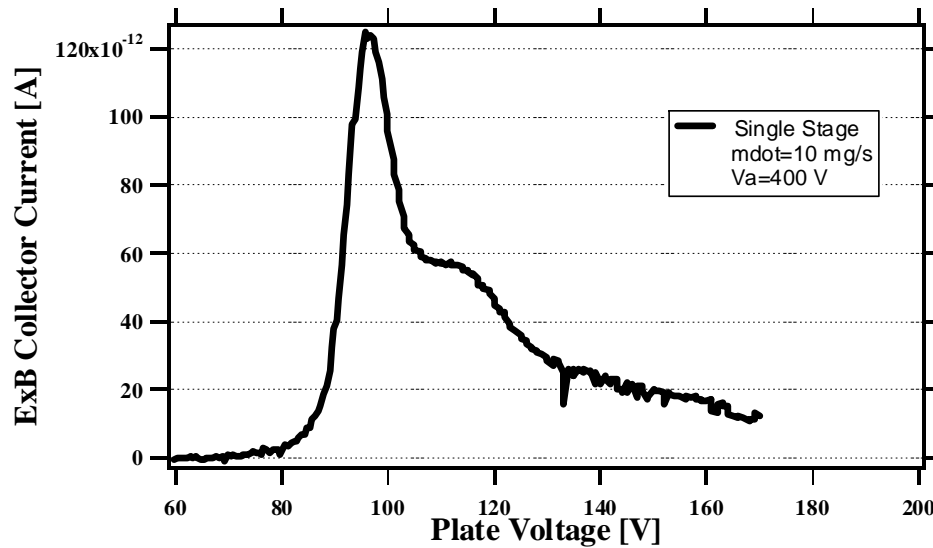


Figure 4-26: **ExB** trace of the NASA-173GT in single-stage at 400 V acceleration potential and a propellant flow rate of 10 mg/s.

#### 4.5.2 Two-stage

The two-stage ion species fractions measurements of the NASA-173GT was performed at 5 and 10 mg/s propellant flow rates, various applied magnetic field topologies, various combinations of propellant distributions between the anode plenum and the ionization cathode, and several ionization stage power levels. The two-stage **ExB** probe traces for NASA-173GT operating at propellant flow rates of 5 and 10 mg/s, ionization currents of 15 A and 25 A, and acceleration voltages ranging from 100 to 500 V are presented in Figure 4-27 to Figure 4-38.

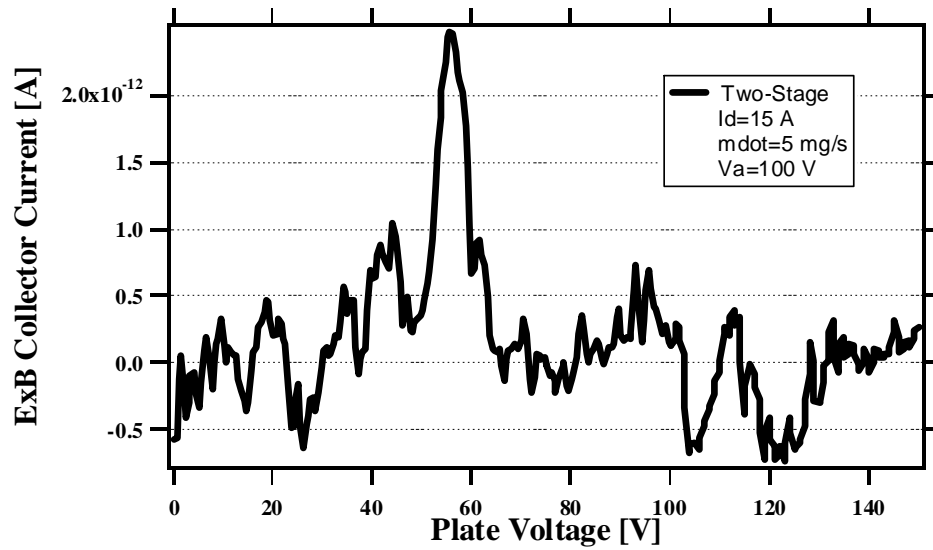


Figure 4-27: **ExB** trace of the NASA-173GT in two-stage at 100 V acceleration potential, ionization current of 15 A, and a propellant flow rate of 5 mg/s.

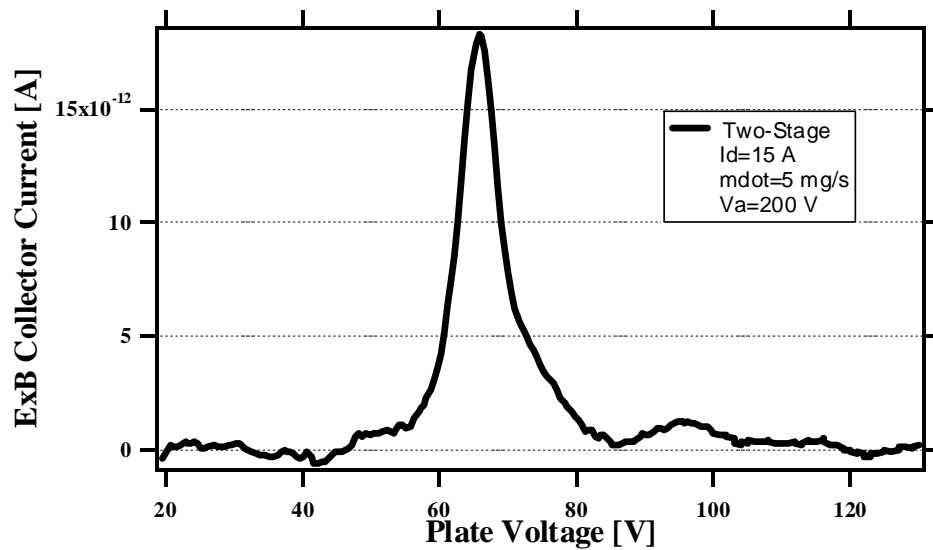


Figure 4-28: **ExB** trace of the NASA-173GT in two-stage at 200 V acceleration potential, ionization current of 15 A, and a propellant flow rate of 5 mg/s.

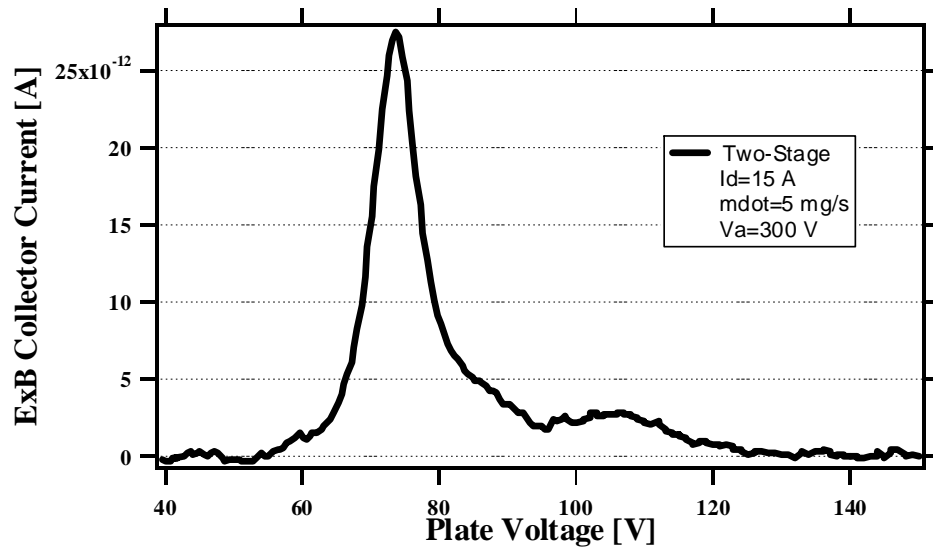


Figure 4-29: **ExB** trace of the NASA-173GT in two-stage at 300 V acceleration potential, ionization current of 15 A, and a propellant flow rate of 5 mg/s.

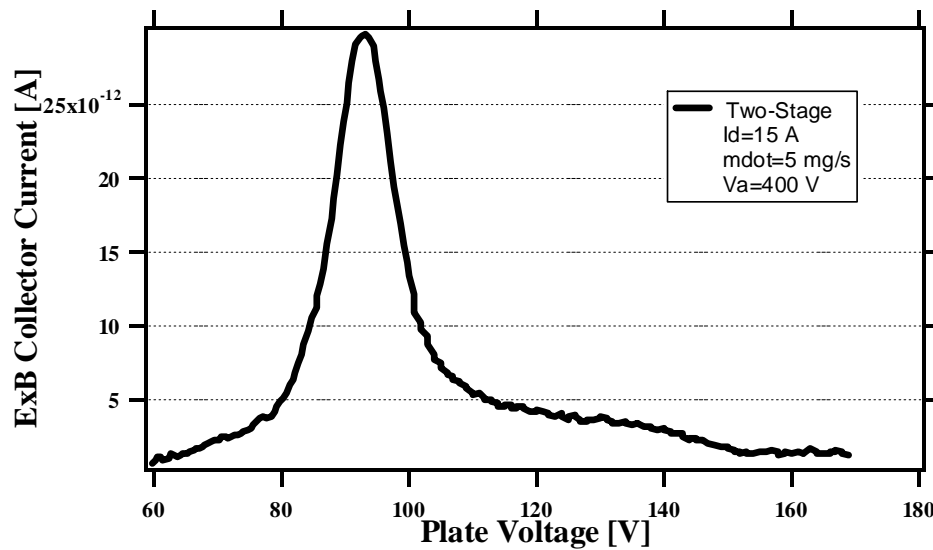


Figure 4-30: **ExB** trace of the NASA-173GT in two-stage at 400 V acceleration potential, ionization current of 15 A, and a propellant flow rate of 5 mg/s.

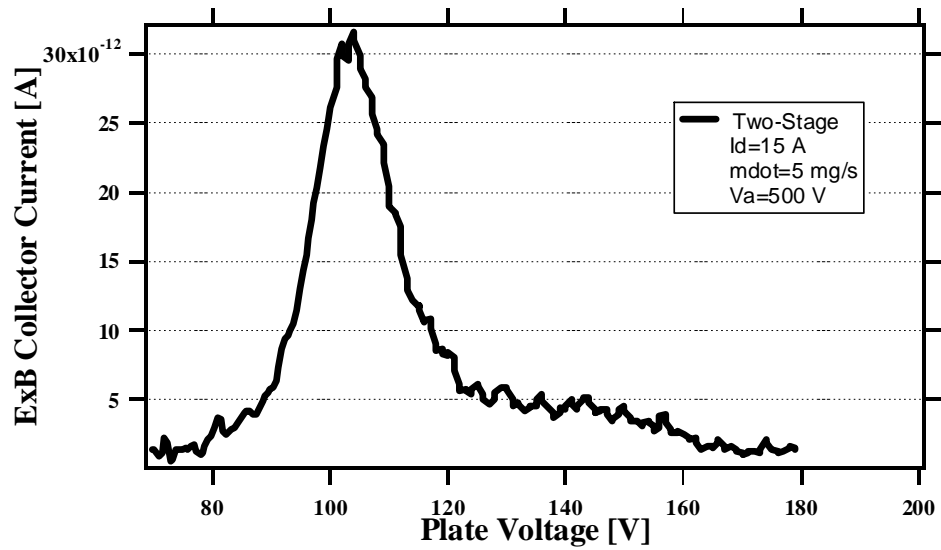


Figure 4-31: **ExB** trace of the NASA-173GT in two-stage at 500 V acceleration potential, ionization current of 15 A, and a propellant flow rate of 5 mg/s.

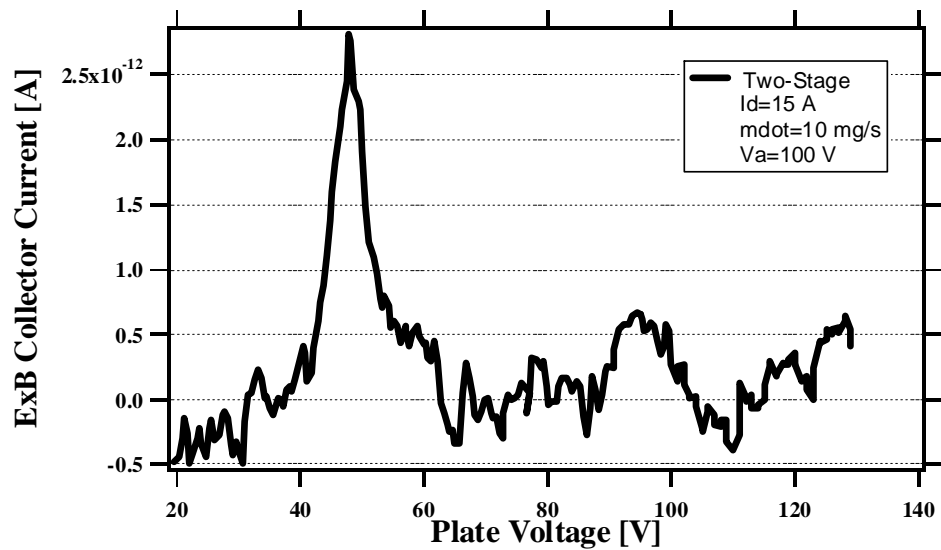


Figure 4-32: **ExB** trace of the NASA-173GT in two-stage at 100 V acceleration potential, ionization current of 15 A, and a propellant flow rate of 10 mg/s.

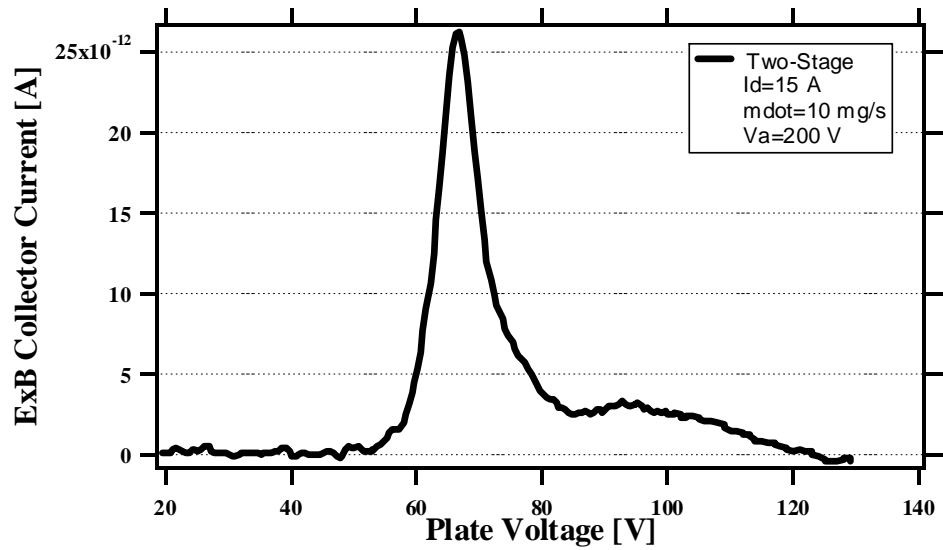


Figure 4-33: **ExB** trace of the NASA-173GT in two-stage at 200 V acceleration potential, ionization current of 15 A, and a propellant flow rate of 10 mg/s.

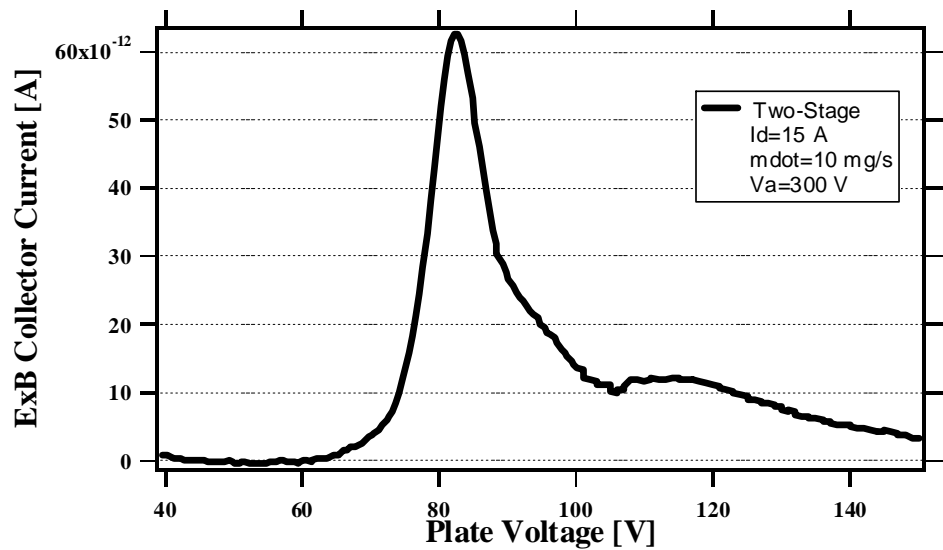


Figure 4-34: **ExB** trace of the NASA-173GT in two-stage at 300 V acceleration potential, ionization current of 15 A, and a propellant flow rate of 10 mg/s.

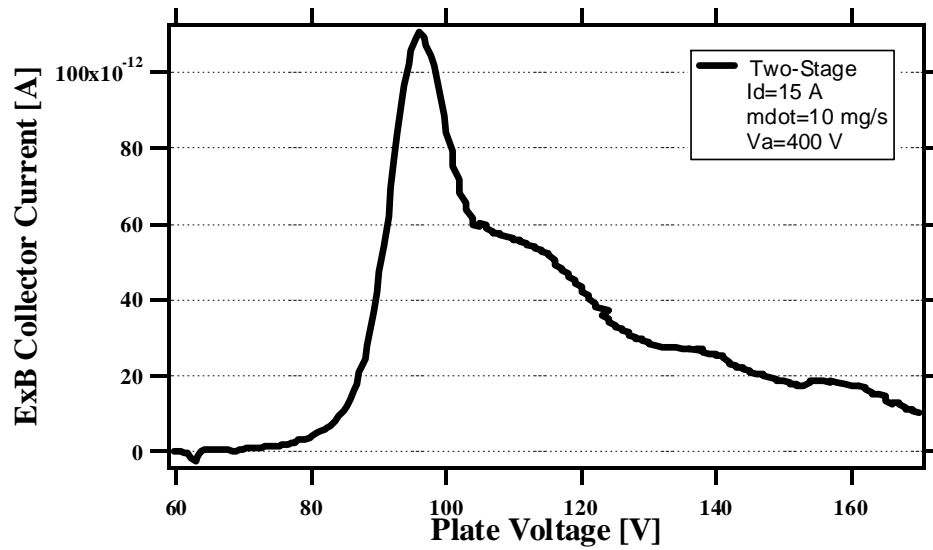


Figure 4-35: **ExB** trace of the NASA-173GT in two-stage at 400 V acceleration potential, ionization current of 15 A, and a propellant flow rate of 10 mg/s.

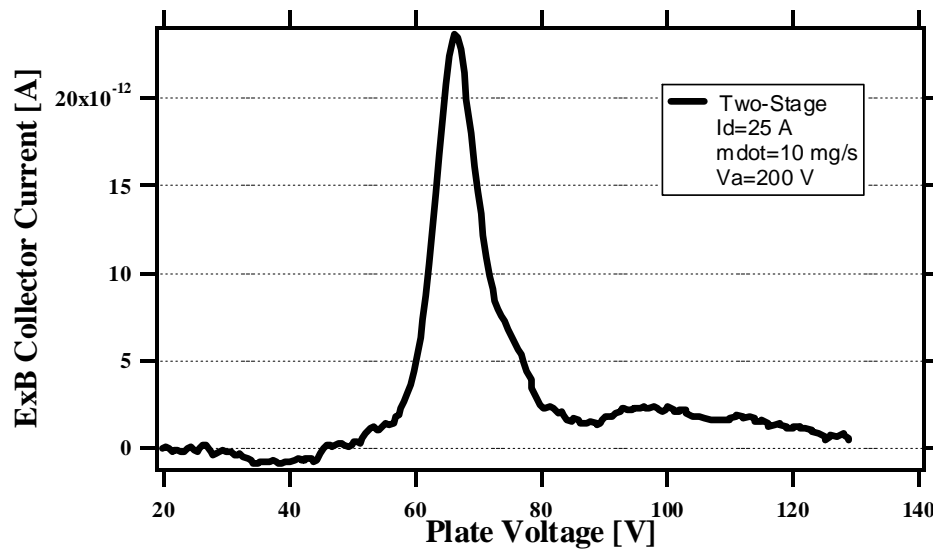


Figure 4-36: **ExB** trace of the NASA-173GT in two-stage at 200 V acceleration potential, ionization current of 25 A, and a propellant flow rate of 10 mg/s.

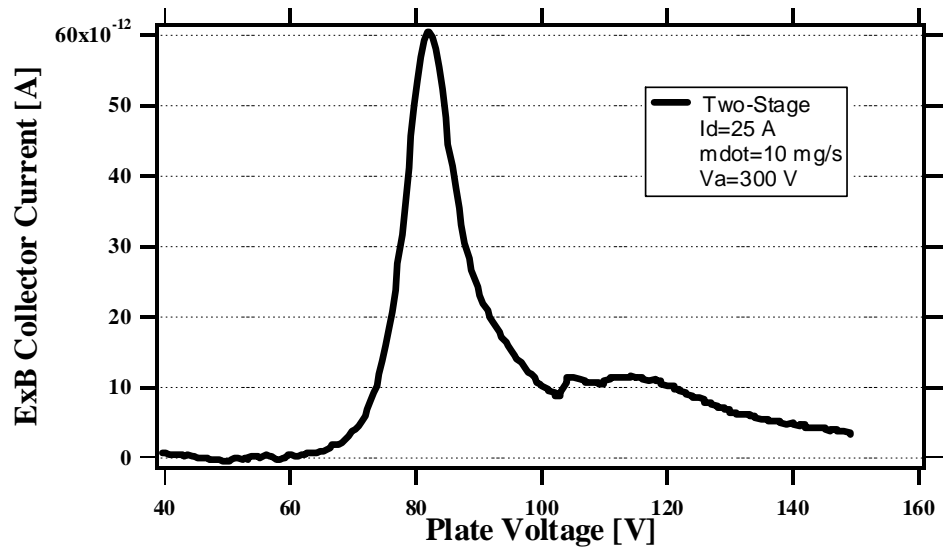


Figure 4-37: **ExB** trace of the NASA-173GT in two-stage at 300 V acceleration potential, ionization current of 25 A, and a propellant flow rate of 10 mg/s.

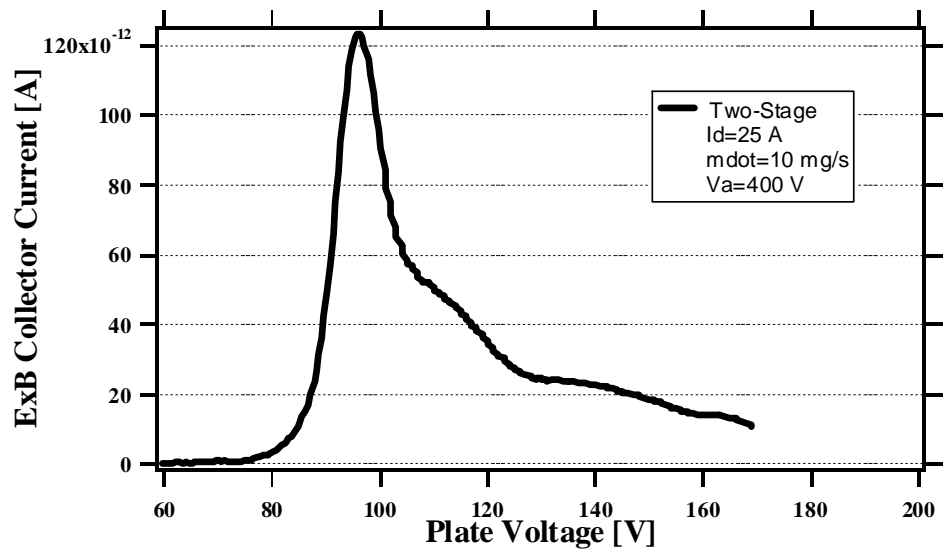


Figure 4-38: **ExB** trace of the NASA-173GT in two-stage at 400 V acceleration potential, ionization current of 25 A, and a propellant flow rate of 10 mg/s.

## 4.6 Gridded Faraday probe investigation

The NASA-173GT far field ion current density distributions were measured with NASA GRC gridded Faraday probes, discussed in Section 3.2.3, in VF-12 at NASA GRC. The thruster was operated in both single- and two-stage configurations for propellant flow rates of 5 and 10 mg/s xenon and acceleration voltages ranging from 100 to 500 V. The single-stage results are presented in Section 4.6.1 and the two-stage results are presented in Section 4.6.2. The ion current density measurements were obtained from  $-90^\circ$  to  $+90^\circ$  with respect to the thruster exit plane. The two gridded Faraday probes were located at 0.45 m for probe #1 and 0.95 m for probe#2 downstream of the exit plane of the thruster.

The gridded Faraday probe configuration included a negatively biased grid for repelling electrons and a positive biased collector plate. To determine a sufficient ion repelling voltage for the collector plate, each of the two probes were placed behind the thruster at full probe arm rotation. The gridded Faraday probe was allowed to float to a potential of the thermal CEX ions, due to facilities background pressure, with the electron repelling grid energized to -30 V bias. The collector plate for each of the probes floated to positive voltages between +3 and +5 V. It was determined that a collector plate bias of +5 V would be sufficient to repel low-energy CEX ions generated by the background pressure of the vacuum facility.

### 4.6.1 Single-stage

The single-stage ion current density measurements of the NASA-173GT were performed by disconnecting the ionization stage power supplies and allowing the ionization cathode to float. The distribution of the propellant in the ionization stage was maintained between the cathode and the anode shell plenum in similar ratios as investigated in the two-stage operation. The ionization stage electromagnetic coils were designed not to influence the formation of the magnetic field topology in the acceleration channel; therefore, the ionization stage coils were not energized during the single-stage experiments. The single-stage gridded Faraday probe trace of the NASA-173GT operating at a propellant flow rate of 10 mg/s and an acceleration voltage of 400 V is presented in Figure 4-39. Figure 4-39 represents the only ion current trace acquired with the NASA-173GT operating in single-stage.

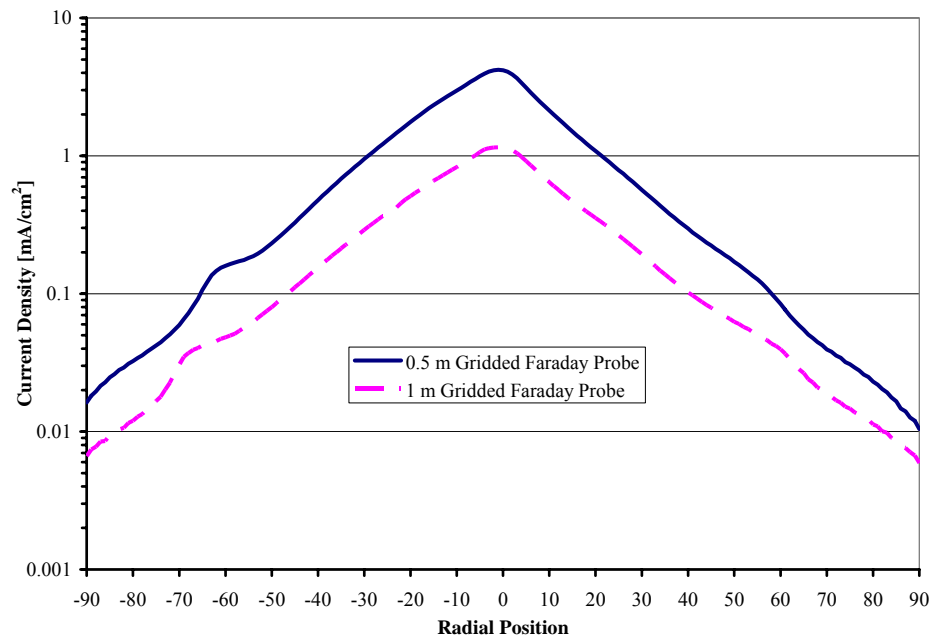


Figure 4-39: Ion current trace of the NASA-173GT operating in single-stage at 400 V acceleration potential and propellant flow rate of 10 mg/s.

## 4.6.2 Two-stage

The two-stage ion current density measurements of the NASA-173GT were performed at 5 and 10 mg/s propellant flow rates, various applied magnetic field topologies, various combinations of propellant distributions between the anode plenum and the ionization cathode, and several ionization stage power levels. The two-stage gridded Faraday probe traces for NASA-173GT operating at propellant flow rates of 5 and 10 mg/s, ionization currents of 15 A and 25 A, and for acceleration voltages ranging from 100 to 500 V are presented in Figure 4-40 to Figure 4-56.

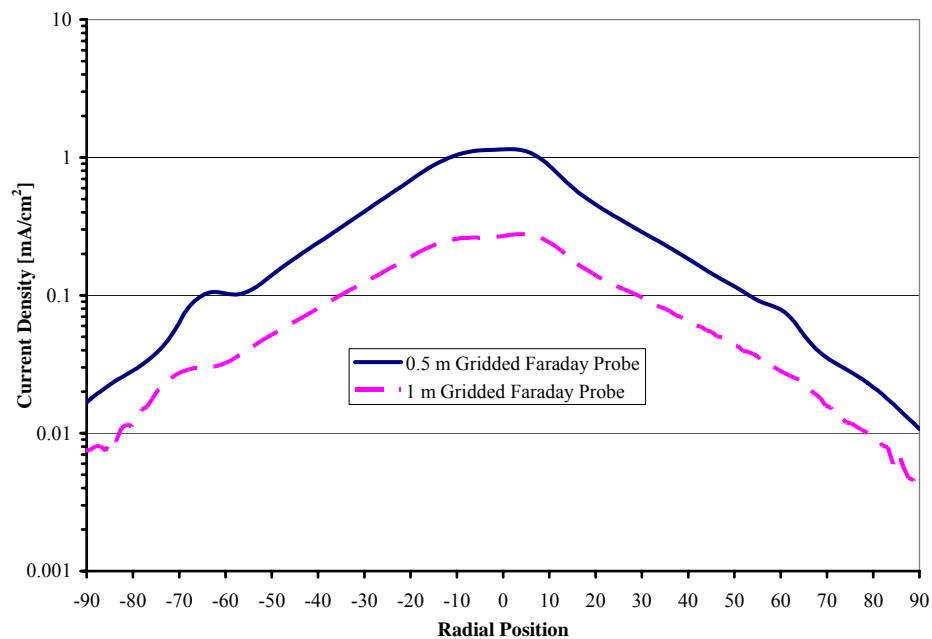


Figure 4-40: Two-stage ion current trace of the NASA-173GT at 200 V, propellant flow rate of 5 mg/s, and  $I_d$  of 15 A.

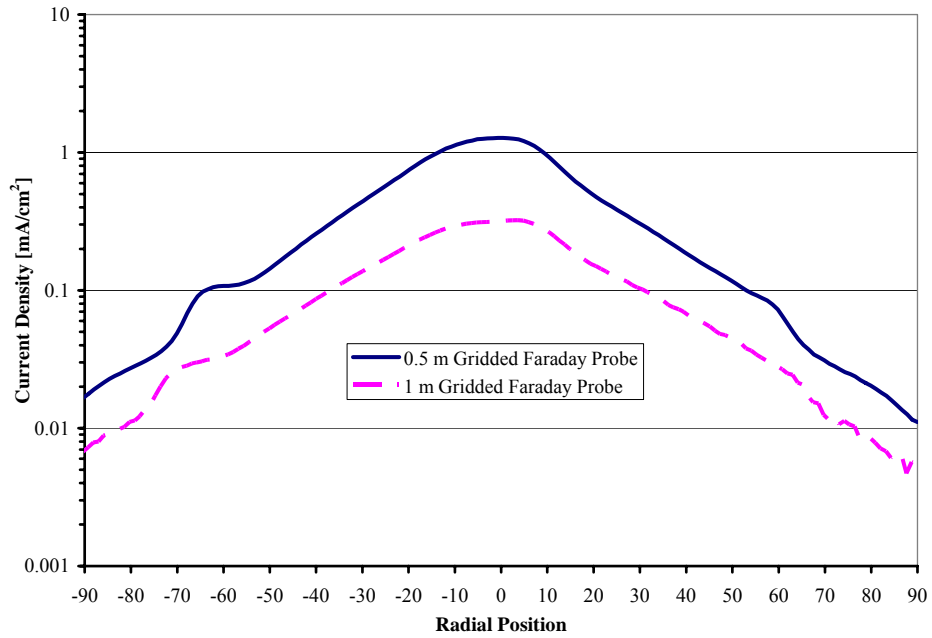


Figure 4-41: Two-stage ion current trace of the NASA-173GT at 300 V, propellant flow rate of 5 mg/s, and  $I_d$  of 15 A.

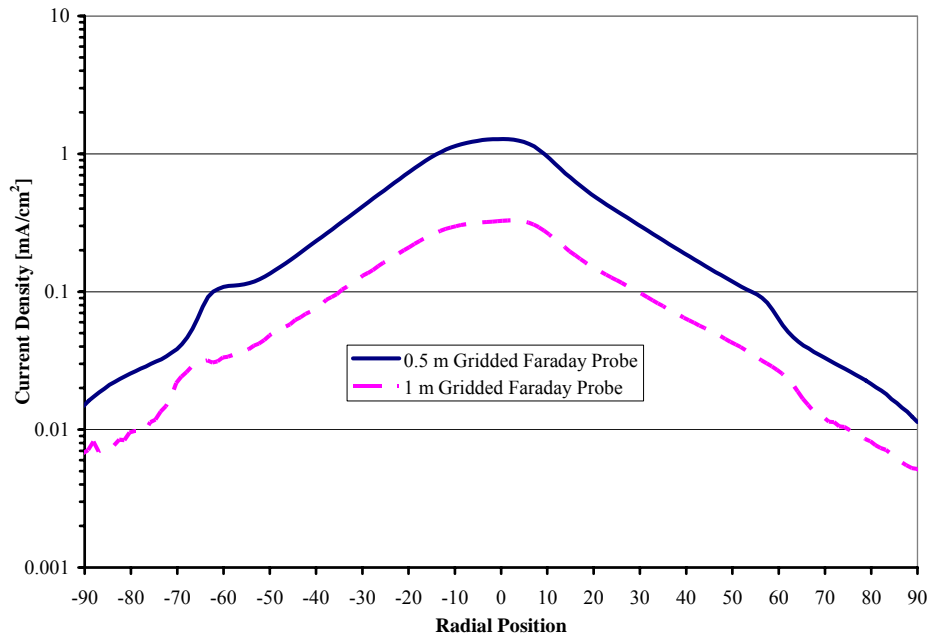


Figure 4-42: Two-stage ion current trace of the NASA-173GT at 400 V, propellant flow rate of 5 mg/s, and  $I_d$  of 15 A.

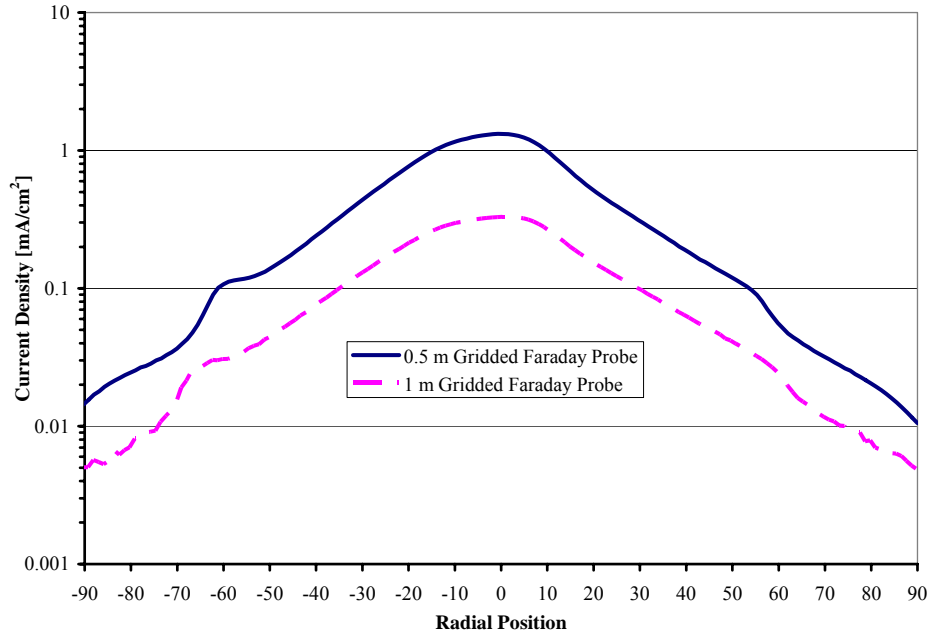


Figure 4-43: Two-stage ion current trace of the NASA-173GT at 500 V, propellant flow rate of 5 mg/s, and  $I_d$  of 15 A.

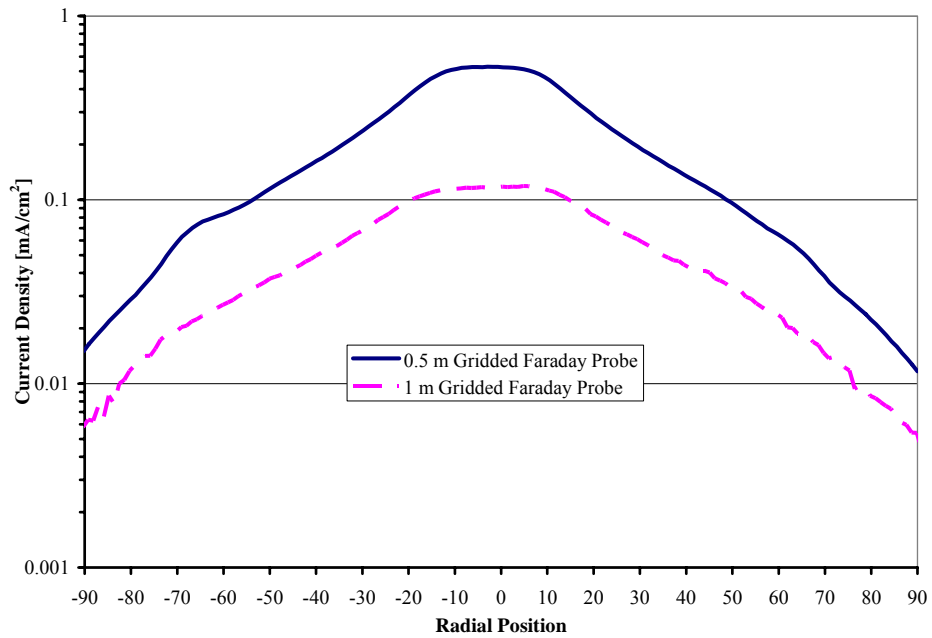


Figure 4-44: Two-stage ion current trace of the NASA-173GT at 100 V, propellant flow rate of 5 mg/s, and  $I_d$  of 25 A.

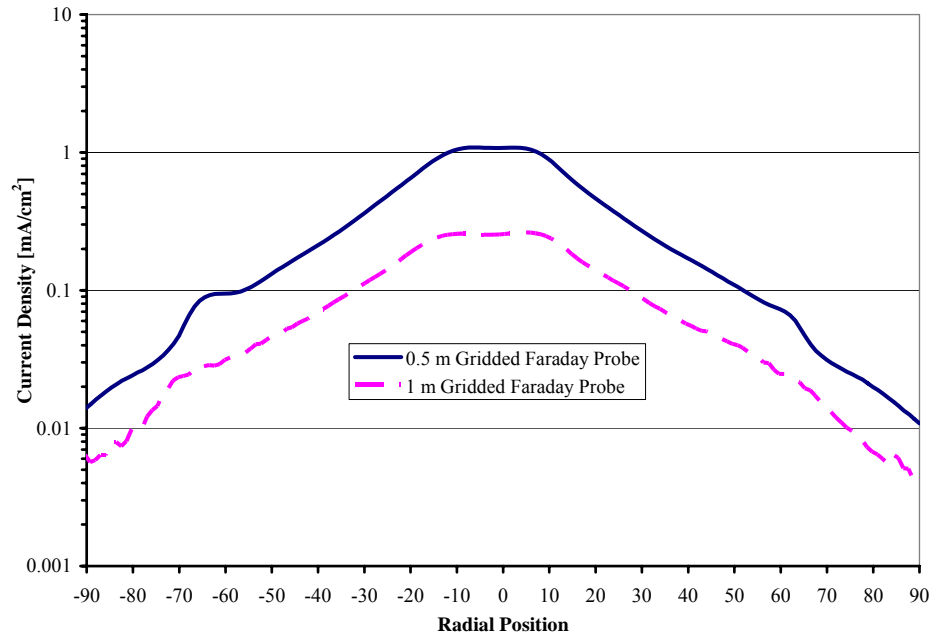


Figure 4-45: Two-stage ion current trace of the NASA-173GT at 200 V, propellant flow rate of 5 mg/s, and  $I_d$  of 25 A.

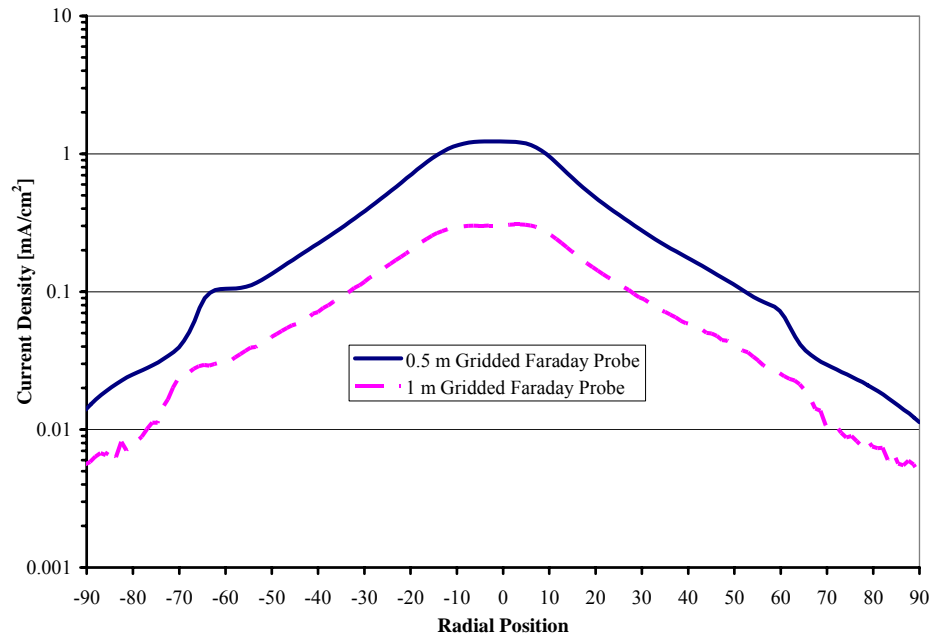


Figure 4-46: Two-stage ion current trace of the NASA-173GT at 300 V, propellant flow rate of 5 mg/s, and  $I_d$  of 25 A.

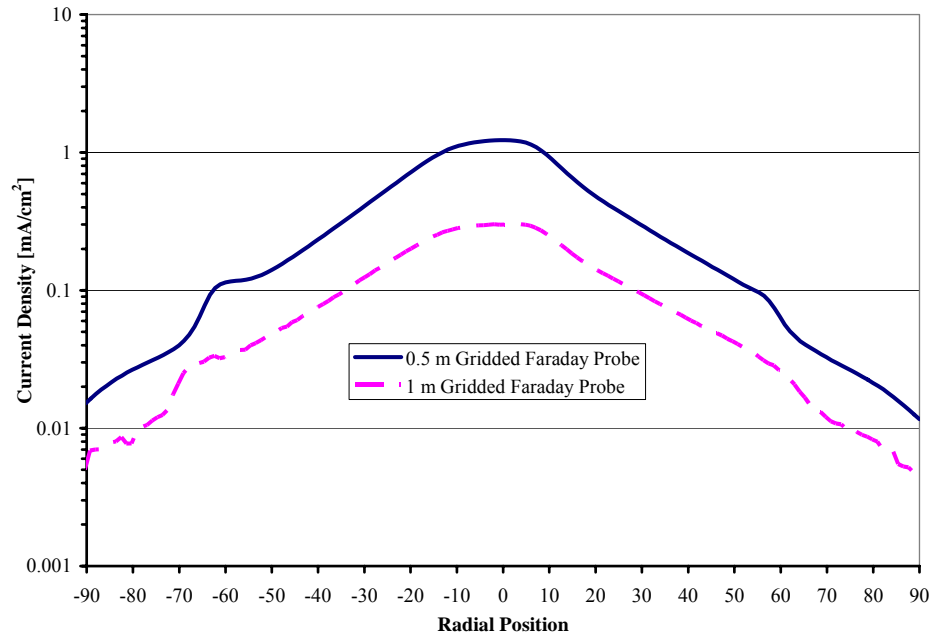


Figure 4-47; Two-stage ion current trace of the NASA-173GT at 400 V, propellant flow rate of 5 mg/s, and  $I_d$  of 25 A.

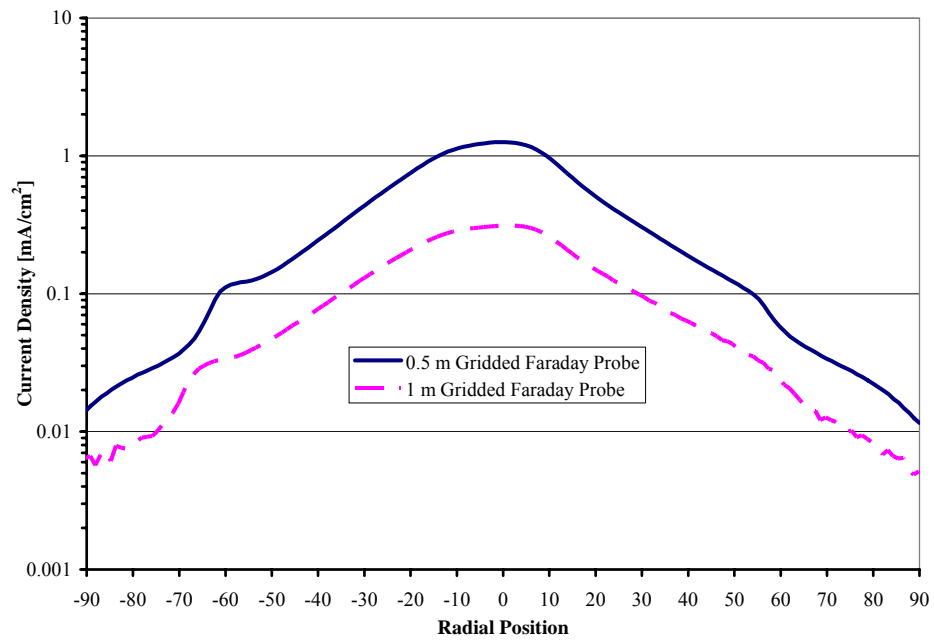


Figure 4-48: Two-stage ion current trace of the NASA-173GT at 500 V, propellant flow rate of 5 mg/s, and  $I_d$  of 25 A.

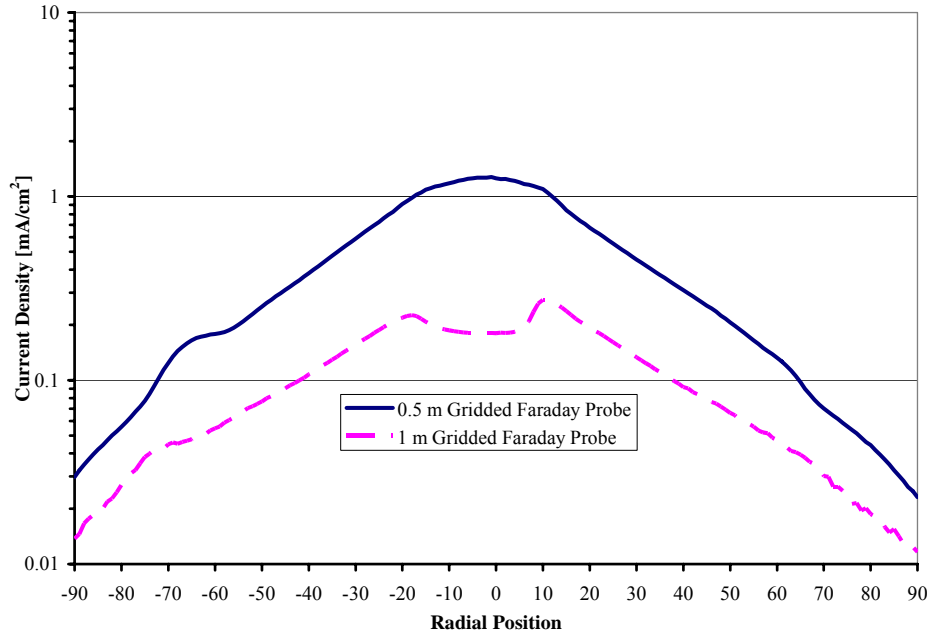


Figure 4-49: Two-stage ion current trace of the NASA-173GT at 100 V, propellant flow rate of 10 mg/s, and  $I_d$  of 15 A.

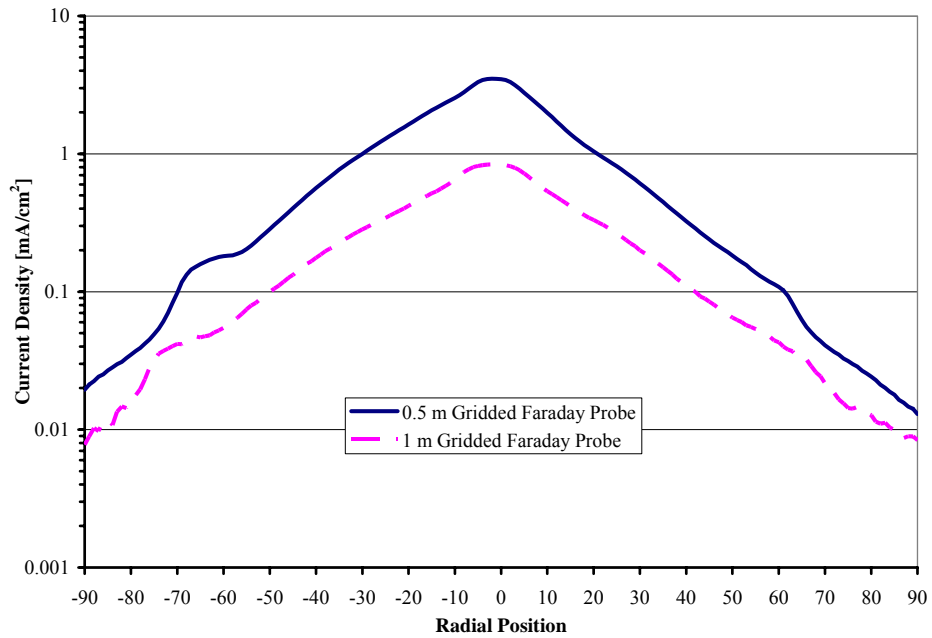


Figure 4-50: Two-stage ion current trace of the NASA-173GT at 200 V, propellant flow rate of 10 mg/s, and  $I_d$  of 15 A.

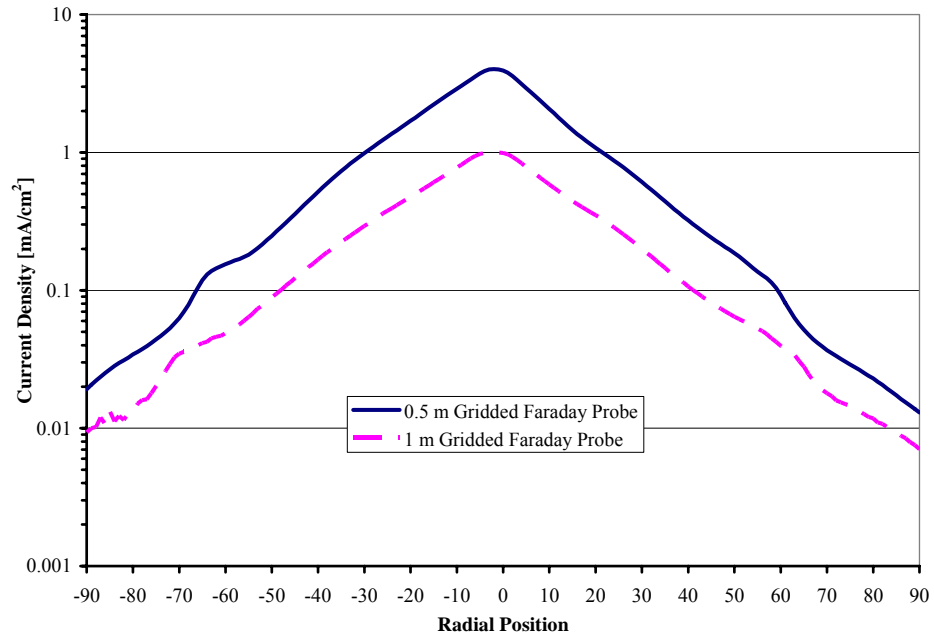


Figure 4-51: Two-stage ion current trace of the NASA-173GT at 300 V, propellant flow rate of 10 mg/s, and  $I_d$  of 15 A.

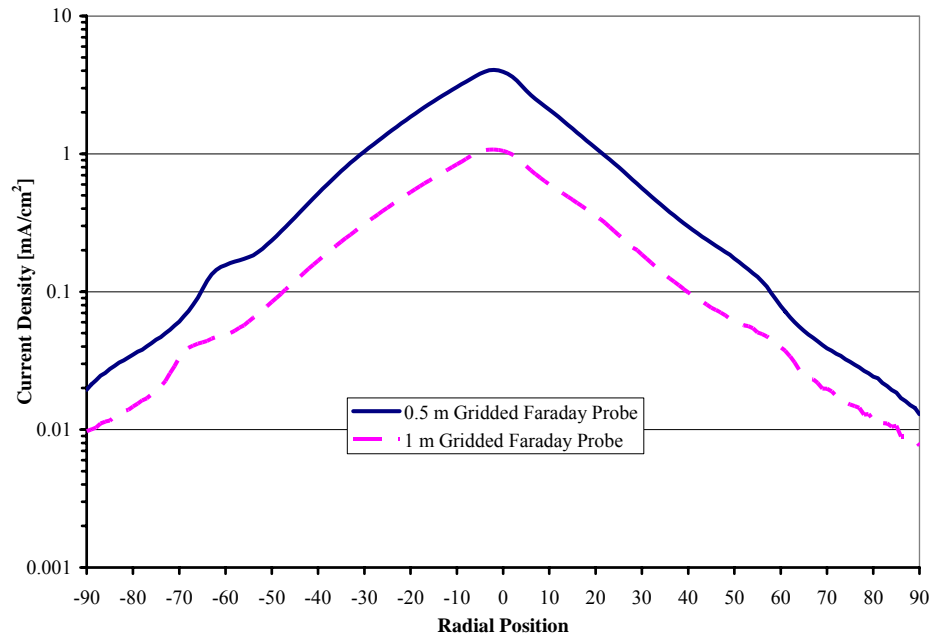


Figure 4-52: Two-stage ion current trace of the NASA-173GT at 400 V, propellant flow rate of 10 mg/s, and  $I_d$  of 15 A.

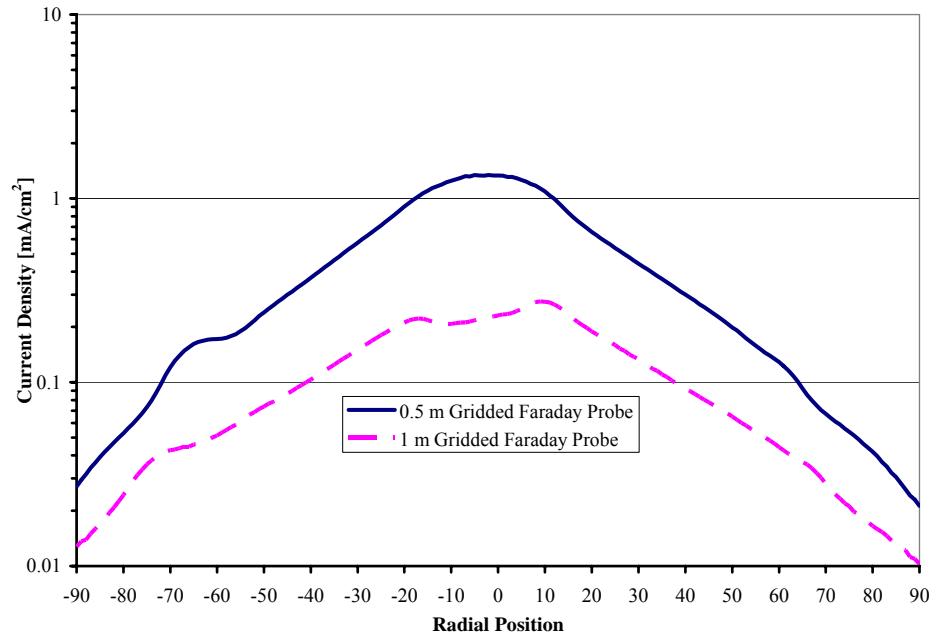


Figure 4-53: Two-stage ion current trace of the NASA-173GT at 100 V, propellant flow rate of 10 mg/s, and  $I_d$  of 25 A.

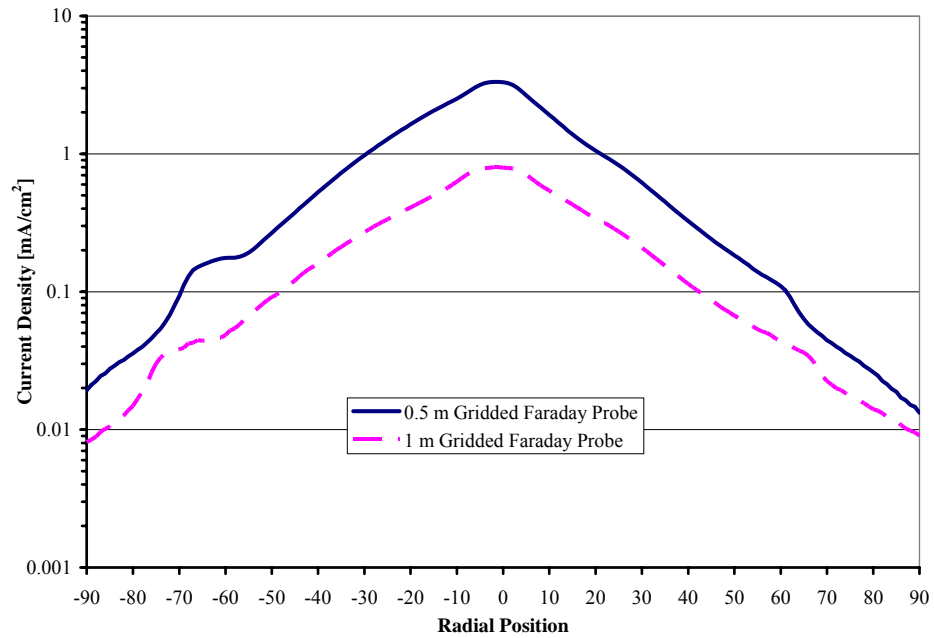


Figure 4-54: Two-stage ion current trace of the NASA-173GT at 200 V, propellant flow rate of 10 mg/s, and  $I_d$  of 25 A.

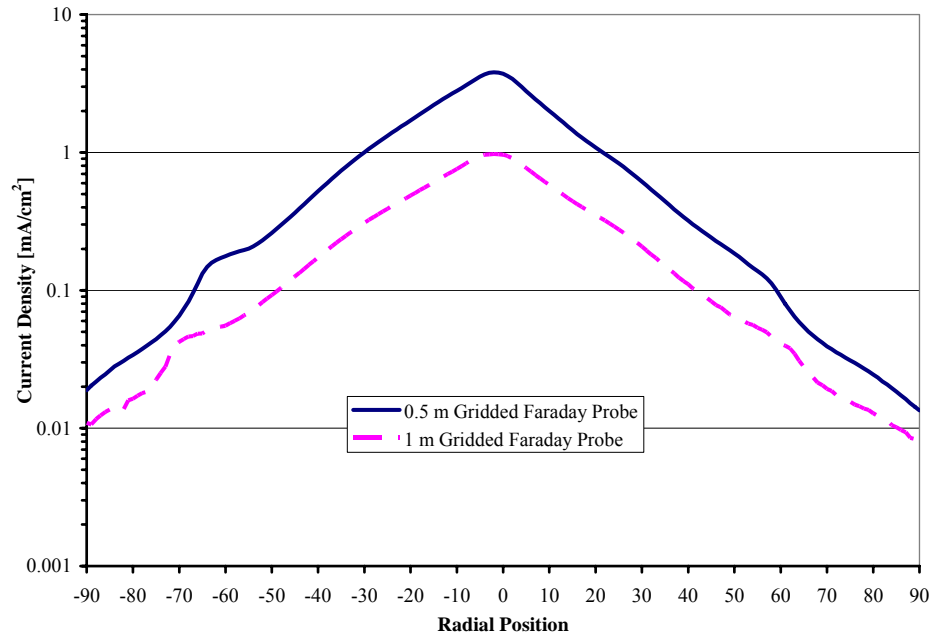


Figure 4-55: Two-stage ion current trace of the NASA-173GT at 300 V, propellant flow rate of 10 mg/s, and  $I_d$  of 25 A.

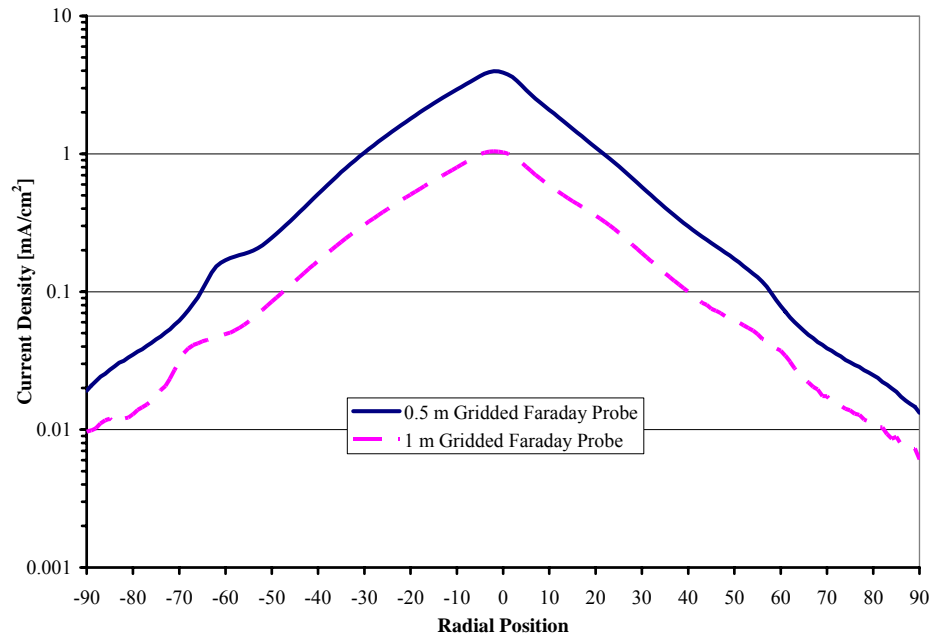


Figure 4-56: Two-stage ion current trace of the NASA-173GT at 400 V, propellant flow rate of 10 mg/s, and  $I_d$  of 25 A.

### 4.6.3 Ion collector bias study

The biasing of the ion collector plate was examined by adjusting the collector potential from 0 to 50 V to study the influence of repelling ion energies up to 50 eV. The ion collector biasing study was conducted with the NASA-173GT in a two-stage configuration operating at 300 V acceleration potential and anode propellant flow rate of 10 mg/s. The results of the bias study for the gridded Faraday probes located at the radial positions of 0.45 m and 0.95 m are presented in Figure 4-57 and Figure 4-58, respectively.

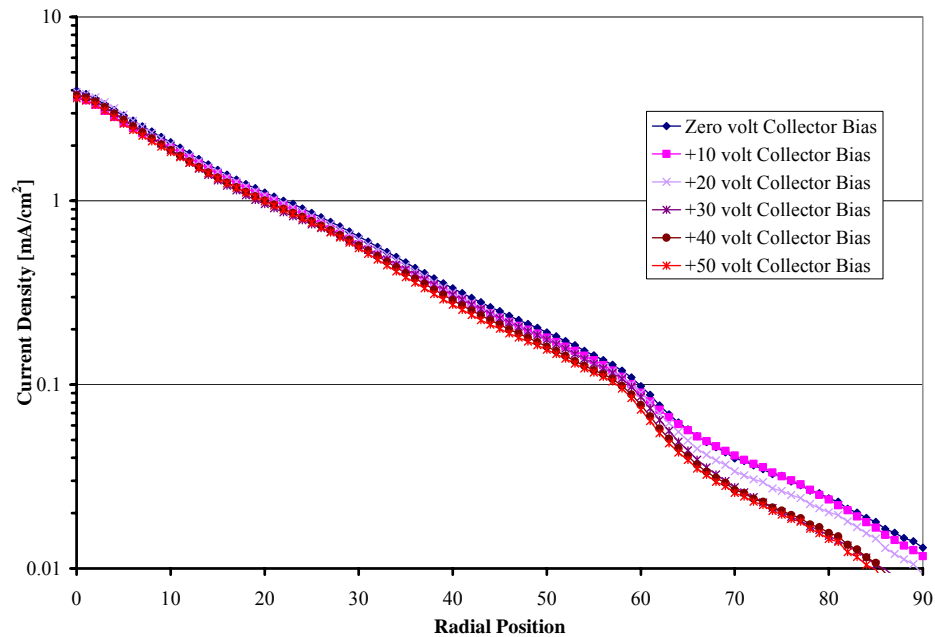


Figure 4-57: Gridded Faraday probe bias study for an ion collector plate ranging from 0 to +50 V at the 0.45 m radial sweep location.

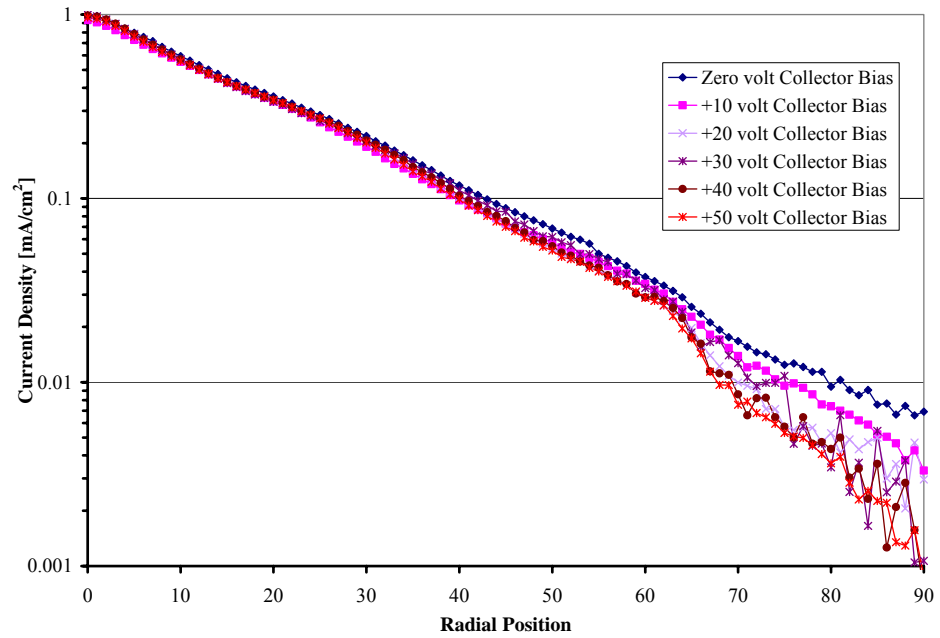


Figure 4-58: Gridded Faraday probe bias study for an ion collector plate ranging from 0 to +50 V at the 0.95 m radial sweep location.

## **Chapter 5 ANALYSIS AND DISCUSSION**

The results of the NASA-173GT characterization presented in Chapter 4 will be discussed in detail in this chapter. The influence of the applied magnetic field of the Hall acceleration stage will be discussed in Section 5.1 and the performance of the ionization stage will be discussed in Section 5.2. The performance of the NASA-173GT in both single-stage and two-stage configurations will be examined in Section 5.3. The plasma plume characterization of the NASA-173GT thruster will be discussed and compared to the performance results of the thruster in Section 5.4.

### **5.1 Applied magnetic field**

The applied magnetic field topology of a Hall thruster is one of the fundamental attributes responsible for the high performance levels of current SOA Hall thruster devices [89], as discussed Section 1.2.2. The NASA-173GT acceleration stage was comprised of a Hall thruster magnetic circuit with allowances for coupling to an electron bombardment ionization source. The magnetic field generated by the magnetic circuit of the acceleration stage was measured with a Hall probe, as described in Section 3.2.5, to confirm the magnetic field topology predicted during the design phase of the NASA-173GT. The results of the magnetic field mapping of the NASA-173GT were presented in Figure 4-1 through Figure 4-5. A comparison of the normalized centerline measured

radial magnetic field strength to the radial field strength predicted by the magnetic circuit model indicated a serious flaw with the acceleration stage magnetic circuit (Figure 5-1).

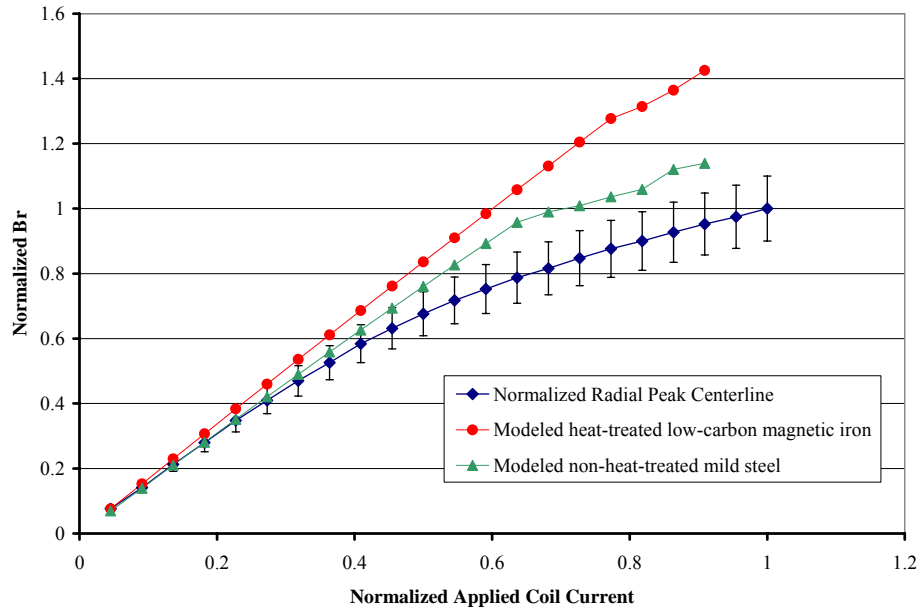


Figure 5-1: A comparison of the measured acceleration stage normalized centerline radial magnetic field, at the axial location of the maximum field, with the modeled results for non-heat-treated and heat-treated iron and coil currents ranging from 0 to 100% of the design maximum.

As it can be seen in Figure 5-1, the measured radial magnetic field strength does not increase linear with applied coil current as predicted. The centerline maximum radial field stops increasing lineally with increasing coils currents between 20% and 40% of the design maximum applied current. These results (Figure 5-1) emphasize a flaw with the acceleration stage magnetic circuit of the NASA-173GT. The accuracy of the three-dimensional magnetostatic code, Magnet 6, has been confirmed a number of times. The error bars associated with the measured Hall probe data, illustrated in Figure 5-1, were

based on a conservative estimate of the accuracy of the probe position with respect to the magnetic circuit. The error in the positioning of the Hall probe was much greater than the inherent error of the probe itself.

The acceleration stage of the NASA-173GT was modeled additionally with non-heat-treated mild steel in which the material BH-curves characteristics were less than the heat-treated low-carbon magnetic iron used in the fabrication of the thruster, as illustrated in Figure 2-12. The results of modeling the acceleration stage with the lower quality iron indicated that by changing the material properties of the magnetic circuit the centerline maximum radial magnetic field begins to approach the measured field results of the NASA-173GT, as shown in Figure 5-1.

Analysis of the chemical composition of the NASA-173GT magnetic circuit iron indicated a large contamination of carbon. The carbon contamination was approximately three times the maximum carbon content specified by the ASTM 848-01 material standard for low-carbon magnetic iron, and fifty times greater than what has been observed in the raw material supplied by the vendor for previous thrusters. The carbonation issue was tracked down to be the result of an improper heat-treatment of the magnetic circuit material. The heat-treatment of the magnetic iron was conducted by placing the raw iron on a graphite stand. Cross-contamination of carbon to the iron components occurred during the high temperature phase of the heat-treatment. Due to timing and funding issues, and the non-accountability of the thruster fabricator<sup>35</sup>, the

---

<sup>35</sup> The NASA-173GT fabricator claimed that the potential of cross-contamination issues was not specified in the contract and that they were not responsible for faulty components.

NASA-173GT operational envelope was compromised before the beginning of the thruster characterization.

The ability of a Hall thruster to achieve efficient and stable operation at elevated acceleration potentials has been found to be proportional to the applied radial magnetic field. The NASA-173Mv1<sup>36</sup> and the NASA-173Mv2 performance evaluations indicated that the relationship between the applied voltage and magnetic field can be described as a power law scaling [64, 89], ranging from 0.5 to 1.5. This power law scaling depended on the propellant flow rate for efficient and stable operation with the following expression:

$$\frac{B_{r\max}}{B_0} \approx V_{\text{accel}}^{0.5 \rightarrow 1.5}, \quad \text{Eqn. 5-1}$$

where  $B_{r\max}$  is the centerline maximum radial magnetic field and  $B_0$  is the required radial magnetic field at 300 V thruster operation. Examining the significance of Equation 5-1 and the measured radial magnetic field of the NASA-173GT, presented in Figure 5-1, the maximum efficient acceleration voltage of the NASA-173GT should be approximately 500 to 600 V. The actual voltage limitation of the NASA-173GT was also found to be dependent on thermal issues and physical characteristics of the thruster, which will be discussed later in Section 5.3.5.

---

<sup>36</sup> The NASA-173Mv1 thruster and the NASA-173GT acceleration stage shared similar applied magnetic field topologies and physical characteristics.

One of the primary differences between the heat-treated low-carbon magnetic and the non-heat-treated mild steel was illustrated in Figure 2-12. The non-heat-treated mild steel will reach saturation, at a lower applied field, than the heat-treated magnetic iron. The design of the magnetic circuit of the NASA-173GT acceleration stage required the magnetic circuit to operate at a higher permeability, in regards to the heat-treated magnetic iron, to reach the full potential of the thruster design. The magnetic circuit design of the ionization stage of the NASA-173GT did not require the same performance level as the acceleration stage circuit. The carbon contamination of the ionization stage magnetic circuit components did not hinder the desired performance sought during the design phase.

## **5.2 Ionization stage**

The ionization stage of the NASA-173GT was fitted with a transparent ion collection grid in an effort to understand the general performance of the ionization stage prior to the full thruster investigation. The extractable ion current from the ionization stage, as a function of power, was acquired by applying an increasing negative bias, with respect to the ionization cathode, to the collector grid until ion saturation occurred, as described in Section 3.2.4. The ionization stage characterization was conducted before the two-stage performance characterization of the NASA-173GT, thus only a limited amount of operating points were examined. The total anode propellant flow rate of 5 mg/s of xenon for various combinations of distributed propellant flow between the anode plenum and the ionization cathode were investigated. The applied magnetic field

topology in the ionization stage was also varied during the ionization stage characterization. A photograph of the operation of the NASA-173GT ionization stage is shown in Figure 5-2.



Figure 5-2: The operation of the ionization stage of the NASA-173GT with ion collection grid viewed from downstream.

Figure 4-6 illustrated the ion production cost as a function of ionization stage power. As expected from published ion thruster references [120], the ion production cost decreased exponentially with increasing ionization stage power. The lowest ion production cost of 210 W/A occurred at approximately 580 W of power. The ionization stage operating points, similar to those experienced during the thruster two-stage characterization, had an ion production cost ranging from 750 to 210 W/A.

As seen with previous ion thruster ionization stage characterizations [120], the available ion current for extraction increased with current for the NASA-173GT, illustrated in Figure 5-3.

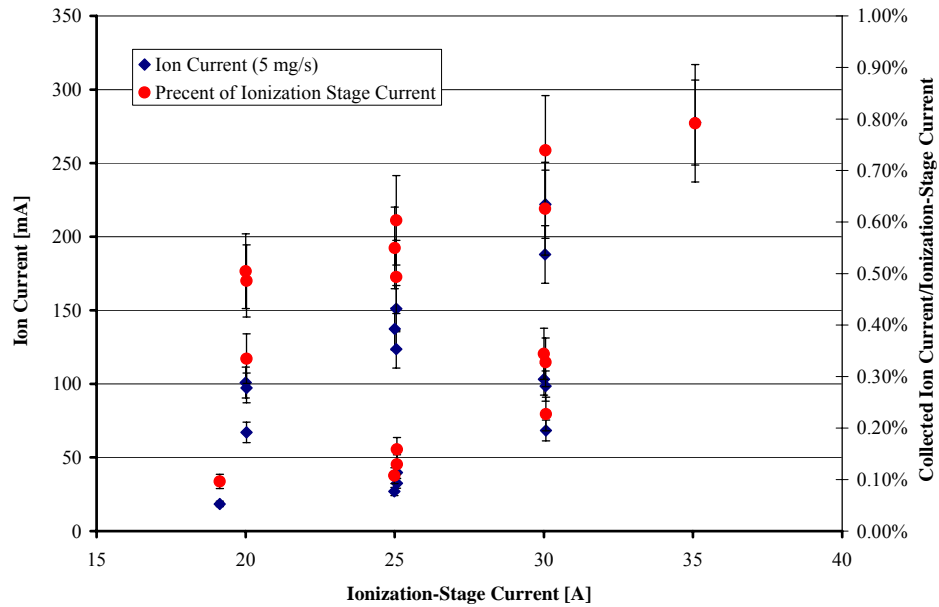


Figure 5-3: Ion current and ion current fraction as a function of ionization stage current.

The spread in the available ion current, at each ionization stage current set point, was due to various combinations of propellant distribution between the anode plenum and the cathode, and the applied magnetic field topology. A minimal propellant flow rate of 2 mg/s through the ionization stage cathode resulted in the highest available ion current for extraction into the acceleration stage. As well, the results presented in Figure 5-3, indicated the electromagnetic coil current set points that would provide the greatest amount of ions for extraction.

Coupling the Hall acceleration stage ionization processes with the ionization stage processes suggest that the results gathered in this section served only as a guide line for beam extraction characterization of the NASA-173GT. Therefore, initial results obtained during the ionization stage characterization were used as a starting point for the two-stage performance investigation.

### 5.3 Thruster performance

The performance characterization of the NASA-173GT was conducted in vacuum facility 12 at NASA GRC on a high fidelity EP thrust stand described in Section 3.2.1. The NASA-173GT thruster was successfully operated in both single- and two-stage configurations with stable ion beam extraction. A photograph of ion beam extraction of the NASA-173GT, in a two-stage configuration, is shown in Figure 5-4.

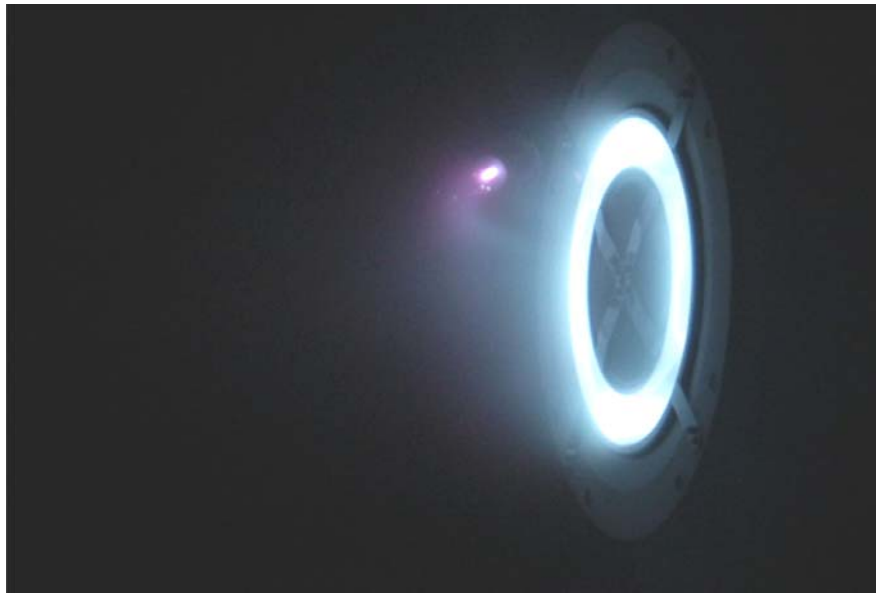


Figure 5-4: The ion beam extraction of the NASA-173GT operating in two-stage configuration.

The performance results of the NASA-173GT operating in single-stage and two-stage configurations are discussed in Section 5.3.1 and 5.3.2, respectively. Comparisons of the NASA-173GT performance in single- and two-stage configurations are discussed in Section 5.3.4. Limitations to the NASA-173GT efficient operation, including thermal effects and thruster design, are described in Section 5.3.5.

### 5.3.1 Single-stage

The single-stage performance characteristics were presented in Figure 4-7 through Figure 4-14 for propellant flow rates of 5 mg/s and 10 mg/s on xenon and acceleration voltages ranging from 100 to 600 V<sup>37</sup>. Single-stage performance was obtained by disconnecting the ionization stage power supplies and allowing the ionization cathode to float. The ionization stage electromagnet coils were not used during the single-stage experiments. During single-stage operation 2 mg/s of xenon propellant was provided through the non-operating ionization cathode. The remainder of the total anode propellant flow was injected through the anode plenum.

Anode efficiency as a function of applied voltage is shown in Figure 5-5 for flow rates of 5 and 10 mg/s. The anode efficiency for the 5 mg/s case reached a maximum between 250 to 400 V and decreased with further increases in voltage. The anode efficiency for the 10 mg/s case reached a maximum at 300 V. Efficiency remained constant as the voltage was increased further for the 10 mg/s case. This difference was

---

<sup>37</sup> The NASA-173GT operation envelope was limited to 500 to 600 V as a consequence of a contaminated acceleration stage magnetic circuit, which was limited to 40% of the designed maximum applied field.

attributed to the higher propellant density at the 10 mg/s operating point. The higher propellant flow rate was thought to increase the neutral density in the Hall acceleration stage improving the Hall stage ionization efficiency and decreasing the electron leakage across the applied field.

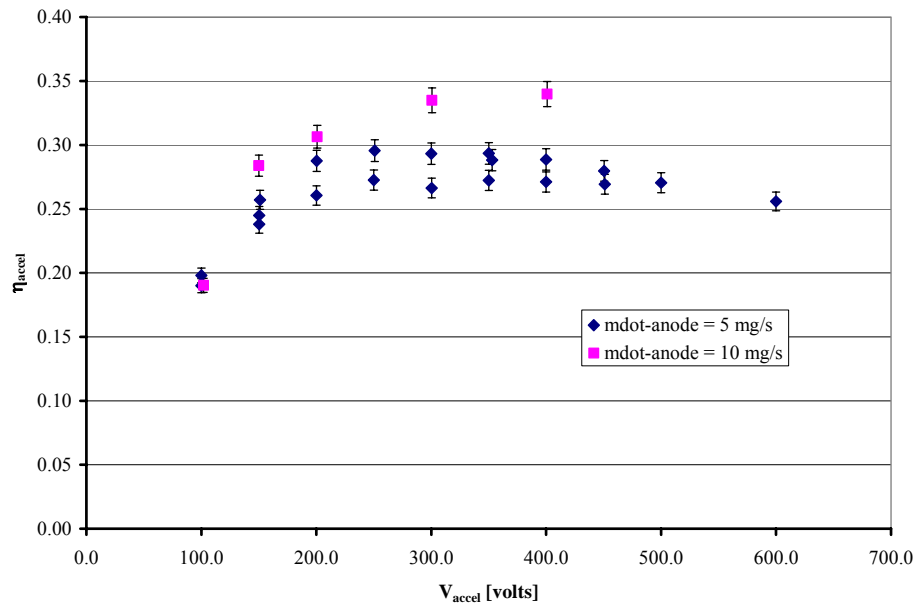


Figure 5-5: Single-stage anode efficiency as a function of acceleration potential for anode flow rates of 5 and 10 mg/s.

SOA Hall thrusters operating on xenon exhibit a linear relationship between anode propellant flow rate and discharge current at nominal operating conditions [60]. This relationship for SOA Hall thrusters is slightly less than or close to unity, as illustrated in Figure 5-6 with the results of the NASA-173Mv2 [64]. Comparing the discharge current to the flow rate gives an indication of the effectiveness of the thruster to efficiently ionize and accelerate the propellant, while simultaneously impeding axial electron current. Figure 5-6 shows the ratio of the acceleration current to the anode

propellant flow rate, expressed in terms of equivalent current, as a function of voltage for the 5 mg/s and 10 mg/s cases.

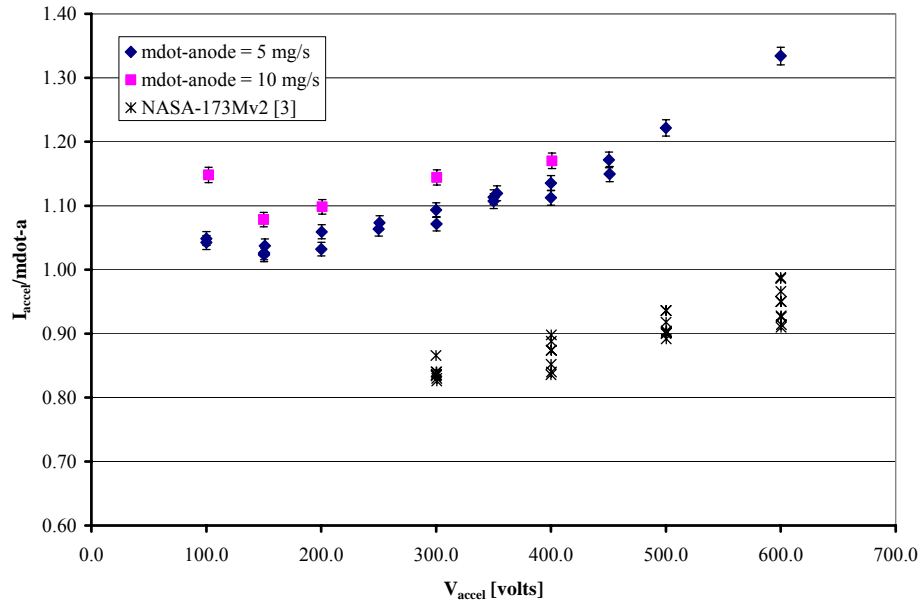


Figure 5-6: The ratio of the acceleration current to the total anode propellant equivalent current as a function of acceleration voltage at propellant flow rates of 5 mg/s and 10 mg/s in single-stage operation mode compared to the NASA-173Mv2 [64].

For the 5 mg/s case, this ratio increased for voltages above 150 V, as illustrated in Figure 5-6. These data in conjunction with the efficiency data shown in Figure 5-5 indicated electron leakage current was increasing with voltage since the efficiency decreased above 150 V. If the efficiency continued to increase with  $I_{\text{accel}}/\dot{m}_{\text{anode}}$ , it would indicate that the ion current was increasing with acceleration voltage. Similar results can be seen with the 10 mg/s case with only a slight difference in that the acceleration efficiency was holding steady while the  $I_{\text{accel}}/\dot{m}_{\text{anode}}$  ratio was increasing.

This conclusion was substantiated by the results from the gridded Faraday probe as subsequently discussed in Section 5.4.2.

The specific impulses obtained from single-stage operation at total anode propellant flow rates of 5 mg/s and 10 mg/s are presented in Figure 5-7. The results in Figure 5-7 were compared to the theoretical specific-impulse for a singly ionized propellant and a corrected theoretical specific impulse that accounts for charge, voltage, current, and propellant utilization efficiencies discussed in Section 1.2.2. The specific impulse results of the NASA-173GT were below the theoretical specific impulse curve. The corrected specific impulse, calculated based on the results measured with the **ExB** and gridded Faraday probes at the 400 V and 10 mg/s single-stage operating point, matched the measured specific impulse results. This corrected specific impulse indicated the NASA-173GT was hampered by a large electron leakage current ranging from 55% to 35% of the acceleration current and large voltage loss of approximately 120 V.

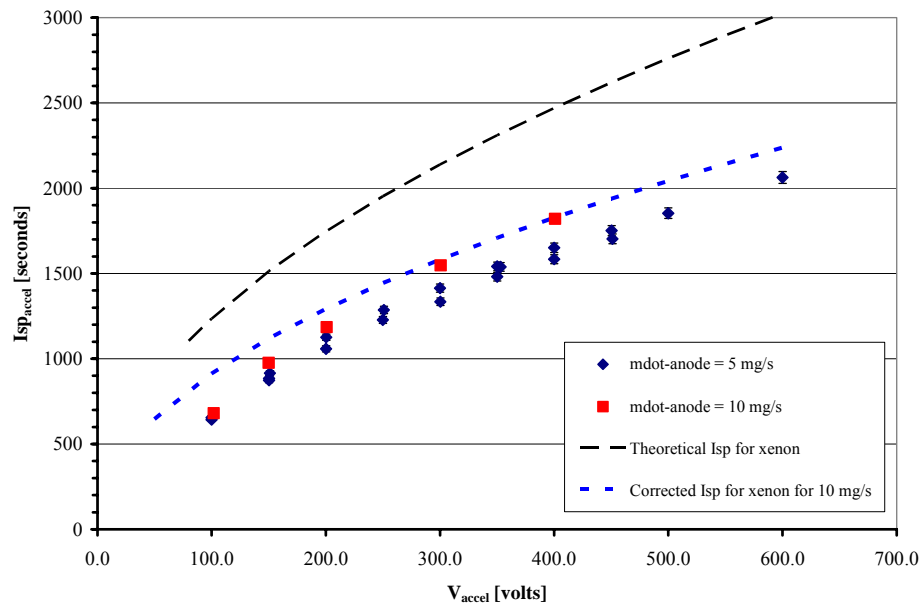


Figure 5-7: The single-stage specific-impulse results for 5 and 10 mg/s propellant flow rates compared to a theoretical and corrected specific-impulse calculation for the 400 V and 10 mg/s measured utilization efficiencies.

Recent high-voltage Hall thruster research at NASA GRC on the NASA-173Mv1 and v2 has shown that electrons, from the discharge cathode, leaking across the magnetic fields represent one of the major efficiency losses for Hall thruster devices [64]. The leakage of the electrons across the applied magnetic field was caused by several factors including non-ionizing electron-neutral collisions [147] and near wall conductivity due to interaction of the electrons with the walls [105]. As discussed in Section 2.1.2, the formation of a plasma lens magnetic field topology assisted in achieving efficient high-voltage Hall thruster operation. A plasma lens field topology reduced excessive wall current from developing with the establishment of an electron pressure gradient near the channel walls. The interface region of the NASA-173GT ionization and acceleration stages and the requirements of the acceleration stage magnetic circuit resulted in a

compromise in the design of the thruster. The placement of four flux shunts, and corresponding BN shields, in the acceleration stage of the NASA-174GT was believed to have a minimal effect on the operation of the thruster. However, after initial beam extraction of the NASA-173GT was accomplished, the faces of the BN shields perpendicular to the direction of the Hall current<sup>38</sup> began to glow from electron collisions. A photograph of the flux shunt shields glowing from Hall current electrons is presented in Figure 5-8.

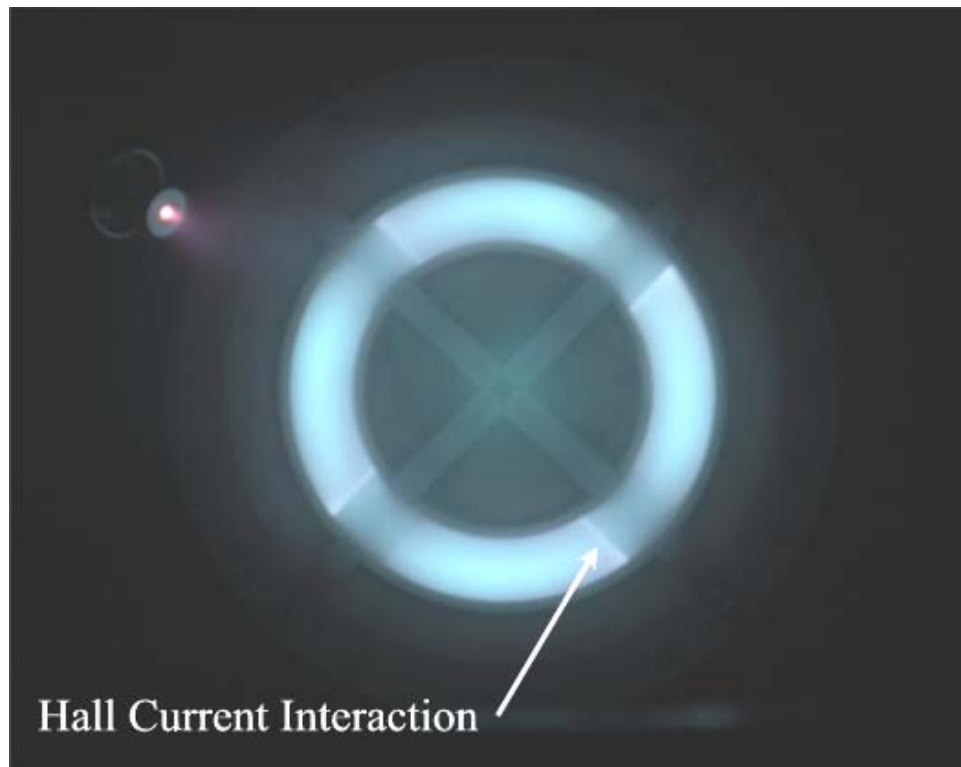


Figure 5-8: A photograph of the NASA-173GT operating in single-stage configuration that illustrates the interaction of the Hall current with the BN flux shunt shields.

---

<sup>38</sup> A detailed discussion of a Hall thrusters Hall current is presented in appendix B

As illustrated in Figure 5-8, the interaction of the acceleration stage Hall current with the BN flux shunt shields leads to the belief that a large percentage of the Hall current was interacting with the internal structure of the thruster. This interaction was believed to be the cause of the observed high electron leakage current determined from the gridded Faraday probe results in Section 5.4.2. As well, the axial location of the four flux shunts and their proximity to the predicted ion density field (Figure 2-7) was in hindsight a poor decision. As the results indicate the large electron leakage current caused by the Hall current interaction with the flux shunts overshadowed any benefits of the shorter channel.

The applied magnetic field topology of the NASA-173GT was similar to those incorporated in successful high-voltage and high-power NASA Hall thrusters. However, the applied magnetic field strength required an increase with the operating potential of the thruster, as discussed in 5.1. The magnetic circuit of the NASA-173GT acceleration stage was estimated to be limited to approximately 500-600 V operation. Combining the voltage limitation of the magnetic circuit and the observed Hall current interaction with the flux shunt shields, the large acceleration efficiency drop observed with the NASA-173GT were the results of the physical design and properties of the thruster. Improved NASA-173GT design possibilities will be discussed in Section 6.3.

The acceleration stage current oscillations for the 5 mg/s and the 10 mg/s, illustrated in Figure 4-10 and Figure 4-14, indicated that the NASA-173GT with the plasma lens magnetic field topology had similar characteristics as NASA Hall thrusters. The acceleration current for the 5 mg/s propellant flow rate oscillated at a frequency of

17 kHz and a peak-to-peak spread of approximately 3 A. The acceleration current for the 10 mg/s propellant flow rate oscillated at a frequency of 33 kHz and a peak-to-peak spread approximately 3 A.

### **5.3.2 Two-stage**

The two-stage performance characteristics, presented in Figure 4-15 through Figure 4-22, were measured for total anode propellant flow rates of 5 and 10 mg/s at acceleration voltages of 100 to 600 V, ionization currents of 15 and 25 Amperes, and ionization-stage powers ranging from 100 to 600 W. During two-stage operation, a flow rate of 2 mg/s was provided through the operating ionization cathode. The remainder of the total anode propellant flow was injected through the anode plenum. Two-stage anode efficiency as a function of applied voltage is shown in Figure 5-9 for flow rates of 5 and 10 mg/s. For the 5 mg/s propellant flow rate, the anode efficiency reached a maximum between 200 to 350 V and decreased with increasing acceleration voltage. For the 10 mg/s propellant flow rate, the anode efficiency reached a maximum at 300 V and remained constant for further increases in acceleration voltage.

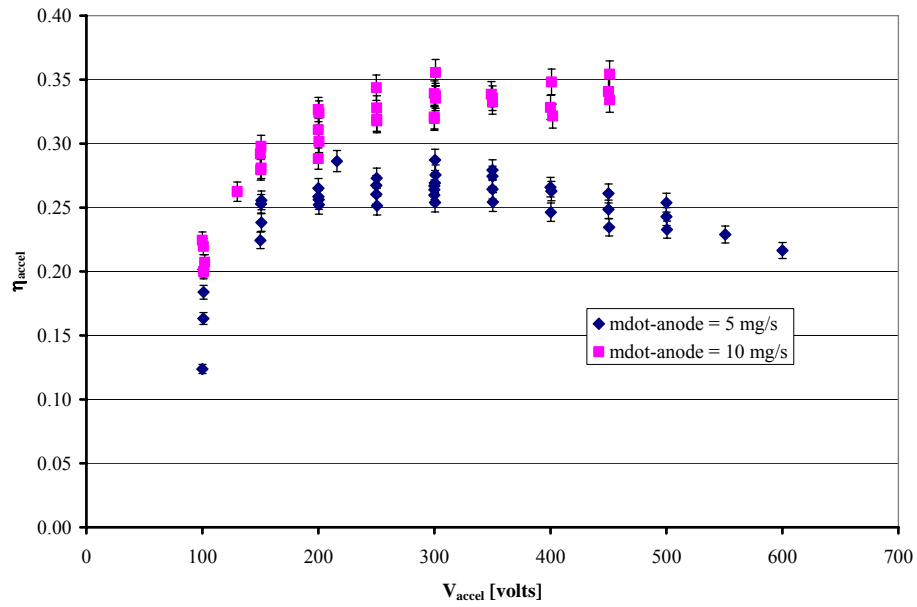


Figure 5-9: Two-stage anode efficiency as a function of acceleration potential for an anode flow rates of 5 and 10 mg/s and an ionization power level between 100 and 600 W.

As with the single-stage data, the ratio of the acceleration current to the anode propellant flow rate was considered. Figure 5-10 illustrates this ratio as a function of the acceleration voltage for 5 mg/s and 10 mg/s cases compared to results of the NASA-173Mv2 [64].

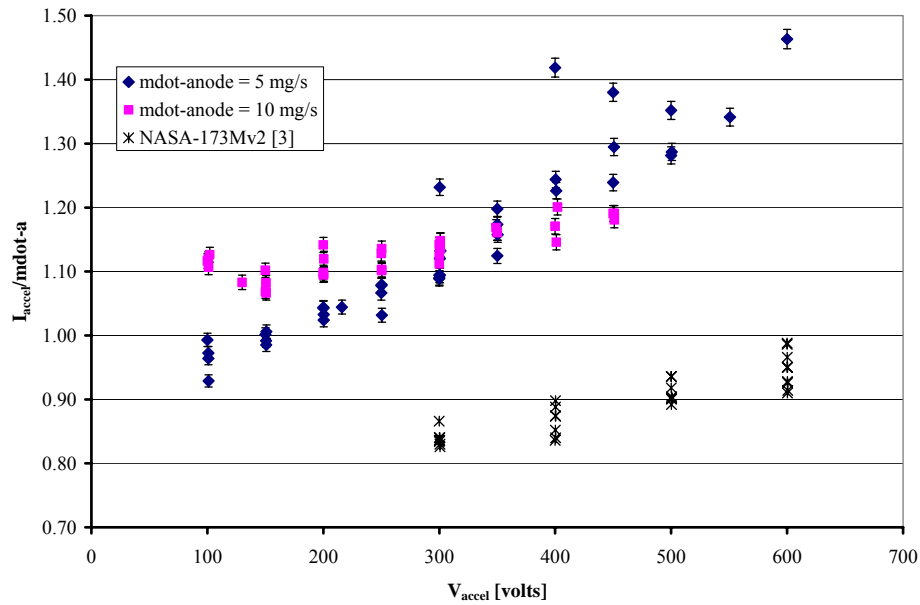


Figure 5-10: The ratio of the acceleration current to the total anode propellant flow rate as a function of acceleration voltage at propellant flow rates of 5 mg/s and 10 mg/s for the NASA-173GT operating in two-stage as compared to the NASA-173Mv2.

For the 5 mg/s case, the ratio of the acceleration current to the anode propellant flow rate increased as the acceleration voltage increased from 100 to 600 V. The anode efficiency of the 5 mg/s two-stage case, shown in Figure 5-9, increased with acceleration voltage between 200 and 350 V, and then decreased with further increases in voltage. The results from Figure 5-9 and Figure 5-10 suggested that these changes in efficiency were the result of electron leakage. Above 350 V, increases in electron leakage dominated the increases in ion current. The interaction of the Hall current with the flux shunt shields again appeared to limit the anode efficiency of the NASA-173GT at higher acceleration potentials. Slightly different results were observed with the 10 mg/s two-stage performance data. The ratio was flat between 100 to 300 V acceleration voltage.

The ratio beyond 300 V acceleration voltage has a slight positive slope, which indicated that the electron leakage current was beginning to over shadow the extracted ion current.

The two-stage specific impulse data for propellant flow rates of 5 mg/s and 10 mg/s, acceleration voltages ranging from 100 to 600 V, and the ionization power levels from 200 to 600 W are presented in Figure 5-11. The theoretical specific-impulse for a singly ionized propellant and a corrected theoretical specific impulse that accounts for charge, voltage, current, and propellant utilization efficiencies discussed in Section 1.2.2 are illustrated in Figure 5-11. The measured specific impulse results of the NASA-173GT were below the theoretical specific impulse curve. The corrected specific impulse, calculated based on the results measured with the **ExB** and gridded Faraday probes, matched the measured specific impulse results. This corrected specific impulse indicated that the NASA-173GT was hindered by a large electron leakage current ranging from 55% to 35% of the acceleration current and a large voltage loss of approximately 131 V. The current utilization efficiencies were approximately the same for both the single- and two-stage thruster operation. These results indicated that the mechanism responsible for the electron leakage current was present in both modes of operation.

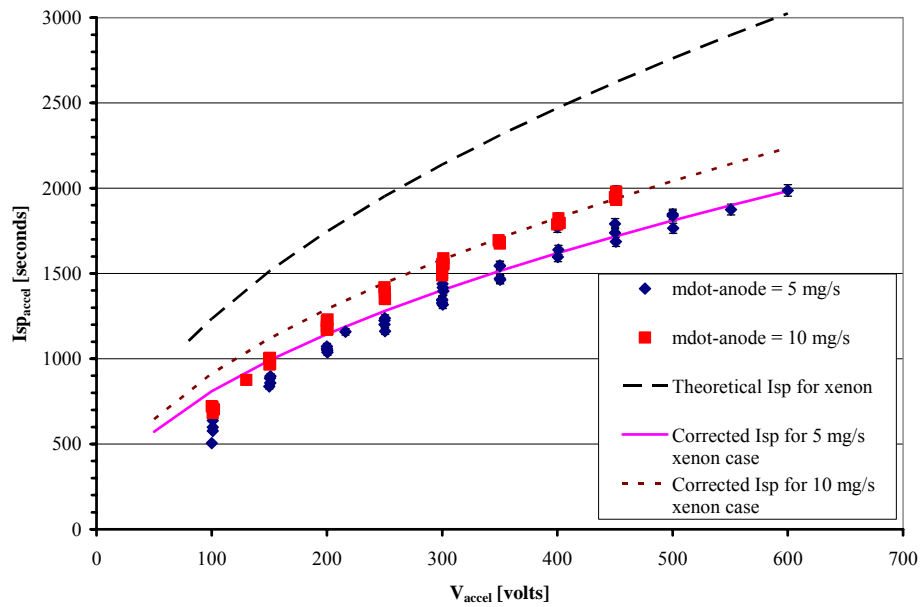


Figure 5-11: The two-stage specific-impulse results for 5 and 10 mg/s propellant flow rates compared to a theoretical and corrected specific-impulse calculation for each case.

The acceleration stage current oscillations for the 5 mg/s and the 10 mg/s, acceleration voltage of 400 V, and ionization power of 500 W are presented in Figure 4-18 and Figure 4-22. The acceleration current oscillations indicated that the NASA-173GT, with the plasma lens magnetic field topology, had similar characteristics as SOA NASA Hall thrusters. The acceleration current for the 5 mg/s propellant flow rate oscillated at a frequency of 24 kHz and a peak-to-peak spread of approximately 2 A. The acceleration current for the 10 mg/s propellant flow rate oscillated at a frequency of 32 kHz and a peak-to-peak spread of 3 A.

The NASA-173GT thruster was designed to operate in two stages with ionization occurring in the Hall acceleration stage and the electron-bombardment ionization stage.

The ionized propellant from the ionization stage was envisioned to augment the ionization mechanism of the Hall stage. It was thought that the additional ionization would improve the operations of the Hall acceleration stage at operating parameters where SOA Hall thrusters are inefficient. However, the NASA-173GT suffered from large electron leakage current and magnetic circuit limitations during two-stage operation as was experienced during single-stage operation. The electron leakage current reduces the efficiency of the thruster, even with the augmented ionization from the ionization stage. A concurrent research effort described in Ref. [64], on a high-voltage single-stage Hall thruster, has shown that the major efficiency limitations at high discharge potentials were due to the electron leakage and that a properly designed magnetic field topology in the discharge channel will improve Hall thruster operation up to a 1000 V. The efficiency results of the NASA-173GT were below the results obtained with the NASA-173 series of thrusters. It was concluded that the electron leakage current and the loss voltage were the primary efficiency reduction mechanisms of the NASA-173GT. If the flux shunts and BN shields were designed out of the NASA-173GT, the thruster should share similar performance values as the rest of the series.

### **5.3.3 Utilization efficiencies**

The utilization efficiencies defined and discussed in Section 1.2.2 were determined with the results from the performance and plume characterization of the NASA-173GT. The results provided by the **ExB** probe, Section 5.4.1, and the gridded Faraday probes, Section 5.4.2, were used to estimate the charge, current, and propellant

utilization efficiencies of the thruster. The acceleration efficiency was redefined in terms of the utilization efficiencies and is expressed as follows:

$$\eta_{accel} = \eta_q \eta_{current} \eta_u \eta_v \cdot \quad \text{Eqn. 5-2}$$

The performance and plume characterization of the thruster provided the acceleration efficiency and estimated charge, current, and propellant utilization efficiencies. The voltage utilization efficiency measurements were not conducted during this investigation. However, the voltage utilization efficiency can be estimated from equation 5-2 given the other factors.

The single-stage plume characterization of the NASA-173GT was not sufficient to determine the current and propellant utilization efficiencies over a range of acceleration voltages. However, **ExB** and gridded Faraday probes results of the single-stage operation at 400 V acceleration potential and 10 mg/s anode flow rate are compared to the two-stage data at similar operating conditions and are presented in Table 5-1.

Table 5-1: Comparison of the single- and two-stage utilization efficiencies.

<i>Thruster Configuration</i>	$V_{accel}$ [V]	$I_{ion}$ [A]	$\dot{m}_{anode}$ [mg/s]	$\eta_{accel}$	$\eta_q$	$\eta_{current}$	$\eta_u$	$\eta_v$
Single-Stage	400	-	10	34%	98%	59%	84%	71%
Two-Stage	400	15	10	35%	97%	62%	82%	71%
	400	25	10	34%	98%	60%	83%	70%

The comparison of the single- and two-stage utilization efficiency results at 400 V and 10 mg/s indicated similar results regardless of the operation mode. The results shown in Table 5-1 indicate the efficiency limiting mechanisms are a result of the acceleration stage.

The acceleration and utilization efficiencies of the NASA-173GT, as a function of the acceleration voltage for two-stage operation at propellant flow rates of 5 and 10 mg/s, are presented in Figure 5-12 through Figure 5-14.

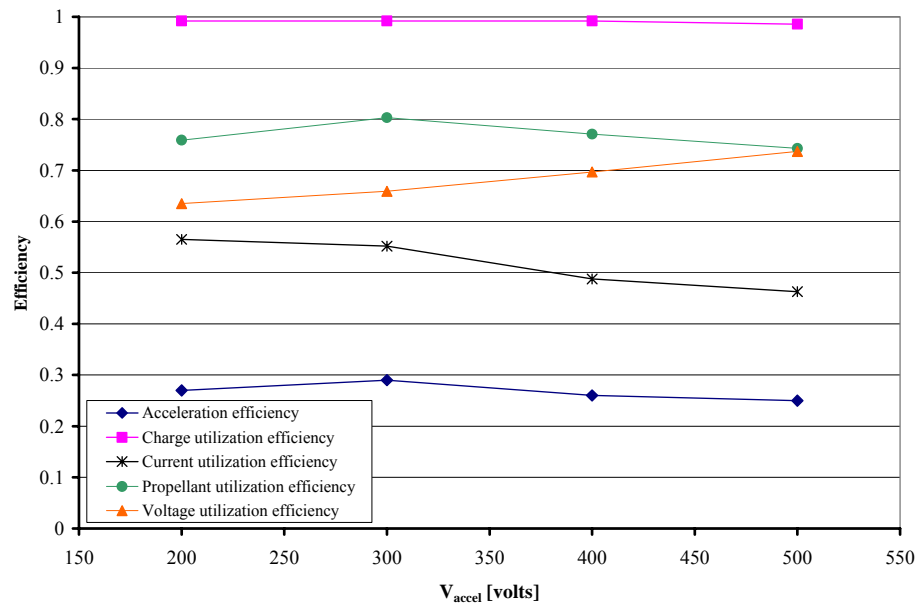


Figure 5-12: The acceleration and utilization efficiencies of two-stage operation at a flow rate of 5 mg/s and an ionization stage current of 15 A.

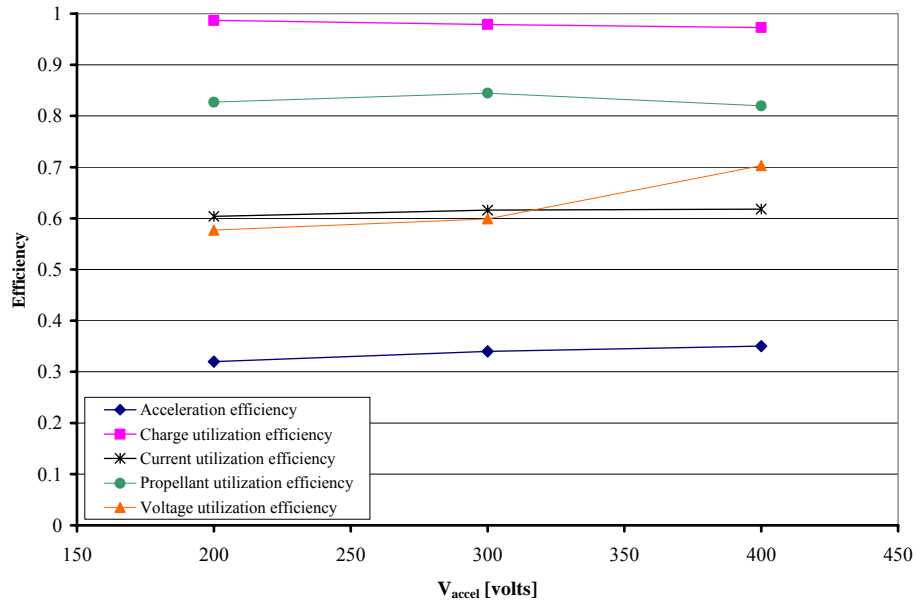


Figure 5-13: The acceleration and utilization efficiencies of two-stage operation at a flow rate of 10 mg/s and an ionization stage current of 15 A.

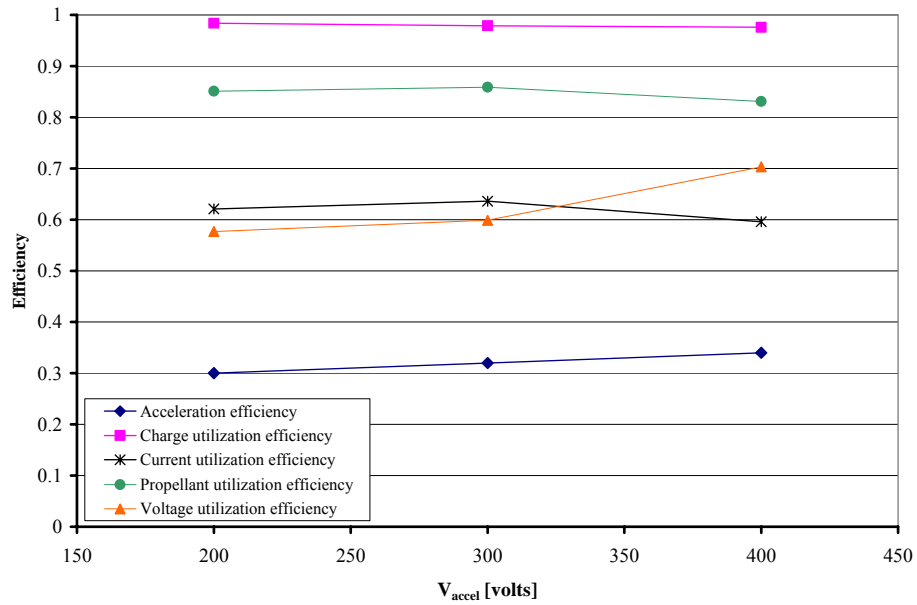


Figure 5-14: The acceleration and utilization efficiencies of two-stage operation at a flow rate of 10 mg/s and an ionization stage current of 25 A.

The utilization efficiencies of the two-stage 5 mg/s operation, Figure 5-12, increased until 300 V at which point the charge, current, and propellant utilization efficiencies decreased with voltage. These decreases of the utilization efficiencies corresponded to the measured trends of the acceleration efficiency of the thruster over the acceleration voltage range. Only the voltage utilization efficiency continued to increase with voltage. The results of the two-stage operation at 10 mg/s indicated approximately the same utilization efficiencies for both ionization stage operating conditions. However, the decrease of both the current and propellant utilization efficiencies, in Figure 5-13 and Figure 5-14, were less than the decreases of the utilization efficiencies calculated for 5 mg/s. These differences in utilization efficiencies for the 10 mg/s data resulted in the acceleration efficiency continuing to increase with voltage. The voltage utilization efficiencies for the 10 mg/s operating conditions continued to increase with voltage as was seen in the 5 mg/s two-stage data.

The single- and two-stage results suggested, in conjunction with the favorable ionization stage characterization results discussed in Section 5.2, that the efficiency limiting effects were a consequence of the Hall acceleration stage of the NASA-173GT. Combining these results, with the performance of the thruster and the observed Hall current interaction with the BN shunt shields, implied that the current and voltage utilization efficiencies limit the performance of the NASA-173GT. A comparison of the single- and two-stage utilization efficiencies indicated that the performance limitations of the NASA-173GT were a result of the Hall acceleration stage.

### 5.3.4 Single- vs. Two-stage

The NASA-173GT was operated in both single- and two-stage configurations at propellant flow rates of 5 and 10 mg/s. The single-stage performance characterization was performed by disconnecting the ionization stage power supplies and allowing the ionization cathode to float. The ionization stage electromagnetic coils were designed not to influence the formation of the magnetic field topology in the acceleration channel; therefore, the coils were not energized during the single-stage experiments. The propellant distribution for single-stage operation was set to 2 mg/s through the cathode and the remainder of the propellant was injected through the anode shell plenum. The two-stage performance characterization was performed for various combinations of propellant distribution between the anode plenum and the ionization cathode, total ionization stage propellant flow rates, applied magnetic field topologies, and ionization stage power levels. A comparison of the single- and two-stage acceleration efficiencies as a function of acceleration voltage at the anode propellant flow rates of 5 mg/s and 10 mg/s are illustrated in Figure 5-15 and Figure 5-16, respectively.

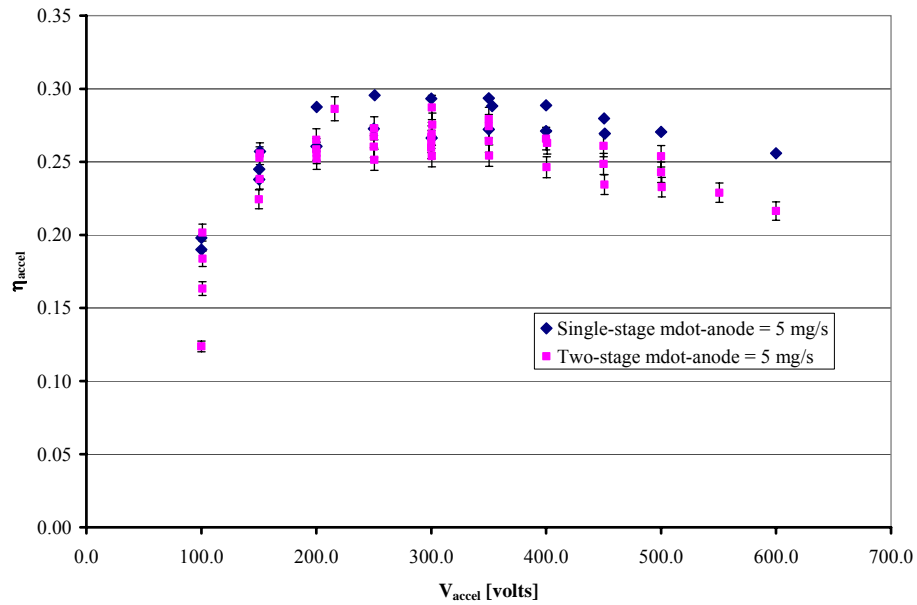


Figure 5-15: Comparison of the single- and two-stage acceleration efficiencies as a function of acceleration potential at 5 mg/s propellant flow rate.

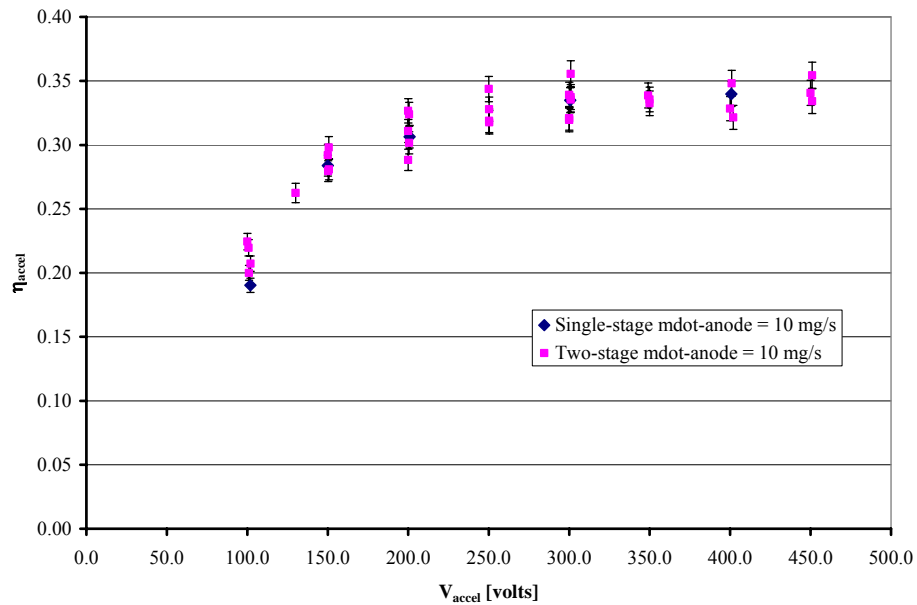


Figure 5-16: Comparison of the single- and two-stage acceleration efficiencies as a function of acceleration potential at 10 mg/s propellant flow rate.

The performance of the NASA-173GT operating in single-stage was slightly improved as compared to the two-stage operation. The thrust-to-acceleration power ratio as a function of acceleration voltage was determined and presented in Figure 5-17 and Figure 5-18 for 5 and 10 mg/s, respectively.

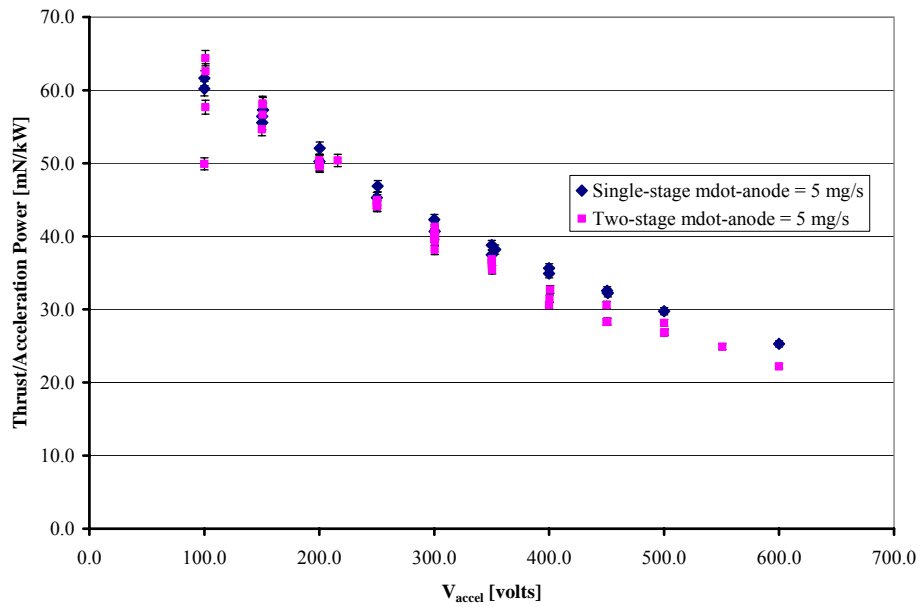


Figure 5-17: The single- and two-stage thrust-to-acceleration power ratios as a function of acceleration voltage for 5 mg/s propellant flow rate.

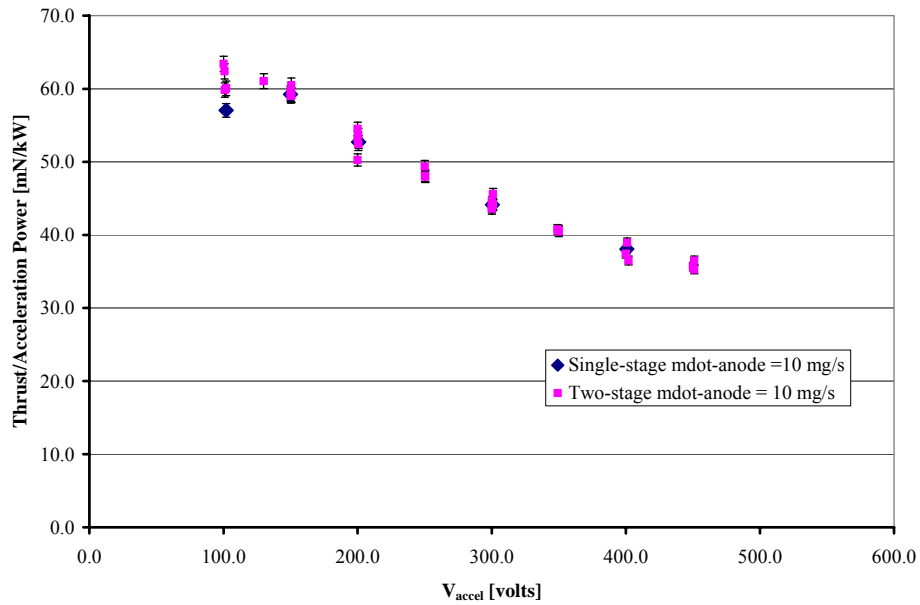


Figure 5-18: The single- and two-stage thrust-to-acceleration power ratios as a function of acceleration voltage for 10 mg/s propellant flow rate.

The thrust-to-acceleration power ratios for the 5 and 10 mg/s propellant flow rates indicated that the NASA-173GT does not gain any observable performance improvements in two-stage configuration over single-stage. The large estimated electron leakage current may be over shadowing any performance increases or losses between the two configurations.

### 5.3.5 Thruster performance limitations

The NASA-173GT performance results indicated that the thruster in both single- and two-stage operations suffered from large electron leakage currents. The magnetic circuit of the acceleration stage was also found to have been contaminated during

fabrication, thereby placing an upper voltage limit on the thruster operational voltages, as discussed in Section 5.1.

A third thruster limitation was discovered during the performance characterization in which the thruster could only be operated for up to 2 hours at a time due to thermal limitations of the magnetic circuit material. Figure 4-23 illustrated the thermal characteristics of the NASA-173GT for a single hour of operation. The measured temperatures of the acceleration stage components were measured at approximately 300° C and were still increasing after an hour of operation. The Curie temperature of the magnetic iron was 770° C. At the highest recorded temperature of approximately 600° C, the NASA-173GT acceleration current would begin to increase steadily regardless of the electromagnetic coil currents. It was concluded that some of the components of the NASA-173GT, the inner magnetic circuit of the acceleration stage, were losing their permeability due to approaching or surpassing the material Curie temperature. The NASA-173GT was envisioned as a laboratory test-bed two-stage thruster, thus thermal considerations were not taken into account during the design phase. The temperature of the inner magnetic circuit of the acceleration stage was continually monitored during the performance and plume characterization of the thruster.

The NASA-173GT operation envelope was limited to 500 to 600 V as a consequence of a contaminated acceleration stage magnetic circuit, as discussed in Section 5.1. The NASA-173GT magnetic field was limited to 40% of the designed maximum applied field. However, the performance of the NASA-173GT, either in single- or two-stage configurations, would not have improved with increased acceleration

potential due to the low current and voltage utilization efficiencies caused by the design of the Hall acceleration stage.

#### **5.4 Plume characterization**

The NASA-173GT was subjected to two forms of plasma diagnostic techniques used in evaluating EP devices. The plasma plume properties were investigated using two gridded Faraday probes at 0.45 m and 0.95 m radial distances from the exit plane of the thruster and an **ExB** probe located 2.04 m downstream of the exit plane. The two gridded Faraday probes were mounted on a probe arm that was connected to a rotation stage, as discussed in Section 3.2.3, such that the ion density profiles could be mapped from  $-90^\circ$  to  $+90^\circ$ . The **ExB** probe was placed on a fixed diagnostic mount, as discussed in Section 3.2.2, downstream of the acceleration channel.

The analysis of the **ExB** probe measurements of the single- and two-stage operation for various acceleration potentials are presented and discussed in Section 5.4.1. The analysis of the gridded Faraday probes are presented in Section 5.4.2 and the difference between single- and two-stage operations for various acceleration potentials will be discussed.

### 5.4.1 Ion species fractions

The theory of **ExB** operation and data analysis was discussed in Section 3.2.2. The raw **ExB** probe measurements for single-stage operation were presented in Figure 4-24 through Figure 4-26 and the two-stage cases in Figure 4-27 through Figure 4-38. The single-stage **ExB** data were taken at a single propellant flow rate of 10 mg/s and acceleration voltages ranging from 200 to 400 V. The two-stage **ExB** data were acquired for 5 and 10 mg/s propellant flow rates, acceleration voltages ranging from 100 to 500 V, and ionization stage currents of 15 and 25 A.

The **ExB** probe responsiveness as a function of acceleration voltage for the single- and two-stage operations at 10 mg/s anode propellant flow rate are presented in Figure 5-19 and Figure 5-20, respectively.

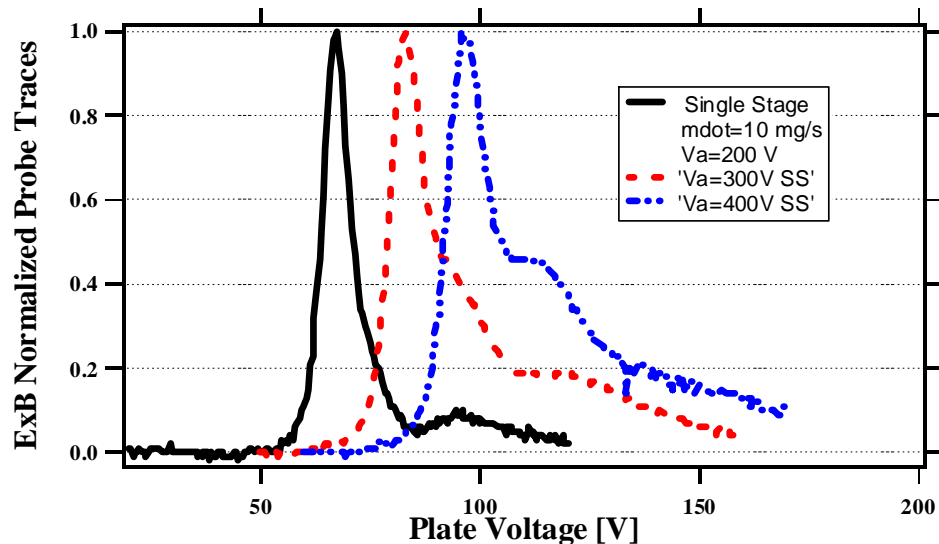


Figure 5-19: The **ExB** responsiveness for single-stage 200, 300, and 400 V acceleration potential data as a function of plate potential.

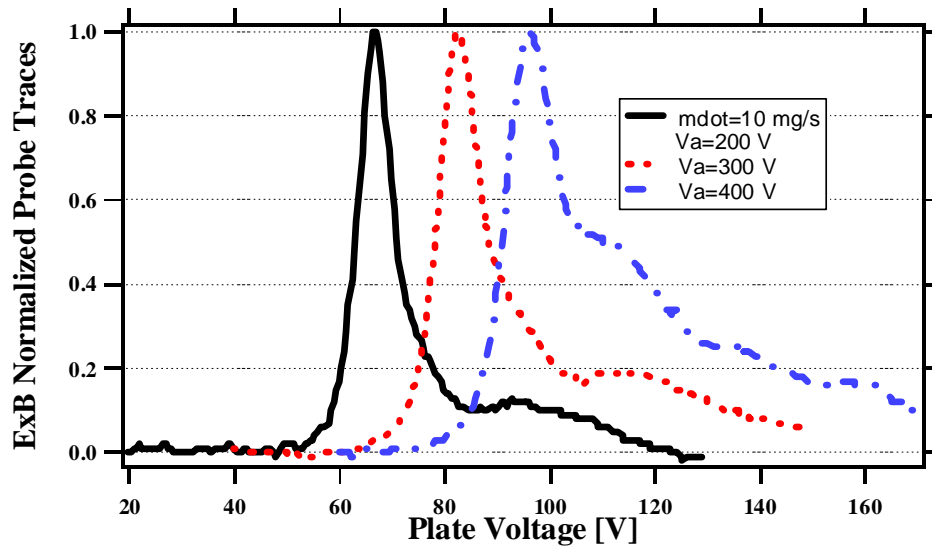


Figure 5-20: The **ExB** responsiveness for two-stage 200, 300, and 400 V acceleration potential data at 10 mg/s propellant flow rate and 15 A ionization stage current as a function of plate potential.

The primary  $\text{Xe}^+$  peaks in Figure 5-19 are separated by **ExB** plate voltages of approximately 16.3 and 13.0 V. These **ExB** plate potential differences corresponded to calculated acceleration potentials of 120 and 126 V. The uncertainty in the **ExB** alignment was determined to be approximately 15% to 30% of the applied acceleration potentials. The lower limit, 15% alignment uncertainty, was calculated based on unpublished ion thruster **ExB** results with the same **ExB** probe. Ion thrusters are capable of generating singly charged ion beam energies at the applied acceleration potential, therefore, the primary  $\text{Xe}^+$  peak was compared to the beam voltage, and a 15% difference was determined to be due to the alignment of the probe components. The upper limit was determined from a comparison of the  $\text{Xe}^+$  peaks for the 200, 300, and 400 V traces in Figure 5-19 and Figure 5-20. The single- and two-stage results indicated a similar alignment uncertainty up to 30%.

The **ExB** probe traces for the single- and two-stage operation yielded distinct  $\text{Xe}^+$  peaks with occasional  $\text{Xe}^{++}$  peaks. The  $\text{Xe}^{+++}$  peaks were not observed in the data gathered with the **ExB** probe, but were incorporated into the calculation of the ion species fractions. The **ExB** probe traces that contained distinctive  $\text{Xe}^{++}$  peaks confirmed that the xenon species **ExB** pass plate voltages follows the  $\sqrt{Z_i}$  relationship between the ion species, therefore measuring the collected ion current at the location  $\text{Xe}^{+++}$  was deemed appropriate. The ion species fractions results for each of the operating cases in single- and two-stage configurations were calculated as discussed in Section 3.2.2.3 and are presented in Table 5-2. The charge utilization efficiencies for the single- and two-stage operating conditions are presented in Table 5-2. A plot of the ion species fractions as a function of acceleration potential for the NASA-173GT in a two-stage configuration is illustrated in Figure 5-21.

The **ExB** ion species fraction results indicated that as the acceleration voltage was increased the production of multiple charged ions increased with a slight decrease of the  $\text{Xe}^+$  fraction. The increase of the multiple charged ions for the NASA-173GT followed a similar trend as was observed in the NASA-173Mv2 for acceleration voltages between 200 and 500 V [64]. The operation of the NASA-173GT in a two-stage configuration did not appear to reduce the amount of multiple ionization events and more importantly did not increase the amount. The increase in multiple ionized propellant with voltage indicated a 0.8% decrease of the charge utilization efficiency ( $\eta_{\text{charge}} = 98.4\%$  to  $97.6\%$ ). The ability to operate the NASA-173GT in a two-stage configuration and at greater

acceleration potentials may have shown a difference over SOA single-stage Hall thrusters.

Table 5-2: The ion species fractions and charge utilization efficiency results for the NASA-173GT in both single- and two-stage configurations.

<i>Thruster Configuration</i>	$V_{accel}$ [V]	$I_{ion}$ [A]	$\dot{m}_{anode}$ [mg/s]	$\zeta_{Xe}^+$	$\zeta_{Xe}^{++}$	$\zeta_{Xe}^{+++}$	$\eta_q$
Single-Stage	200	-	10	96.3%	3.2%	0.5%	98.9%
	300	-	10	92.3%	6.1%	1.6%	97.8%
	400	-	10	93.3%	6.5%	0.2%	97.8%
Two-Stage	200	15	5	97.3%	2.3%	0.4%	99.2%
	300	15	5	96.5%	3.4%	0.1%	99.2%
	400	15	5	96.7%	3.2%	0.1%	99.2%
	500	15	5	95.1%	4.2%	0.7%	98.6%
Two-Stage	200	15	10	95.5%	4.0%	0.5%	98.7%
	300	15	10	92.5%	6.2%	1.3%	97.9%
	400	15	10	89.5%	8.5%	2.0%	97.3%
Two-Stage	200	25	10	95.5%	3.3%	1.2%	98.4%
	300	25	10	92.5%	6.2%	1.3%	97.9%
	400	25	10	91.9%	6.3%	1.8%	97.6%

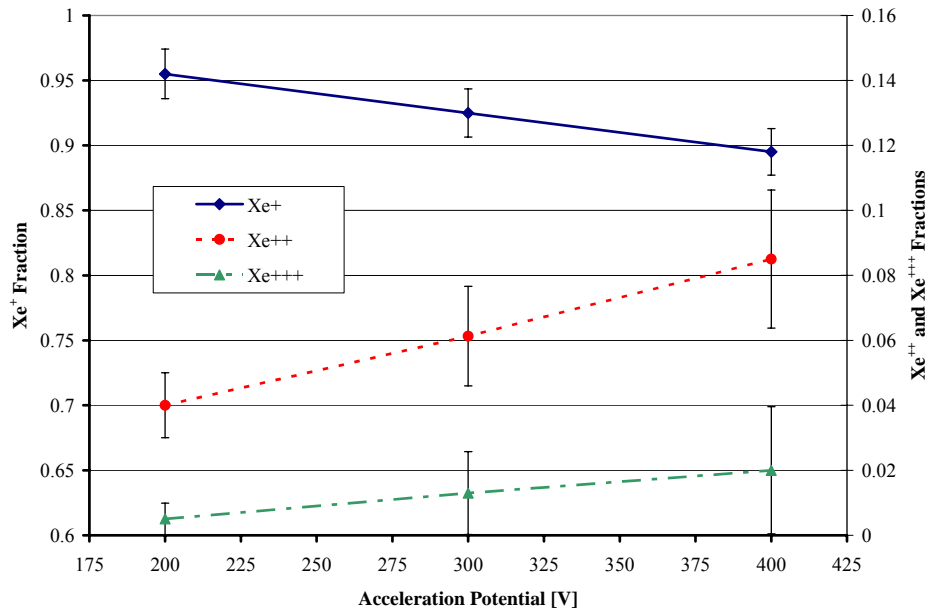


Figure 5-21: The ion species fractions as a function of acceleration voltage for the NASA-173GT operating in a two-stage configuration.

The uncertainties of the **ExB** probe ion species fractions were determined by examining the uncertainty of the applied potential across the plates, the magnitude of the applied magnetic field, the selection of the ion species peaks, the distance between the plates, and the influence of CEX collisions over the axial distance between the thruster and the **ExB** probe. The uncertainty in the ion species fractions was conservatively determined to be  $\pm 2\%$ ,  $\pm 25\%$ , and  $\pm 96\%$  for  $\text{Xe}^+$ ,  $\text{Xe}^{++}$ , and  $\text{Xe}^{+++}$ , respectively.

As the acceleration voltage of the NASA-173GT was increased, the appearance of an additional peak of slightly higher plate pass voltages over the  $\text{Xe}^+$  was observed with the **ExB** probe. The formation of this additional peak was more apparent in the single-stage over the two-stage **ExB** traces at 10 mg/s, as illustrated in Figure 4-24 through Figure 4-26 and Figure 4-33 through Figure 4-38. The two-stage operation at 5 mg/s

propellant flow rate showed no sign of this additional peak, as illustrated in Figure 4-27 through Figure 4-31. The additional peak occurred around an **ExB** plate pass voltage of approximately 111 V and is illustrated in Figure 5-22.

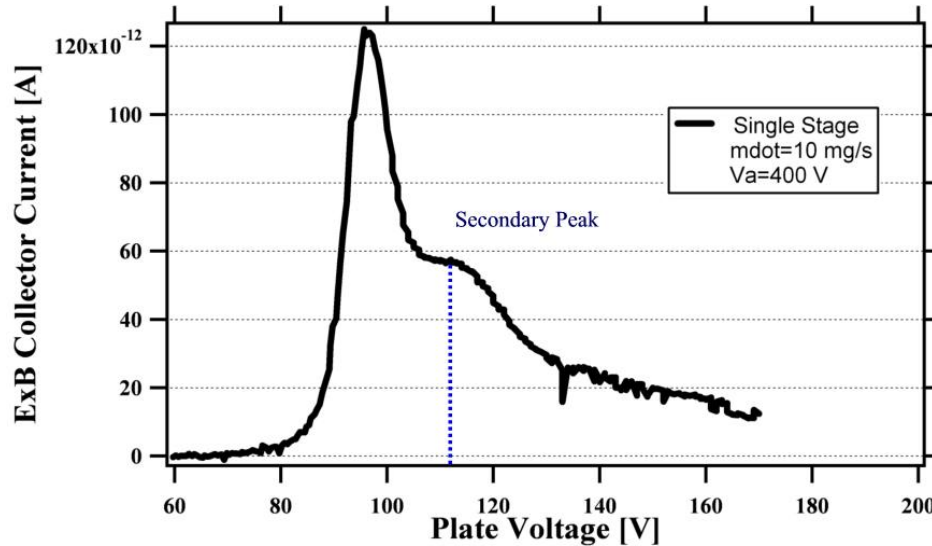


Figure 5-22: **ExB** trace of the NASA-173GT in single-stage mode at 400 V acceleration potential and a propellant flow rate of 10 mg/s with an illustration of the secondary peak.

Recall that the **ExB** probe acts as an ion velocity filter with the capability of resolving different ionized elements and/or compounds that are accelerated in addition to the propellant of the thruster. By examining the primary components of the NASA-173GT thruster to determine what possible materials that could have been ablated and ionized, resulted in two possible candidates. The iron from the anode and magnetic circuit and the BN from the acceleration channel walls. Accounting for the acceleration potential applied to the acceleration stage and the estimated uncertainty in the **ExB** alignment, the BN from the channel walls would appear at **ExB** plate pass voltages ranging from 170 to 235 V if the ions experienced the full acceleration potential. This

calculated pass voltage range does not match the measured secondary peak. The **ExB** plate pass voltage for iron accelerated to the full applied potential would result in **ExB** plate pass voltage ranging between 111 to 153 V. The presence of iron, if accelerated to the full potential of the acceleration stage, could be the cause for this additional peak observed in Figure 5-22. However, to observe traceable amounts of iron with the **ExB** probe significant erosion of the thruster would need to be observed, which was not.

An additional explanation of the secondary peak measured with the **ExB** probe could be the presence of an additional ionization region that forms as the acceleration potential was increased. If all the ionized propellant ions were accelerated to the same potential, the secondary peak illustrated in Figure 5-22 would not correspond to any of the xenon multiple ionization states plate pass voltages. It has been shown that as the acceleration voltage has been increased in Hall thruster devices the ionization and acceleration regions tend to move upstream towards the anode [64]. The movement of the discharge upstream in Hall thrusters is typically accompanied with a physical observation of the expanding erosion band. This phenomenon has been described as a “burn-off” process due to the resemblance of the erosion band burning at discharge voltages greater than 600 V [64]. The NASA-173GT did not exhibit this behavior during the high-voltage operation.

Since this secondary peak has been observed for both the single- and two-stage configurations it is concluded that this peak was the result of the Hall acceleration stage and the 10 mg/s propellant flow rate since the secondary peak was not observed during

the 5 mg/s cases. The secondary peak presence in the **ExB** trace can not be completely explained with the available data and would require further testing to confirm its origin.

#### **5.4.2 Ion density profiles**

The NASA-173GT in single- and two-stage configurations was measured with two gridded Faraday probes located 0.45 m and 0.95 m downstream of the thruster exit. The electron repelling grid was biased to -30 V and the ion collector was biased to +5 V. These voltages were selected based on the measured background CEX floating potential, as discussed in Section 4.6. The ion current density profiles of the NASA-173GT in single- and two-stage configurations were presented in Figure 4-39 through Figure 4-56. The divergence angles and the total ion currents corrected for facility background pressure at 0.45 and 0.95 m probe positions for the single- and two-stage configurations are presented in Table 5-3. Tabulated calculations for the averaged total corrected ion beam currents, and the current and propellant utilization efficiencies from both probes are presented in Table 5-3. The current and propellant utilization efficiencies of the NASA-173GT were determined by averaging the estimated total beam currents from the two gridded Faraday probes. The divergence angle as a function of the acceleration potential and ionization stage currents for the two-stage NASA-173GT operation at propellant flow rates of 5 and 10 mg/s are presented in Figure 5-23 and Figure 5-24, respectively.

Table 5-3: Tabulated results of the gridded Faraday probe investigation of the NASA-173GT.

<i>Thruster Config.</i>	$V_{acce}$ [V]	$I_{accel}$ [A]	$I_{ion}$ [A]	$\dot{m}_{anode}$ [mg/s]	$\beta_{0.45 m}$ [°]	$\beta_{0.95 m}$ [°]	$I_{C-0.45m}$ [A]	$I_{C-0.95 m}$ [A]	$I_{Average}$ [A]	$\eta_{current}$	$\eta_u$
Single-Stage	400	11.8	-	10	41	48	5.59	8.27	6.93	59.0%	83.6%
Two-Stage	200	5.4	15	5	48	57	2.37	3.43	2.90	56.5%	75.9%
	300	5.8	15	5	44	53	2.47	3.67	3.07	55.2%	80.3%
	400	6.0	15	5	45	53	2.41	3.50	2.96	48.8%	77.1%
	500	6.3	15	5	44	51	2.46	3.43	2.95	46.3%	74.3%
Two-Stage	100	4.7	25	5	59	67	1.58	2.20	1.89	60.4%	82.7%
	200	5.4	25	5	48	56	2.23	3.21	2.72	61.6%	84.5%
	300	5.7	25	5	45	52	2.33	3.33	2.83	61.8%	82.0%
	400	6.0	25	5	47	53	2.39	3.38	2.89	62.1%	85.1%
	500	6.3	25	5	44	52	2.45	3.43	2.94	63.6%	85.9%
Two-Stage	100	11.7	15	10	61	72	4.08	5.43	4.76	59.6%	83.1%
	200	11.4	15	10	45	52	5.69	8.08	6.89	56.5%	75.9%
	300	11.7	15	10	42	48	5.68	8.25	6.97	55.2%	80.3%
	400	11.9	15	10	39	45	5.74	8.41	7.08	48.8%	77.1%
Two-Stage	100	11.2	25	10	60	71	3.99	5.30	4.65	46.3%	74.3%
	200	11.1	25	10	45	56	5.60	7.93	6.77	60.4%	82.7%
	300	11.5	25	10	43	49	5.70	8.49	7.09	61.6%	84.5%
	400	11.8	25	10	41	46	5.70	8.25	6.98	61.8%	82.0%

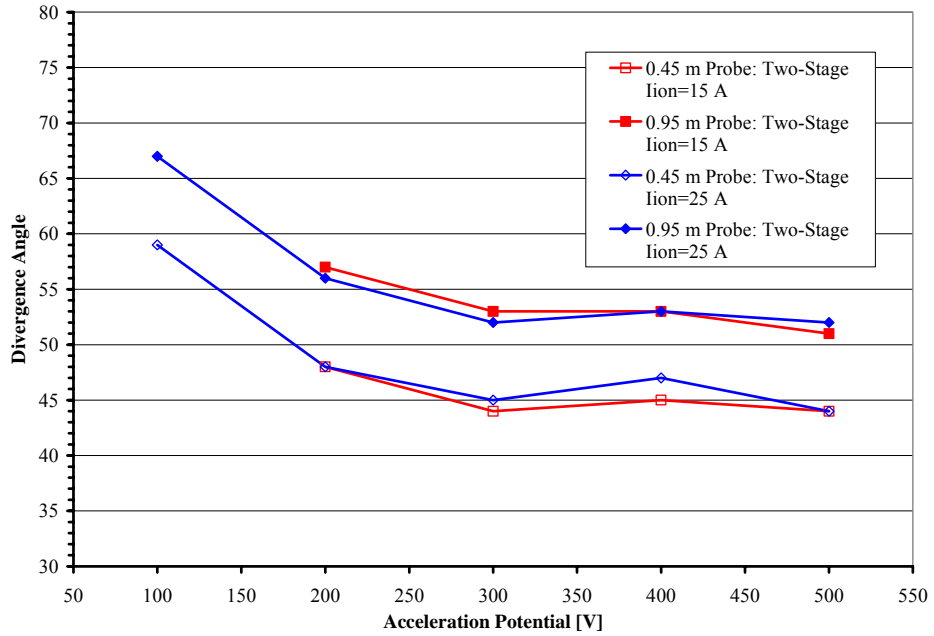


Figure 5-23: The divergence as a function of acceleration potential for 5 mg/s propellant flow rate and ionization stage currents of 15 and 25 A.

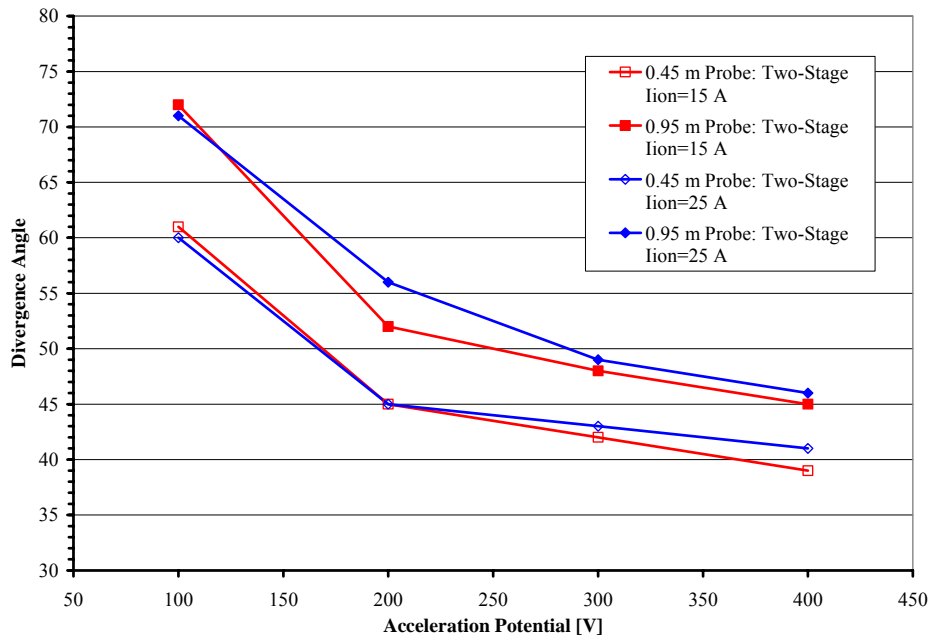


Figure 5-24: The divergence as a function of acceleration potential for 10 mg/s propellant flow rate and ionization stage currents of 15 and 25 A.

As expected, the plume divergence decreased with applied acceleration voltage for both propellant flow rates. This decrease in plume divergence has been observed with other SOA Hall thrusters and was attributed to the increase in the ionized propellant axial velocity component over the ion radial component.

The two-stage plume divergence data at acceleration potential of 400 V, ionization stage current of 15 A, and 10 mg/s propellant flow rate provided the smallest half-angle of  $39^\circ$  for the 0.45 m gridded Faraday probe location. The largest plume divergence occurred at  $61^\circ$  for the 0.45 m probe location at 100 V acceleration potential, 10 mg/s, and ionization stage current of 15 A. The 0.45 and 0.95 m gridded Faraday probe location data was separated by an average of  $7^\circ$  at the same operating conditions. This difference can be attributed to the increased ion current measured by the 0.95 m probe over the 0.45 m probe as shown in Table 5-3

The ion current density traces of the NASA-173GT, as shown in Figure 4-39 through Figure 4-56, illustrated that the traces of the 0.45 m probe location were greater than the 0.95 m probe location traces. The integration of the ion current density traces over the hemisphere, represented by equation 3-10, resulted in the 0.95 m data predicting a larger total ion current as compared to the 0.45 m results due to the square of the axial downstream distance of the radial probe sweeps in equation 3-10. The total ion current calculation results for the 0.45 and 0.95 m gridded probes radial sweeps contradict the results obtained by Haas in Ref. [107]. Haas observed a decrease in the calculated total ion currents between the 0.5 and 1 m nude Faraday probes radial sweeps and attributes these decreases to higher order CEX collisions between the thruster and the probe

locations. Near field total ion current results were obtained by Haas in Ref. [107] with electrostatic probes mounted on PEPL High-speed Axial Reciprocating Probe (HARP), discussed in Appendix B, that indicated a total ion current approximately 70% of the total discharge current. The near field total ion current results agreed with predictions of the actual ion current generated by SOA Hall thrusters [60, 64, 84, 148]. The data acquired from both the gridded Faraday probes will be averaged for the purposes of calculating the ion beam current, and the current and propellant utilization efficiencies for both the single- and two-stage data. The gridded Faraday results indicated that the NASA-173GT operated with a large electron leakage current, 53.7% to 36.4% of the acceleration current, for both single- and two-stage configurations.

A comparison of the 0.45 m gridded Faraday probe traces of the NASA-173GT operating in both single- and two-stage configurations at 400 V, 10 mg/s operating set point is illustrated in Figure 5-25. The two gridded Faraday probe traces for the single- and two-stage operation indicated no substantial variation between the two configurations and implied that the acceleration of the ionized propellant was through the same mechanism.

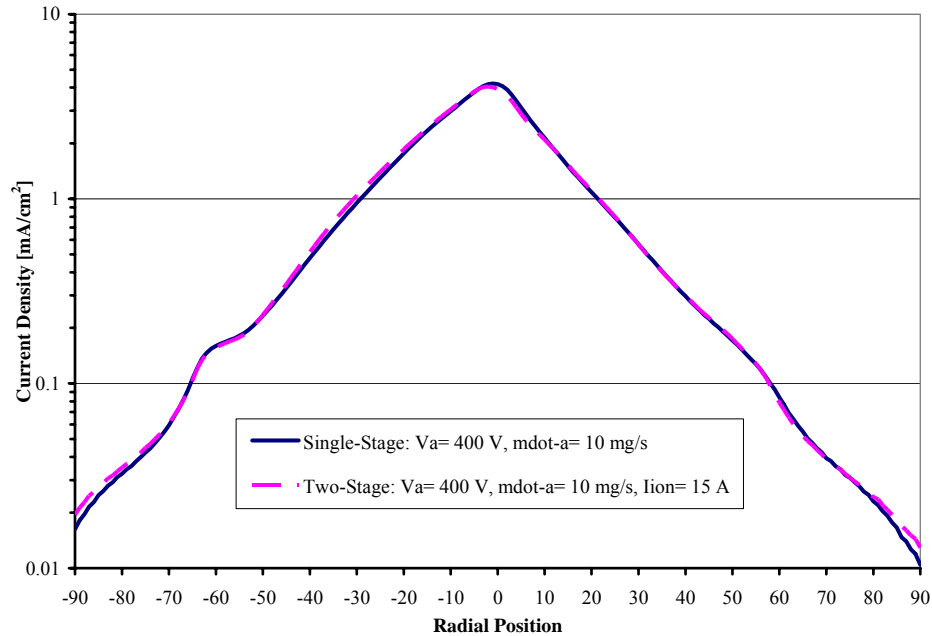


Figure 5-25: Comparison of the single- and two-stage NASA-173GT ion current density traces from the 0.45 m gridded Faraday probe location at similar operating conditions.

The results of the ion collector bias study of the gridded Faraday probe was presented in Figure 4-57 and Figure 4-58. The ion collector bias studies indicated that a potential of +30 V will reduce the collected ion current in the far edges of the thruster plume, while not decreasing the centerline collected current. Increasing the ion collector bias past +30 V had no further influence on the collected ion current density in the far edges of the plume. These results indicated that the ions in the far edges of the thruster plume have energies greater than +50 V. Further measurements with an ion energy analyzer were needed to confirm the energies of the ions in the far edges of the plume. However, the gridded Faraday probe results of the NASA-173GT indicated that the design of the gridded Faraday probe was sufficient in reducing low-energy CEX ions,

with energies below the bias of the ion collector, without influencing the collection of thrust producing ionized propellant.

The uncertainty of the gridded Faraday probes ion current traces was determined by examining the uncertainty of the applied probe potentials, the resistance of the probe current shunt, the open area fraction of the grid, the axial and radial probe locations, the average facility background pressure, the loss of secondary electrons from the collector plate to the guard ring, and the influence of CEX collisions over the axial distance between the thruster and the gridded Faraday probes. The uncertainty in the ion current density measurements and the calculated total ion current was conservatively determined to be approximately  $\pm 25\%$  and is illustrated in Figure 5-26.

This uncertainty of the ion collector bias set point was due to the ion collector floating to a greater positive bias as a result of the voltage drop across the current shunt. The ion collector floated to an additional +2.3 V (46%) above the actual collector set point in the center of the plume and only 0.2% increase in the bias voltage in the far edges of the plume. Comparing ion collector increased bias potentials, due to the current shunt induced probe voltage; the increase in the ion collector voltage was small compared to the uncertainties in the other parameters.

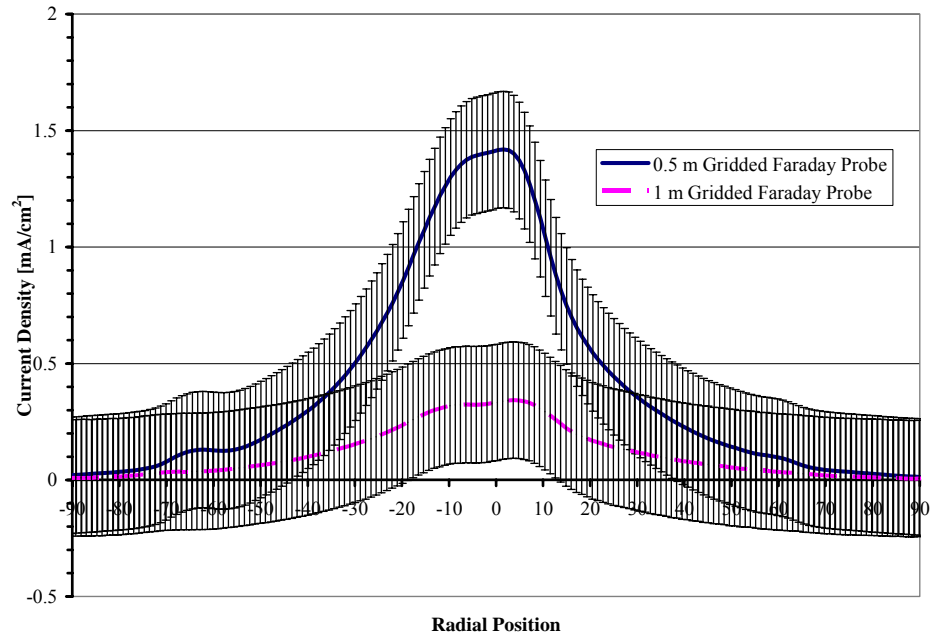


Figure 5-26: Comparison of the uncertainty of the ion current traces between both radial probe locations.

## **Chapter 6 SUMMARY AND FUTURE WORK**

The NASA-173GT was successfully operated in both single- and two-stage configurations. The design goals and materials, of the NASA-173GT, were discussed for both of the ionization and acceleration stages. The design goals for both stages were based on previous SOA ion and Hall thrusters. The conclusions of the ionization stage characterization and the performance and plume characterization of the NASA-173GT in both single- and two-stage configurations are presented in Sections 6.1 and 6.2, respectively.

### **6.1 Performance**

The characterization of the NASA-173GT ionization stage was conducted to determine the ion production cost and the ionization efficiency. The lowest ion production cost of 210 W/A occurred at approximately 580 W of power. The ionization stage ion production cost ranged from 750 to 210 W/A for the operating conditions used in the two-stage performance and plume characterization.

The single- and two-stage thruster configurations provided approximately the same performance at each anode propellant flow rate studied. The performance and plasma plume results indicated that the NASA-173GT operated with a large electron

leakage current, 53.7% to 36.4% of the acceleration current, for both single- and two-stage configurations. Physical observation of the thruster under operation and gridded Faraday probe results indicated that electron Hall current was intersecting the four flux shunt BN shields thereby reducing the energy of the Hall current electrons and allowing them to leak across the applied magnetic field. Another factor limiting the operation of the NASA-173GT was the contamination of the magnetic circuit. The contamination of the magnetic circuit limited the available magnetic field for operation above 500 to 600 V.

## 6.2 Plasma diagnostics and performance

The plume of the NASA-173GT was characterized with an **ExB** probe and two gridded Faraday probes. The **ExB** results indicated that as the acceleration voltage was increased, the  $\text{Xe}^+$  ion species fraction decreased and the  $\text{Xe}^{++}$  and  $\text{Xe}^{+++}$  ion species fractions increased. The **ExB** probe measurements indicated decreased charge utilization efficiency from 98.4% to 97.6% with increased voltage. The gridded Faraday probes measurements indicated that the current utilization efficiency varied from 46.3% to 63.6% depending on the applied propellant flow rate and acceleration voltage. The gridded Faraday probes measurements as well indicated that the propellant utilization efficiencies, based on a multiple charge approximation, ranged from 74.3% to 85.9%. The voltage utilization efficiency was calculated based on the charge, current, and propellant utilization efficiencies, and the measured anode efficiency. The voltage utilization efficiency increased from 57.7% to 73.4% with increased acceleration voltage.

The charge, current, voltage, and propellant utilization efficiencies limited the anode efficiency of the thruster to a maximum of 34% to 36% for both the single- and two-stage configurations.

### **6.3 Thruster design improvements**

The performance and plume characterization of the NASA-173GT indicated several possible improvements that could be made to the thruster. The first was the removal of the four flux shunts and shields from the acceleration stage. It is thought that the flux shunts and BN shields increased the electron leakage across the applied magnetic field in the acceleration stage. The increased electron leakage current decreased the current and voltage utilization efficiencies of the NASA-173GT for both single- and two-stage operation. The removal of the flux shunts and shields would allow the Hall current to circulate around the Hall stage with minimal collisions. A diagram of the non-flux shunt thruster design is presented in Figure 6-1.

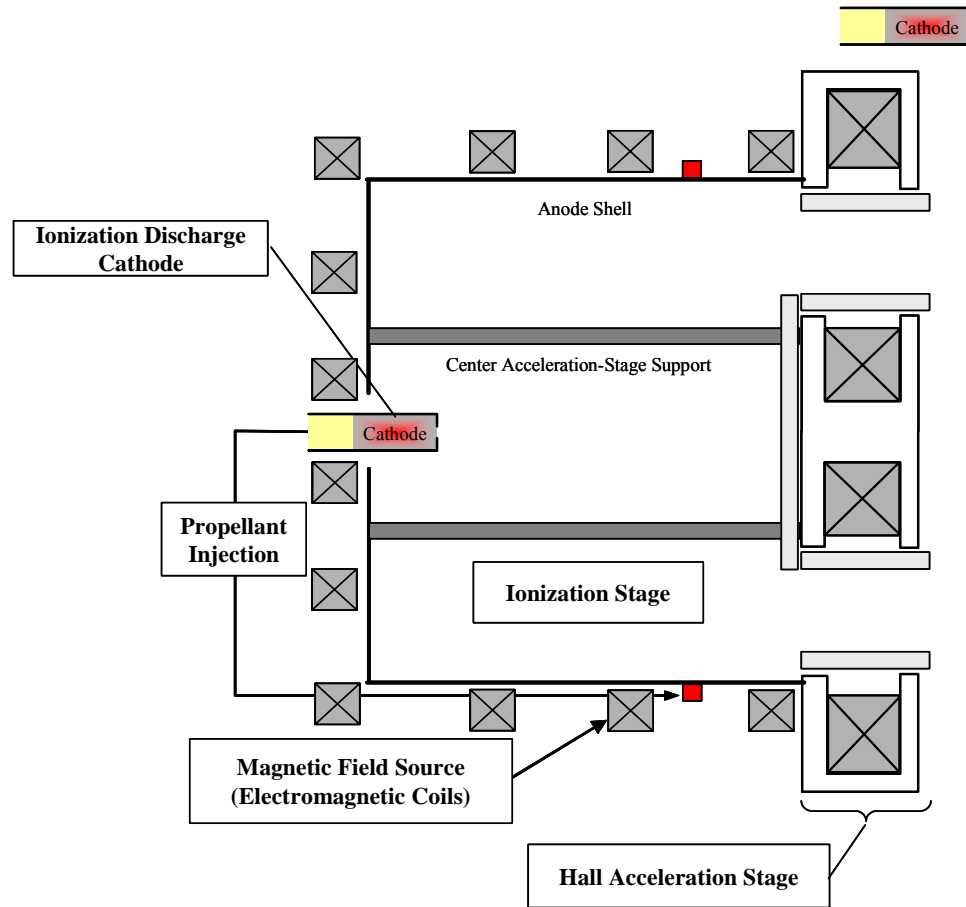


Figure 6-1: Alternative NASA-173GT design.

As discussed in Section 5.1, to achieve stable and efficient Hall acceleration stage required an increasing applied magnetic field. The NASA-173GT was limited to 500 to 600 V acceleration potential due to the contamination of the magnetic circuit material. New Hall acceleration stage magnetic circuit components, in conjunction with the removal of the flux shunts, would increase the thruster ability to operate at acceleration voltages up to and above 1000 V.

The concept of the NASA-173GT design may provide improved thruster operation on alternative propellants, such as krypton or lighter propellants. The efficient

use of krypton on EP devices would increase the performance envelopes of these devices. Hall thrusters operating on krypton have shown a decrease of thruster efficiencies as compared to xenon [100]. It has been thought that these low thruster efficiencies were the result of decreased propellant utilization efficiencies. The propellant utilization efficiencies decreased because of the smaller ionization cross-section of krypton, as compared to xenon. The concept of the NASA-173GT was to increase the ionization of the propellant with the addition of the ionization source upstream of the normal anode location of single-stage Hall thrusters. The operation of an improved NASA-173GT may increase the ionization of krypton propellant, and therefore increase the thruster efficiency to the levels measured with xenon EP devices.

## APPENDICES

### Appendix A

Table A-1: The single-stage performance characterization results of the NASA-173GT.

Va [V]	Ia [A]	Accel Power [kW]	Anode [mg/s]	Ion Cath [mg/s]	Hall Cath [mg/s]	Total Ion Flow [mg/s]	Iin [A]	Tin [C]	Iom [A]	Tot [C]	Vc-g [V]	Pressure [Torr-Xe]	Thrust [mN]	Anode Isp [sec]	Anode Eff
100.0	4.90	0.49	4.70	0.00	0.50	4.70	1.21	30	1.00	30	-9.1	2.6E-06	30.2	655	0.20
100.0	5.20	0.52	4.96	0.00	0.50	4.96	1.21	32	1.00	30	-8.9	2.7E-06	31.3	643	0.19
150.3	5.03	0.76	4.92	0.00	0.50	4.92	1.88	39	2.22	36	-11.0	2.7E-06	42.7	885	0.24
150.3	5.11	0.77	4.98	0.00	0.50	4.98	1.89	43	2.22	40	-11.0	2.7E-06	42.7	873	0.24
200.2	5.14	1.03	4.98	0.00	0.50	4.98	2.76	58	2.80	50	-12.0	2.7E-06	51.7	1058	0.26
250.0	5.16	1.29	4.85	0.00	0.50	4.85	3.88	79	3.96	66	-12.6	2.7E-06	58.4	1228	0.27
300.3	5.29	1.59	4.94	0.00	0.50	4.94	3.80	113	3.93	91	-12.0	2.6E-06	64.6	1335	0.27
350.0	5.49	1.92	4.96	0.00	0.50	4.96	3.84	221	3.72	151	-11.5	2.7E-06	72.0	1481	0.27
400.0	5.54	2.22	4.98	0.00	0.50	4.98	4.90	335	4.35	210	-11.5	2.7E-06	77.4	1583	0.27
451.0	5.70	2.57	4.96	0.00	0.50	4.96	4.30	460	4.38	266	-10.5	2.6E-06	82.9	1703	0.27
151.0	5.17	0.78	2.98	2.00	0.50	4.98	2.40	31	2.45	24	-11.3	2.7E-06	44.7	915	0.26
200.4	5.28	1.06	2.98	2.00	0.50	4.98	2.80	41	3.27	34	-12.0	2.7E-06	55.1	1126	0.29
250.8	5.35	1.34	2.98	2.00	0.50	4.98	3.60	54	3.60	45	-12.4	2.6E-06	62.9	1286	0.30
300.0	5.45	1.64	2.98	2.00	0.50	4.98	3.46	70	3.99	59	-12.0	2.6E-06	69.1	1414	0.29
350.0	5.55	1.94	2.98	2.00	0.50	4.98	3.80	90	4.30	76	-12.3	2.7E-06	75.4	1542	0.29
353.0	5.58	1.97	2.98	2.00	0.50	4.98	3.70	133	4.11	103	-11.0	2.7E-06	75.2	1538	0.29
400.0	5.66	2.26	2.98	2.00	0.50	4.98	4.60	171	4.85	130	-11.4	2.6E-06	80.7	1651	0.29
450.4	5.84	2.63	2.98	2.00	0.50	4.98	5.08	235	4.90	168	-11.2	2.6E-06	85.6	1752	0.28
500.0	6.09	3.05	2.98	2.00	0.50	4.98	4.96	302	4.86	200	-10.5	2.6E-06	90.6	1853	0.27
600.0	6.65	3.99	2.98	2.00	0.50	4.98	5.80	370	4.40	223	-9.6	2.6E-06	100.9	2063	0.26
101.9	11.50	1.17	8.01	2.00	1.00	10.02	2.00	300	2.37	211	-7.8	4.7E-06	66.8	680	0.19
150.0	10.80	1.62	8.01	2.00	1.00	10.02	3.00	394	3.22	218	-9.3	4.7E-06	96.0	977	0.28
200.8	11.00	2.21	8.01	2.00	1.00	10.02	4.08	424	4.78	235	-10.3	4.7E-06	116.4	1185	0.31
300.6	11.46	3.44	8.01	2.00	1.00	10.02	5.38	491	4.81	262	-9.7	4.7E-06	152.0	1547	0.33
400.8	11.72	4.70	8.01	2.00	1.00	10.02	6.01	590	4.74	280	-9.6	4.7E-06	178.8	1820	0.34

Table A-2: The two-stage performance characterization results of the NASA-173GT.

Va [V]	Ia [A]	Id [A]	Accel Power [kW]	Ion Power [W]	Anode [mg/s]	Ion Cath [mg/s]	Hall Cath [mg/s]	Total Ion Flow [mg/s]	Iin [A]	Iot [A]	Idc1 [A]	Idc2 [A]	Idc3-4 [A]	Idc5 [A]	Vc-g [V]	Thrust [mN]	Anode Isp [sec]	Anode Eff
100.9	4.91	15.09	0.50	227	4.06	0.99	0.50	5.05	1.43	1.58	1.27	2.90	2.98	3.49	-10.5	28.6	577	0.16
150.9	4.97	15.09	0.75	229	3.95	0.99	0.50	4.94	1.37	1.52	1.16	3.05	3.03	3.38	-10.8	43.5	898	0.26
200.0	5.13	15.11	1.03	237	3.93	0.99	0.50	4.92	1.83	1.77	1.07	2.99	2.50	2.96	-11.2	51.7	1072	0.27
250.3	5.31	15.12	1.33	236	3.93	0.99	0.50	4.92	2.46	2.43	0.95	3.19	2.69	3.35	-11.6	59.7	1238	0.27
300.4	6.06	15.12	1.82	236	3.93	0.99	0.50	4.92	2.18	2.25	0.96	3.30	2.69	3.32	-10.5	69.4	1439	0.27
100.9	4.93	20.00	0.50	306	4.12	0.99	0.50	5.11	1.14	1.30	0.90	2.90	2.30	3.00	-9.7	32.0	638	0.20
150.6	4.90	20.00	0.74	300	3.95	0.99	0.50	4.94	1.22	1.33	0.99	2.19	2.32	3.10	-10.0	42.9	886	0.25
200.3	5.08	20.00	1.02	310	3.93	0.99	0.50	4.92	1.74	1.90	0.87	2.38	2.20	3.81	-10.7	50.6	1049	0.26
250.0	5.27	20.00	1.32	320	3.95	0.99	0.50	4.94	2.42	2.44	0.85	2.80	2.00	3.37	-11.2	58.2	1201	0.26
299.9	5.38	20.10	1.61	322	3.95	0.99	0.50	4.94	2.74	2.83	0.83	2.75	2.10	3.48	-10.6	64.3	1327	0.26
101.0	4.65	25.00	0.47	390	4.01	0.99	0.50	5.01	1.31	1.22	1.27	2.70	2.30	2.60	-9.5	29.4	599	0.18
150.8	4.91	25.00	0.74	390	3.99	0.99	0.50	4.98	1.34	1.40	0.87	2.72	2.50	2.88	-10.0	41.9	858	0.24
200.4	5.06	25.00	1.01	393	3.95	0.99	0.50	4.94	1.19	1.44	0.89	2.78	2.20	3.20	-9.5	50.3	1037	0.25
250.5	5.12	25.00	1.28	400	3.97	0.99	0.50	4.96	1.21	1.36	1.06	2.73	1.87	3.38	-9.5	56.6	1162	0.25
300.5	5.43	25.00	1.63	400	3.97	0.99	0.50	4.96	2.06	2.01	0.84	2.91	2.32	3.06	-10.0	64.1	1317	0.25
216.0	5.34	15.10	1.15	252	3.11	2.00	0.50	5.11	1.55	1.67	0.83	2.95	2.65	2.06	-11.0	58.1	1159	0.29
300.5	5.56	15.10	1.67	251	2.96	2.00	0.50	4.96	1.76	1.99	0.81	2.94	2.66	2.75	-10.6	69.0	1418	0.29
350.0	5.80	15.10	2.03	248	2.94	2.00	0.50	4.94	2.36	2.56	1.39	2.88	2.64	2.99	-10.0	74.8	1544	0.28
400.8	6.06	15.10	2.43	251	2.94	2.00	0.50	4.94	3.15	3.54	0.50	2.80	2.64	2.98	-10.0	79.4	1639	0.26
450.0	6.15	15.10	2.77	246	2.96	2.00	0.50	4.96	4.07	4.30	0.63	2.00	2.99	2.98	-10.3	84.7	1739	0.26
500.0	6.36	15.10	3.18	244	2.96	2.00	0.50	4.96	4.67	4.67	0.63	3.00	2.99	2.98	-10.8	89.5	1838	0.25
301.0	5.62	20.00	1.69	540	2.96	2.00	0.50	4.96	2.11	2.07	0.71	3.00	3.00	3.00	-11.5	68.0	1397	0.28
350.0	5.97	20.00	2.09	560	2.98	2.00	0.50	4.98	2.25	2.35	0.71	2.90	2.88	3.00	-10.5	75.6	1546	0.27
400.0	6.98	20.00	2.79	600	2.92	2.00	0.50	4.92	3.03	3.40	0.58	2.90	2.88	3.00	-9.8	85.5	1771	0.27
450.0	6.82	20.00	3.07	500	2.94	2.00	0.50	4.94	3.26	3.50	0.82	2.90	2.88	3.00	-9.9	86.8	1791	0.25
500.0	6.68	20.00	3.34	340	2.94	2.00	0.50	4.94	3.80	3.87	0.82	2.90	2.88	3.00	-9.9	89.5	1847	0.24
300.0	5.43	25.10	1.63	432	2.96	2.00	0.50	4.96	1.50	1.78	0.88	3.20	3.00	3.00	-10.7	65.3	1342	0.26
350.3	5.72	25.10	2.00	439	2.94	2.00	0.50	4.94	2.23	2.45	0.73	3.15	3.00	3.20	-10.7	71.0	1464	0.25
400.4	6.12	25.10	2.45	444	2.92	2.00	0.50	4.92	2.54	2.64	0.66	3.15	3.00	3.20	-9.9	77.1	1597	0.25
450.7	6.37	25.10	2.87	449	2.92	2.00	0.50	4.92	3.00	3.25	0.45	2.95	2.90	3.20	-9.6	81.4	1686	0.23
500.5	6.36	25.10	3.18	459	2.94	2.00	0.50	4.94	3.90	3.97	0.47	2.95	2.90	3.18	-10.0	85.6	1765	0.23
550.7	6.60	25.10	3.63	462	2.92	2.00	0.50	4.92	4.30	4.04	0.47	2.95	2.90	3.18	-9.7	90.5	1875	0.23
600.0	7.20	25.10	4.32	462	2.92	2.00	0.50	4.92	4.00	4.00	0.47	2.95	2.90	3.18	-8.7	95.9	1987	0.22
100.0	4.95	15.00	0.50	234	2.98	2.00	0.50	4.98	2.00	2.32	0.47	2.60	3.00	1.94	-10.4	24.7	505	0.12
150.0	4.97	15.00	0.75	234	2.96	2.00	0.50	4.96	2.60	2.75	0.54	2.80	2.98	1.74	-12.2	40.7	837	0.22
200.0	5.18	15.00	1.04	240	2.96	2.00	0.50	4.96	2.86	3.13	0.44	2.93	2.50	1.60	-12.0	51.6	1059	0.26
250.0	5.35	15.00	1.34	240	2.96	2.00	0.50	4.96	2.97	3.50	0.23	2.67	2.70	1.56	-12.0	59.6	1224	0.27
300.0	5.41	15.00	1.62	240	2.96	2.00	0.50	4.96	3.70	3.92	0.43	2.63	2.50	1.93	-11.4	65.6	1347	0.27
350.0	5.58	15.00	1.95	236	2.96	2.00	0.50	4.96	4.10	4.00	0.34	2.77	2.50	2.10	-11.2	71.6	1470	0.26
100.0	11.30	15.00	1.13	198	8.12	2.00	1.00	10.12	1.30	1.30	1.18	2.90	3.15	3.14	-6.7	71.7	722	0.22
150.0	11.20	15.00	1.68	206	8.16	2.00	1.00	10.17	1.90	1.97	1.14	3.00	3.12	3.17	-8.2	99.9	1002	0.29
200.5	11.36	15.00	2.28	211	8.14	2.00	1.00	10.14	2.64	2.86	1.10	3.08	3.07	3.50	-9.1	122.3	1229	0.32
250.3	11.35	15.00	2.84	215	7.99	2.00	1.00	9.99	3.36	3.48	1.14	2.90	3.06	3.20	-9.7	136.5	1392	0.33
300.0	11.34	15.00	3.40	218	7.93	2.00	1.00	9.93	4.07	4.17	1.13	2.90	3.06	3.30	-9.9	151.4	1554	0.34
100.8	11.03	20.00	1.11	285	7.86	1.99	1.00	9.86	1.44	1.51	1.00	2.54	2.90	3.15	-7.0	69.4	717	0.22
150.6	10.85	20.00	1.63	282	8.03	1.99	1.00	10.03	2.10	2.21	0.82	2.82	3.23	2.89	-8.6	98.8	1004	0.30
200.0	10.95	20.00	2.19	288	8.01	1.99	1.00	10.01	3.16	3.46	0.83	2.58	2.63	2.83	-9.7	116.7	1189	0.31
250.3	11.02	20.00	2.76	280	8.01	1.99	1.00	10.01	3.69	3.95	0.50	2.70	2.50	2.64	-10.0	132.7	1352	0.32
300.0	11.27	20.00	3.38	290	8.01	1.99	1.00	10.01	4.28	4.13	0.98	2.70	2.50	2.71	-10.0	147.3	1501	0.32
102.0	11.40	25.00	1.16	358	8.12	2.00	1.00	10.12	1.35	1.32	0.91	2.43	2.99	3.20	-7.0	69.8	703	0.21
150.7	10.68	25.00	1.61	366	8.01	2.00	1.00	10.02	2.53	2.35	0.70	2.70	2.70	2.86	-9.1	95.1	968	0.28
200.5	10.90	25.00	2.19	374	7.95	2.00	1.00	9.95	3.06	3.13	0.66	2.63	2.84	2.82	-9.6	114.5	1173	0.30
250.4	11.00	25.00	2.75	384	7.97	2.00	1.00	9.97	3.58	3.69	0.76	2.72	2.84	2.82	-9.8	132.1	1350	0.32
300.0	11.16	25.00	3.35	394	8.03	2.00	1.00	10.04	4.45	4.41	0.76	2.72	2.84	2.82	-10.0	146.5	1488	0.32
101.0	11.00	25.00	1.11	345	6.94	3.01	1.00	9.94	1.23	1.42	1.11	2.88	2.70	2.67	-6.8	66.5	682	0.20
150.2	10.67	25.00	1.60	360	6.98	3.01	1.00	9.98	1.78	1.84	0.84	2.74	2.67	2.52	-7.9	94.6	966	0.28
200.0	11.20	25.00	2.24	367	6.81	3.01	1.00	9.81	2.35	2.35	0.89	2.68	2.78	2.90	-8.0	112.6	1170	0.29
200.0	11.00	15.00	2.20	237	8.01	2.00	1.00	10.02	3.00	3.20	0.64	2.95	2.90	3.00	-10.3	120.0	1221	0.33
250.0	11.25	15.00	2.81	236	7.97	2.00	1.00	9.97	3.60	3.70	0.65	3.00	2.90	3.00	-10.1	138.8	1419	0.34
301.0	11.30	15.00	3.40	239	7.95	2.00	1.00	9.95	3.88	3.88	0.65	3.00	2.90	3.00	-10.5	155.1	1589	0.36
349.0	11.68	15.00	4.08	245	7.99	2.00	1.00	9.99	4.68	4.99	0.65	3.00	2.90	3.00	-10.6	166.1	1694	0.34
401.0	11.45	15.00	4.59	254	7.99	2.00	1.00	9.99	4.35	4.58	0.64	3.00	2.90	3.00	-10.8	178.8	1823	0.35
451.0	11.80	15.00	5.32	237	7.99	2.00	1.00	9.99	4.80	4.40	0.64	3.00	2.90	3.00	-10.4	194.2	1981	0.35
130.0	10.80	20.00	1.40	300	7.97	2.00	1.00	9.97	1.86	1.99	0.60	3.00	3.00	3.00	-9.0	85.7	876	0.26
301.0	11.40	20.00	3.43	314	7.93	2.00	1.00	9.93	3.60	3.80	0.65	3.00	2.90	3.00	-9.8	151.6	1557	0.34
350.0	11.60	20.00	4.06	320	7.99	2.00	1.00	9.99	4.44	4.70	0.65	3.00	2.90	3.00	-10.5	164.3	1676	0.33
402.0	12.00	20.00	4.82	320	7.99	2.00	1.00	9.99	4.99	5.00	0.58	2.98	2.84	2.96	-9.9	176.1	1796	0.32
451.0	11.90	20.00	5.37	326	7.99	2.00	1.00	9.99	5.60	5.00	0.58	2.98	2.84	2.96	-10.0	189.3	1931	0.33
301.0	11.50	25.1																

## **Appendix B**

### **An experimental investigation of the internal magnetic field topography of an operating Hall thruster**

Peter Y. Peterson, Alec D. Gallimore, and James M. Haas  
Plasmadynamics and Electric Propulsion Laboratory  
Department of Aerospace Engineering  
The University of Michigan  
College of Engineering  
Ann Arbor, MI 48109 USA

#### **ABSTRACT**

Magnetic field measurements were made in the discharge channel of the 5-kW-class P5 laboratory-model Hall thruster to investigate what effect the Hall current has on the static, applied magnetic field topography. The P5 was operated at 1.6 kW and 3.0 kW with a discharge voltage of 300 V. A miniature inductive loop probe (B-Dot probe) was employed to measure the radial magnetic field profile inside the discharge channel of the P5 with and without the plasma discharge. These measurements are accomplished with minimal disturbance to thruster operation with the High-speed Axial Reciprocating Probe (HARP) system. The results of the B-Dot probe measurements indicate a change in the magnetic field topography from that of the vacuum field measurements. The measured magnetic field profiles are then examined to determine the possible nature and source of the difference between the vacuum and plasma magnetic field profiles.

## INTRODUCTION

The requirements of a spacecraft propulsion system for new mission profiles have increased recently beyond the current level of existing technology. An example of one recently prescribed requirement is for a propulsion system to operate in “dual-mode”. Dual-mode is the ability of a thruster to operate efficiently in both a high-thrust and low-specific impulse mode (e.g., for orbit transfer operations) and a high-specific impulse and low-thrust mode (e.g., for station-keeping) [18, 98]. Other design drivers for advanced space propulsion systems revolve around human space exploration. A piloted mission to Mars for example would require a reliable propulsion system with high-power, high performance, and long life.

A favorable candidate for these types of missions is the closed-drift Hall thruster. A Hall thruster is a coaxial plasma device in which an applied magnetic field effectively traps electrons in the discharge channel of the thruster. The electrons are usually emitted from an external cathode while a magnetic circuit composed of electromagnetic solenoids and pole pieces typically creates the applied magnetic field. The magnetic circuit of a typical Hall thruster produces a radial magnetic field topography at the exit of the discharge channel with peak fields on the order of a few hundred-gauss. If the magnetic field topography in the discharge channel is designed properly, the accelerating ions will experience a focusing effect through what is referred to as a magnetic lens [148].

One of the main characteristics of a Hall thruster is the azimuthally drifting electrons. These electrons form a region of azimuthal current in the discharge channel

that is typically on the order of 5-10 times the discharge current. This estimate is based on Hall parameters expected in Hall thruster discharge chambers; e.g., 200-300 [60]. This estimate can lead to Hall currents on the order of 150 A for a 5 kW Hall thruster.

Recent plasma measurements inside the discharge channel of the P5 as well as in other laboratory Hall thrusters indicate that the true, effective Hall parameter ranges from 10-20 near the anode to approximately 1000 in the acceleration region [106, 149]. These results suggest that the Hall current may be larger than previously thought, and that the induced magnetic field could impact the applied magnetic field topography significantly. As the magnitude of the Hall current increases at higher thruster power levels, the effects of the self-magnetic field induced by the Hall current may become important. As the self-magnetic field magnitude increases, the effect on the magnetic circuit applied field topography is greater, thus decreasing the chances of maintaining the desired magnetic lens profile in the discharge channel. In designing next-generation Hall thrusters, the magnetic field topography for a given magnetic circuit design can be predicted with great precision by using 3-D magnetostatic computer codes. However, to predict the magnetic field topography during thruster operation accurately, a better understanding of the effects of the magnetic field induced by the Hall current is needed.

The University of Michigan Plasmadynamics and Electric Propulsion Laboratory (PEPL) has endeavored in the past to develop and improve plasma diagnostic techniques to be used on plasma propulsion systems [66, 150-155]. An attempt to map the magnetic field topography near the exit of a D-55 Anode Layer Thruster (TAL) was performed at PEPL [155]. The D-55 magnetic field measurements were limited to 15 mm downstream

of the exit plane due to the large perturbations in thruster discharge current that resulted when the Hall probe was moved closer to the thruster. It was concluded that the Hall probe was entering the Hall current region and thus disrupting the stable operation of the thruster. To continue the research effort initiated by the D-55 very-near-field investigation, and to gather knowledge on the effects of the self-induced magnetic field at high-power operation for a Stationary Plasma Thruster (SPT), a miniature inductive loop probe (B-Dot probe) system was developed and used in conjunction with the PEPL High-speed Axial Reciprocating Probe (HARP) system to map the radial magnetic field of the P5 Hall thruster.

The University of Michigan HARP system was designed to address concerns associated with placing probes within the plasma of an operating Hall thruster. These concerns include probe life and thruster perturbation. The HARP system provides a unique opportunity to incorporate a time response B-Dot probe by virtue of its motion. B-Dot probes are typically used for pulsed and inductive plasma discharges with time-varying magnetic fields [156-158]. However, by combining the high speed characteristics of the HARP table ( $dx/dt$ ) with the B-Dot probe response to a time-varying magnetic field ( $dB/dt$ ), one can measure a change in a magnetic field magnitude ( $dB/dx$ ) as the probe is swept into the discharge channel of the thruster.

This article will briefly describe the experimental facilities, the Hall thruster, and the HARP system. The theory of inductive loop operation is reviewed, as are the construction, set-up, and calibration of the B-Dot system. The thruster magnetic field profiles both in vacuum and in the presence of the plasma discharge are presented and

discussed. Finally, several avenues are investigated to examine the nature of the observed change in the magnetic field profiles between the vacuum and plasma conditions.

## **Experimental Apparatus**

### **A. Vacuum Facilities**

All the experiments were conducted in the University of Michigan Large Vacuum Test Facility (LVTF), which has a diameter of 6 meters and a length of 9 meters. Two 2000 cubic feet per minute (CFM) blowers and four 400 CFM mechanical pumps evacuate the LVTF chamber to moderate vacuum (30 - 100 mTorr). To reach high vacuum, the LVTF is equipped with seven CVI TM-1200 cryopumps, with a combined pumping speed of  $\sim 500\,000$  l/s on air, and  $\sim 240\,000$  l/s on xenon. The cryopump system can be operated with any number of pumps in use. For the experiments reported here the LVTF was operated with only four cryopumps to match the operating conditions of prior experiments [149, 159]. At the four-cryopump configuration, the combined pumping speed of  $140\,000$  l/s on xenon with a base pressure  $1.6 \times 10^{-7}$  Torr was achieved. At an anode mass flow rate of  $10.2$  mg/s and a cathode mass flow rate of  $0.6$  mg/s, the operating pressure of the LVTF was  $1.1 \times 10^{-5}$  Torr (xenon). The tank pressure during Hall thruster operation at  $1.6$  kW was  $6.6 \times 10^{-6}$  Torr (xenon). The Hall thruster was mounted in the center of the vacuum chamber on an X-Y computer-controlled linear positioning system.

## B. Hall Thruster

The experimental results presented in this paper were conducted on the 5-kW-class laboratory model P5 Hall thruster. The P5 Hall thruster was developed by the University of Michigan and the Air Force Research Laboratory to serve as a test-bed for new diagnostics and for investigating Hall thruster processes. Depicted in Fig. 1, the P5 has an outer diameter of 170 mm, a channel width of 25 mm, and a channel depth of 38 mm.

The P5 performance characteristics, presented in a previous work [87], are comparable to commercially available 5 kW thrusters. Table I shows the measured performance characteristics of the P5 for the two operating conditions used in this experiment. The hollow cathode used for this test was provided by the Moscow Aviation Institute (MAI). The cathode provides thermally emitted electrons to the discharge by a small disk of lanthanum hexaboride (LaB6).

## C. High-speed Axial Reciprocating Probe

The HARP system consists of a LM1210 high-speed linear motor and encoder manufactured by Trilogy. The linear encoder provides a linear resolution of 5 microns to a Pacific Scientific SC950 digital brushless servo drive controller. A computer controls the position, speed, acceleration, deceleration, and sweep configuration for the HARP system. The linear table is placed within a stainless steel shroud encased with graphite plates to protect it from the plume of the Hall thruster.

The primary issue involving internal probe measurements of a Hall thruster is the ability of the probe to survive in the presence of the discharge plasma and Hall current. Ablation of probe material also affects thruster operation. Therefore, the main driving factor in determining the maximum resonance time that a probe can remain in the discharge channel of a thruster is the characteristic time for probe material ablation. The ablation time for 99%-pure alumina has been determined to be approximately 150 ms for a 5 kW plasma discharge<sup>5</sup>. The time that the B-Dot probe spent in the discharge channel for these experiments was approximately 80 ms  $\pm$ 10 ms. The peak velocity and acceleration of the HARP for these experiments was approximately  $\pm$ 5.5 m/s and +130 to -100 m/s<sup>2</sup>, respectively.

Another important issue is the actual heating of the probe during the sweep into the discharge plasma. If the probe resonance time in the discharge plasma is significantly long to allow the probe to heat up, thus changing the electrical characteristics of the probe circuit, the results of the mapped magnetic field profile for the plasma case may differ from that of the vacuum measurements. Employing the same method for estimating the amount of time before ablation of the probe material in a 5 kW plasma discharge [149], one can determine a bulk heating of a probe of a given size, material, discharge plasma parameters, and exposure time. It was determined analytically that the maximum increase in temperature for a typical ceramic probe used during this investigation will be approximately 1.5 degrees per sweep. The calculated temperature increase of the probe in the discharge plasma was relatively low; therefore no experimental measurements of the probe temperature characteristics were attempted.

#### D. Inductive Loop Probe

The inductive loop probe is a well-established plasma diagnostic technique for time-varying magnetic fields. Typical plasma discharges that make use of the B-Dot probing technique include pulsed and inductive plasmas [156-158]. The basic operating principle of the B-Dot probe is based on the observation that current is induced in a conducting coil immersed within a time-varying magnetic field. The ensuing output voltage from the coil is proportional to its cross-sectional area ( $A$ ), the number of turns in the coil ( $n$ ), and the time characteristic of the magnetic field ( $dB/dt$ ). The expression of the voltage output from a B-Dot probe is given as Eq. (1).

$$V = nA \frac{dB}{dt} \quad (1)$$

Since Hall thrusters typically operate with a steady applied magnetic field, direct application of the B-Dot probe is problematic. To circumvent this issue, the HARP position system was used to provide a time-varying magnetic field signal by virtue of moving the probe into (and out of) the applied, steady magnetic field. Therefore, by combining the motion of a high-speed table ( $dx/dt$ ) with the integrated signal of a B-Dot probe in a time-varying magnetic field ( $dB/dt$ ), one is able to measure the DC applied magnetic field as the probe is swept into and out of the Hall thruster discharge channel.

A dual-supply integrator that incorporates an Analog Devices AD549 ultra-low input bias current operational amplifier and an AD624 precision instrumentation

amplifier was chosen to integrate the B-Dot probe raw signal. The expression of the integrated output voltage from a B-Dot probe is shown in Eq. (2)

$$V = \frac{nA}{RCG} B \quad (2)$$

Where the G is the amplifier gain, RC is the integrator resistance and capacitance, respectively, and B is the magnetic field strength. The amplified voltage output from the B-Dot probe integrator circuit was recorded with a Tektronix TDS 540 digital oscilloscope in high-resolution acquisition mode. The data were then downloaded to a computer for processing.

The B-Dot probe support structures used for this investigation were constructed of 99% alumina ceramic tubes and high-temperature ceramic paste. A number of probe configurations were built evaluated for this effort. The inductive loops were wound with 38 and 40 gauge magnetic wires with enamel nonconductor coatings. The coils used in this investigation were wound around 1.6 to 2.5 mm diameter alumina ceramic tubes 2.2 to 2.5 mm in length. The number of turns in the probe coils ranged from 89 to 136. The average data collection area of the probes used in this investigation was 3.3 mm<sup>2</sup> over an average length of 2.35 mm. The final dimensions of the B-Dot probes, including a protective layer of 99% alumina ceramic, used in this investigation ranged from 4 to 4.3 mm in diameter and 4 to 4.2 mm in length.

Figure 2 shows the mapped area inside the discharge channel of the P5 thruster. The B-Dot probe was axially swept from 150 mm downstream of the exit plane to 10 mm downstream of the anode. This axial sweep profile was repeated for three radial positions, 3.81 mm from the inner wall, the centerline (at 12.7 mm), and 3.81 mm from the outer wall of the discharge channel. In an attempt to minimize the heating of B-Dot probe between sweeps, the probe home position was set to 152 mm downstream of the thruster exit plane. The cathode plane was located 50 mm downstream of the thruster exit plane and was oriented 45° counter-clock wise from the plane mapped. The results presented in this paper will cover the first 100 mm downstream of the anode.

## Results and Analysis

### A. Calibration of B-Dot Probe

The initial goal of this experiment was to calibrate the B-Dot probe and integrator circuit with an electric and magnetic field (**ExB**) source. The idea behind the **ExB** source was to approximate, under a controlled and understood manner, the fields that the B-Dot probe would experience when the probe was traveling through the discharge channel of an operating thruster. The **ExB** source was comprised of two electromagnetic coils, to provide the magnetic field, and two parallel plates for the electric field. The configuration of the **ExB** source can be seen in FIG. 3.

The magnetic field of the **ExB** source was first mapped using a NIST-traceable Walker Scientific MG-5DAR Hall probe. Then the B-Dot probe and HARP systems

were configured to measure the  $\mathbf{ExB}$  source with the applied magnetic field, or the applied magnetic field with a static or time-varying electric field. A time-varying electric field was simulated to approximate the oscillations of the discharge plasma in a Hall thruster during normal operation. All parameters of the B-Dot probe and HARP, such as speed, acceleration, deceleration, probe sweep length, and transmission line length that would be used during experiments with the P5 were used in the calibration runs.

Figure 4 shows the measured magnetic field profile of the  $\mathbf{ExB}$  source as measured by the B-Dot and Hall probes at atmospheric pressure with and without an applied static or time-varying (11 kHz) electric field of 15 kV/m. The peak electric field, which resides in a small region of the discharge chamber at the onset of the acceleration zone, can reach 25 kV/m at 300 V and 5.4 A, and 20 kV/m at 300 V and 10 A according to the internal emissive probe measurements [149, 159]. The 15 kV/m that was used during the calibration of the B-Dot probes should still indicate if the B-Dot probes are influenced by the presence of a steep steady or time-varying electric field. The measured data presented in FIG. 4 are composed of five sets of B-Dot traces averaged together at the same  $\mathbf{ExB}$  source input settings. Figure 4 also contain the Hall probe traces of the  $\mathbf{ExB}$  source at the two investigated conditions. As can be seen in FIG. 4, the B-Dot probe captured the profile and magnitude of the  $\mathbf{ExB}$  source. The presence of the 15 kV/m static and time-varying electric fields had no noticeable influence on the measured magnetic field from the B-Dot probe.

## B. Vacuum Field Measurements with B-Dot Probe

The vacuum magnetic field profiles of the P5 thruster were mapped using the B-Dot and HARP systems along the radial and axial positions described earlier. Two thruster power levels were investigated; 1.6 kW and 3.0 kW, both at a discharge voltage of 300 V. The inner and outer electromagnetic coils were operated in a manner that minimized the discharge current of the thruster. Once these coil currents were determined for both power levels, the P5 discharge was extinguished while the magnets were left on for vacuum field measurements.

The B-Dot and Hall probe vacuum field measurements of the P5 at coil current settings for 1.6 kW and 3.0 kW are shown in Figs 5 and 6, respectively. The thruster exit plane and the mid-plane of the magnetic circuit outer and inner front poles are labeled in these figures. Once again, each B-Dot profile presented represents the average of 5 or more data sweeps. All trends observed in individual B-Dot sweeps are captured in the average profile. Figures 5 and 6 show that magnetic field profiles measured with the B-Dot probe match those of the NIST-traceable Hall probe for both coil settings.

### C. Magnetic Field Measurements with Discharge

The discharge channel radial magnetic field with the P5 thruster operating at 1.6 kW and 3.0 kW was mapped at three radial positions. The P5 was operated for a minimum of forty minutes before B-Dot sweeps were made to allow the engine to reach thermal equilibrium; i.e., when the electromagnetic coil voltages of the magnetic circuit stabilized. This step was conducted to ensure that any anomalies measured with the B-Dot probe were not due to thermal expansion of the magnetic circuit components

throughout the duration of the experiment. The results of the B-Dot probe sweeps for the 1.6 kW thruster power level (300 V, 5.4 A) are shown in FIG. 7. Figure 7 also contains a plot of the thruster discharge current as a function of probe position and the corresponding bench top Hall probe magnetic field measurements. As can be seen in FIG. 7, the magnitude and profile of the magnetic field in the discharge channel of the P5 Hall thruster was influenced by the presence of the plasma discharge.

The B-Dot probe results for a 3 kW plasma, the vacuum Hall probe measurements, and thruster discharge current data at three different radial positions for the 3.0 kW power level are shown in FIG. 8. Once again the B-Dot profiles with the thruster operating at 3.0 kW differ from those in vacuum at the identical magnet settings. There are several possible explanations to account for these measured differences in the magnetic field profiles. The first and foremost explanation, assuming that the B-Dot probe is functioning properly, is the effect of the azimuthal electron drift (Hall current) self magnetic field. As discussed earlier, the Hall current of a closed-drift thruster can be 5 to 10 times the discharge current [60] or in light of recent internal plasma parameter measurements [149], possibly much higher.

In both the 1.6 kW and the 3.0 kW cases we see that the B-Dot probe magnetic field profiles with the discharge plasma closely match the vacuum field profiles along the inner wall of the discharge channel. However, the profiles are significantly different near the outer wall of the discharge channel and particularly along the center of the channel. The largest difference in the profiles occur slightly downstream of the thruster exit plane. In the 1.6 kW results, there is a spike in the measured magnetic field 10 mm inside of the

discharge channel. A characteristic spike exists in the 3.0 kW data as well; however in this case the spike is 7 mm inside the thruster channel. Neither of these spikes nor the large increases in the B-Dot magnetic field profiles corresponds to locations of peak electric fields in the thruster [149]. The peak electric fields of the P5 are located approximately 5 mm inside the discharge channel for the 1.6 kW thruster power level and approximately 2 mm inside the channel for the 3.0 kW power level [87] (data not shown). Thruster discharge current was recorded as the probe entered the discharge channel for the two power conditions investigated and are shown in Figs. 7 and 8. The maximum disturbance to the thruster discharge current was 8%; during the centerline sweep at the 1.6 kW power level. The axial region where the greatest perturbation in the thruster discharge current was recorded corresponds to a drop in the measured magnetic field profiles for each of the three radial sweeps for the 3.0 kW test condition. This can also be seen in the outer wall sweep of the 1.6 kW case. A possible explanation for these features is that the probe is blocking the natural path of the Hall current in the thruster channel. This explanation can also be argued by the greater perturbation to the thruster discharge current for the centerline and outer wall sweeps, since this region of the discharge channel is where most of the Hall current is for the P5 thruster [149].

Another possible explanation, though less likely, for the observed disturbances in the discharge current is thermal expansion of the magnetic circuit. However, this prospect was investigated by measuring the vacuum field profiles of the thruster before and immediately after the thruster was operated for an extended amount of time. No discernable changes in the vacuum field profiles were observed during the analysis of the data (not shown).

One final possibility for the measured difference in the results from the vacuum and plasma discharge profiles is that the B-Dot probe output voltage is perturbed by the high electric field in the discharge channel of the thruster. Several precautions were addressed during the fabrication and calibration of the B-dot probe system. The first was to place the integrator circuit as near as possible to the probe, which meant that the integrator was located in the shroud that covers the HARP table. There was no indication, from the baseline sweeps of the HARP table and the B-Dot system, of electrostatic interference in the probe or the circuit from the operation of the HARP table alone. Another precaution addressed was to add a low resistance to the output of the B-Dot probe through the selection of the transmission lines and circuit design, thus effectively providing the B-Dot probe with a voltage divider for any unavoidable electrostatic pickup [156]. The final precaution was to calibrate the B-Dot system with an **ExB** source as described earlier. It was shown in FIG. 4 that as the B-Dot probe swept the **ExB** source with either a known applied magnetic, static or time-varying electric fields that there was no indication of the probe being affected by the presence of a large electric field.

## Discussion

To understand the data presented in this paper several avenues were investigated. The first approach was to make use of recent Hall parameter calculations inside the discharge chamber of a Hall thruster [106, 149], which determined that the Hall parameter could be as high as 1000 at the exit of the discharge channel. The Hall parameter is defined as the ratio between the azimuthal electron current (Hall current,

$I_{Hall}$ ) and transverse electron current ( $I_{ez}$ ) and the ratio of the transverse current region ( $A_{ez}$ ) to the Hall current region ( $A_{Hall}$ ) as seen in the following expression.

$$\Omega = \frac{j_{Hall}}{j_{ez}} = \frac{I_{Hall}}{I_{ez}} \frac{A_{ez}}{A_{Hall}} \quad (3)$$

The axial electron current ranges from 25 to 30 percent of the discharge current [84] for the P5 Hall thruster. Assuming the majority of the Hall current resides in a region near the exit of the discharge channel and encompasses the width of the channel, and given a Hall parameter of 1000, we find that the Hall current is on the order of 90 A. A simple calculation for a self magnetic field, induced by the Hall current, can be made using the Biot-Savart law for a current flowing in a long straight wire. This first-order calculation yields an induced self-field of approximately 15 Gauss 7 mm downstream of the center of the prescribed Hall current region.

The first order calculation of the self-field does not express the overall mechanism of the induced magnetic field profile in a Hall thruster. The Hall thruster applied magnetic field topography is a consequence of the design of the system magnetic circuit. It is known that changing one component of the magnetic circuit (e.g. screen length, thickness, or width) could lead to considerable modification to the magnetic field topography in the channel of a thruster [71]. To address the concerns of a self-field influence on the applied magnetic field, a 3D magnetostatic simulation using Magnet6 by Infolytica was performed. Figure 9 is an illustration of the 3D model used in the simulation.

The model of the P5 Hall thruster, presented in Fig. 9, was created to simulate the influence that the Hall current self-field has on the applied magnetic field from the region 10 to 100 mm downstream of the anode. The area of investigation continued past the exit of the discharge channel since it has been shown that a good portion of the ion acceleration occurs past the thruster exit [149, 160]. Therefore, this region was investigated as another source of self-field for the thruster. The 3D model also took into account the influence of the induced self-fields from each Hall current region on a single point of interest. The Hall current for this simulation was determined in a similar manner as in the first order calculation presented above, except five sets of Hall parameter data across the channel width and ranging from 10 to 100 mm downstream of the anode was used. To reduce the computational time and model complexity, the calculated Hall current profiles were interpolated to 90 regions, approximately 5 mm by 5 mm each, as seen in Fig. 9. The sum current for all the Hall current regions inside and outside of the discharge channel equated to a total Hall current of 156 A, which was different than the predicted 27 to 54 amps for the P5 operating at 5.4 A [60]. The ratio of the Hall to the discharge currents for the calculated Hall current above was  $I_{\text{Hall}}/I_d = 28.8$ . This ratio indicated that the average Hall parameter for the P5 thruster, for the 90 regions method, was approximately 478 ( $\Omega \approx 478$ ). The main difference in the Hall parameter for the P5, as compared to the value given by Kim [60], was that the calculation of the Hall parameter accounted for the ion acceleration that occurs downstream of the exit plane. Figure 10 illustrates the axial profiles of the calculated Hall current for five radial sweeps across the discharge channel and the sum of the Hall current as a function of axial

position. The self-field modeling results for the 300 V 5.4 A thruster discharge condition is presented in Fig. 11.

As can be seen in Fig. 11, the model predicts a change in the radial magnetic field profile along the center of the discharge channel. Similar results are obtained for the 300 V and 10 A thruster condition (not shown). However, these observed changes are not as large as the measured field profiles from the B-Dot probe. This could possibly be due to the technique used to calculate the Hall current from the Hall parameters, a problem with the calculated Hall parameters, or the B-Dot probe measurements.

Another issue that has not been discussed in this paper, so far, is the possibility of a dielectric sheath forming around the probe [161, 162]. Since the probe is constructed of a dielectric material and is inserted into the discharge plasma of a thruster, the azimuthal electron current would dominate the collisions with the probe surface thus establishing a negative sheath that might redirect the Hall current around the probe. The threshold electron energy for the establishment of an electron-repellant sheath for alumina has been measured to be approximately 20 eV [162]. According to the measurements by Haas in Ref. [149] the peak electron drift energy for the 1.6 kW case was upwards of 25 eV and the observed electron thermal energy had a maximum of 40 eV. The presence of a negative sheath encompassing the probe could increase the electron current density to either side of the probe, thereby changing the normal Hall current profile, and therefore the local magnetic field. The dielectric sheath thickness is on the order of a Debye length, which is approximately 0.05 mm for the internal plasma parameters of the P5 thruster operating a 1.6 kW. The sheath thickness is not large compared to the size of the

probe, but the probe and the thin sheath could sway the profile of the Hall current. A Magnet6 model was created to test the possibility of this modified Hall current. The results from the model (data not shown) did not indicate a significant change in the self-field radial magnetic field profile as seen in Fig. 11. A final issue with a dielectric probe is that it could be absorbing high-energy electrons and re-emitting low temperature electrons through secondary electron emission [163]. According to Ref. [162] the maximum secondary electron emission coefficient for alumina is 4.8 for electrons impacting at normal incidence and at 1300 eV. At the drift and thermal energies of the electrons measured in the P5 thruster (25-40 eV), the general trend is for the secondary electron emission coefficient to be less than unity [162]. The formation of a negative sheath around the probe would prohibit a majority of the primary electrons from reaching the probe and thereby limit the influence of secondary electron emission.

The predicted thrust, for a Hall thruster, can be obtained analytically from the magnetohydrodynamic (MHD) momentum equation shown in Eq. (4) and knowing the azimuthal Hall current ( $j_{\text{Hall}}$ ) in a given volume ( $V$ ) and the radial magnetic field ( $B_r$ ).

$$\mathbf{F} = -\nabla P + \rho_c \mathbf{E} + \mathbf{j} \times \mathbf{B} \quad (4)$$

Assuming that the electron pressure term ( $P$ ) is small and a quasineutral plasma ( $c=0$ ), Eq. (4) reduces to the following  $\mathbf{j} \times \mathbf{B}$  force.

$$F_y(r, z) = j_{Hall}(r, z)B_r(r, z)V(r, z) \quad (5)$$

Equation (5) can be used to calculate the thrust in each individual Hall current region, as described above, and then the total thruster can be found by summing all the regions. The calculated thrust for the Hall current shown in Fig. 10 using Eq. (5) and the measured radial magnetic field profiles from the B-Dot probe at the 1.6 kW plasma case is approximately 300 mN, which is much greater than the measured thrust of 98 mN [87]. When the Hall current density profiles from Ref. 5 are combined with the vacuum magnetic fields shown on Fig. 5, the resulting thrust predicted is 105 mN. The conclusion of this exercise is that a Hall current that is significantly large enough to produce the self-field observed in the B-Dot probe traces would equate to a thrust that is much larger than what is measured. However, other investigations have uncovered evidence that the Hall current may be significant in some cases. One such investigation involved the magnetic field integration impact testing of a D-55 TAL by NASA GRC for the RHETT2/EPDM program [164]. The magnetic dipole measured 1.28 m upstream of the thruster exit plane was observed to increase by 22% above the vacuum applied field during thruster operation at 300 V and 2.5 A. A Hall current of 50 A is required to produced the observed change in the axial magnetic field [165]. However, a Hall current of this magnitude would produce a thrust of 86 mN, which is twice the measured thrust of 43.2 mN [166]. Clearly, further investigations are needed before our understanding of the role that the Hall current plays in establishing the Hall thruster magnetic field topography becomes complete.

## SUMMARY

The magnetic field topography of the P5 Hall thruster was successfully mapped during operation of the thruster with a plasma discharge. The experimentally-mapped magnetic field profiles along the width of the discharge channel of a Hall thruster deviated from the vacuum field profile, previously measured with a Hall probe. The largest increase observed was approximately 70 G (70%) on the centerline sweep of the 1.6 kW operation condition. The Hall current of the P5 was then calculated from previously determined Hall parameters and incorporated into a 3D magnetostatic model to estimate the influence of the Hall current self-magnetic field on the applied magnetic field topography. The  $\mathbf{j} \times \mathbf{B}$  forces were then solved to establish if the Hall current required to influence the magnetic field topography, as observed in the B-Dot probe measurements, yields engine thrust levels that are consistent with those measured. The calculated thrust values from the  $\mathbf{j} \times \mathbf{B}$  force were 2 to 3 times the actual measured values at the given operating parameters. Several experiments and calculations were conducted to test the B-Dot probe system reliability under the plasma conditions of a typical Hall thruster discharge. The experiments and calculations did not demonstrate any conclusive evidence of a flaw in the design or methodology utilized for measuring the magnetic field discussed in this paper. Furthermore, the topic was complicated by documentation of independent non-intrusive magnetic dipole measurements of the D-55 TAL at NASA GRC. The magnetic dipole measurements of the D-55 show a 22% increase of the measured magnetic dipole when the discharge was ignited. It is clear that a better understanding of the influence of a Hall thruster self-field is required if higher-power thrusters are to be developed.

**Table I.** P5 thruster performance ranges for the experiments discussed in this work [19].

Case	Vd [V]	Id [A]	Power [kW]	Total Specific Impulse [sec]	Total Efficiency
(1)	300	5.4	1.6	1550	48%
(2)	300	10.1	3.0	1650	51%



**FIG. 1.** P5, 5 kW class laboratory model Hall thruster.

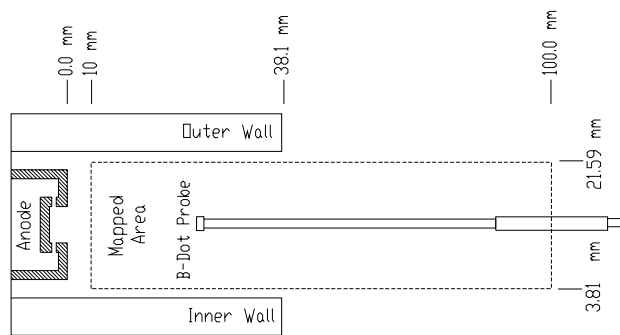


**FIG. 2.** B-Dot probes mapped area inside and outside of the P5 discharge channel.

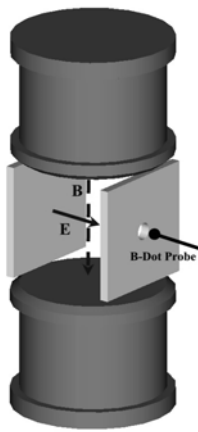


**FIG. 3.** The **ExB** source configuration.

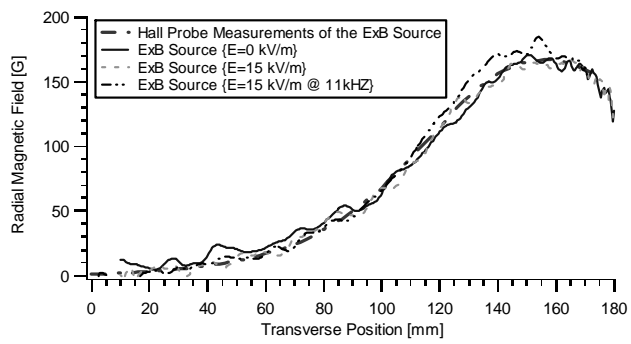


**FIG. 4.** B-Dot and Hall probe measurements of the **ExB** source at atmospheric pressure [ $I_{\text{Coil}} = 9 \text{ A}$ ].

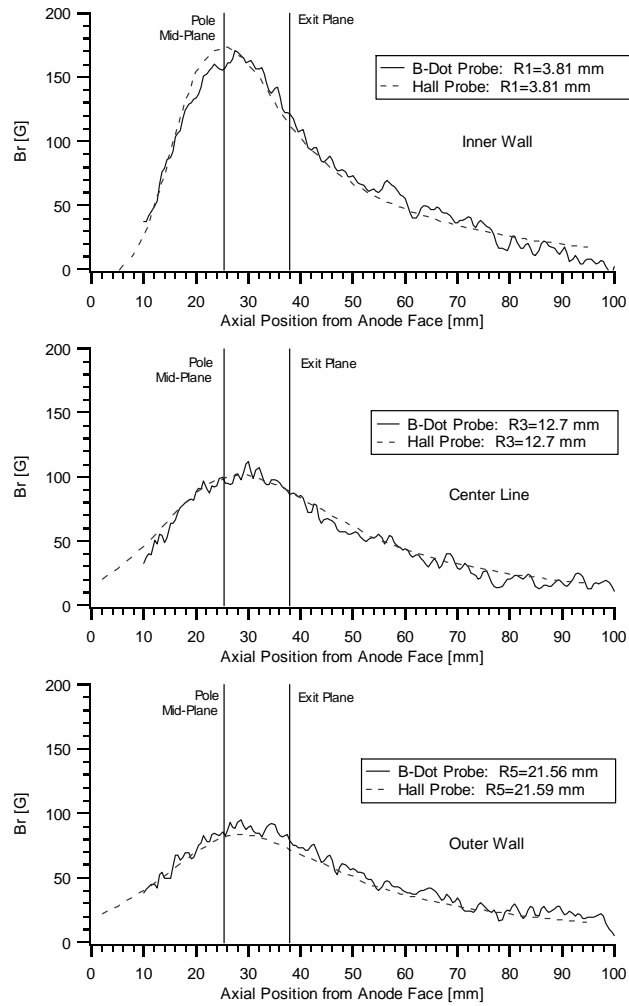


**FIG. 5.** Vacuum magnetic field profiles of the P5 at

1.6 kW [ $I_{in} = 2$  A,  $I_{out} = 1$  A]

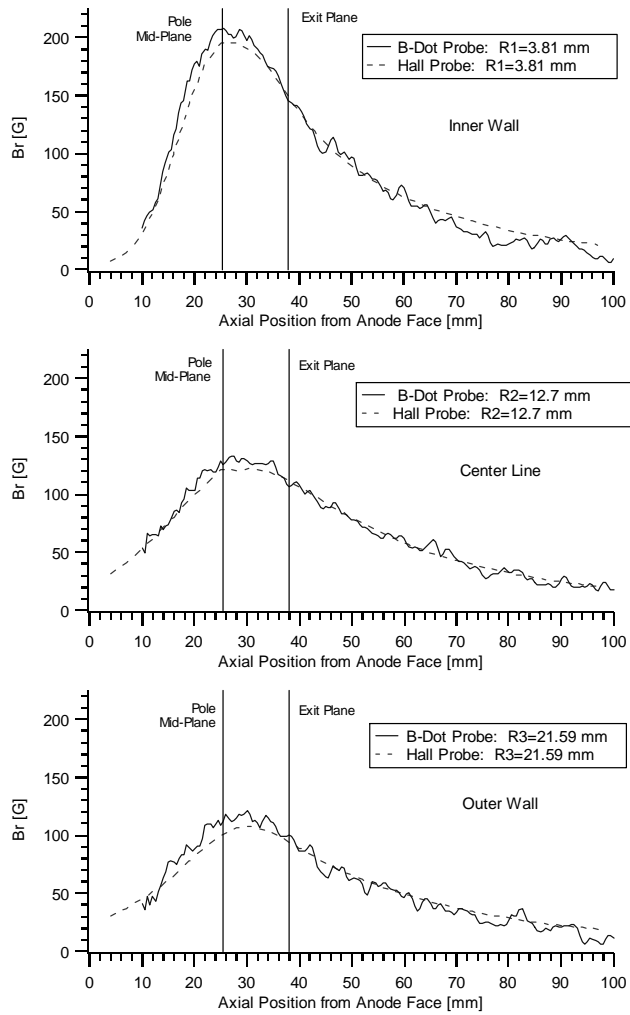


**FIG. 6.** Vacuum magnetic field profile of the P5 at

3.0 kW [ $I_{in} = 3$  A,  $I_{out} = 2$  A]

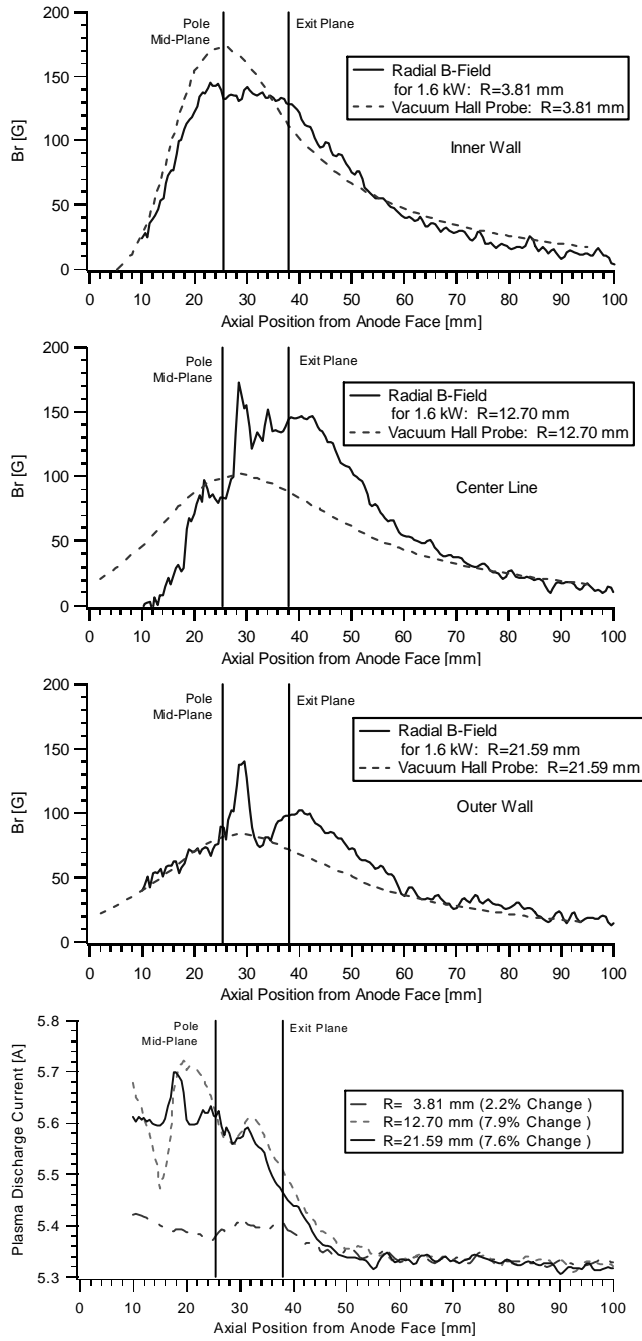


**FIG. 7.** B-Dot probe magnetic field data at 1.6 kW and thruster discharge current as a function of probe position.

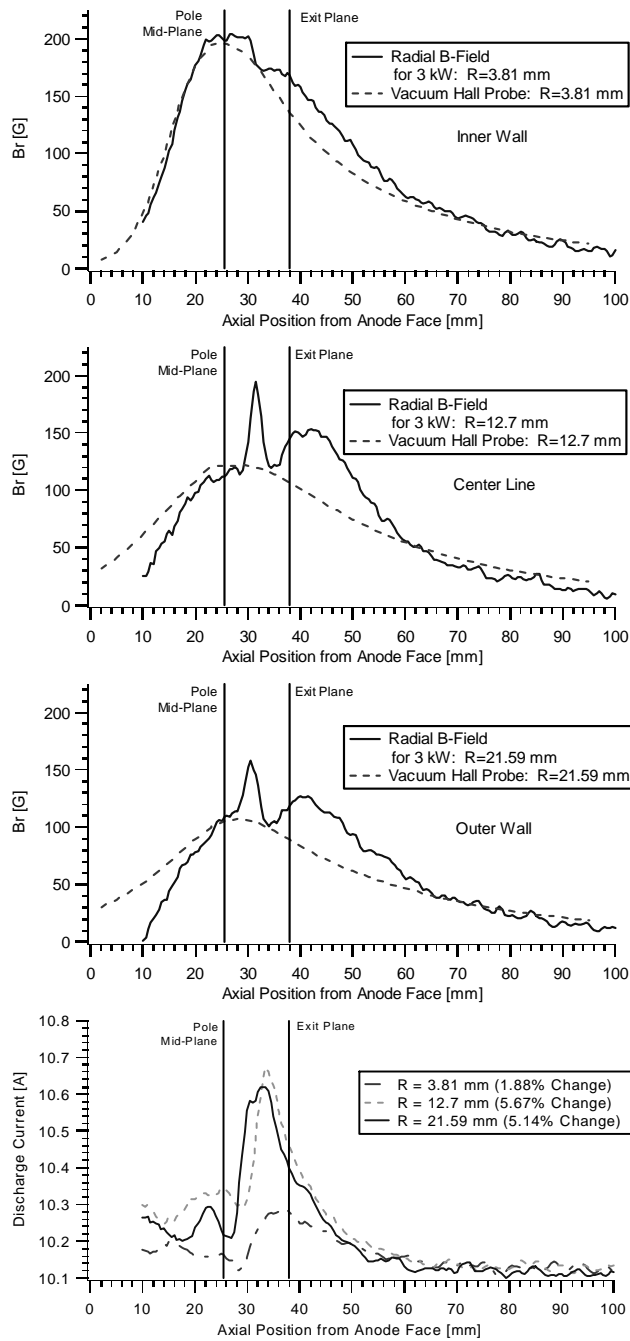


**FIG. 8.** B-Dot probe magnetic field data at 3.0 kW and thruster discharge current as a function of probe position.

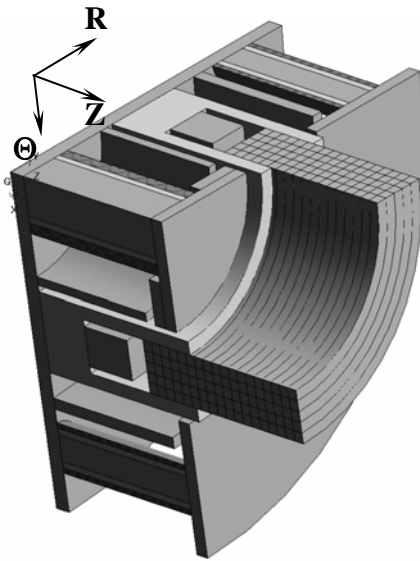


**FIG. 9.** The 3D quarter model used in Magnet6 to simulate P5 self-fields.

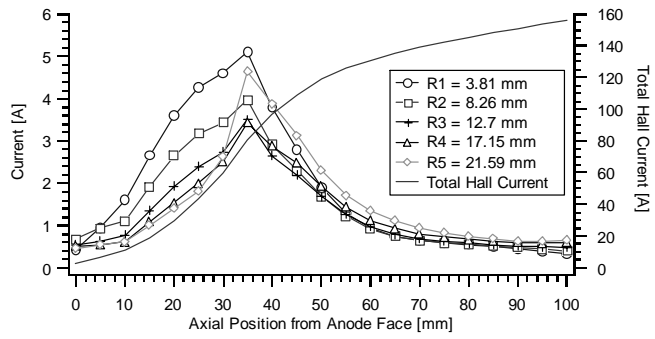


**FIG. 10.** The calculated Hall current radial profiles across the discharge channel and the sum of the profiles as a function of axial position (note that the thruster exit is at 38 mm).

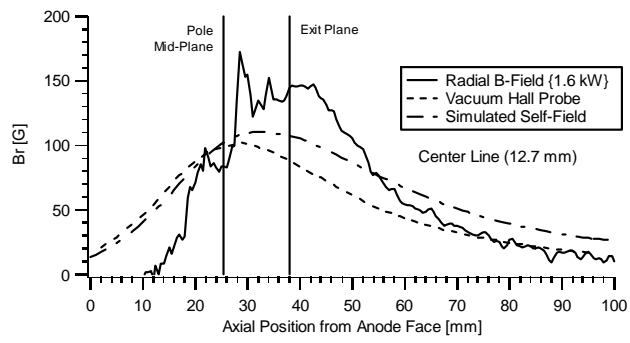


**FIG. 11.** The simulated self-field for the P5 operating at 1.6 kW.

## BIBLIOGRAPHY

- [1] E. Stuhlinger, *Ion Propulsion for Space Flight*. New York: McGraw-Hill, 1964.
- [2] R. G. Jahn, *Physics of Electric Propulsion*. McGraw-Hill Book Company, 1968.
- [3] K. Komurasaki, "An Overview of Electric Propulsion Activities in Japan," presented at Joint Propulsion Conference, Huntsville, Alabama, 2003.
- [4] J. Blandino, N. Gatsonis, M. Cappelli, A. Gallimore, I. Boyd, R. Burton, M. Martinez-Sanchez, O. Batischev, J. Williams, A. P. Yalin, P. J. Wilbur, P. Wilbur, R. Winglee, P. Mikellides, N. Fisch, Y. Raitses, E. Choueiri, S. Roy, and J. Wang, "Overview of Electric Propulsion Research in U.S. Academia," presented at Joint Propulsion Conference, AIAA-03-4442, Huntsville, Alabama, 2003.
- [5] V. Hruby, "Review of Electric Propulsion Activities in the US Industry," presented at Joint Propulsion Conference, AIAA-03-4441, Huntsville, Alabama, 2003.
- [6] V. Kim, G. Popov, S. Tverdokhlebov, A. Semenkin, V. Garkusha, V. Murashko, A. Koryakin, A. Nyatin, A. Romashko, Y. Yermoshkin, V. Petrusevich, O. Gorshkov, A. Koroteyev, and A. Nadiradze, "Overview of Russian EP Activities," presented at Joint Propulsion Conference, AIAA-03-4440, Huntsville, Alabama, 2003.
- [7] K. Komurasaki, "An Overview of Electric Propulsion Activities in Japan," presented at Joint Propulsion Conference, AIAA-03-5272, Huntsville, Alabama, 2003.
- [8] M. J. Patterson, J. E. Foster, T. W. Haag, L. Pinero, and G. C. Soulas, "Ion Propulsion Development Activities at the NASA Glenn Research Center," presented at Joint Propulsion Conference, AIAA-03-4709, Huntsville, Alabama, 2003.
- [9] J. E. Polk, D. Goebel, J. R. Brophy, J. Beatty, J. Monheiser, D. Giles, D. Hobson, F. Wilson, J. Christensen, M. D. Pano, S. Hart, W. Ohlinger, D. N. Hill, J. Williams, P. Wilbur, D. M. Laufer, and C. Farnell, "An Overview of the Nuclear Electric Xenon Ion System (NEXIS) Program," presented at Joint Propulsion Conference, AIAA-03-4713, Huntsville, Alabama, 2003.

- [10] G. Saccoccia and J. Gonzalez, "European Activities in Electric Propulsion," presented at Joint Propulsion Conference, Huntsville, Alabama, 2003.
- [11] S. Nakanishi and E. V. Pawlik, "Experimental Investigation of a 1.5 M Diameter Kaufman Thruster," *Journal of Spacecraft*, Vol. 5, No. 7, pp. 801-807, 1968.
- [12] M. Martinez-Sanchez and J. E. Pollard, "Spacecraft Electric Propulsion--An Overview," *Journal of Propulsion and Power*, Vol. 14, No. 5, pp. 688-699, 1998.
- [13] V. K. Rawlin, G. J. Williams, and R. F. Roman, "High Specific Impulse, High Power Ion Engine Operation," presented at Joint Propulsion Conference, Indianapolis, Indiana, 2002.
- [14] B. E. Beal, "Clustering of Hall Effect Thrusters for High-Power Electric Propulsion Applications," in *Department of Aerospace Engineering*. Ann Arbor, MI: The University of Michigan, 2004.
- [15] F. S. Gulczinski and J. H. Schilling, "Comparison of Orbit Transfer Vehicle Concepts Utilizing Mid-Term Power and Propulsion Options," presented at Internal Electric Propulsion Conference, IEPC-03-022, Toulouse, France, 2003.
- [16] S. R. Oleson, "Electric Propulsion for Low Earth Orbit Communications Satellites," presented at Internal Electric Propulsion Conference, IEPC-97-102, Cleveland, OH, 1997.
- [17] S. R. Oleson and R. M. Myers, "Advanced Propulsion for Geostationary Orbit Insertion and North-South Station Keeping," *Journal of Spacecraft and Rockets*, Vol. 34, No. 1, pp. 22-28, 1997.
- [18] S. R. Oleson, "Mission Advantages of Constant Power, Variable Isp Electrostatic Thrusters," presented at Joint Propulsion Conference, AIAA-00-3413, Huntsville, AL, 2000.
- [19] S. R. Oleson and S. W. Benson, "Electric Propulsion for International Space Station Reboost: A Fresh Look," presented at Joint Propulsion Conference, AIAA-01-3644, Salt Lake City, UT, 2001.
- [20] J. W. Dunning and R. S. Jankovsky, "NASA's Electric Propulsion Program," presented at Joint Propulsion Conference, AIAA-03-4437, Huntsville, Alabama, 2003.
- [21] R. A. Spores and M. Birkan, "Overview of USAF Electric Propulsion Program," presented at Joint Propulsion Conference, AIAA-02-3558, Indianapolis, Indiana, 2002.
- [22] J. W. Dunning and S. W. Benson, "NASA's Electric Propulsion Program," presented at Joint Propulsion Conference, AIAA-02-3557, Indianapolis, Indiana, 2002.

- [23] R. S. Jankovsky, D. T. Jacobson, C. J. Sarmiento, L. R. Piñero, D. H. Manzella, R. R. Hofer, and P. Y. Peterson, "NASA's Hall Thruster Program 2002," presented at Joint Propulsion Conference, AIAA-02-3675, Indianapolis, Indiana, 2002.
- [24] R. G. Jahn and E. Y. Choueiri, "Electric Propulsion," in *Encyclopedia of Physical Science and Technology*, vol. 5, Third ed: Academia Press, 2002, pp. 125-141.
- [25] S. Nakanishi and E. V. Pawlik, "Experimental Investigation of a 1.5 M Diameter Kaufman Thruster," presented at AIAA, 1967.
- [26] S. Oleson and I. Katz, "Electric Propulsion for Project Prometheus," presented at Joint Propulsion Conference, AIAA-03-5279, Huntsville, Alabama, 2003.
- [27] D. Manzella, D. Jacobson, P. Peterson, and R. Hofer, "Scaling Hall Thrusters to High Power," presented at JANNAF, Las Vegas, NV, 2004.
- [28] R. R. Hofer and R. S. Jankovsky, "The Influence of Current Density and Magnetic Field Topography in Optimizing the Performance, Divergence, and Plasma Oscillations of High Specific Impulse Hall Thrusters," presented at Internal Electric Propulsion Conference, IEPC-03-142, Toulouse, France, 2003.
- [29] D. T. Jacobson, R. S. Jankovsky, V. K. Rawlin, and D. H. Manzella, "High Voltage TAL Performance," presented at Joint Propulsion Conference, AIAA-01-3777, Salt Lake City, UT, 2001.
- [30] D. Manzella and D. Jacobson, "Investigation of Low-Voltage/High-Thrust Hall Thruster Operation," presented at Joint Propulsion Conference, AIAA-03-5004, Huntsville, Alabama, 2003.
- [31] D. Jacobson and D. Manzella, "50 kW Class Krypton Hall Thruster Performance," presented at Joint Propulsion Conference, AIAA-03-4550, Huntsville, Alabama, 2003.
- [32] D. Manzella, R. Jankovsky, and R. Hofer, "Laboratory Model 50 kW Hall Thruster," presented at Joint Propulsion Conference, AIAA-02-3676, Indianapolis, Indiana, 2002.
- [33] J. R. Brophy, "NASA's Deep Space 1 Ion Engine," *Review of Scientific Instruments*, Vol. 73, No. 2, pp. 1071-1078, 2002.
- [34] P. J. Wilbur, V. K. Rawlin, and J. R. Beattie, "Ion Thruster Development Trends and Status in the United States," *Journal of Propulsion and Power*, Vol. 14, No. 5, pp. 708-715, 1998.
- [35] P. Wilbur, "Broad Beam Ion Sources," Course Notes for ME-567 at Colorado State University.

- [36] G. R. Brewer, *Ion Propulsion Technology & Applications*: Gordon and Breach Science Publishers, 1970.
- [37] V. N. Korovkin, L. A. Latyshev, V. A. Obukhov, and V. G. Grigoyan, "Research of Ion Thrusters in the USSR," presented at International Electric Propulsion Conference, IEPC-91-081, Viareggio, Italy, 1991.
- [38] W. R. Kerslake and L. R. Ignaczak, "Development and Flight History of SERT II Spacecraft," presented at Joint Propulsion Conference, AIAA-92-3516, 1992.
- [39] G. Saccoccia and J. Gonzalez, "European Activities in Electric Propulsion," presented at Joint Propulsion Conference, AIAA-03-5271, Huntsville, Alabama, 2003.
- [40] M. T. Domonkos, "Evaluation of Low-Current Orificed Hollow Cathodes," in *Department of Aerospace Engineering*. Ann Arbor, MI: The University of Michigan, 1999.
- [41] J. S. Sovey, "Improved Ion Containment Using a Ring-Cusp Ion Thruster," *Journal of Spacecraft*, Vol. 21, No. 5, pp. 488-495, 1983.
- [42] J. E. Foster and M. J. Patterson, "Characterization of a 40 cm Microwave Ion Thruster," presented at Joint Propulsion Conference, AIAA-03-5012, Huntsville, Alabama, 2003.
- [43] M. J. Patterson, M. T. Domonkos, J. E. Foster, T. W. Haag, G. C. Soulas, and S. Kovaleski, "NEXT: NASA's Evolutionary Xenon Thruster Development Status," presented at Joint Propulsion Conference, AIAA-03-4862, Huntsville, Alabama, 2003.
- [44] M. J. Patterson, J. E. Foster, T. W. Haag, G. C. Soulas, and R. Roman, "NEXT: NASA's Evolutionary Xenon Thruster," presented at Joint Propulsion Conference, AIAA-02-3832, Indianapolis, Indiana, 2002.
- [45] F. F. Chen, *Introduction to Plasma Physics and Controlled Fusion: Plasma Physics.*, 2nd ed. ed: Plenum Publishing, 1984.
- [46] J. E. Foster, R. Roman, G. C. Soulas, and M. J. Patterson, "Electron Backstreaming Mitigation via a Magnetic Grid," presented at International Electric Propulsion Conference, IEPC-01-091, Pasadena, Ca, 2001.
- [47] J. Williams, D. Goebel, and P. Wilbur, "Analytical Model of electron Backstreaming for Ion Thrusters," presented at Joint Propulsion Conference, AIAA-03-4560, Huntsville, Alabama, 2003.
- [48] H. Kuninaka, I. Funaki, and K. Toki, "Life Test of Microwave Discharge Ion Thrusters for MUSES-C in Engineering Model Phase," presented at Joint Propulsion Conference, AIAA-99-2439, Los Angeles, Ca, 1999.

- [49] J. E. Polk, D. Brinza, R. Y. Kakuda, J. R. Brophy, I. Katz, J. R. Anderson, V. K. Rawlin, M. J. Patterson, J. S. Sovey, and J. Hamley, "Demonstration of the NSTAR Ion Propulsion System on the Deep Space One Mission," presented at International Electric Propulsion Conference, IEPC-01-075, Pasadena, Ca, 2001.
- [50] J. E. Polk, R. Y. Kakuda, J. R. Anderson, J. R. Brophy, V. K. Rawlin, M. J. Patterson, J. S. Sovey, and J. Hamley, "Validation of the NSTAR Ion Propulsion System on the Deep Space One Mission: Overview and Initial Results," presented at Joint Propulsion Conference, AIAA-99-2274, Los Angeles, Ca, 1999.
- [51] A. Sengupta, J. R. Brophy, and K. D. Goodfellow, "Status of the Extended Life Test of the Deep Space 1 Flight Spare Ion Engine after 30,352 Hours of Operation," presented at Joint Propulsion Conference, AIAA-03-4558, Huntsville, Alabama, 2003.
- [52] M. A. Cappelli, Q. E. Walker, N. B. Meezan, and W. A. Hargus, "Performance of a Linear Hall Discharge with an Open Electron Drift," presented at Joint Propulsion Conference, AIAA-01-3503, Salt Lake City, UT, 2001.
- [53] B. E. Beal and A. D. Gallimore, "Development of the Linear Gridless Ion Thruster," presented at Joint Propulsion Conference, AIAA-01-3649, Salt Lake City, UT, 2001.
- [54] B. Pote, V. Hruby, and R. Tedrake, "Performance of A Multi-Kilowatt Non-Circular Discharge Hall Thruster," presented at Joint Propulsion Conference, AIAA-00-3249, Huntsville, AL, 2000.
- [55] Y. Yamagiwa and K. Kuriki, "Performance of Double-Stage Discharge Hall Ion Thruster," *Journal of Propulsion*, Vol. 7, No. 1, pp. 65-70, 1991.
- [56] S. D. Grishin, V. S. Erofeev, A. V. Zharinov, V. P. Naumkin, and I. N. Safronov, "Characteristics of a Two-Stage Ion Accelerator with an Anode Layer,," *Journal of Applied Mathematics and Technical Physics*, No. 2, pp. 28-36, 1978.
- [57] A. I. Morozov, A. I. Bugrova, A. D. Desiatskov, V. K. Kharchevnikov, M. Prioul, and L. Jolivet, "Research on Two-Stage Engine SPT-MAG," presented at Internal Electric Propulsion Conference, IEPC-03-290, Toulouse, France, 2003.
- [58] S. O. Tverdokhlebov, A. V. Semenkin, and J. E. Polk, "Bismuth Propellant Option for Very High Power TAL Thruster," presented at Joint Propulsion Conference, AIAA-02-0348, Indianapolis, Indiana, 2002.
- [59] V. V. Zhurin, H. R. Kaufman, and R. S. Robinson, "Physics of Closed Drift Thrusters," *Plasma Sources Science and Technology*, Vol. 8, No. 1, pp. R1-R20, 1999.

- [60] V. Kim, "Main Physical Features and Processes Determining the Performance of Stationary Plasma Thrusters," *Journal of Propulsion and Power*, Vol. 14, No. 5, pp. 736-743, 1998.
- [61] R. Hofer, J. M. Haas, and A. D. Gallimore, "Ion Voltage Diagnostics in the Far-Field Plume of a High-Specific Impulse Hall Thruster," presented at Joint Propulsion Conference, AIAA-03-4556, Huntsville, Alabama, 2003.
- [62] E. Y. Choueiri, "Fundamental difference between the two Hall thruster variants," *Physics of Plasmas*, Vol. 8, No. 11, pp. 5025-5033, 2001.
- [63] R. Hofer and J. R., "A Hall Thruster Performance Model Incorporating the Effects of a Multiply-Charged Plasma," presented at Joint Propulsion Conference, AIAA-01-3322, Salt Lake City, UT, 2001.
- [64] R. R. Hofer, "Development and Characterization of High-Efficiency, High-Specific Impulse Xenon Hall Thrusters," in *Department of Aerospace Engineering*. Ann Arbor, MI: The University of Michigan, 2004.
- [65] L. B. King and A. D. Gallimore, "Mass Spectral Measurements in the Plume of an SPT-100 Hall Thruster," *Journal of Propulsion and Power*, Vol. 16, No. 6, pp. 1086-1092, 2000.
- [66] F. S. Gulczinski and A. D. Gallimore, "Field Ion Energy and Species Measurements of a 5-kW Hall Thruster," *Journal of Propulsion and Power*, Vol. 17, No. 2, pp. 418-427, 2001.
- [67] A. Fruchtman, N. J. Fisch, and Y. Raitses, "Hall Thruster with Absorbing Electrodes," presented at Joint Propulsion Conference, AIAA-00-3659, Huntsville, AL, 2000.
- [68] N. J. Fisch, Y. Raitses, A. A. Litvak, and L. A. Dorf, "Design and Operation of Hall Thruster with Segmented Electrodes," presented at Joint Propulsion Conference, AIAA-99-2572, Los Angeles, Ca, 1999.
- [69] N. J. Fisch, Y. Raitses, A. A. Litvak, and L. A. Dorf, "Segmented Electrode Hall Thruster Operation in Single and Two Stage Regimes," presented at International Electrical Propulsion Conference, IEPC-99-101, Kitakyushu, Japan, 1999.
- [70] N. J. Fisch, Y. Raitses, L. A. Dorf, and A. A. Litvak, "Variable Operation of Hall thruster with Multiple Segmented Electrodes," *Journal of Applied Physics*, Vol. 89, No. 4, pp. 2040-2046, 2001.
- [71] R. Hofer, P. Peterson, and A. Gallimore, "A High Specific Impulse Two-Stage Hall Thruster with Plasma Lens Focusing," presented at International Electric Propulsion Conference, IEPC-01-036, Pasadena, Ca, 2001.

- [72] P. Molina-Morales, H. Kuninaka, K. Toki, and Y. Arakawa, "Preliminary Study of an ECR Discharge Hall Thruster," presented at International Electric Propulsion Conference, IEPC-01-069, Pasadena, Ca, 2001.
- [73] B. Pote and R. Tedrake, "Performance of a High Specific Impulse Hall Thruster," presented at International Electric Propulsion Conference, IEPC-01-35, Pasadena, Ca, 2001.
- [74] J. Szabo, N. Warner, and M. Martinez-Sanchez, "Instrumentation and Modeling of a High Specific Impulse Hall Thruster," presented at Joint Propulsion Conference, AIAA-02-4248, Indianapolis, Indiana, 2002.
- [75] A. E. Solodukhin, A. V. Semenkin, S. O. Tverdohlebov, and A. V. Kochergin, "Parameters of D-80 Anode Layer Thruster in One- and Two- Stage Operation Modes," presented at International Electric Propulsion Conference, IEPC-01-032, Pasadena, Ca, 2001.
- [76] C. E. Garner, J. E. Polk, J. R. Brophy, C. Marrese, S. Semenkin, and S. Tverdokhlebov, "Experimental Evaluation of a Russian Anode Layer Thruster," presented at 3rd Russian-German Conference on Electric Propulsion Engines and their Technical Applications, 1994.
- [77] S. O. Tverdokhlebov and V. Garkusha, "High-Voltage Mode of a TAL Thruster Operation," presented at Internal Electric Propulsion Conference, IEPC-97-023, Cleveland, OH, 1997.
- [78] D. Jacobson and Jankovsky R., "Performance Evaluation of a 50 kW Hall Thruster," presented at Aerospace Sciences Meeting and Exhibit, AIAA-99-0457, 1999.
- [79] K. D. Diamant, J. E. Pollard, R. B. Cohen, Y. Raitses, and N. J. Fisch, "Plume Characteristics of the PPPL Segmented Electrode Hall Thruster," presented at Joint Propulsion Conference, AIAA-03-5159, Huntsville, Alabama, 2003.
- [80] Y. Raitses, D. Staack, and N. J. Fisch, "Plasma Characterization of Hall Thruster with Active and Passive Segmented," presented at Joint Propulsion Conference, AIAA-02-3954, Indianapolis, Indiana, 2002.
- [81] Y. Raitses, D. Staack, A. Smirnov, A. A. Litvak, L. A. Dorf, T. Graves, and N. J. Fisch, "Studies of Non-Conventional Configuration Closed Electron Drift Thrusters," presented at Joint Propulsion Conference, AIAA-01-3774, Salt Lake City, UT, 2001.
- [82] Y. Raitses, L. A. Dorf, A. A. Litvak, and N. J. Fisch, "Plume Reduction in Segmented Electrode Hall Thruster," *Journal of Applied Physics*, Vol. 88, No. 3, pp. 1263-1270, 2000.

- [83] Y. Raitses, L. A. Dorf, A. A. Litvak, and N. J. Fisch, "Parametric Investigations of Segmented Electrode Hall Thruster," presented at International Electrical Propulsion Conference, IEPC-99-245, Kitakyushu, Japan, 1999.
- [84] R. Hofer and R. Jankovsky, "A Hall Thruster Performance Model Incorporating the Effects of a Multiply-Charged Plasma," presented at Joint Propulsion Conference, AIAA-01-3322, Salt Lake City, UT, 2001.
- [85] C. Mclean, J. McVey, and D. T. Schappell, "Testing of a U.S.-built HET system for orbit transfer applications," presented at Joint Propulsion Conference, AIAA-99-2574, Los Angeles, Ca, 1999.
- [86] B. Pote, V. Hruby, and J. Monheiser, "Performance of an 8 kW Hall Thruster," presented at International Electrical Propulsion Conference, IEPC-99-080, Kitakyushu, Japan, 1999.
- [87] J. M. Haas, F. S. G. III, and A. D. Gallimore, "Performance characteristics of a 5 kW laboratory Hall thruster," presented at Joint Propulsion Conference, AIAA-98-3503, Cleveland, Oh, 1998.
- [88] M. B. Belikov, O. A. Gorshkov, R. N. Rizakhanov, A. A. Shagaida, and S. A. Khartov, "Hall-type low- and mean-power thrusters output parameters," presented at Joint Propulsion Conference, AIAA-99-2571, Los Angeles, Ca, 1999.
- [89] R. Hofer and A. D. Gallimore, "The Role of Magnetic Field Topography in Improving the Performance of High-Voltage Hall Thrusters," presented at Joint Propulsion Conference, AIAA-02-4111, Indianapolis, Indiana, 2002.
- [90] D. Q. King, K. H. d. Grys, and J. R., "Multi-mode Hall thruster development," presented at Joint Propulsion Conference, AIAA-01-3778, Salt Lake City, UT, 2001.
- [91] J. Gallardo and E. Ahedo, "Effects of an Intermediate Emissive Cathode on the Hall Thruster Discharge," presented at Joint Propulsion Conference, AIAA-02-4112, Indianapolis, Indiana, 2002.
- [92] F. Parra and E. Ahedo, "Study of the Hall Thruster discharge with an Intermediate Electrode," presented at Joint Propulsion Conference, AIAA-03-4703, Huntsville, Alabama, 2003.
- [93] H. R. Kaufman, "Technology of Closed-Drift Thrusters," *AIAA Journal*, Vol. 23, No. 1, pp. 78-87, 1985.
- [94] D. H. Manzella, D. T. Jacobson, and R. S. Jankovsky, "High Voltage SPT Performance," presented at Joint Propulsion Conference, AIAA-01-3774, Salt Lake City, UT, 2001.

- [95] D. Jacobson, "High Voltage TAL Erosion Characterization," presented at Joint Propulsion Conference, AIAA-02-4257, Indianapolis, Indiana, 2002.
- [96] P. Peterson and D. Manzella, "Investigation of the Erosion Characteristics of a Laboratory Hall Thruster," presented at Joint Propulsion Conference, AIAA-03-5005, Huntsville, Alabama, 2003.
- [97] C. Marrese, J. E. Polk, L. B. King, A. D. Gallimore, C. Garner, S. Semenkin, V. Garkusha, and S. Tverdokhlebov, "Analysis of Anode Layer Thruster Guard Ring Erosion," presented at Internal Electric Propulsion Conference, IEPC-95-196, Moscow, Russia, 1995.
- [98] G. W. Butler, J. L. Yuen, S. O. Tverdokhlebov, A. V. Semenkin, A. V. Kochergin, A. E. Solodukhin, and R. S. Jankovsky, "Multimode, High Specific Impulse Hall Thruster Technology," presented at Joint Propulsion Conference, AIAA-00-3254, Huntsville, AL, 2000.
- [99] V. M. Gavryshin, V. Kim, V. I. Kozlov, and N. A. Maslennikov, "Physical and Technical Bases of the Modern SPT Development," presented at Internal Electric Propulsion Conference, IEPC-97-, Moscow, Russia, 1995.
- [100] A. I. Bugrova, A. I. Morozov, A. S. Lipatov, A. M. Bishaev, V. K. Kharchevnikov, and M. V. Kozintseva., "Integral and Spectral Characteristics of ATON Stationary Plasma Thruster Operating On Krypton and Xenon," presented at Internal Electric Propulsion Conference, IEPC-03-366, Toulouse, France, 2003.
- [101] C. Marrese, J. M. Haas, M. T. Domonkos, A. D. Gallimore, S. O. Tverdohlebov, and C. Garner, "The D-100 Performance and Plume Characterization on Krypton," presented at Joint Propulsion Conference, AIAA-96-2969, Lake Buena Vista, FL, 1996.
- [102] V. Kim, D. Grdlichko, V. Kozlov, A. Lazourenko, G. Popov, and A. Skrylnikov, "Local Plasma Parameter Measurements by Nearwall Probes Inside the SPT Accelerating Channel Under Thruster Operation with Kr," presented at Joint Propulsion Conference, AIAA-02-4108, Indianapolis, Indiana, 2002.
- [103] V. Kim, G. Popov, V. Kozlov, A. Skrylnikov, and D. Grdlichko, "Investigation of SPT Performance and Particularities of it's Operation with Kr and Kr/Xe Mixtures," presented at International Electric Propulsion Conference, IEPC-01-065, Pasadena, Ca, 2001.
- [104] L. Biagioni, M. Saverdi, and M. Andrenucci, "Scaling and Performance Prediction of Hall Effect Thrusters," presented at Joint Propulsion Conference, AIAA-03-4727, Huntsville, Alabama, 2003.
- [105] N. B. Meezan and M. A. Cappelli, "Electron Energy Distribution Function in a Hall Discharge Plasma," presented at Joint Propulsion Conference, AIAA-01-3326, Salt Lake City, UT, 2001.

- [106] N. B. Meezan and M. A. Cappelli, "Electron Density Measurements for Determining the Anomalous Electron Mobility in a Coaxial Hall Discharge Plasma," presented at Joint Propulsion Conference, AIAA-00-3420, Huntsville, AL, 2000.
- [107] J. M. Haas, "Low-Perturbation Interrogation of the Internal and Near-Field Plasma Structure of a Hall Thruster Using a High-Speed Probe Positioning System," in *Department of Aerospace Engineering*. Ann Arbor, MI: The University of Michigan, 2001.
- [108] P. Renaudin, V. Cagan, M. Guyot, A. Cadiou, P. Lasgorceix, M. Dudeck, V. Vial, and P. Dumazert, "Magnetic Circuits for Hall Thrusters: Use of Permanent Magnets," presented at Internal Electric Propulsion Conference, IEPC-03-284, Toulouse, France, 2003.
- [109] L. S. Mason, R. Jankovsky, and D. Manzella, "1000 Hours of Testing on a 10 Kilowatt Hall Effect Thruster," presented at Joint Propulsion Conference, AIAA-01-3773, Salt Lake City, UT, 2001.
- [110] F. S. Gulczinski, "Examination of the Structure and Evolution of Ion Energy Properties of a 5 Kw Class Laboratory Hall Effect Thruster at Various Operational Conditions," in *Department of Aerospace Engineering*. Ann Arbor, MI: The University of Michigan, 1999.
- [111] N. A. Maslenikov, "Russian Electric Propulsion Seminar." Massachusetts Institute of Technology, 1991.
- [112] A. Cohen-Zur, A. Fruchtman, J. Ashkenazy, and A. Gany, "Channel length and wall recombination effects in the Hall thruster," presented at Joint Propulsion Conference, AIAA-00-3654, Huntsville, AL, 2000.
- [113] V. Vial, A. Lazurenko, C. Laure, A. Bouchoule, and D. Pagnon, "Xenon Gas Injection in SPT Thrusters," presented at Internal Electric Propulsion Conference, IEPC-03-221, Toulouse, France, 2003.
- [114] L. Biagioni, M. Saverdi, M. Berti, U. Cesari, and M. Andrenucci, "Design and Preliminary Characterization of a 5 Kw Hall Thruster Prototype," presented at Internal Electric Propulsion Conference, IEPC-03-228, Toulouse, France, 2003.
- [115] J. W. Koo, I. D. Boyd, J. M. Haas, and A. D. Gallimore, "Computation of the interior and near-field flow of a 2-kW class Hall thruster," presented at Joint Propulsion Conference, AIAA-01-3321, Salt Lake City, UT, 2001.
- [116] S. Locke and J. M. Fife, "Effect of a channel wall discontinuity in an SPT-type Hall thruster," presented at Joint Propulsion Conference, AIAA-01-3327, Salt Lake City, UT, 2001.

- [117] N. Gascon, C. A. Thomas, W. A. Hermann, and M. A. Cappelli, "Operating regimes of a linear SPT with low secondary electron-induced wall conductivity," presented at Joint Propulsion Conference, AIAA-03-5156, Huntsville, Alabama, 2003.
- [118] Y. Garnier, V. Viel, J. F. Roussel, and J. Bernard, "Low-energy xenon ion sputtering of ceramics investigated for stationary plasma thrusters," *Journal Vacuum Science Technology*, Vol. 17, No. 6, pp. 3246-3254, 1999.
- [119] J. A. Menart and M. J. Patterson, "Magnetic circuit for enhanced discharge chamber performance of a small ion thruster," presented at Joint Propulsion Conference, AIAA-98-3343, Cleveland, Oh, 1998.
- [120] J. E. Foster and M. J. Patterson, "Internal Plasma Properties and Enhanced Performance of 8-Centimeter Ion Thruster Discharge," *Journal of Propulsion and Power*, Vol. 17, No. 2, pp. 428-432, 2001.
- [121] M. J. Patterson, S. P. Grisnik, and G. C. Soulas, "Scaling of Ion Thrusters to Low Power," presented at Internal Electric Propulsion Conference, IEPC-97-098, Cleveland, OH, 1997.
- [122] H. R. Kaufman, "Technology of Electron Bombardment Ion Thrusters," *Advances in Electron and Electron Physics*, Vol. 36, pp. 266-272, 1974.
- [123] M. J. Patterson, "Low-power ion thruster development status," presented at Joint Propulsion Conference, AIAA-98-3347, Cleveland, Oh, 1998.
- [124] M. J. Patterson, M. T. Domonkos, C. Capenter, and S. Kovaleski, "Recent Development Activities in Hollow Cathode Technology," presented at International Electric Propulsion Conference, IEPC-01-270, Pasadena, Ca, 2001.
- [125] J. A. Vaughn and P. J. Wilbur, "Ring Cusp / Hollow Cathode Discharge Performance Studies," presented at International Electric Propulsion Conference, IEPC-88-064, Colorado Springs, Co, 1988.
- [126] M. Walker and A. D. Gallimore, "Hot Flow Pressure Map of a Vacuum Facility as a Function of Flow Rate to Study Facility Effects," presented at Internal Electric Propulsion Conference, IEPC-03-077, Toulouse, France, 2003.
- [127] R. S. Jankovsky, C. Mclean, and J. McVey, "Preliminary evaluation of a 10 kW Hall thruster," presented at Joint Propulsion Conference, AIAA-99-0456, Los Angeles, Ca, 1999.
- [128] S. Dushman, *Scientific foundations of vacuum technique*, vol. 4: New York, Wiley, 1958.

- [129] R. Hofer and A. D. Gallimore, "Ion Species Fractions in the Far-Field Plume of a High-Specific Impulse Hall Thruster," presented at Joint Propulsion Conference, AIAA-03-5001, Huntsville, Alabama, 2003.
- [130] R. R. Hofer and A. D. Gallimore, "Recent Results from Internal and Very-Near-Field Plasma Diagnostics of a High Specific Impulse Hall Thruster," presented at Internal Electric Propulsion Conference, IEPC-03-037, Toulouse, France, 2003.
- [131] T. W. Haag, "Thrust stand for high-power electric propulsion devices," *Review of Scientific Instruments*, Vol. 62, No. 5, 1991.
- [132] T. W. Haag and M. Osborn, "RHETT/EPDM performance characterization," presented at Internal Electric Propulsion Conference, IEPC-97-107, Cleveland, OH, 1997.
- [133] S.-W. Kim and A. D. Gallimore, "Plume Study of a 1.35-kW SPT-100 Using an ExB Probe," *Journal of Spacecraft and Rockets*, Vol. 39, No. 6, pp. 904-909, 2002.
- [134] S.-W. Kim, "Experimental Investigations of Plasma Parameters and Species-Dependent Ion Energy Distribution in the Plasma Exhaust Plume of a Hall Thruster," in *Department of Aerospace Engineering*. Ann Arbor, MI: The University of Michigan, 1999.
- [135] R. L. Seliger, "ExB mass-separator design," *Journal of Applied Physics*, Vol. 43, No. 5, 1972.
- [136] J. H. Moore, C. C. Davis, and M. A. Coplan, *Building Scientific Apparatus*, second ed. College Park: Perseus Books, 1989.
- [137] D. Manzella, "Stationary Plasma Thruster Ion Velocity Distribution," presented at Joint Propulsion Conference, AIAA-94-3141, 1994.
- [138] I. H. Hutchinson, *Principles of Plasma Diagnostics*. Massachusetts: Cambridge University Press, 2000.
- [139] J. M. Fife, W. A. Hargus, D. A. Jaworske, C. Sarmiento, L. S. Mason, J. R., J. S. Snyder, S. Malone, J. M. Haas, and A. D. Gallimore, "Spacecraft interaction test results of the high performance Hall system SPT-140," presented at Joint Propulsion Conference, AIAA-00-3521, Huntsville, AL, 2000.
- [140] M. Walker, R. Hofer, and A. D. Gallimore, "The Effects of Nude Faraday Probe Design and Vacuum Facility Backpressure on the Measured Ion Current Density Profile of Hall Thruster Plumes," presented at Joint Propulsion Conference, AIAA-02-4253, Indianapolis, Indiana, 2002.

- [141] R. Hofer, M. Walker, and A. Gallimore, "A Comparison of Nude and Collimated Faraday Probes for Use with Hall Thrusters," presented at International Electric Propulsion Conference, IEPC-01-020, Pasadena, Ca, 2001.
- [142] J. E. Pollard, K. D. Diamant, V. Khayms, L. Werthman, D. Q. King, and K. H. D. Grys, "Ion flux, energy, and charge-state measurements for the BPT-4000 Hall thruster," presented at Joint Propulsion Conference, AIAA-01-3351, Salt Lake City, UT, 2001.
- [143] D. Manzella, "Hall Thruster Ion Beam Characterization," presented at Joint Propulsion Conference, AIAA-95-2927, San Diego, CA, 1995.
- [144] K. Mikami, K. Komurasaki, and T. Fujiware, "Optimization of Channel Configuration of Hall Thrusters," presented at Internal Electric Propulsion Conference, IEPC-95-033, Moscow, Russia, 1995.
- [145] J. S. Sovey and M. J. Patterson, "Ion Sputtering in Electric Propulsion Facilities," presented at Joint Propulsion Conference, AIAA-91-2117, Sacramento, CA, 1991.
- [146] S. Pullins, Y.-H. Chiu, D. J. Levandier, and R. A. Dressler, "Ion dynamics in Hall effect and ion thrusters - Xe(+) + Xe symmetric charge transfer," presented at Aerospace Sciences Meeting and Exhibit, AIAA-00-0603, Reno, NV, 2000.
- [147] T. B. Smith, "Deconvolution of Ion Velocity Distributions from Laser-Induced Fluorescence Spectra of Xenon Electrostatic Thruster Plumes," in *Department of Aerospace Engineering*. Ann Arbor, MI: The University of Michigan, 2003.
- [148] V. M. Gavryshin, V. Kim, V. I. Kozlov, and N. A. Maslennikov, "Physical and Technical Bases of the Modern SPT Development," presented at Internal Electric Propulsion Conference, IEPC-97-38, Moscow, Russia, 1995.
- [149] J. M. Haas and A. D. Gallimore, "Internal plasma potential profiles in a laboratory-model Hall thruster," *Physics of Plasmas*, Vol. 8, No. 2, pp. 652-660, 2001.
- [150] J. M. Haas, A. D. Gallimore, K. McFall, and G. Spanjers, "Development of a high-speed, reciprocating electrostatic probe system for Hall thruster interrogation," *Review of Scientific Instruments*, Vol. 71, No. 11, pp. 4131-4138, 2000.
- [151] G. J. Williams, T. B. Smith, F. S. Gulczinski, and A. D. Gallimore, "Correlating Laser Induced Fluorescence and Molecular Beam Mass Spectrometry Ion Energy Distributions," *Journal of Propulsion and Power*, Vol. 18, No. 2, pp. 489-491, 2002.
- [152] R. Hofer, J. M. Haas, and A. D. Gallimore, "Development of a 45-Degree Parallel-Plate Electrostatic Energy Analyzer for Hall Thruster Plume Studies:

- Preliminary Data," presented at International Electrical Propulsion Conference, IEPC-99-113, Kitakyushu, Japan, 1999.
- [153] A. D. Gallimore, "Near- and Far-Field Characterization of Stationary Plasma Thruster Plumes," *Journal of Spacecraft and Rockets*, Vol. 38, No. 3, pp. 441-453, 2001.
- [154] L. B. King and A. D. Gallimore, "Gridded retarding pressure sensor for ion and neutral particle analysis in flowing plasmas," *Review of Scientific Instruments*, Vol. 68, No. 2, pp. 1183-1188, 1997.
- [155] M. T. Domonkos, A. D. Gallimore, C. Marrese, and J. M. Haas, "Very-Near-Field Plume Investigation of the Anode Layer Thruster," *Journal of Propulsion and Power*, Vol. 16, No. 1, pp. 91-98, 2000.
- [156] R. H. Lovburg, "Plasma Diagnostic Techniques," A. PressInc., Ed., 1965, pp. Chapter 3.
- [157] R. Piejak, V. Godyak, and B. Alexandrovich, "The electric field and current density in a low-pressure inductive discharge measured with different B-dot probes," *Journal of Applied Physics*, Vol. 81, No. 8, pp. 3416-3421, 1997.
- [158] D. C. Black, "Direct Magnetic Field Measurements of Flow Dynamics and Micro-Turbulence Enhanced Electron Collisionality in Magnetized Coaxial Accelerator Channels," in *Department of Nuclear Engineering*. Raleigh, NC: North Carolina State University, 1996.
- [159] J. M. Haas and A. D. Gallimore, "Characterization of the Internal Plasma Structure of a 5 kW Hall Thruster," presented at International Electrical Propulsion Conference, IEPC-99-078, Kitakyushu, Japan, 1999.
- [160] G. J. Williams, T. B. Smith, F. S. Gulczinski, B. E. Beal, A. D. Gallimore, and R. P. Drake, "Laser Induced Fluorescence Measurement of Ion Velocities in the Plume of a Hall Effect Thruster," presented at Joint Propulsion Conference, AIAA-99-2424, Los Angeles, Ca, 1999.
- [161] E. Ahedo, P. M. Cerezo, and M. Martinez-Sanchez, "Model of plasma-wall interaction effects in a Hall thruster," presented at Joint Propulsion Conference, AIAA-01-3323, Salt Lake City, UT, 2001.
- [162] S. C. Brown, *Basic Data of Plasma Physics*, 1994.
- [163] E. Y. Choueiri, "Fundamental difference between the two variants of Hall thrusters - SPT and TAL," presented at Joint Propulsion Conference, AIAA-01-3504, Salt Lake City, UT, 2001.

- [164] J. M. Sankovic, E. J. Pencil, and D. Jacobson, "RHETT2/EPDM Magnetic Field Integration Impacts," presented at Internal Electric Propulsion Conference, IEPC-97-109, Cleveland, OH, 1997.
- [165] P. Peterson, J. M. Haas, and A. D. Gallimore, "Experimental Investigation of a Hall Thruster Internal Magnetic Field Topography," presented at International Electric Propulsion Conference, IEPC-01-030, Pasadena, Ca, 2001.
- [166] J. M. Sankovic, D. Manzella, and M. Osborn, "RHETT2/EPDM Development Testing," presented at Internal Electric Propulsion Conference, IEPC-97-102, Cleveland, OH, 1997.